



# Tandem mass spectrometry for investigation of binding energies of host-guest complexes and structural elucidation of oligosaccharides

Parisa Bayat

## ► To cite this version:

Parisa Bayat. Tandem mass spectrometry for investigation of binding energies of host-guest complexes and structural elucidation of oligosaccharides. Theoretical and/or physical chemistry. Sorbonne Université, 2018. English. NNT : 2018SORUS108 . tel-02953259

**HAL Id: tel-02953259**

**<https://theses.hal.science/tel-02953259>**

Submitted on 30 Sep 2020

**HAL** is a multi-disciplinary open access archive for the deposit and dissemination of scientific research documents, whether they are published or not. The documents may come from teaching and research institutions in France or abroad, or from public or private research centers.

L'archive ouverte pluridisciplinaire **HAL**, est destinée au dépôt et à la diffusion de documents scientifiques de niveau recherche, publiés ou non, émanant des établissements d'enseignement et de recherche français ou étrangers, des laboratoires publics ou privés.

# Sorbonne Université

Ecole doctorale 406

*Institut Parisien de Chimie Moléculaire (IPCM) / Chimie Structurale Organique et Biologique  
(CSOB)*

## **Spectrométrie de masse en tandem pour l'étude des énergies de liaison de complexes "hôte-invité" et l'élucidation structurale d'oligosaccharides**

Par Parisa Bayat

Thèse de doctorat de Chimie moléculaire

Directeur de thèse : Prof. Richard B. Cole

Encadrant : Dr. Denis Lesage

Présentée et soutenue publiquement le 28 septembre 2018

Devant un jury composé de :

Pr. David RONDEAU	Rapporteur
Pr. László DRAHOS	Rapporteur
Pr. Guillaume VAN DER REST	Examineur
Dr. Sandrine SAGAN	Examinatrice
Pr. Richard B COLE	Directeur de thèse
Dr. Denis LESAGE	Encadrant



Except where otherwise noted, this work is licensed under  
<http://creativecommons.org/licenses/by-nc-nd/3.0/>

## Résumé

En faisant progresser la chimie hôte-invité (H-G), des efforts importants ont été déployés pour synthétiser des molécules hôtes avec des caractéristiques de reconnaissance moléculaire spécifiques et bien définies, y compris de sélectivité et d'affinité ajustable. Une étape importante dans le processus est la caractérisation des forces de liaison des complexes H-G. Cette caractérisation est typiquement réalisée en solution en utilisant la RMN ou la fluorescence. L'étude en phase gazeuse de l'énergétique des systèmes H-G est très importante pour fournir des informations concernant leurs propriétés intrinsèques de liaison.

La majeure partie de cette thèse est consacrée à l'étude de l'énergétique des complexes H-G formés par trois hôtes en cage d'hémicryptophane avec diverses molécules invitées biologiquement pertinentes. Parmi les techniques basées sur la spectrométrie de masse en tandem, nous utilisons ici la dissociation radiative infrarouge de corps noir (BIRD), la dissociation induite par collision basse énergie (CID à basse énergie), la dissociation de collision de plus haute énergie (HCD) et la CID haute pression pour les mesures énergétiques des complexes HG. Ces techniques ont été utilisées soit seules, soit en combinaison les unes avec les autres, soit avec la modélisation Rice-Ramsperger-Kassel-Marcus (RRKM). Ce travail nous a permis de développer la CID à basse énergie, technique prometteuse mais jusqu'à présent peu employée.

En plus des études de chimie H-G, nous avons comparé l'énergie de dissociation de la  $\beta$ -cyclodextrine lithiée et du maltoheptaose lithiée à l'aide de la CID basse énergie. Ces deux espèces sont relativement similaires à l'exception du fait que la première est cyclique et la seconde est un oligosaccharide linéaire. Enfin, nous avons utilisé les propriétés des différentes techniques de CID à basse énergie, de CID et du HCD pour l'analyse structurale des sucres, et aussi pour explorer le mécanisme de dissolution des oligosaccharides dans *N,N*-diméthylacétamide/chlorure de lithium (DMAc/LiCl).

Mots-clés: BIRD, CID à basse énergie, modélisation RRKM, CID, HCD, chimie hôte-invité, caractérisation structurale des oligosaccharides, DMAc/LiCl

## Summary

Subject: Tandem mass spectrometry for investigation of binding energies of host-guest complexes and structural elucidation of oligosaccharides

In advancing host-guest (H-G) chemistry, considerable effort has been spent to synthesize host molecules with specific and well-defined molecular recognition characteristics including selectivity and adjustable affinity. An important step in the process is the characterization of binding strengths of the H-G complexes. This characterization is typically performed in solution using NMR or fluorescence. Gas-phase investigation of energetics of H-G systems is of great importance in providing information regarding their intrinsic binding properties.

The major portion of this thesis is devoted to the study of the energetics of H-G complexes formed by three hemicryptophane cage hosts with various biologically-relevant guest molecules. Among the existing tandem mass spectrometry-based techniques, here we employ blackbody infrared radiative dissociation (BIRD), low-energy collision induced dissociation (low-energy CID), higher-energy collision dissociation (HCD) and high-pressure CID for measurements of energetics of H-G complexes. These techniques were used either alone, or in combination with each other, or with Rice–Ramsperger–Kassel–Marcus (RRKM) modeling. This work has allowed us to develop the low-energy CID, a promising technique, but so far infrequently used.

In addition to the H-G chemistry studies, a comparative investigation of dissociation energetics of lithiated  $\beta$ -cyclodextrin and lithiated maltoheptaose which are relatively similar to each other except that the former is a cyclic and the latter is a linear oligosaccharide, were performed using low-energy CID. Finally, the capabilities of low-energy CID, CID and HCD for structural analysis of carbohydrates, and also for exploring the dissolution mechanism of oligosaccharides in *N,N*-dimethylacetamide/lithium chloride (DMAc/LiCl) were investigated.

Keywords: BIRD, low-energy CID, RRKM modeling, CID, HCD, host-guest chemistry, structural characterization of oligosaccharides, DMAc/LiCl



## Dédicace

شکر و سپاس خدا را که بزرگ‌ترین امید و یاور در محطه محطه زندگی است

پیشکش به پدر و مادرم

استوارترین تکیه‌گاه و امن‌ترین پناه زندگانی ام

به دست‌های زحمکش پینه بسته‌شان

این رساله‌ی دکتری مرهون حمایت سخاوتمندانه و اعتمادشاد تمام مراحل زندگی ام هست

امروز، دهنخشی ام به وجودشاد و فردا کلید باغ بهشت رضای شماست

تقدیم به همسر

به سایه سار زندگی ام، پناه دل‌خستگی‌هایم و بهدم شادی‌ها و غم‌هایم

به پاس مهربانی‌ها، صبوری‌ها و حمایت‌های بی‌دریغش

به او که زندگی سرشار از عشق و محبت و آرامش برایم فراهم آورده است

## Remerciements

*First, I would like to express my sincere gratitude to my advisor Prof. Richard B. Cole for his continuous support of my Ph.D study, for his patience and encouragement. His advices always helped me during my research.*

*I am extremely thankful and indebted to Dr. Denis Lesage for his great support, sincere and valuable supervision and encouragement. The door of Denis's office was always open whenever I had a question.*

*I also acknowledge all the jury members: Prof. David Rondeau, Prof. László Drahos, Prof. Guillaume van der Rest and Dr. Sandrine Sagan who were willing to participate in my defense committee.*

*I place on record, my heartfelt thanks to Dr. David Gatineau for his excellent guidance, caring, patience and continuous support.*

*I express my sense of gratitude to Dr. Cédric Przybylski for his help, encouragement and attention.*

*I would like to thank Prof. Vincent Robert and Prof. Alexandre Martinez who were willing to collaborate with us in our host-guest chemistry projects.*

*I take this opportunity to express gratitude to all of the CSOB, "plateforme de MS" and "protéomique de l'IBPS" members, who directly or indirectly assisted me through this period.*

*I also thank my husband, Dr. Sina Marhabaie, for his sympathy, kindness and encouragement. He was always there cheering me up and stood by me through the good times and bad.*

*Finally, I would like to thank my parents, my sisters and my brother for their attention, encouragement, and support throughout my life.*

# Table of contents

<i>Table of contents</i> .....	<i>I</i>
<i>List of Abbreviations</i> .....	<i>IV</i>
<i>Introduction générale</i> .....	<i>1</i>
Chimie hôte-invité .....	2
Hémicryptophanes .....	4
Spectrométrie de masse en tandem .....	6
Ionisation par électronébulisation .....	11
Préface.....	17
<i>Chapter 1: Fundamentals of unimolecular ion dissociation</i> .....	<i>22</i>
Lindemann mechanism.....	23
Hinshelwood theory .....	27
RRK theory .....	28
Transition state theory .....	30
The RRKM/QET theory.....	32
<i>Chapter 2: A general introduction to the utilized fragmentation techniques</i> .....	<i>41</i>
Blackbody infrared radiative dissociation (BIRD) .....	42
Low-energy collision induced dissociation (low-energy CID).....	47
Higher-energy collision dissociation (HCD) .....	64
<i>Chapter 3: Low-energy CID, CID and HCD mass spectrometry for structural elucidation of saccharides and clarification of their dissolution mechanism in DMAc/LiCl</i> .....	<i>67</i>
Introduction.....	68
Experimental section .....	70
Results and discussion .....	71

Conclusion .....	88
<b>Chapter 4: Investigation of hemicryptophane host-guest binding energies using high-pressure collision induced dissociation in combination with RRKM modeling .....</b>	<b>90</b>
Introduction .....	91
Experimental Section.....	93
Modeling Detail.....	95
Results and Discussion.....	96
Conclusion .....	113
<b>Chapter 5: Investigating binding energies of host-guest complexes in the gas-phase using low-energy collision induced dissociation .....</b>	<b>115</b>
Introduction .....	116
Methodology Background.....	118
Experimental section .....	122
Results and discussion .....	123
Conclusion .....	133
<b>Chapter 6: Investigating binding energies of host-guest complexes using higher-energy collision dissociation in the gas-phase .....</b>	<b>135</b>
Introduction .....	136
Experimental section .....	137
Modeling detail .....	137
Results and discussion .....	138
Conclusion .....	146
<b>Chapter 7: Dissociation energetics of lithium-cationized <math>\beta</math>-cyclodextrin and maltoheptaose studied by low-energy collision induced dissociation .....</b>	<b>148</b>
Introduction .....	149
Experimental section .....	150

<b>Results and discussion .....</b>	<b>151</b>
<b>Conclusion .....</b>	<b>162</b>
<b><i>General conclusion.....</i></b>	<b><i>163</i></b>
<b><i>References .....</i></b>	<b><i>167</i></b>
<b><i>List of Figures.....</i></b>	<b><i>190</i></b>
<b><i>List of Tables.....</i></b>	<b><i>197</i></b>
<b><i>Curriculum Vitae .....</i></b>	<b><i>198</i></b>

## *List of Abbreviations*

<b>AC</b>	<i>Alternating current</i>
<b>APCI</b>	<i>Atmospheric pressure chemical ionization</i>
<b>APPI</b>	<i>Atmospheric pressure photo ionization</i>
<b>BDE</b>	<i>Bond dissociation energy</i>
<b>BIRD</b>	<i>Blackbody infrared radiative dissociation</i>
<b>CAD</b>	<i>Collision activated dissociation</i>
<b>CCS</b>	<i>Collision cross section</i>
<b>CD</b>	<i>Cyclodextrin</i>
<b>CEM</b>	<i>Chain ejection model</i>
<b>CID</b>	<i>Collision induced dissociation</i>
<b>CRM</b>	<i>Charge residue model</i>
<b>CTV</b>	<i>Cyclotrimeratrylene</i>
<b>DC</b>	<i>Direct current</i>
<b>DOF</b>	<i>Degree of freedom</i>
<b>DMAc</b>	<i>N,N-dimethylacetamide</i>
<b>ESI</b>	<i>Electrospray ionization</i>
<b>FEC</b>	<i>Fragmentation efficiency curve</i>
<b>FRET</b>	<i>Förster resonance energy transfer</i>
<b>FT-ICR</b>	<i>Fourier transform ion cyclotron resonance</i>
<b>HCD</b>	<i>Higher-energy collision dissociation</i>
<b>H-G</b>	<i>Host-guest</i>
<b>ICR</b>	<i>Ion cyclotron resonance</i>
<b>IEM</b>	<i>Ion evaporation model</i>
<b>KS</b>	<i>Kinetic shift</i>
<b>LMCO</b>	<i>Low mass cut off</i>
<b>Low-energy CID</b>	<i>Low-energy collision induced dissociation</i>
<b>LTD</b>	<i>Linear trapping quadrupole</i>
<b>MALDI</b>	<i>Matrix assisted laser desorption/ionization</i>
<b>MD</b>	<i>Molecular dynamics</i>
<b>MS/MS</b>	<i>Tandem mass spectrometry</i>

<b><i>m/z</i></b>	<i>Mass to charge ratio</i>
<b><i>NCE</i></b>	<i>Normalized collision energy</i>
<b><i>NMMO</i></b>	<i>N-methylmorpholine N-oxide</i>
<b><i>QET</i></b>	<i>Quasi equilibrium theory</i>
<b><i>REX</i></b>	<i>Rapid energy exchange</i>
<b><i>RF</i></b>	<i>Radiofrequency</i>
<b><i>RRK</i></b>	<i>Rice-Ramsperger-Kassel theory</i>
<b><i>RRKM</i></b>	<i>Rice–Ramsperger–Kassel–Marcus theory</i>
<b><i>SID</i></b>	<i>Surface induced dissociation</i>
<b><i>SY</i></b>	<i>Survival yield</i>
<b><i>TIMS</i></b>	<i>Trapped ion mobility mass spectrometry</i>
<b><i>TCID</i></b>	<i>Threshold collision induced dissociation</i>
<b><i>Tren</i></b>	<i>Tris(2-aminoethyl)-amine</i>
<b><i>TS</i></b>	<i>Transition state</i>
<b><i>WUB</i></b>	<i>Wang Chang–Uhlenbeck–de Boer</i>

---

## ***Introduction générale***

---



## Chimie hôte-invité

La chimie supramoléculaire est définie comme la chimie des liaisons non-covalentes,<sup>1</sup> ce qui concerne des structures artificielles telles que des récepteurs, des capteurs, des complexes d'inclusion, etc., dont les blocs de construction sont maintenus ensemble en utilisant des interactions non covalentes. La portée de la chimie supramoléculaire n'est pas définie avec précision, et elle peut inclure une large gamme de liaisons non-covalentes provenant d'interactions très faibles de Van-der-Waals jusqu'à des liaisons de coordination métalliques très fortes. La comparaison du système supramoléculaire avec les molécules améliore notre compréhension à leur égard. Dans la chimie supramoléculaire, l'accent est mis sur un système dans son ensemble, dans lequel les interactions entre les blocs moléculaires sont étudiées, alors que dans le système moléculaire, l'accent est mis sur une molécule, où la connectivité entre les atomes doit être considérée. Dans un système supramoléculaire, les interactions entre les blocs sont réversibles et fortement dépendantes de l'environnement. Par contre, dans une molécule, les interactions entre les atomes sont irréversibles et indépendantes de l'environnement.<sup>1</sup>

La chimie hôte-invité (Host-Guest, H-G) est une subdivision de la chimie supramoléculaire qui implique l'établissement de multiples liaisons non covalentes entre une molécule organique grande et concave géométriquement (l'hôte) et une molécule ou ion organique ou inorganique plus simple (l'invité) **Figure 1.**<sup>2</sup> Diverses interactions non covalentes sont impliquées : liaisons hydrogène, interactions cation- $\pi$ , interactions polaire- $\pi$ , interactions CH- $\pi$ , interactions CH- $\pi$  aromatique, interactions  $\pi$ - $\pi$ , attractions électrostatiques des paires d'ions, et coordination métallique peuvent être impliquées. Ces interactions mentionnées sont différentes les unes des autres non seulement du point de vue de leur force, mais aussi de leur orientation. Par exemple, alors que pour la liaison hydrogène mais également pour la coordination métallique, une disposition géométrique correcte du donneur et de l'accepteur (ou ligand et métal, respectivement) est d'une grande importance, pour les forces électrostatiques, la distance entre centres de charge est importante.

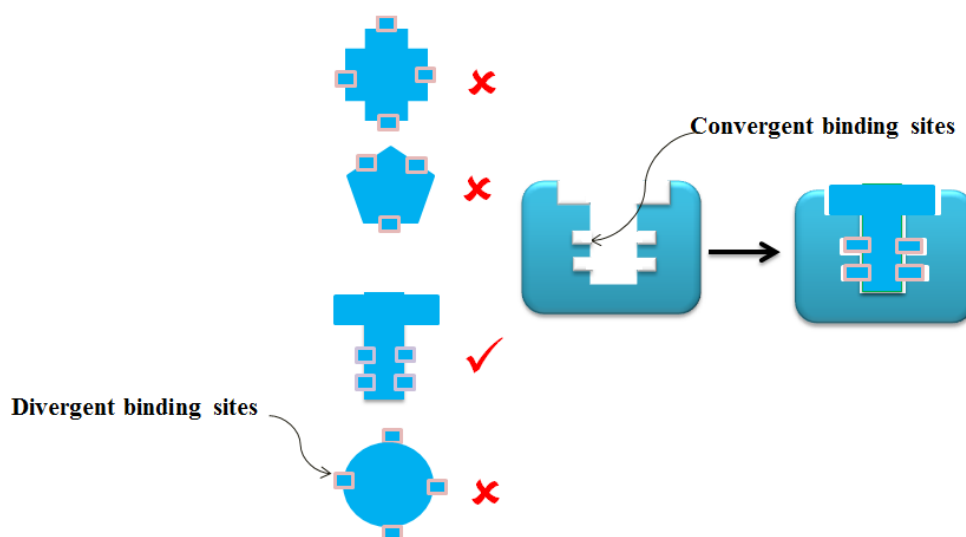


**Figure 1-** Complexe H-G entre un hôte avec des sites de liaison concaves et un invité ayant une géométrie appropriée et des sites de liaison convexes.

Diverses techniques analytiques ont été utilisées pour l'analyse et la caractérisation des complexes H-G. Parmi les plus courantes citons, la cristallographie aux rayons X, la spectroscopie de résonance magnétique nucléaire et la spectroscopie UV-visible. En développant des techniques d'ionisation douces telles que l'ionisation par électrobulbion ou électrospray (ESI)<sup>3-5</sup> et la désorption/ionisation laser assistée par matrice (MALDI),<sup>6,7</sup> la spectrométrie de masse (**Figure 2**) est devenue un outil analytique important pour les études H-G. Les études en phase gazeuse des complexes « hôte-invité » peuvent fournir des informations utiles qui sont soit difficiles à obtenir en utilisant d'autres techniques, soit complémentaires à celles-ci.<sup>8</sup> En utilisant la spectrométrie de masse, on peut obtenir des informations sur le poids moléculaire, la composition élémentaire et l'état de charge des complexes non-covalents. Des conditions sans environnement dans le vide poussé d'un spectromètre de masse peuvent être exploitées pour étudier les propriétés intrinsèques de l'interaction H-G. Par la conception systématique de systèmes modèles, la contribution de divers types d'interactions dans l'énergie de liaison finale peut être mesurée. De plus, la comparaison des résultats en phase gazeuse avec ceux de la solution peut être utilisée pour étudier l'influence du solvant et du contre-ion en l'absence de phénomène d'échange rapide. En outre, les quantités thermodynamiques et cinétiques des systèmes supramoléculaires en plus du mécanisme des différentes voies de dissociation peuvent être déterminées en

utilisant la spectrométrie de masse. Enfin, grâce à l'absence d'environnement des ions dans le spectromètre de masse, contrairement aux données de la phase de condensation, les résultats obtenus à l'aide de cette technique peuvent être directement comparés aux résultats de la chimie théoriques.<sup>8</sup>

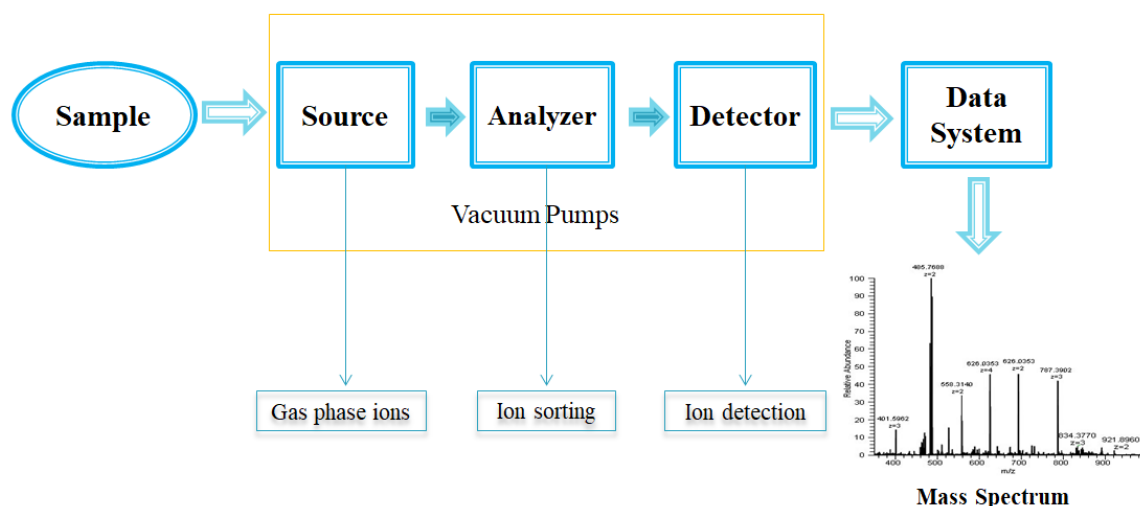


*Figure 2- Un schéma général d'un spectromètre de masse.*

## Hémicryptophanes

Les « conteneurs moléculaires », définis comme des structures contenant une cavité tridimensionnelle, ont diverses applications dans la reconnaissance moléculaire,<sup>9–11</sup> la livraison de médicaments,<sup>12–14</sup> la catalyse,<sup>15–17</sup> les capteurs biologiques,<sup>18–20</sup> les dispositifs de piégeage<sup>21,22</sup> etc. Jusqu'à présent, une large variété de cages a été introduite et utilisée comme contenant moléculaires tels que les éthers couronnes,<sup>23,24</sup> cryptands,<sup>24</sup> calixarènes,<sup>25,26</sup> résorcinarènes,<sup>27,28</sup> cucurbiturils,<sup>29,30</sup> cyclodextrines,<sup>31,32</sup> pillararènes,<sup>33,34</sup> cryptophanes<sup>35,36</sup> et les hémicryptophanes.<sup>37,38</sup> Parmi les cavités mentionnées ci-dessus, les cryptophanes et les hémicryptophanes sont basés sur un groupe cyclotribenzylène qui, la plupart du temps, est un dérivé du cyclotriarylène (CTV) unité ( $X = Y = -OCH_3$ ) (**Figure 3**).

Les cryptophanes sont constitués de deux unités CTV qui sont connectées entre elles à l'aide de trois ponts ou molécules liantes (linkers), créant ainsi un creux 3D pouvant accueillir diverses molécules comme le méthane, les époxydes, les cations, les anions, etc.<sup>37,39</sup>

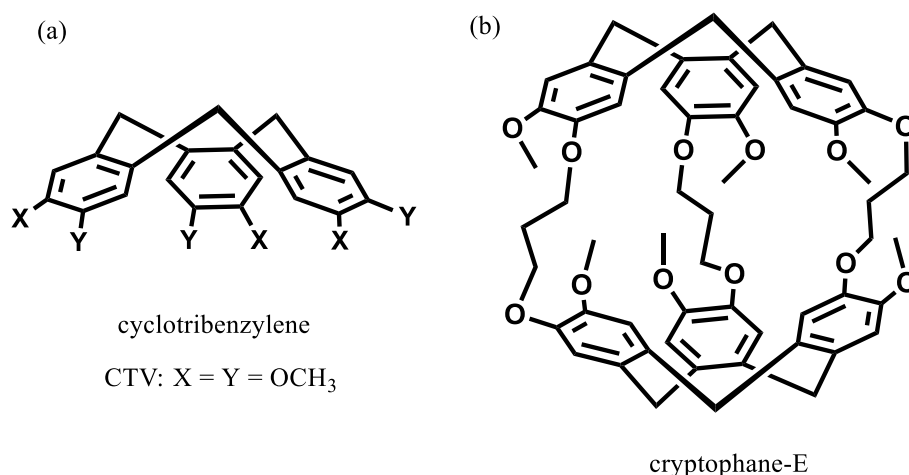


**Figure 3-** (a) Cyclotribenzylène et cyclotrimeratrylène (CTV,  $X = Y = \text{OCH}_3$ ) et (b) Cryptophane-E.<sup>37</sup>

La structure des hémicryptophanes est similaire à celle des cryptophanes mais, dans le cas, l'un des bouchons CTV est remplacé par un groupe organique  $\text{C}_3$ -symétrique. En fonction de leurs structures, les hémicryptophanes sont capables d'encapsuler différents invités, tels que des paires d'ions, des zwitterions, des ammoniums, des hydrates de carbone etc. En tant que récepteurs moléculaires, les hémicryptophanes présentent certains avantages 1) La présence du bouchon CTV donne la rigidité requise à la cavité afin d'avoir une meilleure liaison de l'invité. En outre, la taille du conteneur peut être facilement ajustée en changeant le type de molécules liantes (ou linkers) 2) Le groupe organique  $\text{C}_3$ -symétrique au fond de la cage peut être modifié facilement afin de concevoir différentes architectures d'hôtes homoditopique et hétéroditopique pour l'encapsulation d'invités spéciaux comme des cations, des anions ou des molécules. 3) La détection de la complexation hôte- invité peut être facilement réalisée en incorporant des groupes de signalisation, par exemple des fluorophores, dans la structure de la cage, soit dans la position des linkers, soit dans le nord ou le sud de l'hémicryptophane. 4) Grâce à la chiralité de l'unité CTV, on s'attend à observer une capacité de reconnaissance énantio-diastéréosélective.<sup>38</sup>

Jusqu'à présent, la chimie de l'hôte-invité des hémicryptophanes a été étudiée à la fois en phase solide et en solution. Dans la phase solide, des structures cristallines pour les complexes d'inclusion de diverses cages d'hémicryptophane avec du toluène,<sup>40</sup>  $\text{CH}_2\text{Cl}_2$ ,<sup>41</sup> pentane,<sup>41</sup> eau,<sup>42</sup>  $\text{CH}_3\text{CN}$ ,<sup>43,44</sup> acétylcholine,<sup>45</sup> etc. en tant qu'invités ont été rapportées. Cependant, la plupart des systèmes H-G ont été explorés en solution. Les principales

interactions que l'hémicryptophane peut avoir avec les hôtes sont la liaison hydrogène et les interactions cation- $\pi$  ou anion- $\pi$  dues à la présence d'une unité CTV qui fournit un environnement aromatique sur la cage. En outre, comme il a été mentionné précédemment, la chiralité de la coiffe CTV peut être utilisée pour la reconnaissance énantiosélective.<sup>46,47</sup>

Les Hemicryptophanes ont été largement utilisés pour la reconnaissance des invités d'ammonium tels que les ammoniums primaires,<sup>48,49</sup> neurotransmetteur choline,<sup>50</sup> invités chiraux d'ammonium,<sup>51,52</sup> acétylcholine,<sup>45</sup> et les sels de chlorure d'ammonium.<sup>45</sup> Des hémicryptophanes hétéroditopiques ont été utilisés pour la reconnaissance de paires d'ions<sup>53–55</sup> et zwitterions<sup>42,56–58</sup> par complexation du côté cationique des invités avec la coiffe CTV en utilisant les interactions -C-H ...  $\pi$  et cation ...  $\pi$ , et le côté anionique de l'invité avec le groupe sud de la cage. Les Hemicryptophanes sont également apparus comme des récepteurs potentiels pour la reconnaissance des glucides<sup>59–62</sup> et des fullerènes.<sup>63</sup>

En résumé, les hémicryptophanes sont des conteneurs moléculaires remarquables qui peuvent accueillir une variété d'invités neutres ou chargés et chiraux ou achiraux. Grâce à la présence du bouchon CTV, ils bénéficient d'une cavité pré-organisée dont la taille et la forme peuvent être ajustées en variant le type de linkers. En outre, un groupe organique  $C_3$ -symétrique au sud de la cage peut être sélectionné de manière à avoir une capacité de reconnaissance hétéroditopique vis-à-vis des paires d'ions et des invités zwitterioniques.

## Spectrométrie de masse en tandem

La spectrométrie de masse, au cours des dernières décennies, est devenue une technique importante qui a de nombreuses applications en chimie et en biologie. Initialement, les spectromètres de masse étaient constitués d'un seul étage d'analyseur de masse et la caractérisation structurale des ions était basée sur la fragmentation des ions moléculaires au cours de leur formation ou à l'intérieur de la source d'ionisation. Le développement de techniques d'ionisation douces telles que l'ionisation par électrospray et la désorption/ionisation laser assistée par matrice a aidé à produire des ions moléculaires intacts, mais en même temps, ces techniques ont minimisé la formation d'ions fragments limitant ainsi l'élucidation structurale d'ions en utilisant des spectromètres de masse à un

seul étage. Par conséquent, la spectrométrie de masse en tandem (MS/MS) est apparue comme un outil crucial pour l'étude structurale des molécules chimiques et biologiques.

La spectrométrie de masse en tandem est une technique qui implique la sélection d'un ion particulier, à savoir l'ion précurseur, puis son activation, généralement par collision ou absorption de photons, pour le dissocier et produire des ions fragments.<sup>64</sup> La MS/MS peut être réalisée à différentes fins telles que la caractérisation structurale des ions ou la mesure de propriétés intrinsèques des ions telles que la mesure d'énergies de liaison ou la combinaison des deux. Lorsque l'activation des ions est réalisée par des collisions simples ou multiples avec un gaz neutre, la technique est appelée dissociation induite par collision (CID) ou anciennement dissociation activée par collision (CAD), et lorsqu'un matériau solide est utilisé pour l'activation ionique, la technique est appelée dissociation induite par collision sur surface (SID). Lors des collisions, une partie de l'énergie cinétique de l'ion est convertie en énergie interne pouvant conduire à la dissociation et formation d'ions fragments.

La MS/MS a d'abord été réalisée en tandem dans l'espace, ce qui implique d'agencer les analyseurs comme les quadripôles, les secteurs, le temps de vol, puis d'effectuer séquentiellement des analyses primaires et secondaires dans les analyseurs couplés. L'instrument triple quadripôle, le spectromètre de masse en tandem dans l'espace le plus largement utilisé, est représenté sur la **Figure 4**. Il est constitué d'un premier quadripôle fonctionnant à la fois avec des potentiels continus DC et alternatifs RF (requis pour la sélection de masse), une cellule de collision fonctionnant uniquement avec la tension RF où a lieu l'activation et la dissociation des ions, et enfin un troisième quadripôle similaire au premier utilisé pour l'analyse de masse des ions qui proviennent des étapes précédentes.

D'autres instruments en tandem ont été développés dans lesquels l'isolement et la fragmentation des ions sont effectués consécutivement dans le même espace. A partir de ce type d'instrument, on peut citer les pièges ioniques quadripolaires et les spectromètres de masse à résonance cyclotronique ionique (ICR).

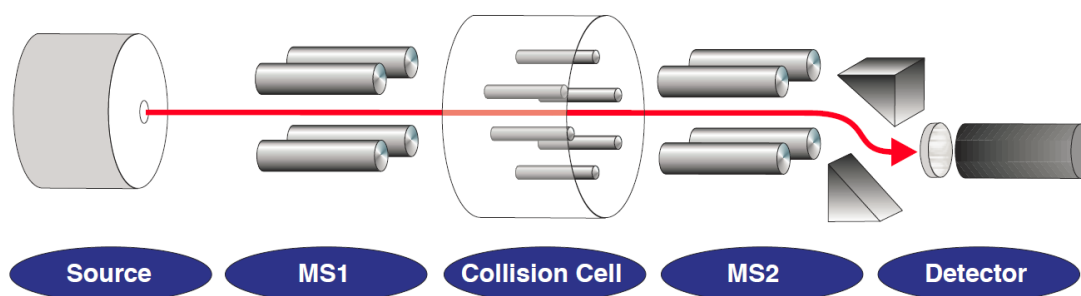


**Figure 4-** *Spectromètre de masse quadripolaire triple comme exemple d'instrument tandem-dans-l'espace (Quattro LC, Waters, Manchester, UK).*

Ces instruments permettent la sélection des ions précurseurs d'intérêt par éjection des autres. Ensuite, ces ions isolés peuvent être stockés, excités et dissociés pendant une période de temps sélectionnée. La période de temps entre la formation des ions et leur transmission au détecteur est généralement courte, et par conséquent, le taux de dissociation doit être suffisamment rapide pour permettre l'observation des ions fragments. Parfois, la vitesse de dissociation est lente, et des fragments se forment au cours de leur transmission, dans ce cas, les ions sont enregistrés comme des ions métastables. Dans le cas des pièges à ions (cellule ICR et pièges à ions quadripolaires), le temps disponible pour la dissociation des ions est plus long, et ils peuvent être utilisés pour étudier les processus de fragmentation lente.

Au cours de la fragmentation, divers phénomènes tels que l'isomérisation et/ou le réarrangement des ions précurseurs et la dissociation consécutive des ions fragments en fragments plus petits peuvent se produire. Pour les molécules organiques complexes, différents canaux réactionnels concurrents peuvent exister.<sup>65</sup> Pour étudier de tels systèmes, il faut disposer d'informations précises sur le contenu énergétique interne de l'ion précurseur et également sur la fenêtre temporelle du spectromètre de masse. La MS/MS permet l'exploration des processus mentionnés ci-dessus et c'est pourquoi c'est un outil puissant pour étudier la cinétique et les mécanismes de réactions de dissociation à l'intérieur du spectromètre de masse.

Après des décennies d'études dans le domaine de la spectrométrie de masse en tandem, le CID est devenu une technique de routine essentielle dans tous les instruments disponibles

dans le commerce. Au cours des expériences CID, initialement en appliquant un champ électrique et/ou magnétique, l'énergie de translation des ions augmente. Ensuite, par des collisions inélastiques avec un gaz neutre, une fraction de l'énergie cinétique de l'ion est transférée dans ses modes internes. Cette énergie interne est répartie entre tous les degrés de liberté de l'ion et les ions deviennent activés, ce qui entraîne une fragmentation ultérieure des ions précurseurs activés en fragments.

Pour expliquer le transfert de l'énergie cinétique en l'énergie interne, il est plus pratique d'utiliser l'énergie dans le cadre du centre de masse (c.m.) plutôt que de l'énergie dans le laboratoire (laboratoire), car seule une partie de l'énergie laboratoire est transférée lors du choc. Dans le cadre du laboratoire, les deux particules en collision (ions et neutres) sont caractérisées par leur propre position et leur propre vitesse, mais dans le cadre de comparaison, l'ensemble du système est considéré comme un tout dont le moment est toujours nul. Par conséquent, l'énergie cinétique maximale disponible qui peut être convertie en énergie interne est donnée par:

$$E_{c.m.} = \left( \frac{m_{gas}}{m_{ion} + m_{gas}} \right) E_{lab} \quad (1)$$

où  $E_{c.m.}$  est l'énergie dans le cadre du centre de masse,  $E_{lab}$  est l'énergie dans le cadre de laboratoire,  $m_{gas}$  dans la masse du gaz neutre, et  $m_{ion}$ , est celle de l'ion précurseur. D'après l'équation 1, il est évident que la quantité d'énergie cinétique maximale transférable dans le processus CID dépend de la masse des partenaires de la collision. Plus la masse du gaz cible est grande, plus  $E_{c.m.}$  est élevée, ce qui signifie une conversion plus efficace de l'énergie cinétique en énergie interne en utilisant des gaz cibles plus lourds. D'autre part, pour les ions précurseurs plus grands ( $m_{ion}$  élevé), l'énergie du centre de masse est faible, ce qui signifie moins d'énergie interne disponible pour la dissociation des gros ions.

Généralement, deux types de collisions existent : élastique et inélastique. Dans une collision élastique, l'énergie interne de l'un ou l'autre des partenaires de collision ne changera pas. Ceci n'est généralement vrai que lorsque les deux espèces en collision sont des atomes et que la collision n'est pas accompagnée d'un changement d'énergie électronique des partenaires. Dans le procédé CID, l'un des partenaires de collision est habituellement un ion



polyatomique, et le second est un gaz cible atomique ou diatomique. Dans cette situation, les collisions s'accompagnent du changement d'énergie interne de l'espèce. Ce type de collision est appelé collision inélastique. La quantité d'énergie cinétique qui est transférée en l'énergie interne est appelée endothermicité de collision ( $q$ ), qui est minimale pour la collision élastique ( $q = 0$ ), et maximale pour les collisions complètement inélastiques. Dans cette dernière condition,  $q_{max}$  est égal à l'énergie au centre de masse initiale.

Dans la technique CID, la fragmentation de l'ion précurseur peut se produire lorsque la quantité d'énergie déposée sur l'ion est plus grande que son seuil (critique) d'énergie pour la dissociation. Cependant, dans la plupart des cas, l'énergie déposée doit être beaucoup plus élevée que l'énergie du seuil afin d'observer la fragmentation. Cette énergie supplémentaire est appelée déplacement cinétique et dépend de divers paramètres tels que l'énergie critique nécessaire pour casser la liaison, l'entropie de l'état de transition, le temps disponible pour la décomposition et la taille des ions.

Pour avoir une meilleure idée du déplacement cinétique, il sera expliqué pour une simple réaction de dissociation de liaison comme suit:



où  $M$  est la molécule précurseur,  $M^+$  est l'ion précurseur,  $F^+$  est l'ion fragment,  $N$  est le fragment neutre,  $E_I$  est l'énergie d'ionisation de l'ion précurseur et  $D$  est son énergie de dissociation. Selon l'équation 2, l'énergie d'apparition de l'ion fragment ( $E_{app}$ ) est la somme de l'énergie d'ionisation de  $M$  et de l'énergie de dissociation de  $M^+$ . Par conséquent, l'énergie de liaison ionique est donnée par:

$$D(F^+ - N) = E_{app}(F^+) - E_I(M) \quad (3)$$

Dans les premières études de l'énergétique de fragmentation ionique à l'intérieur du spectromètre de masse, il a été observé que même si un ion a suffisamment d'énergie pour se dissocier, il peut ne pas avoir suffisamment de temps pour se décomposer dans la fenêtre temporelle disponible du spectromètre de masse. Ce problème est plus prononcé pour les molécules de grandes tailles possédant de nombreux degrés de liberté vibrationnels qui

rendent leur dissociation encore plus lente. Dans cette condition, une quantité supplémentaire d'énergie (déplacement cinétique) doit être déposée sur l'ion pour voir la fragmentation à un taux détectable, et par conséquent, l'équation 3 n'est plus valide. Par conséquent, il faudra estimer ce déplacement cinétique afin de mesurer avec précision l'énergie de dissociation de la liaison.

Le mécanisme de fragmentation dans le processus CID sera expliqué en détail au Chapitre 1.

## Ionisation par électronébulisation

Le développement de l'ionisation par électronébulisation (souvent appelée ionisation électrospray ou ESI)<sup>3-5</sup> et de la désorption/ionisation laser assistée par matrice<sup>6,7</sup> (MALDI) a initié une profonde révolution dans le domaine de la spectrométrie de masse car ces techniques d'ionisation douces ont permis d'étudier une grande variété de molécules chimiques mais surtout biologiques. Avec la technique MALDI, les ions en phase gazeuse sont formés en dirigeant une impulsion laser sur les analytes incorporés dans une matrice solide. Avec la technique ESI, les ions en phase gazeuse sont directement formés à partir de la solution en appliquant une haute tension. L'un des principaux avantages de l'ESI par rapport au MALDI est la possibilité de le coupler avec la chromatographie liquide et l'électrophorèse capillaire, ce qui permet la séparation en ligne de mélanges complexes avant l'analyse.

Les bases du fonctionnement de l'ESI sont les suivantes: la solution diluée d'analyte est introduite avec un faible débit dans un capillaire métallique à l'aide d'une pompe à seringue. Une tension électrique élevée est appliquée entre le capillaire métallique et l'entrée du spectromètre de masse, généralement entre 2 et 5 kV. Cela conduit le liquide à la pointe du capillaire à faire saillie et à former un cône de Taylor à partir duquel de petites gouttelettes contenant une quantité excessive de charges sont émises (**Figure 5**). Ces gouttelettes se déplacent vers l'entrée du spectromètre de masse et, en cours de route, produisent les ions de l'analyte. Pour faciliter le processus de pulvérisation, un gaz de nébulisation est habituellement introduit coaxialement à la solution d'échantillon. De plus, un gaz chauffé est également utilisé pour aider à la désolvatation des gouttelettes chargées.

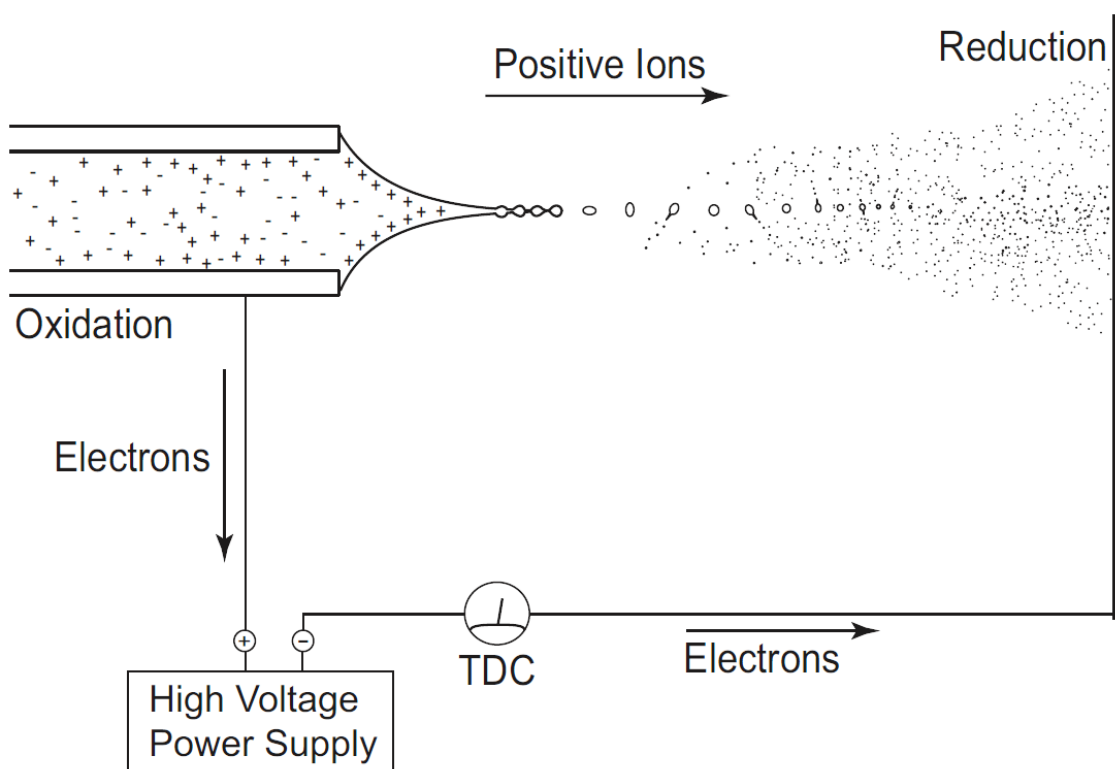


**Figure 5-** Schéma général d'une source d'ionisation par électronébulisation fonctionnant en mode ions positifs (TDC: courant total de gouttelettes).<sup>66</sup>

En travaillant en mode ions positifs, les gouttelettes contiennent principalement un grand nombre de protons qui peuvent être générés à l'intérieur du capillaire métallique (qui agit comme une cellule électrochimique) par exemple par oxydation de l'eau. En plus du proton, l'ion ammonium et les métaux alcalins (principalement  $\text{Na}^+$ ) sont d'autres ions qui peuvent exister à l'intérieur des gouttelettes chargées. En mode ions négatifs, la principale source d'ions en excès est la réduction électrochimique. Alors que les gouttelettes volent du cône de Taylor vers l'entrée du spectromètre de masse, leur volume diminue en raison de l'évaporation du solvant, mais leur charge reste constante. En conséquence, leur densité de charges augmente jusqu'à l'arrivée de la limite dite de Rayleigh dans laquelle la tension superficielle est équilibrée avec la répulsion coulombienne. À cette limite, la charge moyenne sur chaque gouttelette,  $Q_{\text{Rayleigh}}$  est donnée par:

$$Q_{\text{Rayleigh}} = 8\pi R^{3/2} \sqrt{\gamma \epsilon_0} \quad (4)$$

où  $R$  est le rayon de la gouttelette,  $\gamma$  est la tension de surface et  $\varepsilon_0$  est la permittivité du vide. Dans la limite de Rayleigh, les gouttelettes deviennent instables et subissent une fission pour produire des gouttelettes descendantes plus petites. Ce processus d'évaporation/fission du solvant sera répété pour produire les ions d'analyte qui seront analysés par le spectromètre de masse.

Trois mécanismes différents ont été proposés pour la production d'ions à partir des gouttelettes chargées: le modèle d'évaporation ionique (IEM), le modèle de résidu chargé (CRM) et le modèle d'éjection de chaîne (CEM). Mais avant d'entrer plus en détail dans les mécanismes, il faut d'abord répondre à cette question: où est la position des charges sur les gouttelettes? En fait, dans tous les mécanismes mentionnés ci-dessus pour l'ESI dont il sera question plus loin, on considère que les ions sont situés à la surface des gouttelettes en se basant sur la loi de Gauss.<sup>67</sup> Cependant, ceci n'est pas conforme à la tendance des ions tels que les cations de métaux alcalins pour la solvation. Konermann et ses collaborateurs ont tenté d'expliquer cette incohérence en effectuant des simulations de dynamique moléculaire (MD) sur des nano-gouttelettes d'eau contenant du  $\text{Na}^+$  près de la limite de Rayleigh.<sup>68,69</sup>

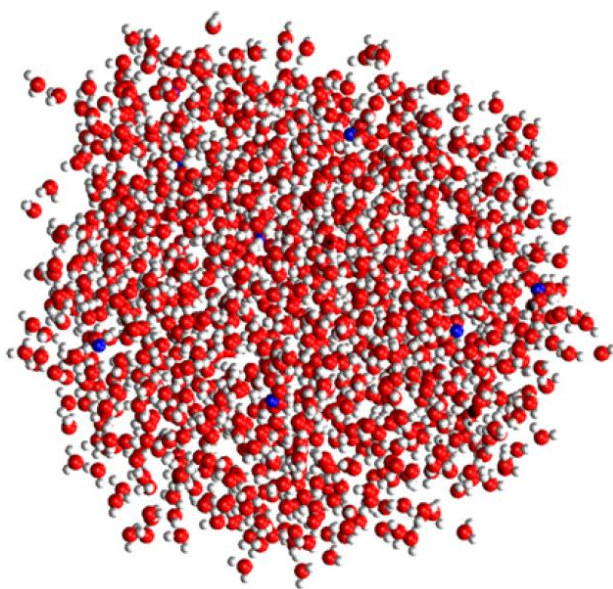


**Figure 6-** Instantané d'une nano-gouttelette d'eau contenant du  $\text{Na}^+$  près de la limite de Rayleigh, générée à l'aide de simulations de dynamique moléculaire ( $\text{Na}^+$  est représenté en bleu, oxygène en rouge et hydrogène en blanc).<sup>68</sup>

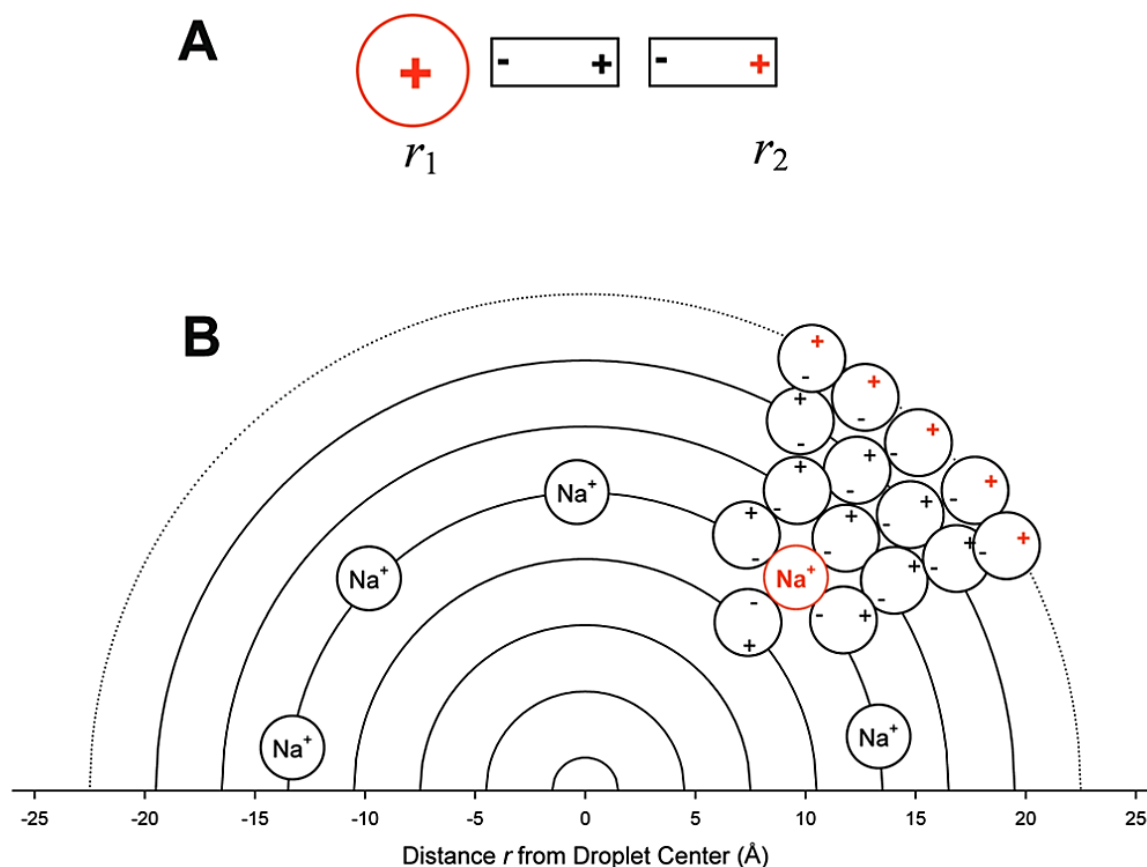


**Figure 7-** A- Interaction d'un ion positif avec deux dipôles, et B- une vue schématique de l'arrangement des molécules d'eau et des ions  $\text{Na}^+$  dans les nano-gouttelettes d'eau.<sup>68,69</sup>

Les simulations MD ont montré que pour une meilleure solvation, les porteurs de charge préfèrent prendre position à l'intérieur des gouttelettes (**Figure 6**). Cependant, même dans ces conditions, la charge nette est située à la surface des gouttelettes. Cela peut s'expliquer par la propriété dipolaire des molécules d'eau et la façon dont elles interagissent avec les ions.

Comme cela est représenté sur la **Figure 7A**, l'orientation et l'agencement de deux dipôles en contact avec un porteur de charge conduit au transfert de charge de la position  $r_1$  à la position  $r_2$ , même si cette charge est partiellement neutralisée par les dipôles. Le même processus se produit dans les nano-gouttelettes. Comme le montre la **Figure 7B**,  $\text{Na}^+$  est situé à l'intérieur des gouttelettes, mais il induit une polarisation et une disposition des molécules d'eau de telle manière telle que sa charge est projetée sur la surface de la gouttelette.

## Modèle d'évaporation d'ions (IEM)

Selon le mécanisme IEM proposé en premier par Iribarne et Thomson,<sup>70,71</sup> lors du processus d'évaporation/fission des solvants lorsque les rayons des gouttelettes deviennent inférieurs à 10 nm, au lieu de la fission de Coulomb, les gouttelettes commencent à émettre les ions d'analyte. En fait, en raison du champ électrique élevé produit par des gouttelettes chargées dont les rayons sont proches du rayon de Rayleigh, les ions solvatés sont éjectés de la surface des gouttelettes (**Figure 8a**). La constante de vitesse d'éjection ( $k_{\text{éjection}}$ ) des ions basée sur la théorie de l'état de transition est donnée par:

$$k_{\text{éjection}} = \frac{k_B T}{h} \exp\left(\frac{-\Delta G^*}{k_B T}\right) \quad (5)$$

où  $k_B$  est la constante de Boltzmann,  $h$  est la constante de Planck,  $T$  est la température et  $\Delta G^*$  est l'énergie libre d'activation. En extrayant l'équation 5, deux forces opposées sur l'ion éjecté ont été considérées : 1) la répulsion coulombienne entre l'ion s'évaporant et les autres ions restants sur la gouttelette, et 2) l'attraction coulombienne entre l'ion et les molécules de solvant polarisées sur la gouttelette. Lorsque ces deux forces opposées sont égales, l'état de transition est atteint. Des simulations MD sur des gouttelettes de mélange eau/méthanol contenant des ions  $\text{NH}_4^+$  ont montré que par rapport aux gouttelettes purement aqueuses, la présence de méthanol augmente la vitesse d'éjection des ions et l'évaporation du solvant due à la tension superficielle inférieure à celle de l'eau.<sup>72</sup>

Les ions éjectés de la surface de la gouttelette forment une petite grappe composée de quelques molécules de solvant qui à l'aide d'un gaz de fond s'évaporeront pendant le vol vers le spectromètre de masse.

Le mécanisme d'électropulvérisation des ions de faible poids moléculaire est supposé être réalisé par le biais du modèle d'évaporation ionique.<sup>70</sup>

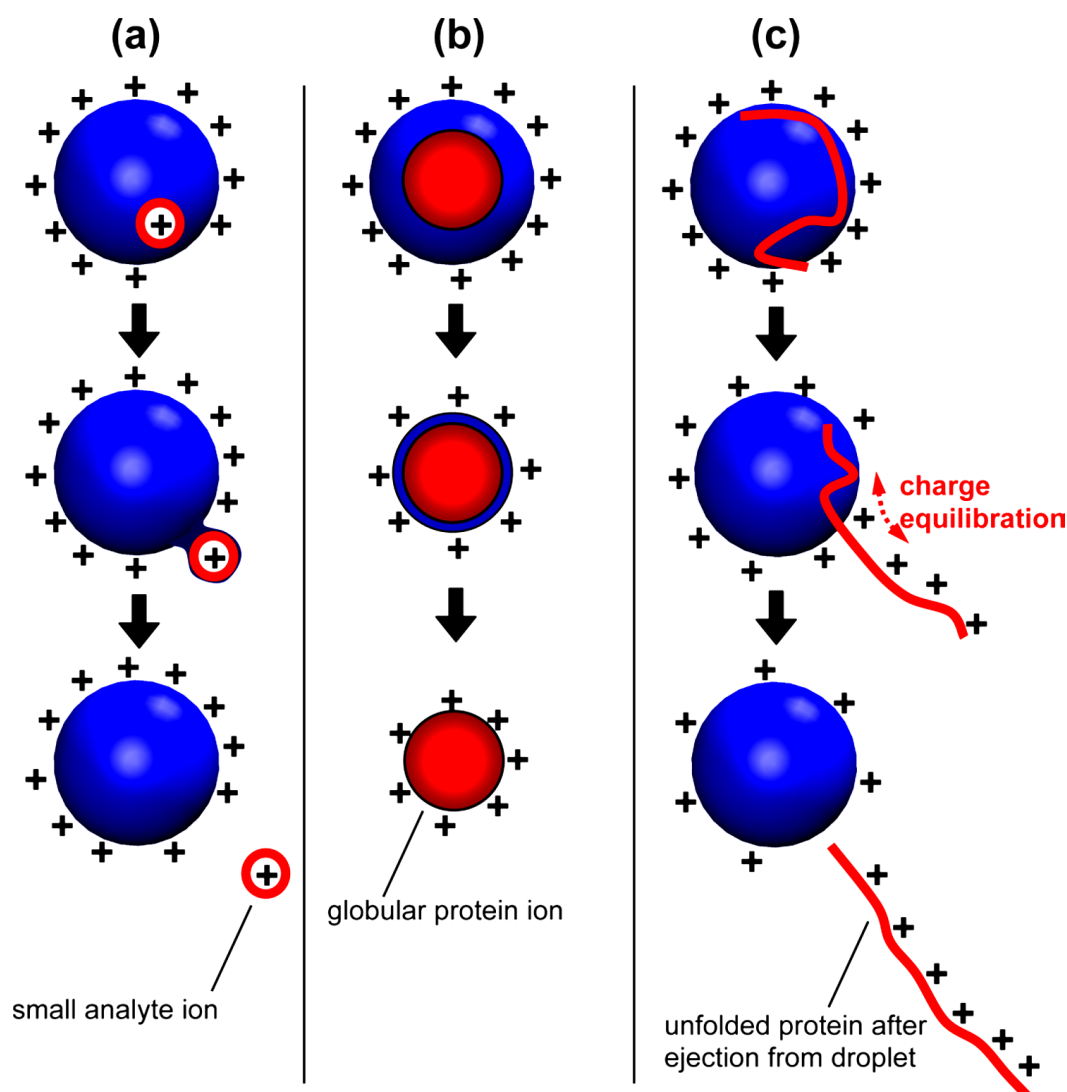


**Figure 8-** Différents mécanismes proposés pour l'ionisation par électrospray ionisation : (a) Modèle d'évaporation ionique, (b) Modèle de résidu chargé, et (c) Modèle d'éjection de chaîne.<sup>68</sup>

### Modèle de résidu chargé (CRM)

Ce mécanisme a été proposé par Dole et al. en 1968<sup>73</sup> pour expliquer la formation d'ions de masse moléculaire élevée à partir des gouttelettes très fines et fortement chargées formées par fission (comme expliqué ci-dessus). Selon le modèle CRM, la répétition du processus d'évaporation/fission du solvant (pendant le temps de vol des gouttelettes entre le cône de Taylor et le spectromètre de masse) conduit finalement à la formation de quelques gouttelettes contenant du solvant, des charges ioniques et une seule macro-molécule. Une nouvelle évaporation du solvant à partir de ces gouttelettes conduit à la génération d'ions analytes dont la charge provient de la charge de la gouttelette (**Figure 8b**). Diverses études

ESI-MS sur les protéines ont montré que leurs ions dans la source d'électronébulisation sont formés à l'aide de CRM.<sup>74,75</sup>

### Modèle d'éjection de chaîne (CEM)

Le modèle CRM, expliqué dans la section précédente, est principalement applicable aux protéines à structure globulaire compacte dans lesquelles les parties hydrophobes sont repliées à l'intérieure de la molécule et où les parties polaires sont situées à l'extérieur. Ces conformations sont dominantes dans les solutions aqueuses neutres. Dans des conditions où les protéines sont dépliées, par exemple dans des solutions acides, les études MD montrent que leur ionisation se produit avec un mécanisme différent qui est appelé modèle d'éjection de chaîne (**Figure 8C**).<sup>68,76,77</sup> La protéine dépliée a une structure désordonnée et étendue, ainsi toute la protéine est exposée au solvant. Dans le processus d'électronébulisation, et après un processus répété d'évaporation/fission de solvant, lorsque de fines gouttelettes sont formées, les chaînes dépliées se déplacent à la surface de la gouttelette. Ensuite, de façon similaire à ce qui se passe dans le modèle IEM, la chaîne protéique est progressivement éjectée de la gouttelette.

Le modèle CEM n'est pas limité aux protéines dépliées et il est également applicable aux chaînes polymères non polaires 1) désordonnées, 2) partiellement hydrophobes et 3) ayant la capacité de se lier à un grand nombre de charges ioniques.<sup>76,78</sup>

### Préface

L'objectif de cette thèse est d'étudier différents systèmes moléculaires (divers complexes H-G et oligosaccharides linéaires et cycliques additionnés de métaux) en utilisant diverses techniques de spectrométrie de masse en tandem. Parmi ces techniques, citons la dissociation radiative infrarouge due au corps noir (BIRD) dans un spectromètre à résonance cyclotronique à transformée de Fourier (FT-ICR), la dissociation induite par collision à basse énergie (CID à basse énergie) et la dissociation par collision à énergie plus élevée (HCD) dans un spectromètre de masse hybride à piégeage linéaire (LTQ)/Orbitrap, et CID haute pression dans un spectromètre de masse triple quadripolaire.



Les techniques mentionnées ci-dessus ont été employées à différentes fins telles qu'expliquer les spectres de fragmentation observés des oligosaccharides linéaires adduits au métal, qu'estimer les énergies de liaison des complexes hôte-invité et obtenir des informations sur la barrière de dissociation et l'entropie des voies de décomposition individuelles d'adduits métalliques d'oligosaccharides cycliques. Dans ce contexte, les deux premiers chapitres de cette thèse sont destinés à fournir des informations théoriques nécessaires pour avoir une meilleure compréhension des techniques utilisées.

Le premier chapitre est consacré à l'explication des fondements de la dissociation unimoléculaire. À cet égard, le mécanisme de Lindeman, la théorie de Hinshelwood, la théorie RRK et la théorie RRKM/QET sont discutés de manière concise. De plus, comme la théorie RRKM est formulée à partir de la théorie de l'état de transition, cette dernière théorie, qui explique la constante de vitesse des réactions bimoléculaires, est brièvement expliquée.

Dans le deuxième chapitre, trois techniques principales de spectrométrie de masse en tandem de BIRD, CID et HCD basse énergie sont présentées. De plus, étant donné que la CID à basse énergie constitue la majeure partie de cette thèse, pour avoir un meilleur aperçu de cette technique, des informations générales sur le fonctionnement des pièges à ions linéaires sont également fournies.

Au Chapitre 3, nous étudions le mécanisme de dissolution des oligosaccharides dans le *N,N*-diméthylacétamide/chlorure de lithium (DMAc/LiCl), un solvant utilisé pour la dissolution de la cellulose. Seront présentées également les capacités des techniques CID, CID et HCD à basse énergie pour l'analyse structurale des carbohydrates. La comparaison des spectres obtenus en utilisant trois techniques montre que, généralement, lorsqu'on travaille avec des sucres monolithiques, les spectres CID fournissent des fragments plus structurellement informatifs, et le clivage de la liaison glycosidique est la voie principale. Cependant, lorsqu'on travaille avec des sucres di-lithiés, les spectres HCD peuvent être plus informatifs en fournissant principalement des fragments de clivage des cycles. En effet, le HCD est une technique d'activation non résonnante qui permet de déposer rapidement une plus grande quantité d'énergie, donnant accès à plus de voies de décomposition endothermiques et à

des fragmentations consécutives. La différence dans les voies de dissociation préférées des sucres monolithiques et di-lithiés indique que la présence du second lithium influence fortement les constantes de vitesse relatives des clivages entre les anneaux transversaux (réarrangement) par rapport aux clivages directs des liaisons glycosidiques, et défavorise ces derniers. En ce qui concerne le mécanisme de dissolution des sucres dans les expériences DMAc/LiCl, CID et HCD sur les sucres di-lithiés et tri-lithiés les résultats révèlent que les intensités des ions produits contenant respectivement  $\text{Li}^+$  ou  $\text{Li}^+$  sont plus élevées que celles des  $\text{Li}^+$ . De plus, la comparaison des spectres de fragmentation (HCD et CID) du sucre lithié additionné de LiCl et du sucre sodé adduit au NaCl montre que si dans ce dernier cas, la perte de NaCl est dominante, dans le premier cas, la perte de HCl se produit préférentiellement. L'ensemble de ces résultats prouve qu'il existe une interaction forte et directe entre le lithium et le saccharide au cours du processus de dissolution dans le système de solvant DMAc/LiCl.

Au Chapitre 4, nous présentons une approche multimodale basée sur la spectrométrie de masse qui permet de classer les stabilités de liaisons de deux cages d'hémicryptophane avec trois molécules hôtes biologiquement pertinentes. Une combinaison de BIRD et de CID à haute pression, ainsi que la modélisation RRKM, ont été utilisées à cette fin. Pour les deux hôtes hémicryptophanes testés, la cage contenant des liaisons naphtyle présentait des interactions plus fortes que les liaisons phényle portant une cage. Pour les deux cages, l'ordre de stabilité des hôtes est: choline > acétylcholine > bétaine. Les informations obtenues par ce type d'études de spectrométrie de masse peuvent fournir un nouvel aperçu des caractéristiques structurales qui influencent le plus la stabilité des paires H-G, fournissant ainsi des conseils pour la synthèse future.

Dans le Chapitre 5, les énergies de liaison en phase gazeuse d'une cage hétéroditopique hémicryptophane ( $\text{Zn(II)}@1$ ) avec une série d'hôtes zwitterioniques sont explorées en utilisant le CID à basse énergie. Pour utiliser cette approche, un étalonnage préliminaire de la température effective des ions subissant une excitation par résonance est nécessaire. Ceci a été accompli en employant la technique BIRD qui permet la mesure directe des paramètres d'activation. Les énergies d'activation et les facteurs pré-exponentiels d'Arrhenius ont été

évalués pour plus de 10 complexes H-G via l'utilisation de CID à basse énergie. Le temps de séjour relativement long des ions à l'intérieur du piège à ions linéaire (maximum de 60 s) a permis l'étude de dissociations avec des constantes de dissociation inférieures à  $1 \text{ s}^{-1}$ . Cette possibilité, associée à la grande taille des ions étudiés, garantit la réalisation des conditions d'échange d'énergie rapide (REX) et, par conséquent, une application directe de l'équation d'Arrhenius. Comparé à la technique BIRD, le CID à basse énergie donne accès à des températures effectives plus élevées, permettant ainsi de sonder davantage de voies de décomposition endothermiques. Sur la base des paramètres d'activation mesurés, les hôtes portant un groupe fonctionnel phosphate ( $-\text{OPO}_3^{2-}$ ) se sont révélés se lier plus fortement à la cage d'encapsulation comparativement à ceux possédant un groupe sulfonate ( $-\text{SO}_3^-$ ); cependant, ces derniers font des liaisons plus fortes que ceux avec un groupe carboxylate ( $-\text{CO}_2^-$ ). En outre, il a été observé que la présence de groupes triméthylammonium ( $\text{N}(\text{CH}_3)_3^+$ ) ou phényle dans la structure de l'hôte, améliore la force des interactions hôte-invité. L'utilisation de cette technique est très simple et ne nécessite aucune modification instrumentale. Ainsi, elle peut être appliquée à d'autres études de chimie H-G dans lesquelles la comparaison des énergies de dissociation de liaison est d'une importance primordiale.

Dans le Chapitre 6, les stabilités relatives des mêmes complexes H-G obtenues dans le Chapitre 5 sont réétudiées en utilisant HCD. Après avoir généré des courbes de rendement de survie (SY), une modélisation Rice-Ramsperger-Kassel-Marcus (RRKM) a été réalisée pour extraire les énergies critiques de dissociation pour les complexes H-G. Des énergies critiques très similaires à celles extraites des expériences CID à basse énergie ont été obtenues. Cette technique est très simple à réaliser et peut fournir des résultats relativement fiables. Cependant, en plus de l'exigence d'étalonnage de la température (technique CID de basse énergie), la principale limite de cette méthode est qu'il est nécessaire de disposer des informations sur le facteur pré-exponentiel d'Arrhenius des complexes pour accéder aux énergies critiques. Par conséquent, l'utilisation de cette technique n'est possible que lorsqu'il existe des informations sur l'état de transition de la dissociation.

Enfin, au Chapitre 7, la première étude de la dissociation de l' $\beta$ -CD lithié et du G<sub>7</sub> lithié en phase gazeuse à l'aide de CID de basse énergie est présentée. Des spectres de fragmentation dissemblables ont été observés pour ces oligosaccharides, ce qui implique que leurs fragmentations passent par différentes voies de dissociation. Dans l'étape suivante, les courbes d'efficacité de fragmentation en fonction du temps ou de l'énergie montrent que la probabilité de fragmentation consécutive est minimisée dans la condition expérimentale CID à basse énergie. Ces courbes donnent ainsi l'assurance que les paramètres d'activation des voies de dissociation individuelles ne peuvent être mesurées expérimentalement à différentes amplitudes d'excitation qu'à la condition qu'une technique fiable soit utilisée pour l'étalonnage de la température effective des ions à l'intérieur du piège à ions. Par conséquent, en utilisant la technique présentée au Chapitre 5, nous avons obtenu des  $T_{eff}$  d'ions à différentes amplitudes d'excitation, puis il a été possible de construire des tracés d'Arrhenius pour les voies générales de dissociation et de dissociation individuelles. Ainsi, l'énergie d'activation et les facteurs pré-exponentiels pour tous les canaux de fragmentation de chaque oligosaccharide ont été obtenus. En dépit de la nature chimique très similaire des deux oligosaccharides, des paramètres d'activation très différents ont été observés, en accord avec leurs modèles de fragmentation observés. Dans cette étude, les résultats montrent clairement que la structure cyclique de la  $\beta$ -CD lithiée aide sa dissociation en passant par une voie entropiquement plus favorable malgré une barrière d'activation plus élevée.

---

## ***Chapter 1: Fundamentals of unimolecular ion dissociation***

---

Tandem mass spectrometry (MS/MS) is one of the most important analytical methods that has plenty of applications in chemistry and biology. This technique involves the selection of a precursor ion, and then its activation, usually by collision or photon absorption, to perform dissociation, and produce fragment ions. In addition to its analytical applications, tandem mass spectrometry can provide a profound insight into the fundamental properties of ions in the gas phase. Here, before explaining the employed activation techniques in this thesis, first, basic theories of unimolecular dissociation will be discussed. In this regard, Lindeman mechanism, Hinshelwood theory, RRK theory and RRKM/QET theory will be described concisely. In addition, since the transition state theory was the basis of the formulation of RRKM/QET theory, it will be explained, as well.

### Lindemann mechanism

In the gas-phase reactions that follow first order kinetics, it seems that only one species is involved. However there is an unclear point: how do reactant ions obtain enough energy to dissociate? At the beginning, it was thought that this energy is only provided by the absorption of radiation from the surrounding. Then, in 1922, Lindemann proposed a mechanism based on collisional activation, which was further developed by Hinshelwood.<sup>79,80</sup> This theory, which is called the Lindemann mechanism, is suitable to describe thermal unimolecular reactions, and it involves both bi- and unimolecular steps. According to this theory, the precursor ion,  $AB^+$ , collides with the target gas,  $M$ , to acquire energy and undergo excitation:



Then, the excited molecular ion,  $[AB^+]^*$ , undergoes unimolecular dissociation to form the products ( $A^+$  and  $B$ ). In Equation 1.1,  $k_1$  is the rate constant for the activation to any vibrational level (no discrimination between various vibrational levels) above the critical energy ( $E_0$ ) that is the minimum required energy for decomposition;  $k_{-1}$  is the rate constant for the deactivation from any energy level above the critical energy to any energy level below it (again no discrimination between various energy levels is considered). This

deactivation rate constant is often taken to be equal to  $\lambda Z$ , in which  $Z$  is the number of collisions and  $\lambda$  is collision efficiency. In Equation 1.2,  $k_2$  is the rate constant for dissociation of the excited molecular ion. Here, the main hypothesis is that after the activated precursor ions achieve by collision the required energy for dissociation, they do not necessarily have to react. After excitation, they have enough time to lose their energy either by deactivation via another collision, or by unimolecular dissociation. Thus, the presence of this time lag is the basis of this theory.

According to the steady state approximation, the rates of the production and consumption of intermediate,  $[AB^+]^*$ , are equal; therefore, its concentration will not change during the reaction. By applying this approximation to the excited molecular ion, we can obtain an overall rate law (Equation 1.3):

$$\frac{d[AB^+]^*}{dt} = 0 = k_1[AB^+][M] - k_{-1}[AB^+]^*[M] - k_2[AB^+]^* \quad (1.3)$$

By rearrangement of Equation 1.3, concentration of  $[AB^+]^*$  can be obtained (Equation 1.4):

$$[AB^+]^* = \frac{k_1[AB^+][M]}{k_{-1}[M] + k_2} \quad (1.4)$$

Therefore, the overall reaction rate is:

$$R = \frac{dA^+}{dt} = k_2[AB^+]^* = \frac{k_1k_2[AB^+][M]}{k_{-1}[M] + k_2} \quad (1.5)$$

$$k_{overall} = \frac{k_1k_2[M]}{k_{-1}[M] + k_2} \quad (1.6)$$

Now, it will be useful to consider the behavior of the reaction rate at two limiting cases: high and low pressure of the target gas.

### High pressure limit

At a high pressure of collision gas, there are a large number of collisions. Therefore, the probability of collisional de-activation of  $[AB^+]^*$  is higher than unimolecular dissociation, i.e.  $k_{-1}[AB^+]^*[M] \gg k_2[AB^+]^*$  and the dissociation step is the rate limiting step. Under this

condition,  $k_2$  term in the denominator of the overall reaction rate can be neglected and the rate law will be simplified to:

$$R = \frac{k_1 k_2}{k_{-1}} [AB^+] \quad (1.7)$$

$$k_{high\ pressure} = \frac{k_1 k_2}{k_{-1}} \quad (1.8)$$

This is a first order rate law with the overall rate constant of  $k_1 k_2 / k_{-1}$ . In this high pressure limit which is also called rapid energy exchange (REX) limit, the population of ions has a Maxwell-Boltzmann distribution of internal energies. It should be noted that the Lindemann theory does not take into account photon absorption and emission, and only considers activation by collision.

### Low pressure limit

At a low pressure of the target gas, there are only a few collisions. In this situation, the rate of the unimolecular dissociation will be higher than collisional de-activation, i.e.  $k_2 [AB^+]^* \gg k_{-1} [AB^+]^* [M]$ . Therefore,  $k_{-1} [M]$  can be neglected in the denominator of the overall reaction rate, and the rate law will be simplified to:

$$R = k_1 [AB^+] [M] \quad (1.9)$$

According to this equation, at the low pressure limit, reaction kinetics is of second order, and bi-molecular activation is the rate determining step.

The pressure at which the rate constant arrives to half of its value at the high pressure limit can be calculated as follows:

$$k_{overall} = \frac{1}{2} k_{high\ pressure} \quad (1.10)$$

$$\frac{k_1 k_2 [M]_{1/2}}{k_{-1} [M]_{1/2} + k_2} = \frac{1}{2} \frac{k_1 k_2}{k_{-1}} \quad (1.11)$$

$$[M]_{1/2} = \frac{k_2}{k_{-1}} = \frac{k_{high\ pressure}}{k_1} \quad (1.12)$$



The equation for the overall rate constant can be also rewritten to obtain:

$$\frac{1}{k_{overall}} = \frac{1}{k_1[M]} + \frac{1}{k_{high\ pressure}} \quad (1.13)$$

Therefore, we can obtain  $k_1$  and  $k_{high\ pressure}$  values from the slope and the intercept of the linear plot of  $1/k_{overall}$  versus  $1/[M]$ .

In addition, according to the Maxwell-Boltzmann distribution, we have:

$$\frac{[AB^+]^*}{[AB^+]} = \frac{k_1}{k_{-1}} = \exp\left(\frac{-E_0}{kT}\right) \quad (1.14)$$

By replacing  $k_{-1}$  with  $\lambda Z$ :

$$k_1 = \lambda Z \exp\left(\frac{-E_0}{kT}\right) \quad (1.15)$$

From the rate constant expression at high pressure, the value of  $k_2$  can be calculated:

$$k_{high\ pressure} = \frac{k_1 k_2}{k_{-1}} = k_2 \exp\left(\frac{-E_0}{kT}\right) \quad (1.16)$$

Since  $k_2$  is constant, the temperature dependence of  $k_{high\ pressure}$  is expected to show Arrhenius behavior, and the plot of  $\log k_{high\ pressure}$  versus  $1/T$  should be linear.

To summarize, the general description of the collisional activation process proposed by the Lindemann theory properly predicts the decrease of the rate constant at low pressures. In addition, it can correctly explain the fact that the reaction rate constant is changing from first order at the high pressure limit to second order at the low pressure condition. However, it has some drawbacks, for example: as the molecules get bigger, discrepancies between experimental results and the theoretical calculations increase. Furthermore, the plot of  $1/k_{overall}$  versus  $1/[M]$  diverges from linearity in the experimental data, indicating that it is not well-described by this theory.

## Hinshelwood theory

Hinshelwood improved the Lindemann theory by taking into account vibrational degrees of freedom in the activation process.<sup>80</sup> According to the Hinshelwood theory, during collisional activation, energy is accumulated in the vibrational modes ( $s$ ) of the molecular ion. After each activation, there is a step of redistribution of internal energy among all vibrational modes. This process repeats itself until the time arrives when the geometrical arrangement of atoms in the excited molecular ion becomes suitable for the reaction.

Here, according to the Maxwell-Boltzmann distribution, we have:

$$\frac{k_1}{k_{-1}} = \frac{(E_0/kT)^{s-1}}{(s-1)!} \exp\left(\frac{-E_0}{kT}\right) \quad (1.17)$$

$$k_1 = \frac{\lambda Z (E_0/kT)^{s-1}}{(s-1)!} \exp\left(\frac{-E_0}{kT}\right) \quad (1.18)$$

By rearrangement of Equation 1.6, we obtain:

$$k_{overall} = \frac{k_2 k_1 / k_{-1}}{1 + k_2 / k_{-1} [M]} \quad (1.19)$$

By substituting of  $k_1/k_{-1}$  value from Equation 1.17, we then obtain:

$$k_{overall} = \frac{k_2}{1 + \frac{k_2}{k_{-1} [M]}} \frac{1}{(s-1)!} \left(\frac{E_0}{kT}\right)^{s-1} \exp\left(\frac{-E_0}{kT}\right) \quad (1.20)$$

According to Equation 1.20, we need the values of  $k_{-1}$ ,  $k_2$ ,  $E_0$  and  $s$  to calculate  $k_{overall}$ . To obtain them, at the beginning, we could approximate the value of  $k_2$  from the pressure in which the rate constant arrives to half of its value at the high pressure limit. Then, this primary  $k_2$  value can be used for the first approximate value of  $k_1$ . In the next step,  $k_2$ ,  $E_0$ , and  $s$  values can be found by successive iterations of this calculation, until arriving at the point where the best fit of the experimental data and the theoretical ones is obtained.

The rate constant at the high pressure limit can be obtained by:

$$k_{high\ pressure} = \frac{k_1 k_2}{k_{-1}} \quad (1.21)$$

$$k_{high\ pressure} = k_2 \frac{1}{(s-1)!} \left(\frac{E_0}{kT}\right)^{s-1} \exp\left(\frac{-E_0}{kT}\right) \quad (1.22)$$

Here, the calculation of  $k_2$ ,  $E_0$  and  $s$  will be iterated until the best fit is obtained. In spite of the fact that  $k_2$  is constant, the above equation predicts a non-linear plot for  $\ln(k_{high\ pressure})$  versus  $1/T$ , for which the linear plots are observed!

To summarize, compared to the Lindemann theory, Hinshelwood theory results in an improved fitting between experiment and theory ( $k_{overall}$  equation) by taking into account the number of normal modes ( $s$ ). Nonetheless, it still suffers from some limitations; among them, the most important one is that the observed curvature in the plots of  $1/k_{overall}$  versus  $1/[M]$  is poorly accounted for.

## RRK theory

Rice, Ramsperger,<sup>81,82</sup> and Kassel<sup>83</sup> introduced a statistical theory for the calculation of the unimolecular dissociation rate suggesting that the reaction rate depends also on the vibrational energy of the excited molecular ion. According to their theory (RRK theory), in order for dissociation to take place, a minimum of energy should be localized in special vibrational modes, and the rate constant is proportional to the probability of this localization. In other words, the unimolecular reaction rate depends on the vibrational modes of the excited molecular ion, no matter how it is activated.

They stated that the precursor ion contains  $s$  identical harmonic oscillators, among them, one is considered as the critical oscillator ( $\nu$ ) where dissociation reaction takes place. In addition, they assumed that the rate of the intramolecular distribution of excess energy is faster than the unimolecular dissociation rate (ergodic assumption), and energy flows freely among all of the oscillators. Then, they defined the transition state as the configuration in which the energy of the critical oscillator is higher than the critical energy (bond energy,  $E_0$ ).

By considering the vibrations as discrete energy levels, a quantum mechanical expression for the probability of having the transition state configuration can be calculated using Equation 1.23:

$$Probability = \frac{(n - m + s - 1)! n!}{(n - m)! (n + s - 1)!} \quad (1.23)$$

Here,  $n$  is the total number of vibrational quanta, and  $m$  is the number of quanta localized in the critical oscillator. By considering the classical limit in which the number of quanta ( $n$ ) is very large compared to the number of oscillators ( $s$ ), the above equation can be simplified as follows:

$$\frac{(n - m + s - 1)!}{(n - m)!} \approx (n - m)^{s-1} \quad (1.24)$$

$$\frac{n!}{(n + s - 1)!} \approx n^{-(s-1)} \quad (1.25)$$

$$Probability = \left(1 - \frac{m}{n}\right)^{s-1} \quad (1.26)$$

By multiplying the above probability with the frequency factor ( $\nu$ ) which is the vibrational frequency of the critical oscillator, we could obtain the dissociation rate constant:

$$k_2(E) \approx \nu \left(1 - \frac{m}{n}\right)^{s-1} \quad (1.27)$$

Then, since  $E = nh\nu$ , we will have:

$$k_2(E) \approx \nu \left(1 - \frac{E_0}{E}\right)^{s-1} \quad (1.28)$$

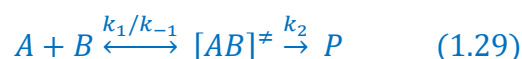
This equation shows that as energy increases, the rate constant goes up, and as the number of oscillators increases, it goes down. To obtain an acceptable agreement between experimental data and the theoretical ones, a smaller value for the number of oscillators,  $s$ , has to be used.

To summarize, the main feature of RRK theory is that when a molecular ion gets energy, this energy is rapidly distributed over all the vibrational modes of the molecule. This process

continues until the point where a sufficient amount of energy quanta is transferred into the critical oscillator, then dissociation reaction takes place. Although this theory is a significant improvement compared to the previous theories, its results have some discrepancies with experiments. These originate from the assumption of s identical oscillators having the same frequency. Nevertheless, this theory can be successfully used for the calculation of binding energies.

## Transition state theory

Transition state (TS) theory explains bi-molecular reaction rates. This theory, also called activated complex theory, was developed simultaneously by Eyring,<sup>84</sup> Evans,<sup>85</sup> and Polanyi<sup>85</sup> in 1935. According to this theory, there is a specific geometrical configuration of all the atoms in the reacting system which is called transition state or activated complex. During the reaction process, this configuration must first be obtained, before the reaction continues thereby converting this complex to the products. In the reaction coordinate (lowest potential energy pathway between reactants and products), the potential energy surface of the transition state is higher than both reactants and products. TS theory assumes that there is a quasi-equilibrium between reactants and the activated complex:



Its equilibrium constant  $K^\ddagger$  can be written as follows:

$$K^\ddagger = \frac{[AB]^\ddagger}{[A][B]} \quad (1.30)$$

Therefore, the concentration of the activated complex is:

$$[AB]^\ddagger = K^\ddagger [A][B] \quad (1.31)$$

Moreover, the rate of the product formation can be expressed as:

$$\frac{d[P]}{dt} = k_2 [AB]^\ddagger = k_2 K^\ddagger [A][B] = k_{overall} [A][B] \quad (1.32)$$

Thus, the rate constant of the overall reaction is given by:

$$k_{overall} = k_2 K^\# \quad (1.33)$$

Furthermore, from the statistical mechanics, we have:

$$k_2 = \frac{k_B T}{h} \quad (1.34)$$

in which  $k_B$  is the Boltzmann constant and  $h$  is Planck's constant. Also,  $K^\#$  relates to the Gibbs free energy difference between the reactants and the transition state ( $\Delta G^\#$ ) by Equation 1.35:

$$K^\# = \exp\left(-\frac{\Delta G^\#}{RT}\right) \quad (1.35)$$

Therefore, the rate constant is expressed by:

$$k_{overall} = k_2 K^\# = \frac{k_B T}{h} \exp\left(-\frac{\Delta G^\#}{RT}\right) \quad (1.36)$$

$\Delta G^\#$  relates to the enthalpy ( $\Delta H^\#$ ) and entropy ( $\Delta S^\#$ ) of activation by:

$$\Delta G^\# = \Delta H^\# - T\Delta S^\# \quad (1.37)$$

Therefore, the rate constant equation may be written as:

$$k_{overall} = \left(\frac{k_B T}{h}\right) \exp\left(-\frac{\Delta H^\#}{RT}\right) \exp\left(\frac{\Delta S^\#}{R}\right) \quad (1.38)$$

This entire equation should be multiplied by the transmission coefficient ( $k$ ) to take into account the probability of conversion of the activated complex to the products. Therefore, we arrive to this final expression for the overall rate constant:

$$k_{overall} = k \left(\frac{k_B T}{h}\right) \exp\left(-\frac{\Delta H^\#}{RT}\right) \exp\left(\frac{\Delta S^\#}{R}\right) \quad (1.39)$$

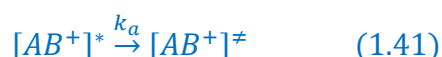
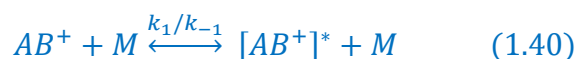
This equation can be used for calculation of Gibbs free energy, enthalpy and entropy of activation.

To summarize, instead of discussing about the collisional activation and deactivation, TS theory speaks about the presence of an activated complex in the reaction coordinate. Therefore, the reaction rate is directly the rate at which reactants arrive and pass through the transition state. This theory along with the RRK theory were then used to formulate RRKM theory to describe unimolecular reaction rate constants.

### The RRKM/QET theory

In the early 1950s, Marcus and Rice<sup>86,87</sup> proposed a new theory for the formulation of unimolecular dissociation rate constant based on transition state theory<sup>84,85</sup> and RRK theory,<sup>81-83</sup> which was named RRKM theory. At the same time, Wallentein, Wahrhaftig, Rosenstock and Eyring introduced quasi equilibrium theory<sup>88</sup> (QET), mainly for application in mass spectrometric systems. Both of these theories resulted in the same equation for the calculation of the reaction rate as a function of energy. Derivation of the RRKM/QET equation is presented elsewhere;<sup>81,83,86,87</sup> here we briefly discuss about physical repercussions of that, and some assumptions of both theories.

According to the RRKM theory, the reaction scheme is as follows:



here,  $[AB^+]^*$  is the energized molecular ion ( $E > E_0$ ), and  $[AB^+]^\ddagger$  is the activated complex (transition state). Actually, the difference between these two species is in their configuration, with the latter having the suitable one for the reaction. Therefore, this theory uses the concept of transition state, and then statistical mechanics to calculate the probability that an energized molecule has the proper configuration as that of the activated complex. In addition, instead of considering a uniform frequency for all of the oscillators of the system, it deals with the real frequencies of both  $[AB^+]^*$  and  $[AB^+]^\ddagger$ .

The RRKM/QET rate constant equation for a molecule having an internal energy of  $E$  and critical energy of  $E_0$ , is as follows:

$$k(E) = \frac{\sigma N^\#(E - E_0)}{h\rho(E)} \quad (1.43)$$

here,  $\sigma$  is the reaction degeneracy (number of the equivalent pathways of the reaction),  $N^\#(E-E_0)$  is the sum of states at the transition state from 0 to  $E-E_0$ ,  $h$  is Planck's constant and  $\rho(E)$  is the density of states of the precursor ion at the internal energy of  $E$ . But, what are the concepts of sum and density of states? Considering a molecule with  $s$  vibrational degrees of freedom (neglecting the rotational energy), and an internal energy of  $E$ , the sum of the states means the number of ways that we could distribute the energy among all the  $s$  oscillators in a way that the total energy is equal to or less than  $E$ .<sup>89</sup> As the energy increases, the sum of states also increases because at higher energies, the number of ways of distributing the energy between the oscillators is higher. Now, the density of states at energy  $E$  is defined as the number of vibrational arrangements with energy content between  $E$  and  $E + \delta E$ . The sum of states is a number without dimensions, and since the density is the number of states per energy interval, its unit is  $E^{-1}$ .<sup>89</sup>

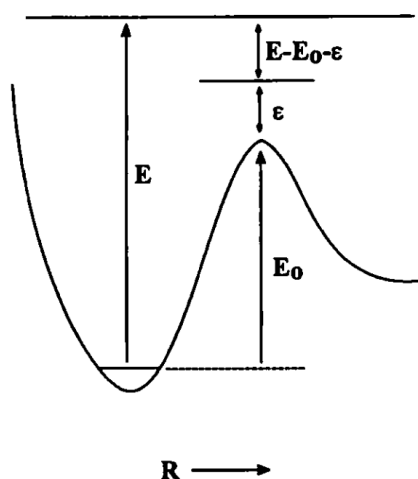


**Figure 1-1-** A schematic representation of a reaction coordinate for dissociation of a precursor ion having a total energy of  $E$ .<sup>89</sup>

To have a better understanding about the RRKM/QET equation, consider a precursor ion with a total internal energy of  $E$  (**Figure 1-1**). At the transition state, a part of this energy should be localized on the critical oscillator that is equal to the bond dissociation energy,  $E_0$ .



Now, the remaining energy that could be distributed among all other oscillators is  $E-E_0$ . So, this is one state (the first term of the following equation). The other possibility is that, we allocate a part of the  $E-E_0$  energy to the translational energy of the fragments,  $\varepsilon_i$ . Therefore, in this case, the total remaining energy that could be distributed between the vibrational modes is  $E-E_0-\varepsilon_i$ , the second and subsequent terms in the following equation:

$$k(E) = \frac{\rho^\#(E-E_0)}{h\rho(E)} + \frac{\rho^\#(E-E_0-\varepsilon_1)}{h\rho(E)} + \frac{\rho^\#(E-E_0-\varepsilon_2)}{h\rho(E)} + \dots \quad (1.44)$$

Thus, sum of states can be obtained by adding up all the terms in the numerators of the above equation.<sup>89</sup> Therefore, the maximum available energy for the oscillators other than the critical oscillator ( $E-E_0$ ) is when the fragments do not have any translational energy, and the minimum energy is when fragments have the highest translational energy ( $E-E_0-\varepsilon_i=0$ ). So, we sum up all the states between these two limits (0 to  $E-E_0$ ). From the above discussion, the minimum dissociation rate will be when the remaining energy for the oscillators is 0, then  $N(0)=1$ , because there is only one state corresponding to this energy (all the oscillators having zero energy). Consequently, the minimum rate constant is:

$$k_{min} = \sigma \frac{1}{h\rho(E_0)} \quad (1.45)$$

which depends neither on the structure of the transition state, nor on the vibrational frequencies.<sup>89</sup>

In the RRKM/QET equation (Equation 1.43), both the sum and the density of states increase with internal energy. However, since  $N^\#(E-E_0)$  increases faster, the rate constant will strongly depend on the internal energy. To calculate the rate constant, in addition to the critical energy, one also needs to determine the sum and the density of states. This can be done by a direct counting of states which itself needs the vibrational frequencies of the reactant and the transition state. However, as it has been shown previously,<sup>90,91</sup> RRKM/QET calculations are not sensitive to the vibrational frequencies, and when there is not a detailed knowledge of the transition state, quantitative studies can still be performed. On the contrary, they depend on the entropy of the activation ( $\Delta S^\#$ ). Therefore, two main parameters in the calculation of the rate constant will be  $E_0$  and  $\Delta S^\#$ .

Detailed discussion about RRKM/QET theory can be found in the related references.<sup>92,93</sup>

### Type of the transition state

**Figure 1-2a** represents the plots of the rate constant versus internal energy for two different dissociation reaction pathways of the same molecular ion but with different critical energies ( $E_{0,2} > E_{0,1}$ ) and entropies of the activation ( $\Delta S_2^\ddagger > \Delta S_1^\ddagger$ ) for the two pathways. The value of critical energy determines the position of the curve, and entropy of activation determines its "steepness".<sup>94</sup>

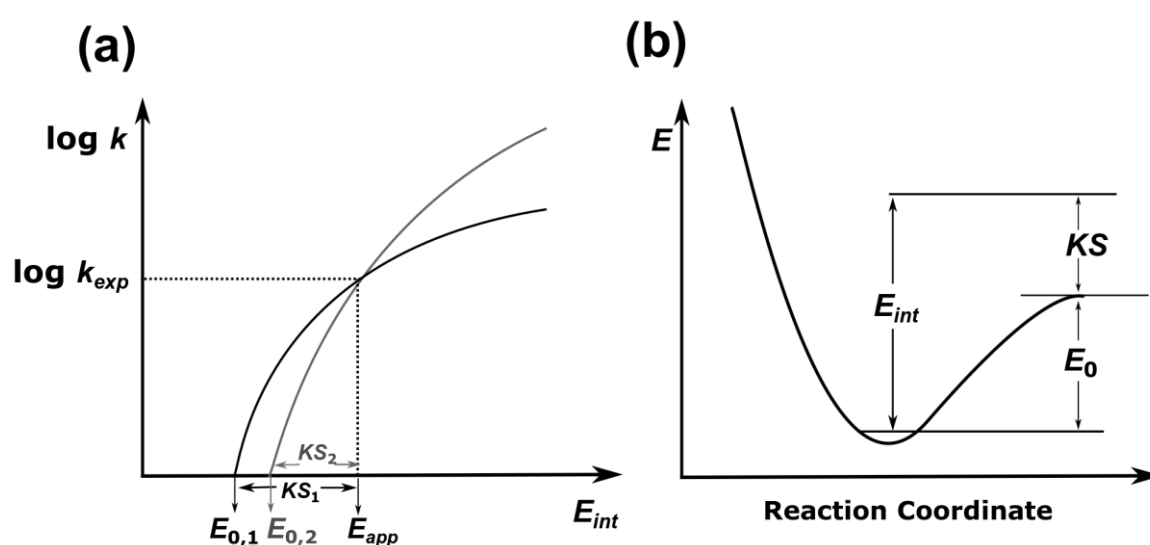


**Figure 1-2-** (a) Plots of rate constant as a function of the internal energy for two hypothetical reactions with loose (in gray) and tight (in black) transition states,<sup>94</sup> and (b) a schematic diagram representing KS.<sup>95</sup>

The type of the transition state directly depends upon the  $\Delta S^\ddagger$ . Rearrangement reactions usually have a low or negative entropy, slowly rising plot (rate constant versus energy) and a tight transition state whose structure is far from that of the fragments (early transition state). On the contrary, direct bond cleavage reactions are characterized by a high value of the activation entropy, steeply rising plot and a loose transition state whose structure is similar to that of the fragments (late transition state). Equation 1.46 exhibits the relationship between the frequency factor ( $\nu$ ) and the entropy of the activation ( $\Delta S^\ddagger$ ).<sup>96</sup>

$$\nu = \left( \frac{E - E_0}{h} \right) e^{\Delta S^\ddagger / R} \quad (1.46)$$

where  $h$  is Planck's constant,  $E$  is the total internal energy,  $E_0$  is critical energy and  $R$  is gas constant. Therefore, a high value of frequency factor (usually between  $10^{13}$  to  $10^{17} \text{ s}^{-1}$ ) corresponds to a loose transition state, whereas a small value (usually between  $10^6$  to  $10^{12} \text{ s}^{-1}$ ) accords with a tight transition state.<sup>97</sup>

In **Figure 1-2a**, critical energies for two reaction channels, and also their appearance energy ( $E_{app}$ ) are indicated. The difference between  $E_{app}$  and  $E_0$ , which is called kinetic shift<sup>98,99</sup> ( $KS$ ), is defined as the excess energy of the precursor ion relative to its critical energy of the dissociation that needs to be applied in order to see the fragmentation in a detectable rate (**Figure 1-2b**). From **Figure 1-2a**, one can see the same appearance energy for two different reactions with unequal critical energies and entropies of activation. Therefore, in situations where the purpose is comparison of various dissociation reactions or the stabilities of the different complexes, the final conclusion should be made with caution. In other words, one needs to have an estimation of the  $KS$  which includes the effects of all parameters, including time frame of the mass spectrometer, size of the molecular ion,  $E_0$  and  $\Delta S^\ddagger$ , before making any conclusion.

### Time scale of the experiment

The appearance of a fragmentation spectrum depends not only on the energetics of the dissociation reaction and internal energy distribution of the excited precursor ions but also, on the time scale of the mass spectrometer. In other words, the extent of the fragmentation has a direct relation with the time allowed for the ions to dissociate.<sup>97</sup> If we define the survival yield ( $SY$ ) as the fraction of the molecular ion that is not decomposed with Equation 1.47 as follows:

$$SY = \frac{I_P}{I_P + \sum I_F} \quad (1.47)$$

where,  $I_P$  is the intensity of the precursor ion, and  $I_F$  is that of the fragment ions; then the  $SY$  at time  $\tau$  is given by:<sup>100</sup>

$$SY = e^{-k(E) \cdot \tau} \quad (1.48)$$

where  $k(E)$  is the microcanonical rate constant which is dependent on the internal energy, and  $\tau$  is the time that precursor ions have in order to dissociate. Therefore, from the above equation, for the instruments with a shorter time scale, a higher rate constant and as a consequence a larger internal energy will be necessary to see the fragmentation.

### Internal energy distribution

As was explained previously, one of the main effective parameters on the appearance of the fragmentation spectrum is the internal energy distribution of the precursor ions. Internal energy is the total energy of the ion above its electronic, vibrational and rotational ground state.<sup>97</sup> If we suppose that we have an ensemble of molecular ions, then most probably, not all of them have the same internal energy, and there is a distribution of the energy between the all species. Therefore, internal energy distribution,  $P(E)$ , is a function that explains the probability of an ion to have a particular energy of  $E$ . This function is usually normalized to unity.<sup>100</sup> Absorption and emission of photons, and also collisional activation and collisional cooling can change the  $P(E)$  function of an ion population. Previously, various theories of unimolecular dissociation reactions were discussed, and it was explained that a dissociation reaction consists of two steps: the first step is activation/de-activation, and the second one is unimolecular dissociation. Now, it is worth noting here that the fact that we have a distribution of the internal energy, and not just a single value for the internal energy is a direct outcome of the competition between various activation and de-activation events.<sup>101</sup> Based on the relative rates of the activation/de-activation and dissociation steps, there are two limiting cases:

**(a)** Rapid energy exchange in comparison with the dissociation, in which the rates of the activation/de-activation far exceed the unimolecular dissociation. In this situation, the ion population arrives to a thermal equilibrium condition and has a Maxwell-Boltzmann distribution of the internal energy. This population is called canonical ensemble which can be characterized by a temperature. Under this condition, the canonical rate constant is the average of the unimolecular dissociation rate over the entire distribution of internal energies:

$$k(T) = \int_0^{\infty} P(E)k(E)dE \quad (1.49)$$

In addition, the Arrhenius equation can be used to explain the rate constant:<sup>102,103</sup>

$$k(T) = A \exp(-E_a/RT) \quad (1.50)$$

In Equation 1.50,  $A$  is the pre-exponential factor and has a similar meaning as the frequency factor. By plotting of  $\ln k$  versus  $1/T$ , one can directly obtain the Arrhenius activation energy,  $E_a$ , and  $A$  from its slope and intercept, respectively. It should be noted that for systems in thermal equilibrium, from Eyring's theory,<sup>104</sup> the rate constant can be given by Equation 1.51:

$$k(T) = \frac{k_B T}{h} \exp\left(\frac{\Delta S^\ddagger}{R}\right) \exp\left(-\frac{E_a}{RT}\right) \quad (1.51)$$

By comparison of Equations 1.50 and 1.51, pre-exponential factor can be explained by Equation 1.52:

$$A = \frac{k_B T}{h} \exp\left(\frac{\Delta S^\ddagger}{R}\right) \quad (1.52)$$

Equation 1.52 expresses the direct relationship between the pre-exponential factor and the entropy of activation. Furthermore, at the REX limit, Arrhenius activation energy relates to the dissociation enthalpy ( $\Delta H^\ddagger$ ) by Equation 1.53:<sup>105</sup>

$$E_a = \Delta H^\ddagger + k_B T \quad (1.53)$$

$\Delta H^\ddagger$  also relates to the critical energy of the dissociation by Equation 1.54:

$$\Delta H^\ddagger = E_0 + \langle E^\ddagger \rangle - \langle E \rangle = E_0 + \Delta E_{corr} \quad (1.54)$$

where  $\langle E^\ddagger \rangle$  is the average internal energy of the transition state,  $\langle E \rangle$  is that of the all molecules at temperature  $T$  and  $\Delta E_{corr}$  is Tolman's correction factor.<sup>105</sup> Therefore, the relation between activation and critical energy is given by:

$$E_a = E_0 + \Delta E_{corr} + k_B T \quad (1.55)$$

Depending on the type of the transition state, the value of the correction factor can be negative or positive. For reactions with loose transition state,  $\Delta E_{corr} > 0$  and  $E_a > E_0$ ; however, for those with tight transition state,  $\Delta E_{corr} < 0$  and  $E_a < E_0$ .

To sum up, the REX limit corresponds to the state in which we have regular activation and de-activation of the molecular ion during the dedicated time for the dissociation.

**(b)** Absence of any energy exchange during fragmentation, where the rate of the unimolecular dissociation is much higher than the activation/de-activation of the ions. In this situation, the higher energy tail of the distribution which has a larger energy than the critical energy will dissociate fast, and as a consequence this part is missing from the distribution. Therefore, the population of the ions will have a truncated Maxwell-Boltzmann distribution of internal energy which is characterized by a characteristic temperature ( $T_{char}$ ) (the temperature corresponding to the distribution of internal energies of the ions before decomposition), and a corresponding mean internal energy ( $\langle E_{int} \rangle$ ).<sup>100</sup>

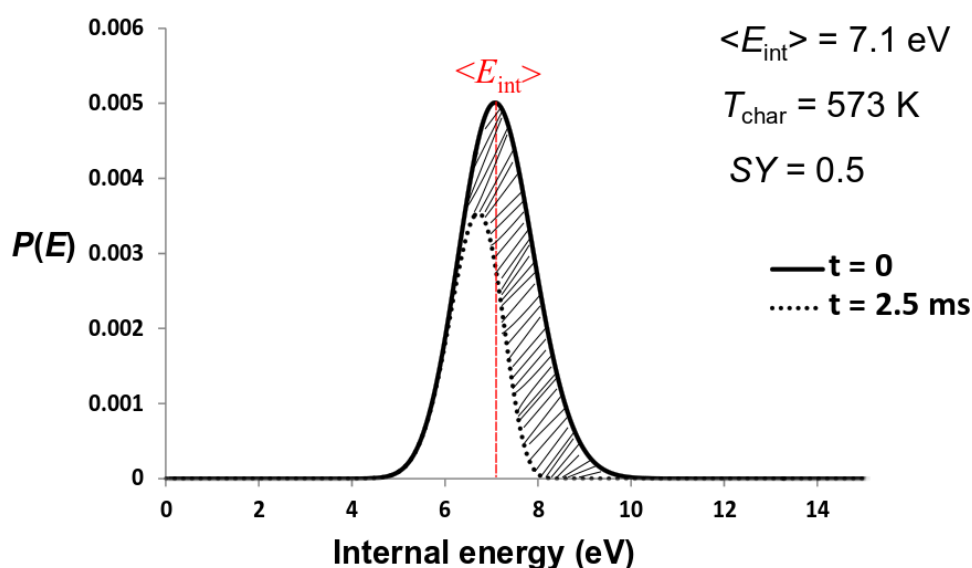


**Figure 1-3-** Truncated Maxwell-Boltzmann internal energy distribution: the solid curve is the internal energy distribution of a model host-guest complex at  $t = 0$  ms and the dotted curve is the internal energy distribution of the ions after 2.5 ms. The hatched area corresponds to the part of the population that is decomposed (50%).

As an example, the internal energy distributions for the dissociation of a model host-guest complex at  $T_{char}$  of 613 K, at 0 ms (before decomposition), and at 2.5 ms (upon

decomposition, dotted curve) are presented in **Figure 1-3**. The hatched area corresponds to the part of the population that is decomposed (50%). It is evident from the picture that after 2.5 ms, only the higher energy part of the distribution has been fragmented and the lower energy part is almost intact, leading to the term "truncated distribution".

Between the above limiting cases, there is a competition between activation/de-activation and unimolecular dissociation.

---

## ***Chapter 2: A general introduction to the utilized fragmentation techniques***

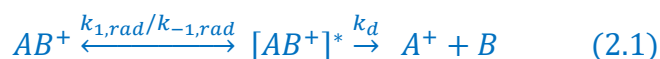
---



In this chapter, to have a better understanding of the techniques and projects that will be presented in this thesis, the utilized fragmentation techniques are introduced briefly.

### Blackbody infrared radiative dissociation (BIRD)

BIRD is one of the mass spectrometry techniques that is of special interest for quantitative study of the binding and dissociation properties of rather weak interactions.<sup>106</sup> In this technique, ions of interest are trapped in an ultra-low pressure ( $\leq 1 \times 10^{-8}$  Torr)<sup>107,108</sup> trapping mass spectrometer where they can experience unimolecular dissociation in the absence of any collision.<sup>109</sup> Therefore, the only source of activation is the absorption of infrared photons from the surroundings (Equation 2.1):<sup>110,111</sup>



In Equation 2.1,  $k_{1,rad}$  and  $k_{-1,rad}$  are rate constants for absorption and emission of infrared photons, respectively, and  $k_d$  is the unimolecular dissociation rate constant. Using the steady state approximation, the overall rate constant for the whole process,  $k$ , is:

$$k = k_d \left( \frac{k_{1,rad}}{k_{-1,rad} + k_d} \right) \quad (2.2)$$

In this technique, in order to see a substantial amount of fragmentation, the time allowed for the observation of the dissociation should be rather long (e.g., several minutes). In addition, pressure must be maintained sufficiently low to make sure that there is not any exchange of energy via unintended collisions. Both of these conditions can be readily fulfilled inside the cell of a Fourier transform ion cyclotron resonance (FT-ICR) mass spectrometer (**Figure 2-1**). In BIRD experiments, the only source of energy is the absorption of multiple low-energy infrared photons (in contrast to visible or ultraviolet dissociations in which a single high-energy photon is used for excitation), and from the practical point of view, only a limited temperature range can be achieved for BIRD dissociations. For these reasons, precursor ions of BIRD have to be fragile enough to dissociate in the available temperature range, and at the same time, they must be stable enough to be able to arrive intact into the ICR cell after formation in the ionization source. Since electrospray ionization (ESI)<sup>3-5</sup> allows

weak interactions to be preserved in the gas phase; it is one of the most convenient techniques for generation of precursor ions of BIRD.

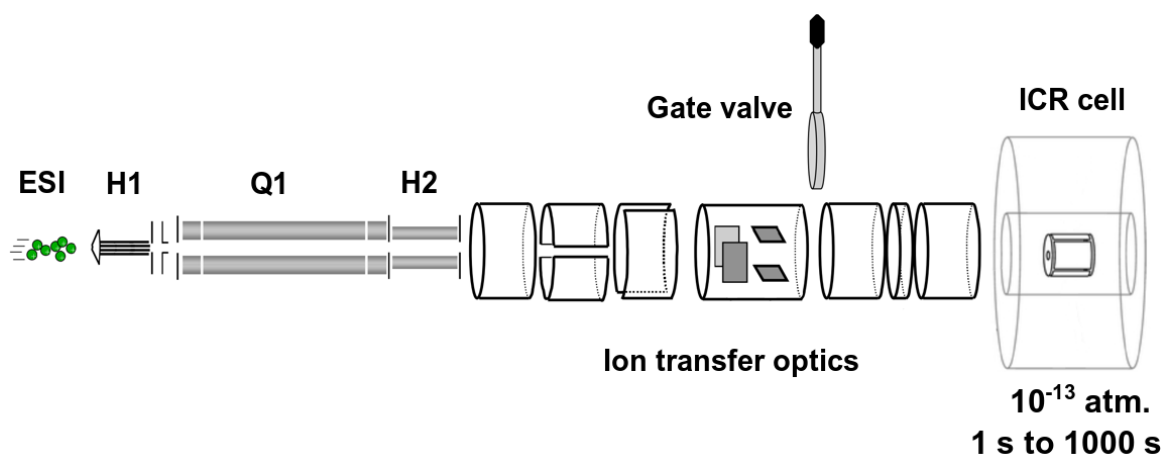


**Figure 2-1-** Schematic of a hybrid quadrupole-FT-ICR mass spectrometer (ApexQe, Bruker Daltonics)

In treating BIRD data, the natural logarithm of the survival yield (Equation 1.47) is plotted as a function of the trapping time in the ICR cell. This plot will be linear for the reactions following first-order kinetics, and the obtained slope gives the rate constant ( $k$ ). The dissociation rate constants are acquired at various temperatures and finally, the subsequent plot of  $\ln k$  versus  $1/T$  allows one to deduce observed activation energy ( $E_a^{obs}$ ) and pre-exponential factor ( $A^{obs}$ ) parameters (Equation 1.50 and **Figure 2-2**).<sup>106</sup>

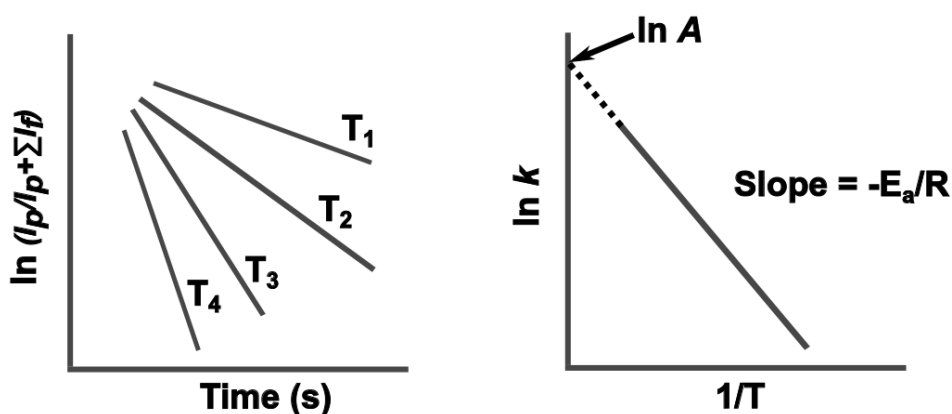


**Figure 2-2-** BIRD's data treatment for extraction of observed activation parameters.

These experimentally-derived Arrhenius parameters ( $E_a^{obs}$  and  $A^{obs}$ ), can be useful for comparison of the kinetics of similar reactions. For more universal comparisons, it is

necessary to derive the corresponding infinite-pressure parameters,  $E_a^\infty$  and  $A^\infty$ . This will help to compare bond energies and the nature of the transition state in different unimolecular dissociation reactions.

One may ask the questions: why are universal comparisons feasible at the high-pressure limit, and how is it possible to have this condition in BIRD experiments that are performed under ultra-low-pressure conditions? In the high-pressure limit condition (a high pressure of collision gas), the ion population experiences very rapid energy exchange, and as a consequence, it is in complete equilibrium with its surroundings at temperature  $T$ . Under this condition, the ion population has a Maxwell-Boltzmann distribution of internal energy, and observed activation energy and pre-exponential factor will approach to the corresponding infinite-pressure values which are characteristics of the dissociation reaction and therefore can be used for universal comparison purposes. In the low-pressure condition of BIRD experiments, this condition of fast energy exchange can be fulfilled by increasing the molecular size (due to a large number of photon absorption and emission events). Therefore, to avoid any confusion, this infinite-pressure limit is called the rapid energy exchange (REX) limit.<sup>106</sup>

For an ensemble of ions in thermal equilibrium (REX limit), the internal energy distribution is given by Maxwell Boltzmann relation:

$$P(E) = \text{Const.} \cdot \rho(E) \cdot \exp\left(-\frac{E}{k_B T}\right) \quad (2.3)$$

where  $P(E)$  is the probability density for an ion to have a special energy of  $E$  at temperature  $T$ ,  $\rho(E)$  is the density of states,  $k_B$  is the Boltzmann constant, and *Const.* is the normalization constant. In BIRD experiments, the rate of energy exchange strongly depends on the size of the molecule. As the size of the ion increases, the rate of the absorption ( $k_{1,rad}$ ) and emission ( $k_{-1,rad}$ ) of infrared photons increases as well. However, the unimolecular dissociation rate ( $k_d$ ) stays almost constant at a given temperature, and is hardly influenced by the molecular size. This means that  $P(E)$  approaches to a Maxwell Boltzmann distribution without any significant loss of the highest energy part of the population via unimolecular dissociation. Therefore, when the size of the molecule is large enough,  $k_{-1,rad}$  far exceeds  $k_d$ , the

population is thermalized, and the observed activation parameters  $E_a^{obs}$  and  $A^{obs}$ , are equal to their infinite-pressure values  $E_a^\infty$  and  $A^\infty$ .

In the case of small molecules (less than 100 degrees of freedom), the rate of energy exchange is small compared to the dissociation rate ( $k_{-1,rad} \ll k_d$ ). In fact, any excitation to any internal energy above the critical energy, leads to a very fast dissociation of ions. In this condition, which is called “sudden death” kinetic limit, the overall dissociation rate of the precursor ion depends only on the rate of photon absorption and emission, and is independent of the unimolecular dissociation rate. In this situation, the high energy portion of the population is lost via unimolecular dissociation, and this reactive depletion<sup>106</sup> leads to a significant deviation of  $E_a^{obs}$  and  $A^{obs}$  from  $E_a^\infty$  and  $A^\infty$ , respectively; as a consequence, difficulties arise in the interpretation of BIRD data. Here, the simplest approach for extracting the critical energy from the BIRD data is a method called the "truncated Boltzmann approximation".<sup>106,108</sup> Based on this model, critical energy is given by:

$$E_0 = E_a^{obs} + \langle E' \rangle - \Delta E_{rad} - \Delta E_{depl} \quad (2.4)$$

where  $\langle E' \rangle$  is the average energy of the truncated Boltzmann distribution,  $\Delta E_{rad}$  is the temperature dependence of the radiation field, and  $\Delta E_{depl}$  is that of the reactive depletion of the higher energy levels. These two latter terms are small and partially cancel each other. In Equation 2.4,  $\langle E' \rangle$  term is dependent on the  $E_0$ , but  $E_a^{obs}$ ,  $\Delta E_{rad}$  and  $\Delta E_{depl}$  are independent of  $E_0$ . Therefore, critical energy can be obtained by iteration: first, using the approximations of harmonic oscillator and Boltzmann statistics, the internal energy distribution of the system is calculated, and then  $\langle E' \rangle$  is calculated using an initial estimate for critical energy. Afterwards, using the calculated  $\langle E' \rangle$ , and Equation 2.4, a new value for critical energy is calculated, and is compared with the initially estimated value. This process will be repeated until the newly obtained  $E_0$  is less than  $5 \text{ cm}^{-1}$  different from the value that is used to calculate  $\langle E' \rangle$  in the previous step. In addition to the truncated Boltzmann approach, master-equation modeling can also be used to extract critical energies from BIRD data in small systems. This method is the most reliable procedure for extraction of critical energies provided that accurate information about the transition state is available. However, it is a more demanding approach compared to the truncated Boltzmann method.<sup>106,108</sup>

For the ions of intermediate size, the rate of energy exchange is comparable to the dissociation rate ( $k_{-1,rad} \approx k_d$ ). Here, the ion population is not completely thermalized and a small part of the population in the higher energy side is lost by unimolecular dissociation. Therefore, the internal energy distribution is Maxwell-Boltzmann-like with a small depletion in its higher energy portion. In this case, master equation analysis has to be performed on the experimentally obtained activation parameters to drive the correct value of the critical energy. In the master equation model, any particular ion can undergo photon absorption, photon emission and unimolecular dissociation, and in fact, each ion, is considered to have a random walk along the internal energy axis. To perform this modeling, one needs to have information about the microcanonical dissociation rate of the molecule as a function of internal energy. It is convenient to use the master equation in a matrix form as follows:

$$\begin{bmatrix} dN_1(t) \\ dN_2(t) \\ dN_3(t) \\ \vdots \end{bmatrix} = \begin{bmatrix} k_{1,1} & k_{1,2} & k_{1,3} & \cdots \\ k_{2,1} & k_{2,2} & k_{2,3} & \cdots \\ k_{3,1} & k_{3,2} & k_{3,3} & \cdots \\ \vdots & \vdots & \vdots & \ddots \end{bmatrix} \begin{bmatrix} N_1(0) \\ N_2(0) \\ N_3(0) \\ \vdots \end{bmatrix} \quad (2.5)$$

where  $dN_i(t)$  is the change in the population of an ion with time relative to the initial population  $N_i(0)$ , and the first matrix in the right side of Equation 2.5 is called the J matrix which includes rate constants of all the energy exchange and dissociation events. Matrix-algebra techniques and computer software can be used to solve Equation 2.5 numerically to predict unimolecular dissociation rate constants at different temperatures, which then can be compared with the experimentally observed rates. For this purpose, some inputs are required as follows: 1) an estimated value of  $E_0$  which can be varied to obtain the best fit with the observed data, 2) radiative energy exchange coefficients which can be determined by *ab initio* quantum calculations, and 3) dissociation rate constants that can be calculated using RRKM theory. Therefore, using these inputs, the master equation is set up and solved by adjusting  $E_0$  and the transition state parameters to give calculated rate constants at different temperatures which are best fitted to the experiment.

So far, we know that by increasing the molecular size we can approach the REX limit, but the question is that at which size can one be sure that the REX limit condition is fulfilled? Actually, the answer to this question depends on different parameters such as temperature,

type of the transition state, critical energy, dissociation rate, and radiative absorption and emission properties of the ions.<sup>112</sup> All of these parameters influence the relative rates of absorption ( $k_{1,rad}$ ) and emission ( $k_{-1,rad}$ ) of infrared photons compared to the unimolecular dissociation rate ( $k_d$ ), thereby indicating whether a molecular system is in the REX limit or not. For instance, Price and Williams have shown that as  $E_0$  increases and  $A$  decreases, kinetics approaches closer to the REX limit,<sup>112</sup> or if we consider the effect of temperature, as it decreases, the dissociation rate decreases faster than the energy exchange rates. Under this condition, a longer observation window is needed to see enough fragmentation. Therefore, at low temperatures, the internal energy distribution is Maxwell-Boltzmann, and kinetics goes toward the REX limit. On the contrary, at high temperature, the situation is reversed and there is a considerable depletion (truncation) in the high energy portion of the distribution, and accordingly a significant deviation from the REX limit especially for smaller ions. Therefore, in BIRD experiments, it is preferable to work in the low temperature range, and high storage time conditions. It should be noted that at very long trapping times, there may be some possible problems related to the signal loss and consecutive fragmentations of the fragment ions. For these reasons, it is better to avoid using overly long storage times. From the above discussion, increasing the molecular size or critical energy, and decreasing of the pre-exponential factor or experimental temperature leads to the approach of the REX limit.<sup>112</sup>

To sum up, BIRD is one of the most reliable and appealing techniques in providing direct information about the dissociation energetics and type of transition state especially for large molecular systems. In this thesis, we will employ BIRD technique, and use it for calibration of temperature in other dissociation techniques.

### Low-energy collision induced dissociation (low-energy CID)

Here in this thesis, by low-energy CID, we mean the collisional activation occurring in quadrupole ion traps, although it can be performed in both quadrupole ion trap and ICR cell. In addition, since almost all the experiments in this thesis were performed using a linear quadrupole ion trap, here, a short introduction of this kind of ion trap is presented.

## Linear ion trap mass spectrometer

The quadrupole ion trap is a device which can function either as a mass analyzer or as an ion trap for confinement of ions. By applying suitable potentials to the two ends of the electrodes of the ion trap, a potential well is built inside the trap which enables storing of the ions for a period of time. Afterwards, by linear scanning of the amplitude of radiofrequency (RF) potential, each ion with specific mass to charge ratio ( $m/z$ ) will be ejected from the potential well at a special RF amplitude; enabling the quadrupole ion trap to act as a mass analyzer.<sup>113</sup>

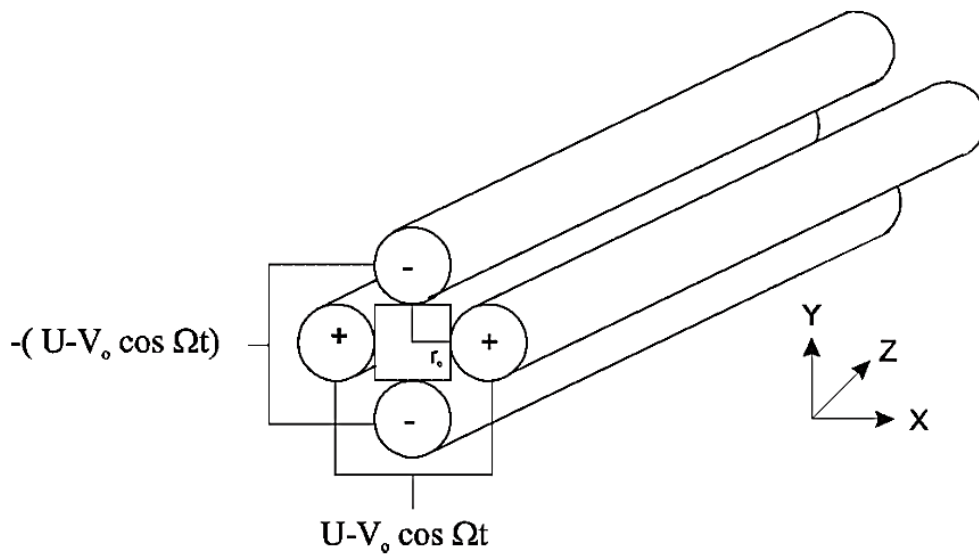


**Figure 2-3-** Quadrupole geometry. Each rod is located at the  $r_0$  distance from the central axis.<sup>114</sup>

Linear ion trap consists of four metal rods which are arranged in parallel and have a distance of  $r_0$  from the central axis (**Figure 2-3**). Potential that is applied to each opposite pair of poles is:

$$\Psi(t) = \pm(U - V_0 \cos \Omega t) \quad (2.6)$$

where  $U$  is the direct current (DC) voltage and  $V_0$  is the amplitude of radio frequency voltage which oscillates with frequency of  $\Omega$  in the time domain. Quadrupole potential between four parallel rods can be explained by:

$$\Phi_2(x, y, t) = \frac{(x^2 - y^2)}{r_0^2} (U - V_0 \cos \Omega t) \quad (2.7)$$

Motion of ions in a pure quadrupole field in directions  $x$  and  $y$  can be explained by:

$$\frac{d^2x}{dt^2} + \frac{2ze}{mr_0^2} (U - V_0 \cos \Omega t) x = 0 \quad (2.8)$$

$$\frac{d^2y}{dt^2} - \frac{2ze}{mr_0^2} (U - V_0 \cos \Omega t) y = 0 \quad (2.9)$$

where  $m$  is mass of ion,  $z$  is its charge, and  $e$  is the elementary charge. Re-writing Equations 2.8 and 2.9 by replacing the variables with dimensionless parameters as follows:

$$a_u = a_x = -a_y = \frac{8eU}{m\Omega^2 r_0^2} \quad (2.10)$$

$$q_u = q_x = -q_y = \frac{4eV_0}{m\Omega^2 r_0^2} \quad (2.11)$$

$$\xi = \frac{\Omega t}{2} \quad (2.12)$$

resulting in the equations of motion as follows:

$$\frac{d^2x}{d\xi^2} + (a_x - 2q_x \cos 2\xi) x = 0 \quad (2.13)$$

$$\frac{d^2y}{d\xi^2} + (a_y - 2q_y \cos 2\xi) y = 0 \quad (2.14)$$

or in general:

$$\frac{d^2u}{d\xi^2} + (a_u - 2q_u \cos 2\xi) u = 0 \quad (2.15)$$

Equation 2.15 is called the Mathieu equation<sup>115</sup> in which,  $a_u$  and  $q_u$  are called stability or trapping parameters which are functions of RF frequency,  $m/z$  ratio of a given ion, and size of the quadrupole ( $r_0$ ). In addition,  $a_u$  is a function of DC voltage and  $q_u$  is a function of RF voltage. Above-mentioned Mathieu equation is defined for quadrupole having rods with hyperbolic cross sections. Although rods with circular cross sections can be employed for



fabrication of quadrupole, using rods with hyperbolic geometry, quality of the quadrupole potential can be maintained at larger distances, and performance of mass spectrometer will be better. Ions inside the ion trap oscillate with a combination of different frequencies. Ions' angular frequencies are given by:

$$\omega_{u,n} = (2n + \beta_u) \frac{\Omega}{2} \quad n = 0, \pm 1, \pm 2, \dots \quad (2.16)$$

where  $\beta_u$  is normalized oscillation frequency and related to the trapping parameters of  $a_u$  and  $q_u$ . Movements of ions in directions  $x$  and  $y$  in quadrupole field are completely independent from each other and can be displayed using so-called stability diagram resulting from solution of Mathieu equation (**Figure 2-4**).

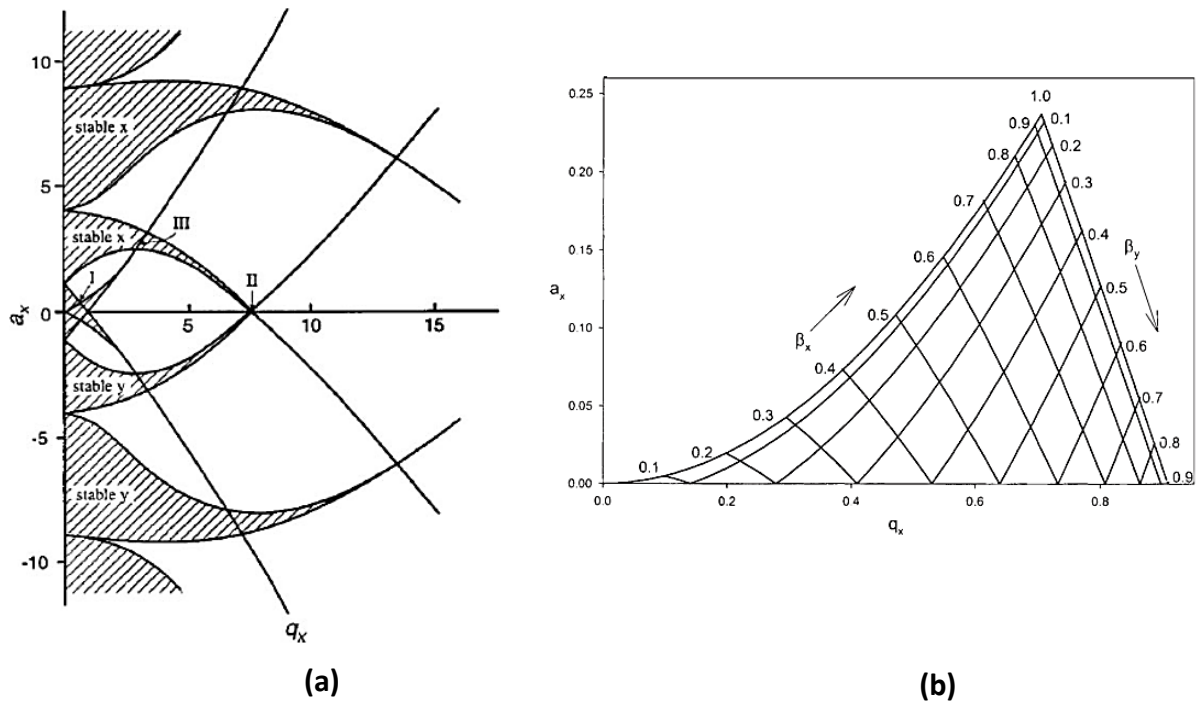


**Figure 2-4-** The Mathieu stability diagram for a linear quadrupole device.<sup>116,117</sup>

The operating region of the quadrupole mass analyzer is represented by I in **Figure 2-4-a**, and also is shown separately in **Figure 2-4-b**. In general, ions remain in the trap only if they have stable trajectories in both radial and axial directions. Therefore, in the stability diagram, ions which fall in the overlap regions of  $x$  and  $y$  stability, will not collide with electrodes and will stay in the trap.

Let's consider the position of the ions in different conditions of DC and RF voltages. When  $U=0$ , and only RF field is applied: under this condition, according to Equation 2.10,  $a_u=0$ , and according to equation 2.11,  $q_u$  value for heavy ions are lower than those for light ions. Therefore, in the diagram, along the line  $a_u=0$ , different ions will be arranged in a way that high  $m/z$  ions fall in the left side (low  $q_u$  value), and low  $m/z$  ions fall in the right side (high  $q_u$  value) of the diagram. If we increase the RF amplitude,  $q_u$  will also increase, therefore, ions will move further to the right side of the diagram. Now, if we also apply a DC voltage, this causes the ions to move along the  $a_u$  axis, in a way that lighter ions move further compared to the heavy ions. The sequence that usually is used in linear ion trap mass spectrometer is that, first, by applying an RF voltage to the rods, a range of  $m/z$  values (Equations 2.8 and 2.9) are allowed to be trapped. Afterwards, by linearly increasing the RF amplitude, gradually, ions will move to the right side (high  $q_u$  value) in the stability diagram, and pass the boundary of  $q_u = 0.908$ . This leads the ions to have unstable trajectories in both dimensions, and eject through the slits present on the rods. Usually, in addition to the RF voltage, an intense auxiliary (alternating current) AC voltage is used in resonance with the secular frequency of the ions, just as the ions are being ejected. This AC voltage is applied radially in order to energize the ions and help them to eject much more tightly through the slits on the rods, thereby increasing the spectral resolution. This phenomenon is called mass-selective ion ejection. In addition, this supplementary AC voltage can be used to remove unwanted ions from the ion trap, for example, for isolating a precursor ion prior to doing tandem mass spectrometry experiments. Finally, when a low amplitude of the AC voltage is used, it can resonantly dissociate precursor ions of interest.

In spite of the quadrupole field, in higher order multipoles, movements of ions in directions  $x$  and  $y$  are greatly coupled. In addition, in these cases, the solutions of the equations of motion strongly depend on initial condition. Therefore, stability diagrams are not readily derived. When trapping voltages are low, ion trajectories in RF multipoles can be approximately expressed as follows:<sup>118</sup>

$$U_{eff}(r) = zeV_{eff}(r) = \frac{N^2 (ze)^2 V^2}{4 m\Omega^2 r_0^2} \left(\frac{r}{r_0}\right)^{2N-2} \quad (2.17)$$

where  $U_{eff}(r)$  is the effective mechanical potential,  $V_{eff}(r)$  is the effective electric potential, and  $N$  is the order of multipole. Therefore, for a linear hexapole with  $N=3$ , the effective potential is proportional to  $r^4$ , for a linear octopole with  $N=4$ , it is proportional to  $r^6$  and so on. This implies that in higher order multipoles, effective potentials near the central axis are relatively flat, and near the rods, they increase rapidly (**Figure 2-5**).

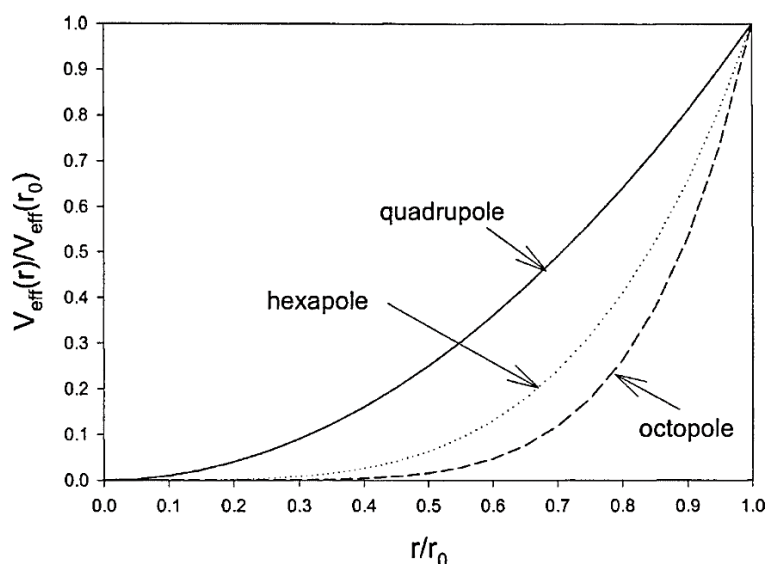


**Figure 2-5-** Plots of effective potentials for quadrupole, hexapole, and octopole fields.<sup>116</sup>

A schematic of the linear trapping quadrupole (LTQ) instrument (Thermo Fisher<sup>®</sup>, San Jose, CA) is represented in **Figure 2-6**. The inlet part of the instrument is an ionization source that can be electrospray ionization (ESI), atmospheric pressure chemical ionization (APCI), atmospheric pressure photo ionization (APPI) ion source and so on. Ions produced in the source pass through a cone and a heated capillary (pressure of  $\sim 1$  mbar), and then through the tube lens, skimmer, first quadrupole ion guide (Q00) and first lens (L0). Then they proceed to the next quadrupole ion guide (Q0) (pressure of  $\sim 0.001$  mbar).

Then, after passing Lens L1 and gate lens, they enter into the Q1 octopole ion guide which is at lower pressure compared to the Q0 (pressure of  $\sim 3 \times 10^{-5}$  mbar). During the injection time, Q1 directs the ions axially into the linear ion trap. Here we used the expression of “ion guide” that can be defined as a linear RF multipole which is used to transfer the ions from the ionization source into the mass analyzer. To convert a linear multipole into a linear ion

trap, stopping potentials should be applied to the front and end of the electrodes to axially confine the ions. Then by applying RF voltages to the rods, radial confinement is fulfilled.

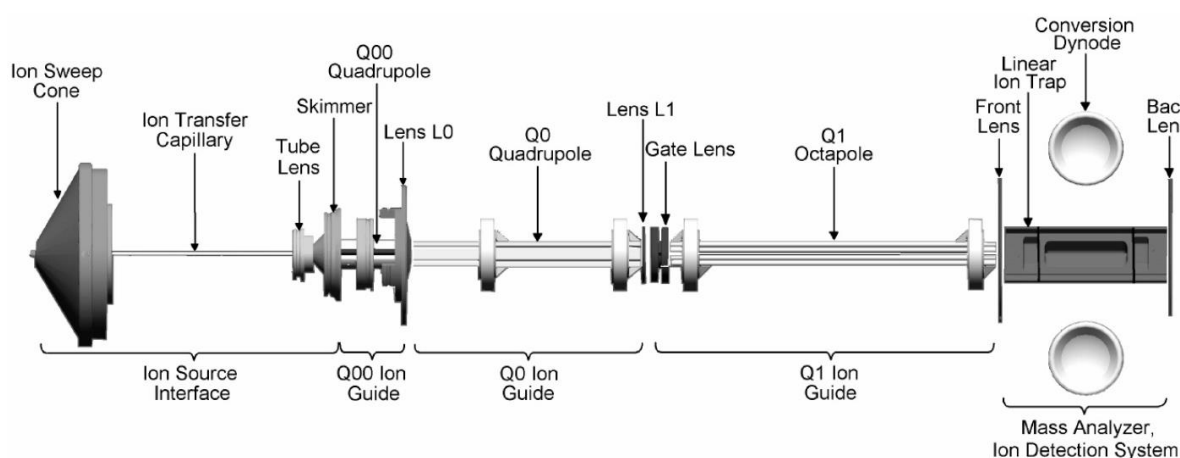


**Figure 2-6-** Schematic of the linear trapping quadrupole (LTQ) instrument (Thermo Fisher®, San Jose, CA).

In a linear quadrupole device, each rod has a front, a center and a back segment (**Figure 2-7**). The central segment of the electrodes defines the trapping volume, and at least one of the rods has a slot in its center segment to allow radial ejection of the ions into the detector. Trapping of the ions in axial directions is achieved by applying electric fields to the ends of the four hyperbolic rods and in the radial direction confinement of ions is done by applying a quadrupole field to the rods.

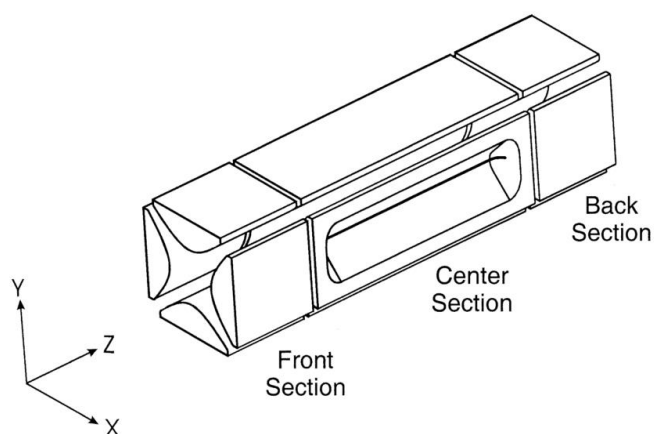


**Figure 2-7-** Basic design of a two-dimensional linear ion trap.<sup>119</sup>

As it is represented in **Figure 2-8**, three separate DC voltages are necessary for the operation of a linear ion trap: DC1, DC2 and DC3 which are applied to the front, center and back

segments in order to inject and also axially trap the ions (**Figure 2-8-a**). Radial trapping of the ions is achieved by applying RF voltage to all three segments of the opposite rod pairs (**Figure 2-8-b**). Isolation, activation and ejection of the ions are accomplished by applying resonance excitation voltage to the pair of rods which include the ejection slot (**Figure 2-8-c**).

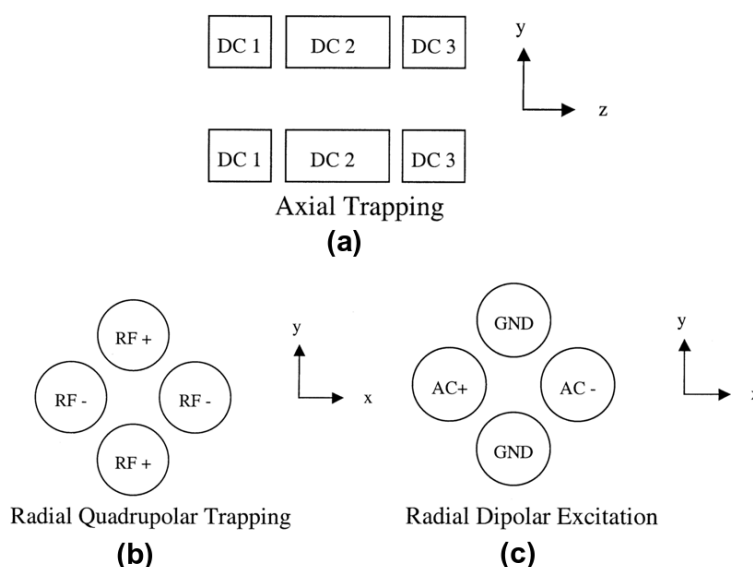


**Figure 2-8-(a)** Application of DC voltages for axial trapping of the ions, **(b)** RF voltages for radial trapping of the ions, and **(c)** AC voltage for their excitation in the two-dimensional ion trap.<sup>119</sup>

It is worth mentioning that in order to have a high mass spectral resolution, the secular frequency of the trapped ions should be constant over the entire length of the ion trap. For this reason, for radial ejection of the ions (by ramping RF voltage in the presence of an intense supplementary AC voltage), fringe field distortions need to be avoided over the whole length of the linear ion trap, to prevent changing of the secular frequency of ions. In the configuration explained above, three sections are intentionally designed to stay away from the problems due to the RF field imperfections in the region of the ejection slits on the rods. At both ends of the quadrupole, because of the termination of RF fields, fringing field effects are high. In these regions, coupling of the radial and axial fields and also prominence of the higher-order terms in the potential can cause ejection of ions from unpredicted points by the stability diagram, and as a consequence, low spectral quality results. Therefore, ions that are intended to be ejected radially from the slits must be properly isolated from the ends of the linear ion trap to avoid these fringing field effects. **Figure 2-9** shows how a configuration having three sections can solve this problem. In a device having three sections

(**Figure 2-9-a**), the radial dipole field is consistent along the entire the center section and it has no axial component. However, in the single section trap (**Figure 2-9-b**), the dipole field has a significant contribution of the axial component near the two end lenses leading to unexpected axial excitation, and as a consequence, axial ejection of ions.

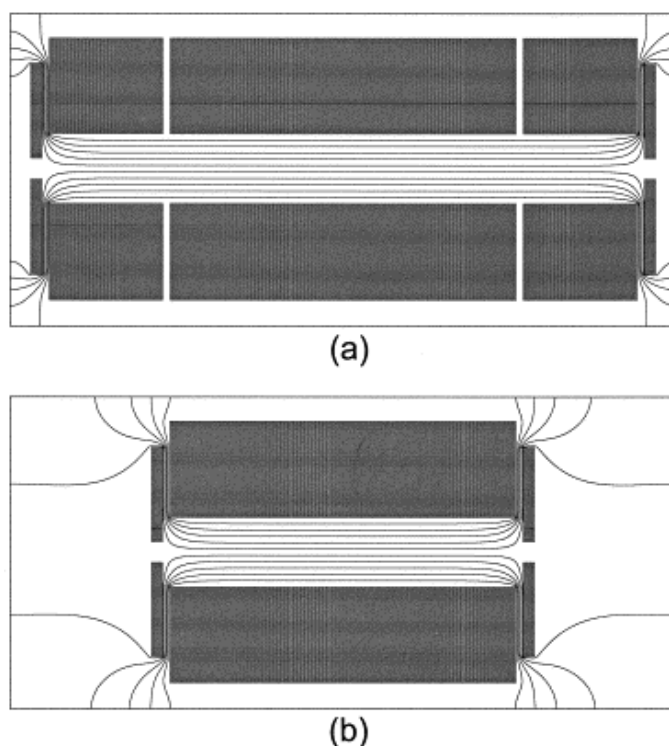


**Figure 2-9- Fringing field effects at (a) a three section and (b) a single section linear ion trap.**<sup>120</sup>

The next point is that, generally, ions in a multipole are not necessarily at the stability boundary. The presence of a light gas inside the multipole leads to the collisions of ions with the gas, resulting in the loss of kinetic energy of the ions. This, in turn, brings the ions towards the center of the multipole which has lower effective potential. This process which is called collisional cooling, not only helps to thermalize the ions to the temperature of the bath gas, but also improves the ion transmission through the multipoles.<sup>121</sup>

After this brief introduction of the linear quadrupole mass spectrometer which is employed in this thesis for performing low-energy CID experiments, we focus on this technique itself.

## Low-energy CID

In 1997, McLuckey and Goeringer, provided a context for classification of different activation techniques by explaining some figures of merit such as activation time scale, amount of deposited energy on the ions, feasibility to change the deposited energy and its distribution, the form of the energy deposition (vibrational or electronic), time scale of the mass spectrometer, and efficiency of the fragmentation which depends on the dissociation rate constant.<sup>101</sup> Based on the above-mentioned figures of merit, an activation technique can be considered as fast, slow, or very slow. In fast activations, the rate of energy deposition is high compared to the unimolecular dissociation rate, and they usually involve a single high-energy collision. However, slow activations usually involve multiple lower energy collisions having a delay interval of around tens to hundreds of microseconds between the discrete collisions. Therefore, between individual collisions, dissociation and isomerization of precursor ions is possible. Similar to the slow activations, "very slow" activations include occurrence of multiple collisions, however, in this case, deactivation processes can happen between the individual collisions. Therefore, a sort of equilibrium can be established between activation and deactivation.

According to the above classification, low-energy CID with its multiple collision property and very long time scale, which facilitates deactivating phenomena, belongs to the very slow activation techniques. In fact, low-energy CID is analogous to the BIRD technique from this point of view that both methods involve multiple activation and deactivation processes. In the ultra-low pressure condition of the BIRD experiments inside the FT-ICR mass spectrometer, ions experience no collision, and absorption and emission of infrared photons is responsible for the activation and deactivation processes. However, in the high pressure environment of low-energy CID experiments inside the ion traps, ion-neutral collisions are responsible for heating or cooling of the ions. In both cases (BIRD and low-energy CID), relative rates of the activation/deactivation processes to the unimolecular dissociation rate, defines the internal energy distribution of the ions as well as the dissociation kinetics. When the rates of the activation/deactivation processes far exceed the rate of the unimolecular dissociation, the rapid energy exchange condition<sup>112</sup> can be established. In this condition, the

precursor ion population can have a Maxwell-Boltzmann distribution of internal energy, and the Arrhenius equation can be used to explain the dissociation kinetics. On the contrary, when the rate of unimolecular dissociation far exceeds the activation and deactivation rates, the excitation rate defines the dissociation kinetics. Under this condition, the higher energy portion of the population will dissociate fast and internal energy is described by a truncated Maxwell-Boltzmann distribution.<sup>97</sup>

In low-energy CID, typically helium (He) at a pressure of around 1 mTorr is used as the buffer gas. The buffer gas not only helps deceleration, thermalization and trapping of the ions in the center of the ion trap, but also, it is used for collisional activation of the ions. Various techniques have been employed to accelerate the ions inside the ion traps to collide with buffer gas;<sup>122–126</sup> among which the resonance excitation is the case in our low-energy CID experiments.<sup>124,127</sup> In the quadrupole ion trap, a radio frequency (RF) voltage is used for trapping of the ions. Depending on the frequency and amplitude of this RF voltage as well as the ions' mass to charge ratio ( $m/z$ ), every ion moves with a special frequency inside the ion trap which is called its secular frequency. In resonance excitation, a supplementary AC voltage with the same frequency as the secular frequency of precursor ions is applied to excite them leading to collisions with buffer gas and conversion of their kinetic energy to internal energy. Despite the relatively low energy deposition, a wide variety of ions can be dissociated using this technique due to its multiple collision nature as well as its very long time scale (tens of milliseconds to tens of seconds). This long time scale allows access to very slow dissociation pathways, and possible rearrangement of the precursor ions before decomposition.

One of the main advantages of very slow activation methods performed in trapping devices is that they allow the study of dissociation energetics by measuring the dissociation rates at different ion temperatures. Using the BIRD technique that was explained in the earlier sections, direct measurement of activation parameters (activation energy and pre-exponential factor) can be achieved, provided that the rapid energy exchange condition is fulfilled. Basically, it should be possible to use low-energy CID to perform the same quantitative measurements. However, special attention must be given to the fact that in this



technique, in contrast to BIRD, we are not dealing with the real temperature of the ions. Therefore, a primary step is determination of the effective temperature of the ions under the employed experimental conditions. In the absence of collision voltage, the initial temperature of the ions inside the ion trap is equal to that of the bath gas. By acceleration of the ions using an additional source of energy, their internal temperature increases above that of the temperature of the bath gas. This acceleration can be performed by different methods<sup>123,125,126,128,129</sup> like heating the buffer gas,<sup>130,131</sup> applying a resonant excitation voltage,<sup>132,133</sup> etc. Using either of the mentioned acceleration techniques, the first question that must be addressed is whether the ions absorb any power from the applied radio frequency trapping voltage or not, a phenomenon which is called RF-heating. In 1999, Asano *et al.* examined the dissociation rates of protonated leucine enkephalin and its  $b_4^+$  fragment ion at different bath gas (He) temperatures, and in the absence of any excitation electric field.<sup>134</sup> They observed that the amplitude of RF trapping voltage has a minimal influence on the internal temperature of the ions inside the trap. Therefore, one can perform kinetic experiments inside the ion trap (under normal ion storage conditions, e.g.  $a_z = 0$ ,  $q_z = 0.1$ - $0.3$ ) by heating the bath gas, and measuring the activation parameters with confidence that the temperature of the ions is characterized by the bath gas temperature.<sup>134</sup> It should be noted that as the mass of the ions increases, and the mass of the bath gas decreases, this approximation gets closer to reality.<sup>134</sup>

When ions are accelerated using a resonance excitation voltage, the above-mentioned approximation (absence of RF-heating due to the trapping voltage) is still valid. However, one complication that exists in this case is that one needs to precisely determine the relation between the AC excitation voltage and the internal temperature of the ions inside the quadrupole ion trap in order to be able to measure activation parameters from kinetic experiments. In 1996,<sup>132,133</sup> Goeringer and McLuckey employed the kinetic theory of ion transport in gases in order to calculate effective temperature of the ion population inside the 3D ion trap at a steady-state condition. They observed that for ions in an atomic gas, effective temperature is the temperature corresponding to a Maxwell-Boltzmann distribution of internal energy. By this, they showed that collisional excitation inside the ion trap produces an ion population with a thermal distribution of the internal energy. Then,

they performed a random walk simulation for collisional energy transfer, and observed that the calculated average internal energy from this simulation is equal to that of a true Maxwell-Boltzmann distribution at the same internal temperature. They used some essential assumptions in their model as follows:

- 1) The number density of the bath gas inside the ion trap is much more than the ions. This assumption allows one to ignore ion-ion collisions.
- 2) The energy absorption per unit time is low and as a consequence, competition between collisional activation and deactivation processes will define the internal energy distribution.
- 3) Spontaneous radiative deactivation is much less probable than collisional deactivation.
- 4) Between activation and deactivation events, internal energy is distributed among many degrees of freedom.

To begin, considering a low number density of ions inside a high number density of a neutral gas, when a weak and uniform electric field is applied to this ion population, the ions move in the direction imposed by the electric field ( $E_e$ ) with a drift velocity of  $u_d$ . Since in this condition, ions move with the constant velocity, the force that is imposed on the ions by the electric field, has to be equal to the loss of momentum per time unit due to collisions with the neutral gas:

$$eE_e = \mu v_d \nu \quad (2.18)$$

In Equation 2.18,  $e$  is the charge of the ion,  $\nu$  is the ion-neutral collision frequency, and  $\mu$  is the reduced mass which is defined as follows:

$$\mu = \frac{m_{ion} m_{gas}}{(m_{ion} + m_{gas})} \quad (2.19)$$

In which,  $m_{ion}$  and  $m_{gas}$  are the masses of the ion and neutral gas, respectively. Under condition of a weak electric field,  $u_d$  is much slower than random thermal motion and can be ignored. Therefore, ions are almost in thermal equilibrium with the bath gas and their mean kinetic energy is given by:

$$\frac{1}{2}m_{ion}\langle v^2 \rangle = (3/2)kT_{bath} \quad (2.20)$$

in which,  $\langle v^2 \rangle$  is the mean square velocity of the ion,  $k$  is the Boltzmann constant, and  $T_{bath}$  is the bath gas temperature. When the electric field increases, the mean velocity of ions will obtain a random field component, and  $v_d$  cannot be ignored anymore. In this condition, the mean ion kinetic energy will have three main components as follows:<sup>135</sup>

$$\frac{1}{2}m_{ion}\langle v^2 \rangle = \frac{1}{2}m_{ion}v_d^2 + \frac{1}{2}m_{gas}v_d^2 + \frac{1}{2}m_{gas}\langle V^2 \rangle \quad (2.21)$$

in which  $\langle V^2 \rangle$  is the mean square velocity of the neutral. The first term on the right-hand side of Equation 2.21 corresponds to the drift motion of the ions due to the electric field; the second term corresponds to the random motion due to the electric field, and the third term is related to the random thermal motion in the absence of the electric field. Two latter terms are related to random motion of the ions, and since ion temperature is also explained as stochastic motion, the total ion energy due to the random motion can be expressed as follows:

$$\frac{3}{2}kT_{eff} = \frac{1}{2}m_{gas}v_d^2 + \frac{1}{2}m_{gas}\langle V^2 \rangle \quad (2.22)$$

In Equation 2.22, the second term on the right-hand side is completely thermal ( $1/2m_{gas}\langle V^2 \rangle = 3/2 kT_{bath}$ ). By rearrangement of Equation 2.18,  $v_d$  can be given as follows:

$$v_d = \frac{eE_e}{\mu v} \quad (2.23)$$

In addition, the steady state power absorption from the electric field,  $A(\infty)$ , can be given by Equation 2.24:

$$A(\infty) = eE_e v_d \quad (2.24)$$

By rearranging and replacing of Equation 2.23 in 2.24, we get to Equation 2.25:

$$v_d^2 = \frac{A(\infty)}{\mu v} \quad (2.25)$$

By replacing the Equation 2.25 in 2.22 and solving Equation 2.22 for  $T_{eff}$ , we obtain:

$$T_{eff} = T_{bath} + \frac{m_{gas}}{3km_{ion}} \frac{A(\infty)}{\xi} \quad (2.26)$$

in which,  $\xi$  is the reduced collision frequency and is given by:

$$\xi = \nu \left[ \frac{m_{gas}}{m_{ion} + m_{gas}} \right] \quad (2.27)$$

In Equation 2.26 which is extracted from momentum transfer theory, it is assumed that the reduced collision frequency is not a function of effective temperature. Employing the Boltzmann theory of ion transport results in a more accurate equation for effective temperature as follows:<sup>133</sup>

$$T_{eff} = T_{bath} + \frac{m_{gas}}{3km_{ion}} \frac{A(\infty)}{\xi(T_{eff})} \quad (2.28)$$

Equation 2.28 is very similar to Equation 2.26 except that in this case, reduced collision frequency is a function of effective temperature, and is given by Equation 2.29:<sup>136</sup>

$$\xi(T_{eff}) = \frac{4}{3} N_{neutral} \frac{\mu}{m_{ion}} \sqrt{\frac{8kT_{eff}}{\pi\mu}} \Omega^{(1,1)}(T_{eff}) \quad (2.29)$$

in which  $N_{neutral}$  is the number density of bath gas, and  $\Omega^{(1,1)}(T_{eff})$  is termed as "collision integral" that is related to the ion-neutral interaction potential.<sup>137</sup>

Using the Boltzmann theory of ion transport employed above for deriving an equation for effective temperature, a main limitation is that it considers that ion-neutral collisions must be elastic, and ion-neutral interaction potential has to be spherically symmetric, which limits the validity of the obtained relation for  $T_{eff}$  to only atomic ions in atomic gases. For polyatomic ions and polyatomic neutrals, instead of the Boltzmann equation, an analogous kinetic equation, namely the Wang Chang–Uhlenbeck–de Boer (WUB) equation<sup>138</sup> is used which considers inelastic collisions in the treatment of ion kinetics. By solving the WUB equation assuming that the internal energy distribution is characterized by an internal-state temperature  $T_i$ , effective temperature for polyatomic systems is given by:

$$T_{eff} = \frac{T_{bath} + \frac{m_{gas}}{3km_{ion}} \frac{A(\infty)}{\xi(T_{eff})}}{1 + \left[ \frac{m_{gas}}{m_{ion}} \right] \gamma(T_{eff}, T_i, T_{bath})} \quad (2.30)$$

in which, the fraction of energy which is lost due to the inelastic collisions is indicated by a dimensionless parameter  $\gamma$  that is a function of  $T_{eff}$ ,  $T_i$  and  $T_{bath}$ . In the case of heavy ions in a light bath gas,  $m_{ion} \gg m_{gas}$ , and therefore, effective temperature of the ions in inelastic ion-neutral collisions (Equation 2.30) becomes similar to Equation 2.28 for elastic ion-neutral collisions. It should be noted that  $T_i$  is not necessarily equal to  $T_{eff}$ , and in fact their relation depends on the cross section for inelastic ion-neutral collision versus the cross section for elastic collision. In a special case, when we have polyatomic ions in an atomic bath gas, the change in internal energy happens only in the ion, and as a consequence,  $T_i$  is equal to  $T_{eff}$  at steady state condition.

So far, a relation for effective temperature of the ions as a function of power absorption,  $A(\omega)$ , in an electric field is obtained. For quantitative evaluation of  $T_{eff}$ , the preliminary step is determination of  $A(\omega)$  in the experimental acceleration condition. Goeringer and McLuckey,<sup>132,133</sup> derived the equation for  $A(\omega)$  in the case of a supplementary AC resonance excitation voltage which is applied to end-cap electrodes. For this purpose, they employed the equation for a forced damped harmonic oscillator.

For a harmonic oscillator (ideal spring-mass problem), according to Newton's second law:

$$m \frac{d^2 z}{dt^2} + kz = 0 \quad (2.31)$$

where  $k$  is the spring constant, related to the angular frequency  $\omega_0$  by:

$$\omega_0 = \sqrt{\frac{k}{m}} \quad (2.32)$$

where  $m$  is the mass of the oscillator. In our case (resonance excitation inside the ion trap), an external force from AC voltage, in resonance with the secular frequency of the ion motion in the  $z$  direction, is applied to the ion which is given by:

$$F(t) = eE_s \cos(\omega_s t) \quad (2.33)$$

where  $e$  is the ionic charge,  $E_s$  is the supplementary AC electric field and  $\omega_s$  is its angular frequency. Therefore, for a forced harmonic oscillator we have:

$$\frac{d^2 z}{dt^2} + \omega_0^2 z = \frac{eE_s}{m_{ion}} \cos(\omega_s t) \quad (2.34)$$

The motion of ions inside the Paul trap, has two fundamental frequency components: one in the radial direction,  $\omega_{r,0}$ , and one in the  $z$  direction,  $\omega_{z,0}$ , which are generally given by:

$$\omega_{u,n} = \left(n + \frac{1}{2}\beta_u\right)\Omega, \quad n = 0, \pm 1, \pm 2, \dots \quad (2.35)$$

where  $\beta$  is the normalized oscillation frequency and related to the trapping parameters:  $a$  and  $q$ .  $\Omega$  is the radial frequency of the RF trapping voltage applied to the ring electrode. In the current case, the supplementary AC excitation voltage is in resonance with the secular frequency of the ion motion in the  $z$  direction. Therefore, from Equation 2.35, the fundamental  $z$ -motion frequency  $\omega_{z,0}$  is  $\beta(\Omega/2)$ . In addition, during excitation of ions inside the ion trap, oscillation of ions is damped by collisions with the bath gas. Therefore, for forced and damped harmonic oscillation of ions, the balance of forces based on Newton's second law is given by:

$$\frac{d^2 z}{dt^2} + \xi \frac{dz}{dt} + \left(\beta \frac{\Omega}{2}\right)^2 z = \frac{\Gamma e E_s}{m_{ion}} \cos(\omega_s t) \quad (2.36)$$

where the second term in the left side is added for damping by ion-neutral collisions, and  $\Gamma$  is a factor for compensation of the hyperbolic geometry of the endcaps.<sup>133</sup> At steady state condition, solution of Equation 2.36 is given by:

$$z(t) = \frac{\Gamma e E_s}{m_{ion} \left[ (\omega_0^2 - \omega_s^2)^2 + 4 \left(\frac{\xi}{2}\right)^2 \omega_s^2 \right]^{1/2}} \cos(\omega_s t - \delta) \quad (2.37)$$

$$\tan \delta = \frac{\omega_s \xi}{\omega_0^2 - \omega_s^2} \quad (2.38)$$

In the above equations,  $\delta$  is defined as the phase angle at  $t = 0$ . Power absorption in the excitation AC electric field is given by:

$$A(\infty) = \frac{\omega_s}{2\pi} \int_0^{2\pi/\omega_s} \xi m v^2 dt = \frac{\Gamma^2 e^2 E_s^2 \omega_s^2 \xi}{2m_{ion}[(\omega_0^2 - \omega_s^2)^2 + \xi^2 \omega_s^2]} \quad (2.39)$$

For resonant excitation,  $\omega_0$  is equal to the  $\omega_s$  and therefore,  $A(\infty)$  becomes:

$$A(\infty) = \frac{\Gamma^2 e^2 E_s^2}{2m_{ion}\xi} \quad (2.40)$$

Replacing Equation 2.40 in Equation 2.30 results in an expression for the effective temperature of heavy ions as follows:

$$T_{eff} = T_{bath} + \frac{m_{gas}}{6k(m/z)_{ion}^2} \frac{\Gamma^2 E_s^2}{\xi (T_{eff})^2} \quad (2.41)$$

Equation 2.41 was preliminarily extracted for the resonant excitation of ions inside the Paul trap, however, in our LTQ, because precursor ions are similarly excited by applying a dipolar-resonant excitation voltage to one pair of quadrupole rods, the same equation is applicable as well. The differences in the geometry of LTQ and Paul trap appear in their associated compensation factor,  $\Gamma$ . Therefore, we employ Equation 2.41 in latter chapters for calibration of the effective temperature of ions under resonant excitation in the LTQ.

## Higher-energy collision dissociation (HCD)

HCD is a fragmentation technique which is available in LTQ/orbitrap hybrid mass spectrometers. Initially, the idea for developing this technique was in view of performing triple quadrupole-like fragmentation by isolation of the precursor ions in the LTQ and then dissociation of them inside a C-trap.<sup>139</sup> C-trap is a curved linear ion trap located between LTQ and orbitrap, and its initial purpose is storing the ions before being analyzed in the orbitrap. Mann and co-workers performed ions' dissociation inside the C-trap by increasing its radiofrequency voltages up to 1000 V higher than the normal value, which was 1500 V peak to peak.<sup>139</sup> The configuration of this fragmentation technique which is called higher-energy C-trap dissociation is presented in **Figure 2-10**. First, precursor ions of interest are isolated in

the LTQ. Then, by reducing the voltage (see inset at the top of **Figure 2-10**), they are allowed to pass through a transfer octopole and enter to the C-trap. In the C-trap, under the influence of accelerating voltage, ions experience collisions with the nitrogen gas at a pressure of about 1 mTorr, and then dissociate. Afterwards, remaining precursor ions and produced fragments are transferred into the Orbitrap for analysis. The main limitation of this configuration is the unsatisfactory trapping efficiency of the low mass ions at the increased radiofrequency voltage. As a matter of fact, normally, the C-Trap has a high trapping efficiency for both low mass ions and high mass ions. But, during HCD, ions enter to the C-trap with a high kinetic energy, and due to the curved geometry of the C-trap, high mass ions are especially susceptible to be lost. To reduce this problem, it is necessary to increase the amplitude of the radiofrequency voltage which in turn moves the low mass cut off (LMCO) limit to higher  $m/z$  values.

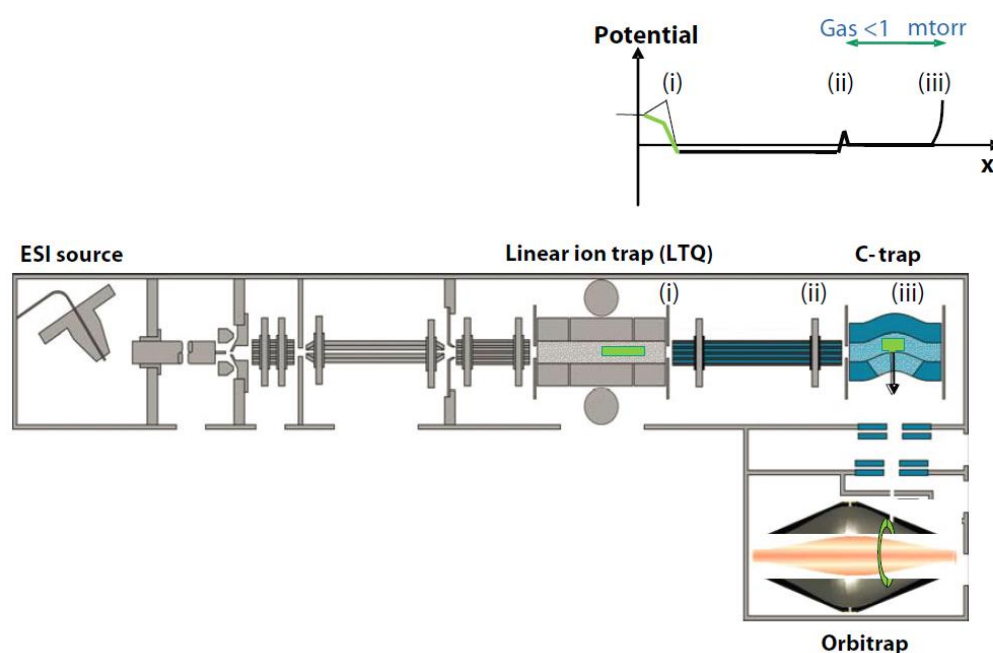


**Figure 2-10-** Original configuration of HCD where fragmentation takes place in the C-trap.<sup>139</sup>

To overcome this limitation, a second configuration for HCD was introduced, where a dedicated octopole is used as the collision cell instead of the C-trap. This octopole collision cell is located after the C-trap, and contains nitrogen as a collision gas ( $\sim 5$  mbar). This configuration is presented in **Figure 2-11**. An RF voltage with a frequency of 2.6 MHz, and a peak-to-peak voltage of 500 V is applied to the octopole. In addition, a DC offset which can



be varied between -250 V to +250 V is applied for excitation of the ions. Here, precursor ions of interest are isolated in the LTQ, and then, they pass through a transfer octopole and the C-trap to enter into the octopole collision cell. After fragmentation, all the ions are transferred back to the C-trap by increasing the potential of the octopole, and then they will be injected into the Orbitrap for high resolution mass analysis.

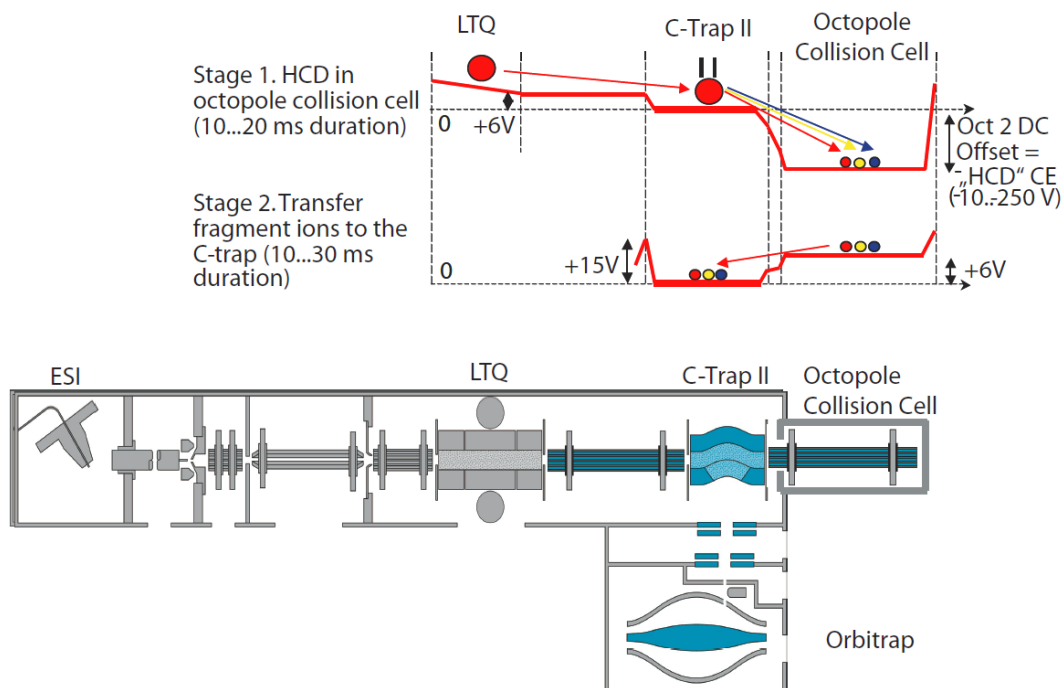


**Figure 2-11-** Second configuration of HCD where fragmentation takes place in a dedicated octopole.<sup>139</sup>

In this configuration, problems related to the curved geometry of the C-trap, and also LMCO do not exist anymore, and access to the low  $m/z$  range is feasible. Another advantage of performing HCD in the dedicated octopole collision cell is the possibility to change the type and pressure of the collision gas. Changing the pressure of the gas was not possible in the C-trap due to its influence on the pressure of the Orbitrap.

In this thesis, we use the HCD dissociation technique for ranking the stabilities of a series of host-guest (H-G) complexes in the gas phase which will be discussed in Chapter 6.

---

***Chapter 3: Low-energy CID, CID and HCD mass spectrometry for structural elucidation of saccharides and clarification of their dissolution mechanism in DMAc/LiCl***

---

## Introduction

Cellulose consists of a network of very long-chain saccharides composed of D-glucose monomers, bearing the general formula  $(C_6H_{10}O_5)_n$ .<sup>140</sup> This carbohydrate which is the main constituent of plant cell walls, has a plethora of applications including use in the fabrication of numerous products such as paper, wood, textiles, cosmetics, pharmaceuticals, and insulating materials.<sup>140–142</sup> One of the main distinctive characteristics of cellulose is its insolubility in common solvents. This resistance to dissolution is largely due to the presence of a very strong inter- and intra- molecular hydrogen bond network that extends along its three-dimensional structure. Research efforts have focused on finding viable solvent systems capable of dissolving cellulose, and among those reported to offer success are NaOH–water,<sup>143,144</sup> Urea/NaOH/water,<sup>145</sup> *N*-methylmorpholine *N*-oxide (NMMO)/water,<sup>146</sup> ionic liquids,<sup>147,148</sup> and *N,N*-dimethylacetamide/lithium chloride (DMAc/LiCl).<sup>149,150</sup>

DMAc/LiCl is an unconventional solvent system which is capable of dissolving large carbohydrates such as cellulose which are not soluble in common solvents. So far, various condensed phase studies have been performed in order to investigate the dissolution mechanism of cellulose in DMAc/LiCl. Generally, two different mechanisms have been proposed. First, McCormick et al.<sup>151</sup> in 1985 suggested that during the dissolution process,  $Li^+$  cations are coordinated by the carbonyl group of DMAc, making macrocations of the form  $Li^+(DMAc)_n$ . At the same time,  $Cl^-$  anions interact strongly with the protons of the hydroxyl groups on the cellulose, and consequently perturb the hydrogen bond network inherent to cellulose. This proposed mechanism did not portray any direct interaction between  $Li^+$  and the sugar. In 1992, however, Morgenstern et al.<sup>152</sup> hypothesized that during dissolution, one of the DMAc molecules in the coordination sphere of  $Li^+$  is replaced by one hydroxyl oxygen of the sugar. In this way, a direct interaction between lithium and cellulose is achieved, thereby involving both  $Li^+$  and  $Cl^-$  in the disruption of the hydrogen bond network of cellulose. Recently, Zhang et al.<sup>153</sup> tried to revise previously proposed mechanisms, and they explained that in the absence of sugar molecules,  $Li^+$  and  $Cl^-$  ions in DMAc exist in the form of ion pairs. During dissolution of a sugar,  $Cl^-$  ions start to interact strongly with hydroxyl protons of the sugar resulting in a breaking apart of its hydrogen bond network. At the same

time,  $\text{Li}^+$  ions become solvated by DMAc molecules resulting in further separation of  $\text{Li}^+\text{-Cl}^-$  ion-pairs. This process results in dispersion and eventual dissolution of cellulose chains in the solvent system. The above studies offer a coherent picture of the dissolution mechanism of cellulose, with the only discrepancy between the proposed mechanisms being the point about the presence or absence of a direct interaction between  $\text{Li}^+$  and the sugar. In this chapter, electrospray ionization mass spectrometry has been employed to shed additional light on the previous findings in order to gain a better understanding about the precise dissolution mechanism of sugars in DMAc/LiCl. This approach can provide some unique information that can be complementary to data obtained using other techniques.

In addition to the interest in the mechanistic aspect of saccharides dissolution, mass spectrometry-based techniques have made significant analytical contributions to the structural elucidation of carbohydrates.<sup>154–157</sup> Complete, unambiguous structural determination of large sugar molecules can be a daunting task owing to the large variety of monomers, linkage types, branching, and anomeric configurations that are possible. Using ESI-MS, sugars are usually detected as metal adducts or protonated molecules<sup>158</sup> in positive ion mode, or as anionic adducts or de-protonated molecules in the negative ion mode. Generally, MS/MS experiments on sugars produce two types of fragments: product ions that result from glycosidic bond cleavages, involving rupture of a single bond, and those that result from more complicated cross-ring cleavages.

One of the metal ions that has been extensively investigated for ionization and structural characterization of saccharides is lithium ion.<sup>159–161</sup> Leary and co-workers utilized fast atom bombardment to produce mono-lithiated<sup>162</sup> and di-lithiated<sup>163,164</sup> adducts of isomeric oligosaccharides. They then employed tandem mass spectrometry experiments to differentiate linkage type and position in various isomers. They also elucidated dissociation mechanisms of mono- and di- lithiated adducts of disaccharides.<sup>162,164</sup> In 1994, Ngoka *et al.*<sup>165</sup> investigated metastable decay rates of protonated and metal coordinated oligosaccharides, and they observed the order of decay rate as follows:  $\text{H}^+ > \text{Li}^+ > \text{Na}^+ > \text{K}^+ > \text{Cs}^+$ . In comparing the relative affinities of the alkali cations towards oligosaccharides ( $\text{Li}^+ > \text{Na}^+ > \text{K}^+ > \text{Cs}^+$ ), as was suggested earlier by Veith in 1977,<sup>166</sup> Ngoka *et al.* explained that

among the alkali metals, lithium is the best option for structural analysis of sugars because it strongly coordinates to the sugars, stays attached to them during fragmentation processes, and produces structurally-informative fragment ions.<sup>160,165,167,168</sup>

In the current work, the main goal is to use tandem mass spectrometry techniques, namely low-energy CID,<sup>169</sup> CID<sup>169</sup> and HCD<sup>139</sup> to: 1) evaluate and compare the capabilities of these techniques for structural characterization of sugars and, 2) improve current knowledge about the dissolution mechanism of sugars in DMAc/LiCl. For this purpose, we extend the work of a previous ESI-MS study<sup>170</sup> which demonstrated the production of multiple neutral salt adducted lithiated sugars. Our re-examination investigates MS/MS fragmentation patterns of these LiCl adducts and their potential use for structural elucidation of two model carbohydrates, maltoheptaose (G<sub>7</sub>) and maltodecaose (G<sub>10</sub>).

## Experimental section

Maltodecaose and maltoheptaose were purchased from Elicityl (Crolles, France). *N,N*-Dimethylacetamide, and LiCl were purchased from Sigma-Aldrich (Saint-Quentin Fallavier, France). Preparation of stock solutions was performed with the same method as explained in a previously published paper.<sup>170</sup> Briefly, stock solutions (concentration of sugar: 0.3 mM, and LiCl: ~ 2.3 mM) were prepared as follows: solvent was heated to 100°C, then sugar was added and solution was stirred and heated for 30 min. Vials were then capped and heated and stirred for another 30 min. Next, at 80°C, LiCl was added and stirred for 2 hours. Afterwards, overnight stirring was performed at 50°C. Working solutions were prepared by dilution of the stock solution to the final concentration of 10 µM (sugar), and ~ 70 µM (LiCl).

Experiments were performed using a LTQ-XL/Orbitrap hybrid instrument (Thermo Fisher®, San Jose, CA). ESI-MS acquisitions were performed in the positive ion mode using a mass resolving power of  $3 \times 10^4$  at  $m/z$  400. Average scan number was set at 2, and maximum ion injection time at 500 ms. Electrospray voltage was set at 3.8 kV, capillary voltage at 30 V, and tube lens offset at 70 V. Drying gas temperature was 275°C, and sheath, auxiliary and sweep gas (all were N<sub>2</sub>) flows were set at 35, 0 and 2, respectively (arbitrary units). Solutions were injected into the ion source using a syringe pump with a flow rate of 5 µLmin<sup>-1</sup>.

For HCD experiments, the precursor ions were isolated with an isolation window of 10  $m/z$  units in the LTQ. These ions were decomposed in the HCD cell with an activation time of 30 ms, using  $N_2$  as collision gas and finally analyzed in the Orbitrap. For CID experiments, helium was used as trapping and collision gas,  $q$  was set at 0.25, activation time at 30 ms and isolation window at 10  $m/z$  units. To obtain time- and energy-dependent fragmentation efficiency curves, the instrument was set to “ion trap mass analyzer”, and instead of normalized collision energy (NCE), peak-to-peak excitation voltage ( $V_{p-p}$ ) was utilized. In addition, activation time was changed from 1 s to 60 s, and activation voltage was varied from 0 to about 3 V. Detailed explanations about CID and HCD decomposition modes in LTQ/Orbitrap hybrid instrument were presented in a previous publication.<sup>171</sup>

## Results and discussion

Before presenting our findings, it should be noted that Domon and Costello nomenclature<sup>172</sup> has been used for annotation of the observed fragment ions. In addition, because of the symmetry of the  $G_7$  and  $G_{10}$  model oligosaccharides investigated in this study, there is one ambiguity as to the exact origin of some fragment ions that may be formed from specific decompositions at both the reducing and non-reducing ends of the saccharide chains. Therefore, both possible types of product ion (having the same  $m/z$ ) are displayed in the cleavage maps, and also in the spectra (in parentheses). Differentiation of these kinds of fragments is beyond the scope of the current work, however, it can be performed with the help of isotopic labelling.<sup>173</sup>

**Figure 3-1** shows the ESI mass spectrum of  $G_7$  dissolved in DMAc/LiCl. Similar to what has been observed previously,<sup>170</sup> in this spectrum, the presence of  $m/z$  1159.4 which is  $[G_7+Li]^+$  and neutral LiCl attachments to this ion:  $[G_7+Li+nLiCl]^+$ , are evident ( $n$  is the number of LiCl adducts). For instance, 1201.4 is attributed to  $[G_7+Li+LiCl]^+$ ; 1243.4 to  $[G_7+Li+2LiCl]^+$ ; 1285.4 to  $[G_7+Li+3LiCl]^+$ ; 1327.4 to  $[G_7+Li+4LiCl]^+$  and so on.

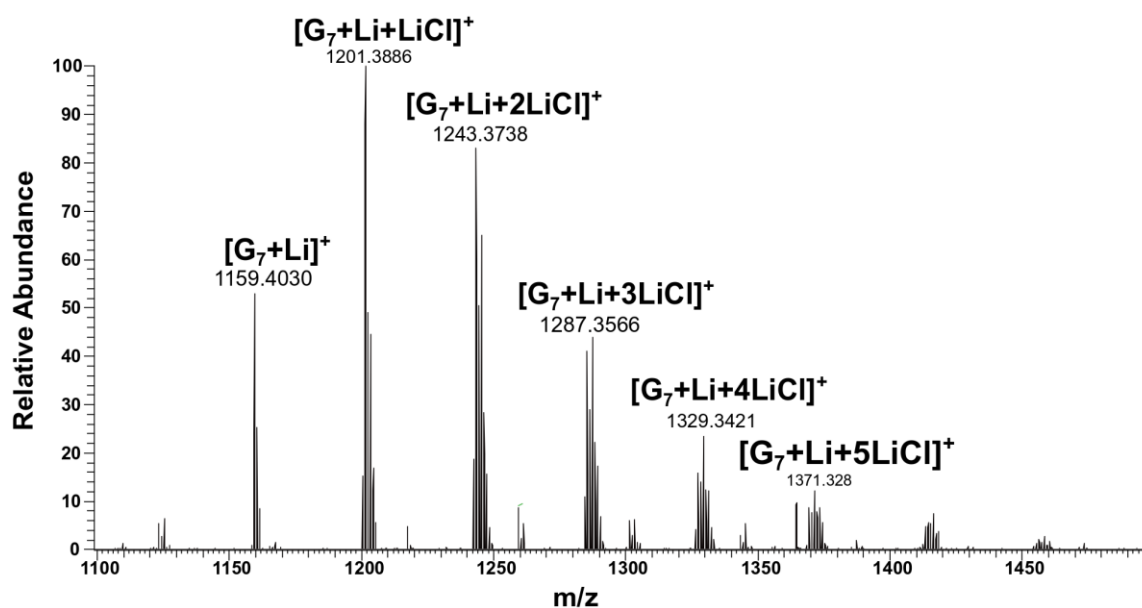


**Figure 3-1-** ESI mass spectrum of the maltoheptaose dissolved in DMAc/LiCl. Presence of multiple LiCl adducts of lithiated maltoheptaose is evident in the spectrum.

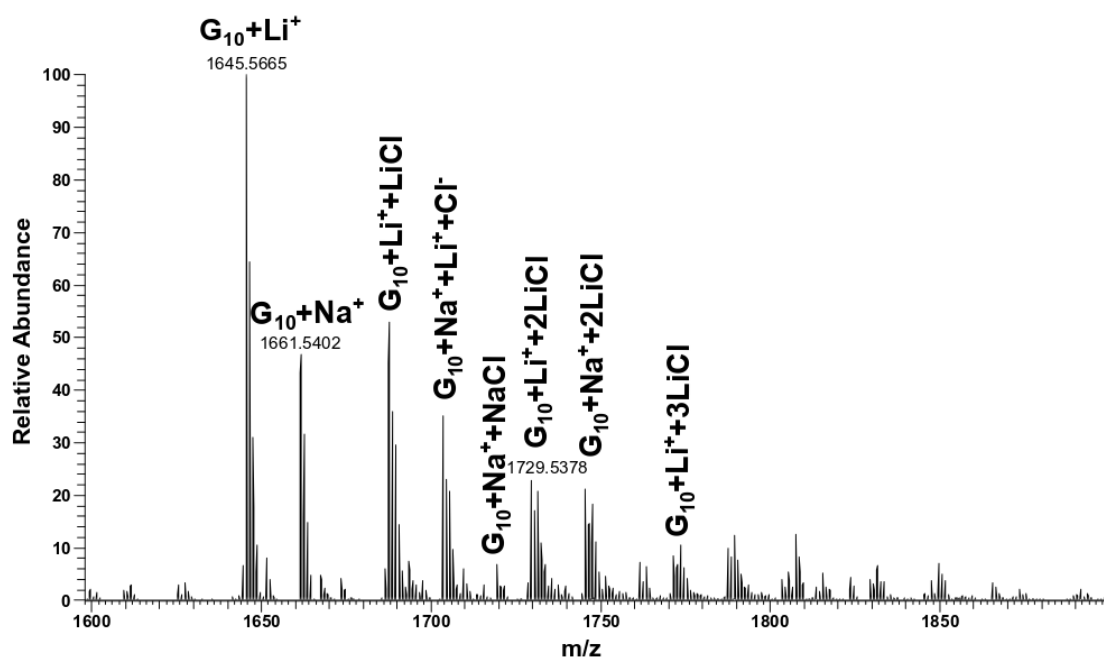


**Figure 3-2-** ESI mass spectrum of maltodecaose dissolved in DMAc/LiCl. The presence of multiple LiCl adducts of lithiated and sodiated maltodecaose, and also NaCl adducted to the sodiated maltodecaose are evident in the spectrum.

In the ESI mass spectrum of  $G_{10}$  dissolved in DMAc/0.01% LiCl, the same multiple neutral LiCl attachments were observed (**Figure 3-2**). However, in this case, sodium-bound sugar, and NaCl adducts of the sodiated and lithiated maltodecaose were also observed, implying sodium contamination.

**Figure 3-3** presents low energy CID spectra of  $[G_7+Li]^+$  acquired using the ion trap mode of the mass spectrometer. From this figure, at very low peak-to-peak voltages of 2.2 or 2.6 V, and a quite long activation time (60 s), the major observed fragments are  $[^{2,4}X_6(^{0,2}A_7)+Li]^+$  and  $[G_7+Li-H_2O]^+$ . Other lower intensity fragments include  $Y_6(C_6)$ ,  $Z_6(B_6)$ ,  $Y_5(C_5)$ ,  $Z_5(B_5)$ ,  $Y_4(C_4)$  and  $Z_4(B_4)$ . It should be noted that the peak at  $m/z$  779 in **Figure 3-3**, most probably, is resulting from dissociation of a contaminant precursor ion located near the precursor ion. This was due to the relatively large employed isolation window of 10  $m/z$  units in the LTQ.

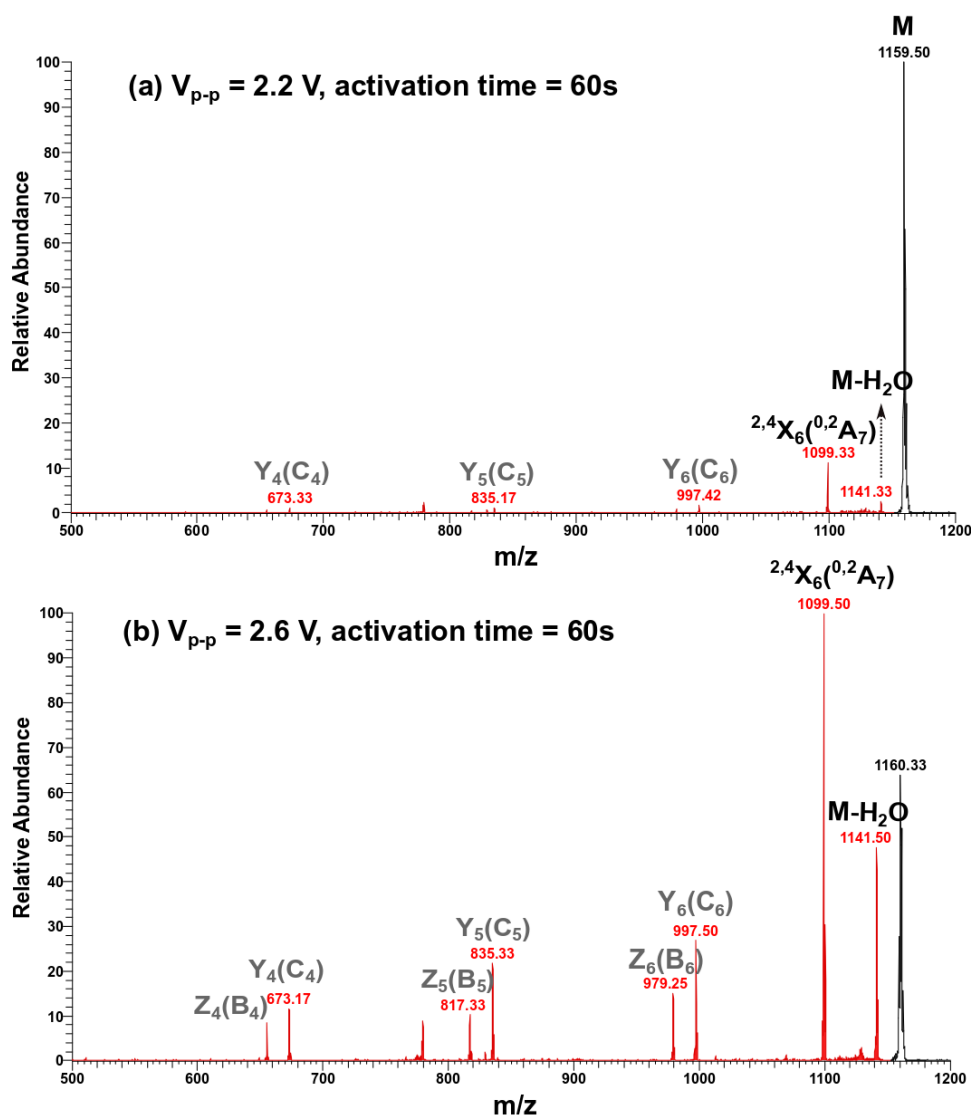
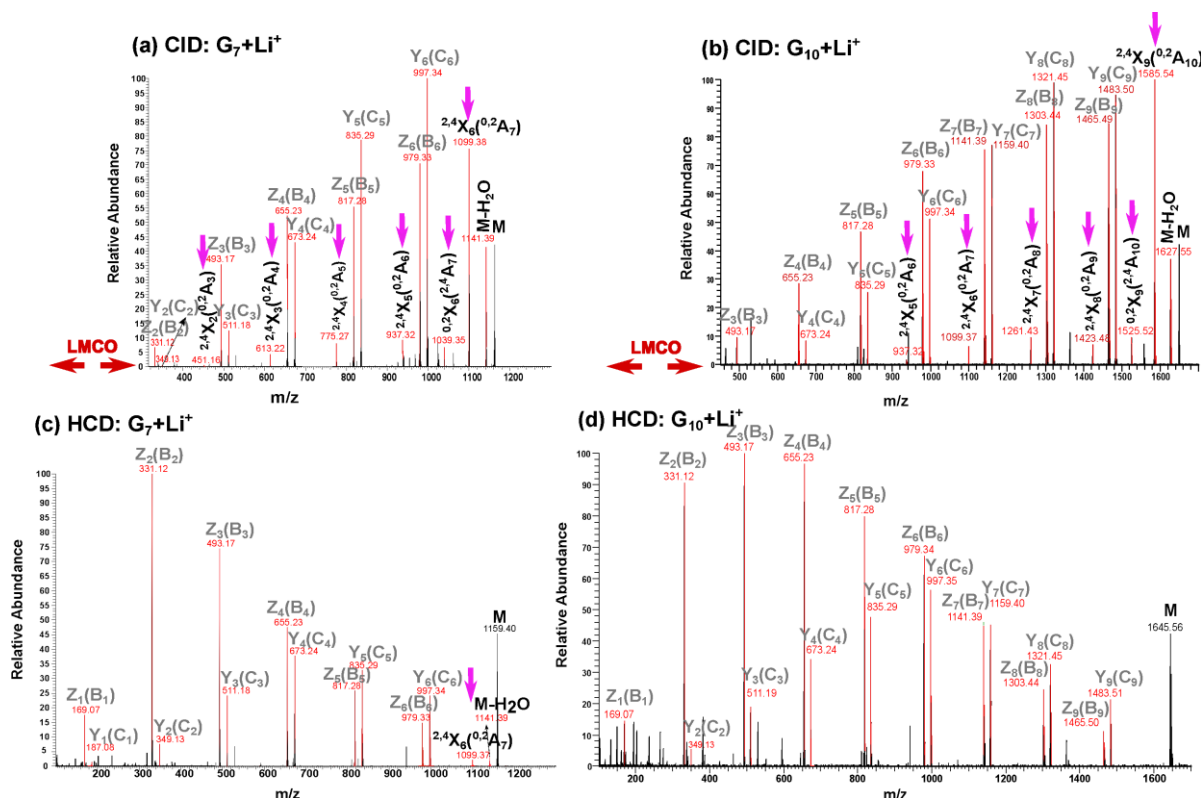


**Figure 3-3-** CID MS/MS spectra of  $M = [G_7+Li]^+$  precursors obtained with 60 s activation time and at collision voltages of (a) 2.2 V, and (b) 2.6 V using a linear ion trap mass spectrometer.

**Figure 3-4** exhibits CID and HCD spectra of  $[G_7+Li]^+$  and  $[G_{10}+Li]^+$  (the corresponding cleavage maps are presented in **Figure 3-5**). It should be noted that the reason for presenting the CID



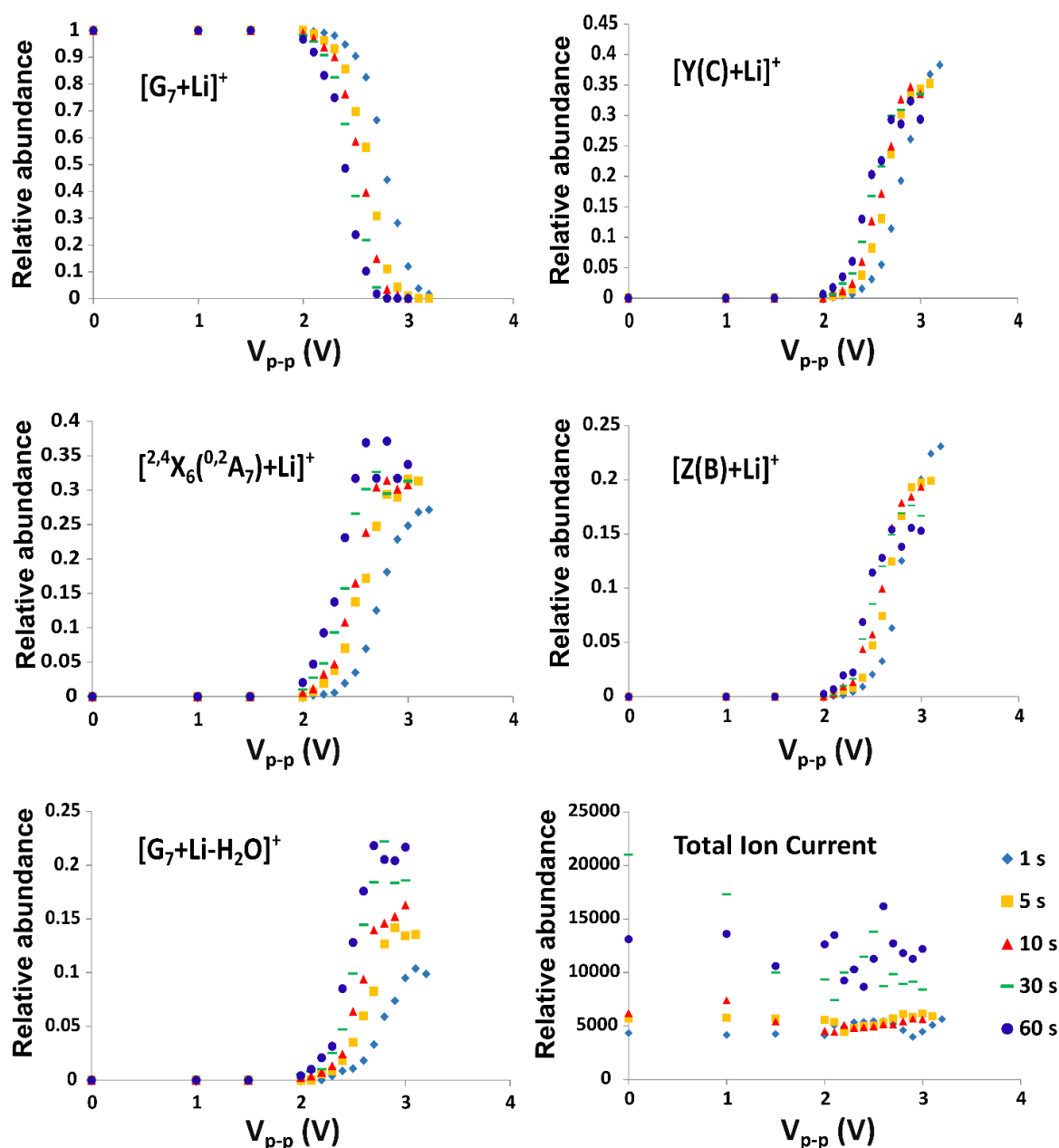
and HCD spectra in dissimilar  $m/z$  ranges is that in the CID technique due to the low mass cut off we are not able to observe low  $m/z$  ions. However, in the HCD technique, this problem does not exist, and access to low  $m/z$  ions is possible. From the spectra, it is evident that, in both CID and HCD, fragments resulting from glycosidic bond cleavages are dominant. However, in CID, fragment ions resulting from cross-ring cleavages (mainly  $^{2,4}X_n$  and  $^{0,2}X_n$ , or  $^{0,2}A_{n+1}$  and  $^{2,4}A_{n+1}$  types) are present as well.



**Figure 3-4-** (a) CID spectrum of  $M = [G_7+Li]^+$  (NCE of 17 %) and (c) its HCD spectrum (NCE of 45 %); (b) CID spectrum of  $M = [G_{10}+Li]^+$  (NCE of 24 %) and (d) its HCD spectrum (NCE of 45 %). Peaks of fragments containing one metal ion are shown in red. Because of the LMC0, access to the low  $m/z$  fragments in the CID spectra of (a) and (b) was not possible.

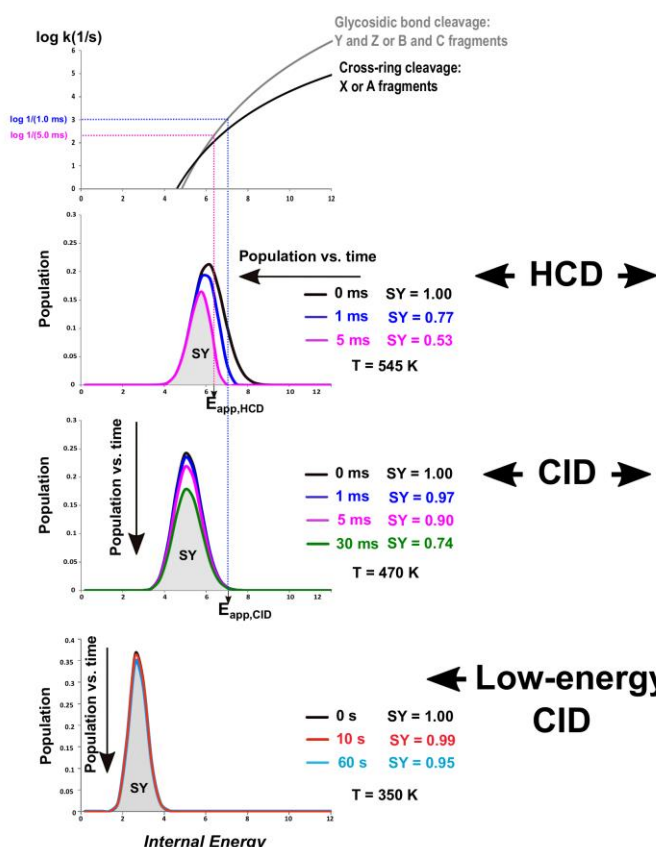
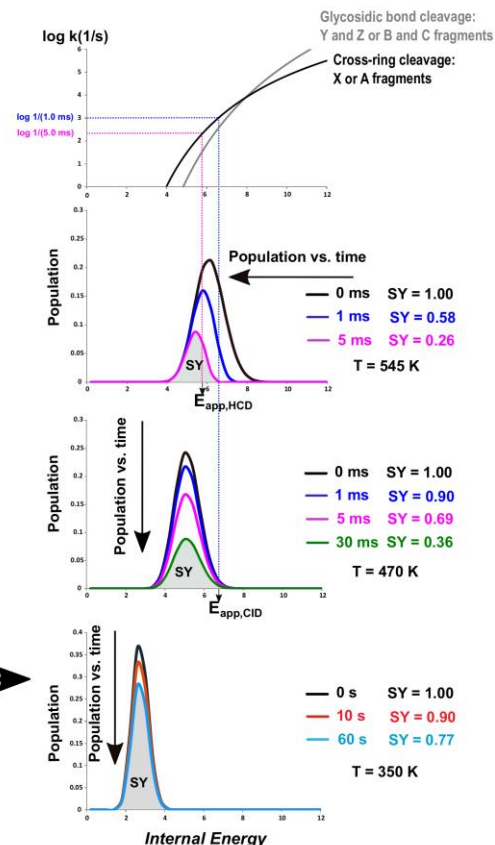
As is already well known, and based on time and energy dependent fragmentation efficiency curves<sup>105</sup> performed on  $[G_7+Li]^+$  (**Figure 3-6**), formation of cross-ring cleavage fragments is less entropically favorable than formation of glycosidic bond cleavage fragments. In fact, the fragments whose production involves extensive rearrangements (e.g., cross-ring cleavages) exhibit a strong time dependence in the time- and energy dependent fragmentation efficiency curves ( $^{2,4}X_6(^{0,2}A_7)$  and  $[G_7+Li-H_2O]^+$  ions in **Figure 3-6**) and their formation is entropically unfavorable.<sup>105,97</sup> In other words, rearrangement of the precursor ion is a slow





**Figure 3-6-** Time- and energy-dependent fragmentation efficiency curves for the  $[G_7+Li]^+$  precursor and its fragments at reaction times of 1 s, 5 s, 10 s, 30 s and 60 s. Relative intensities for each type of fragment are combined. For instance, in the plot labeled Y, intensities of all the Y type ions are summed together. In the case of  $[^{2,4}X_6(^{0,2}A_7)+Li]^+$ , this ion was the only fragment from this type that was observed. Plots of total ion current using different reaction times are also presented.

It should be noted that, for improved clarity, the pathway corresponding to the loss of water is not shown in **Figure 3-7a**. In this figure,  $E_{app}$  is the appearance energy, i.e. the minimum energy that must be acquired by the precursor ion to produce fragments in the time scale of the mass spectrometer.

**(A) Sugar + Li<sup>+</sup>****(B) Sugar + Li<sup>+</sup> + LiCl****(C)**

<ul style="list-style-type: none"> <li>Long residence time inside the ion trap (up to 60 s)</li> <li>Low internal energy deposition (He collision gas)</li> <li>Equilibrated Maxwell-Boltzmann internal energy distribution</li> <li>Rapid activation and deactivation rates compared to dissociation of activated species</li> <li>Preference to competitive, and rearrangement pathways</li> </ul>	<ul style="list-style-type: none"> <li>Short excitation time (30 ms)</li> <li>Higher internal energy deposition compared to low-energy CID (He collision gas)</li> <li>Slightly truncated, equilibrated Maxwell-Boltzmann internal energy distribution</li> <li>Partial replacement of dissociated population by a subsequently activated population</li> </ul>	<ul style="list-style-type: none"> <li>Short excitation time (5 ms)</li> <li>Higher amount of internal energy deposition compared to CID (N<sub>2</sub> collision gas)</li> <li>Truncated Maxwell-Boltzmann internal energy distribution</li> <li>Almost no replacement of dissociated population by a subsequently activated population (depending on the experimental condition)</li> <li>Preference to consecutive pathways</li> </ul>
<b>Low-energy CID</b>	<b>CID</b>	<b>HCD</b>

**Figure 3-7-** (a) Schematic plot representing logarithm of dissociation rate constant versus deposited internal energy for  $[\text{sugar} + \text{Li}]^+$ , and (b) that of  $[\text{sugar} + \text{Li} + \text{LiCl}]^+$ . Internal energy distributions during low-energy CID, CID and HCD processes are also displayed. The portion indicated with gray color corresponds to the surviving population at the end of the decomposition time. (c) Comparison of the three techniques of low-energy CID, CID and HCD.

**Figure 3-7** also schematically displays the evolution of the internal energy distribution of precursor ions with time for HCD, CID and low-energy CID processes. By considering a reaction time of 5 ms for HCD and 1 ms for CID<sup>171</sup> ( $\log k$  of 2.3 (pink line) and 3 (blue line), respectively, **Figure 3-7a**), it is evident that in both CID and HCD, the rates of glycosidic bond cleavage processes are higher than those of cross-ring cleavages (**Figure 3-4**).

In low-energy CID, because of the relatively high pressure of the bath gas (He), and also the long residence time of the ions inside the ion trap, the precursor ion population experiences a large number of collisions. In addition, considering the large size of the precursor ion and also the low amount of internal energy that is acquired by the precursor ion (compared to the HCD and CID processes), it can be expected that the rates of the activation and de-activation processes are comparable, or even higher, than the dissociation rate of activated species. As a consequence, the precursor ion population has a thermal (Maxwell-Boltzmann) distribution of internal energy. In this condition (low internal energy and long decomposition time), mainly competitive processes, yielding fragment ions just above threshold energy, can be observed. Moreover, according to **Figure 3-7**, product ions arising from cross-ring cleavages are expected to be dominant. This is consistent with the observed fragmentation spectra appearing in **Figure 3-3**.

In CID under short excitation time (30 ms) and higher deposited energy (compared to low-energy CID), the decomposition time is shorter than the activation time and the population is not in thermal equilibrium. Instead, it is characterized by a slightly truncated thermal distribution which is in equilibrium.<sup>171</sup> In other words, initially, the precursor ion population has a thermal distribution of internal energy. At higher collision energies and thus increased internal energy, the higher energy part of the population is decomposed but becomes partially replaced by a new activated population that acquires energy later in the activation process. Therefore, the internal energy distribution will remain thermal during the activation process with a slight truncation at the higher energy portion of the population. Notably, it is not possible to sustain the survival of high energy precursor ions because this population is decomposed prior to reaching very high energies. Thus, in CID, competitive fragmentations may be observed but consecutive decompositions are disfavored.

On the contrary, in HCD, a high amount of energy is deposited on the ions in a very short time (maximum 5 ms). Again, initially, the precursor ion population has a thermal distribution of internal energy, but upon internal energy uptake, the high energy tail of the distribution is decomposed. However, in this case, because energy deposition occurs all at once, in a pulsed fashion, the dissociated population cannot be replaced by a subsequently activated population. Therefore, we have a distribution of internal energy which is not in equilibrium, and is truncated on the high-energy end. It should be noted that compared to CID, HCD results in a broader distribution of precursor ion internal energy which is a result of the higher deposited energy, the larger size of the collision gas ( $N_2$  versus He) and the shorter excitation time. Furthermore, in HCD, a non-resonant process, access to higher energies is possible compared to CID. Thus, both competitive and consecutive fragmentations are favorable. Another very important difference between HCD and CID in ion trap is that HCD also excites fragment ions while CID in ion trap does not. A brief comparison low-energy CID, CID and HCD is presented in **Figure 3-7c**.

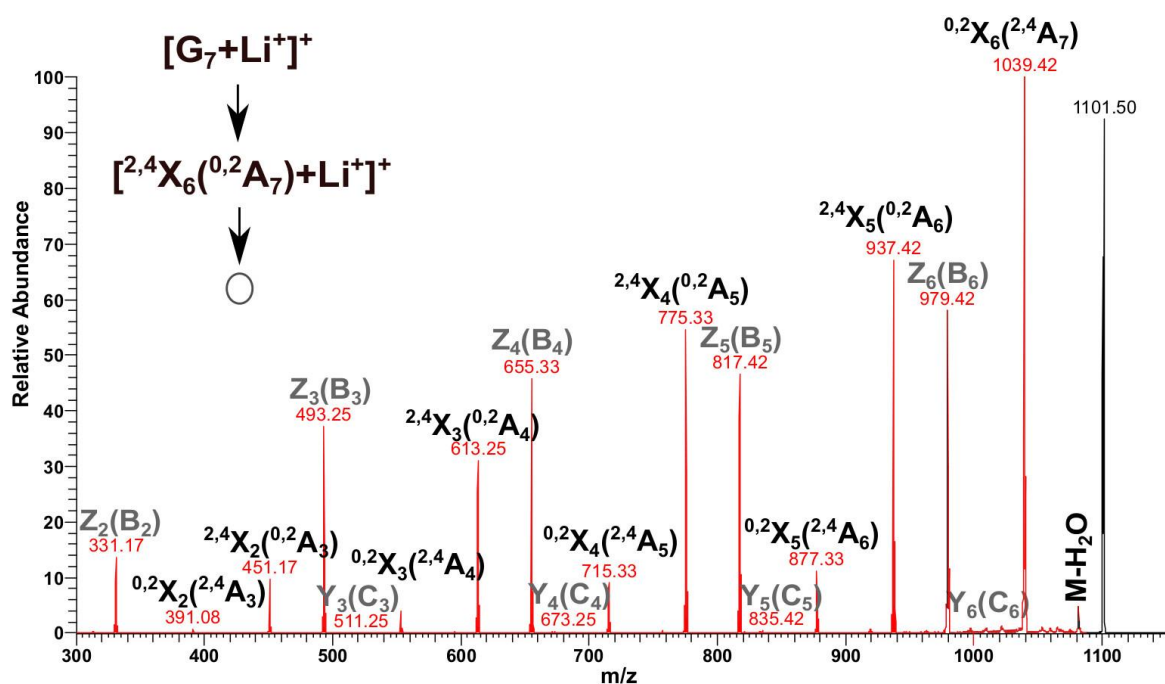


**Figure 3-8-** MS/MS/MS spectrum of  $[G_7 + Li^+]^+$  (NCE of 30 %)  $\rightarrow M = [{}^{2,4}X_6({}^{0,2}A_7) + Li^+]^+$  (NCE of 30 %)  $\rightarrow o$  recorded using the CID mode of the ion trap mass spectrometer.

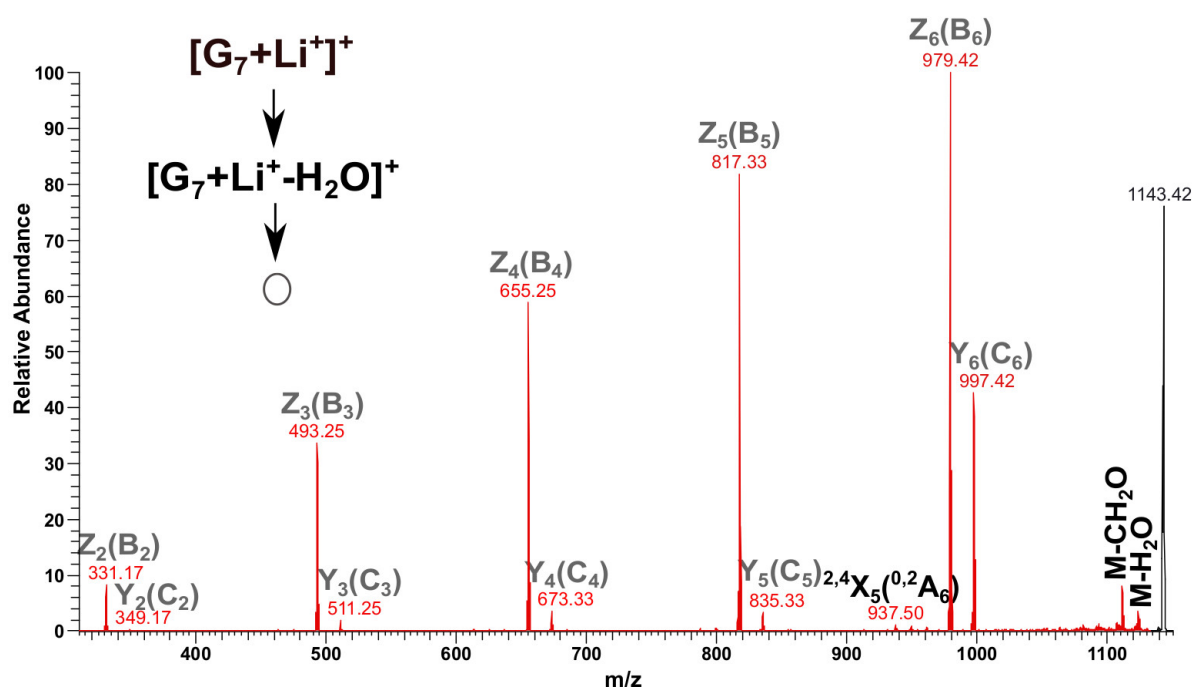


Figure 3-9- MS/MS/MS spectrum of  $[G_7+Li^+]^+$  (NCE of 30 %) →  $M = [G_7+Li^+-H_2O]^+$  (NCE of 30 %) →  $o$  recorded using the CID mode of the ion trap mass spectrometer.

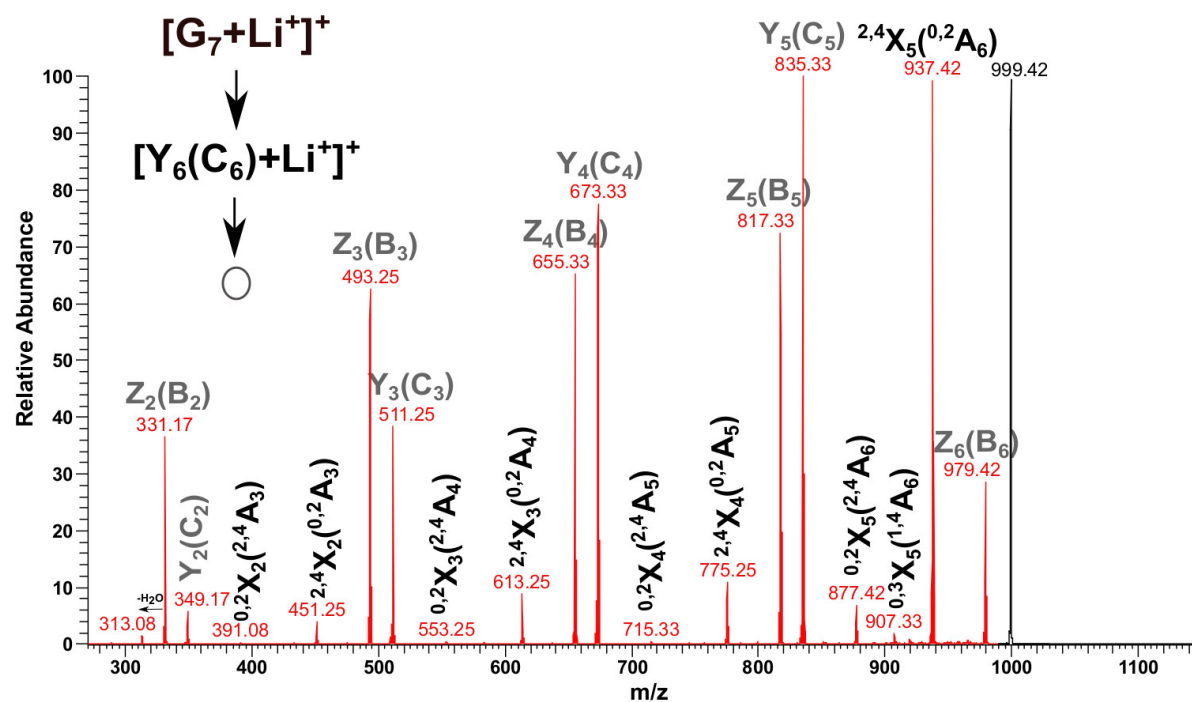
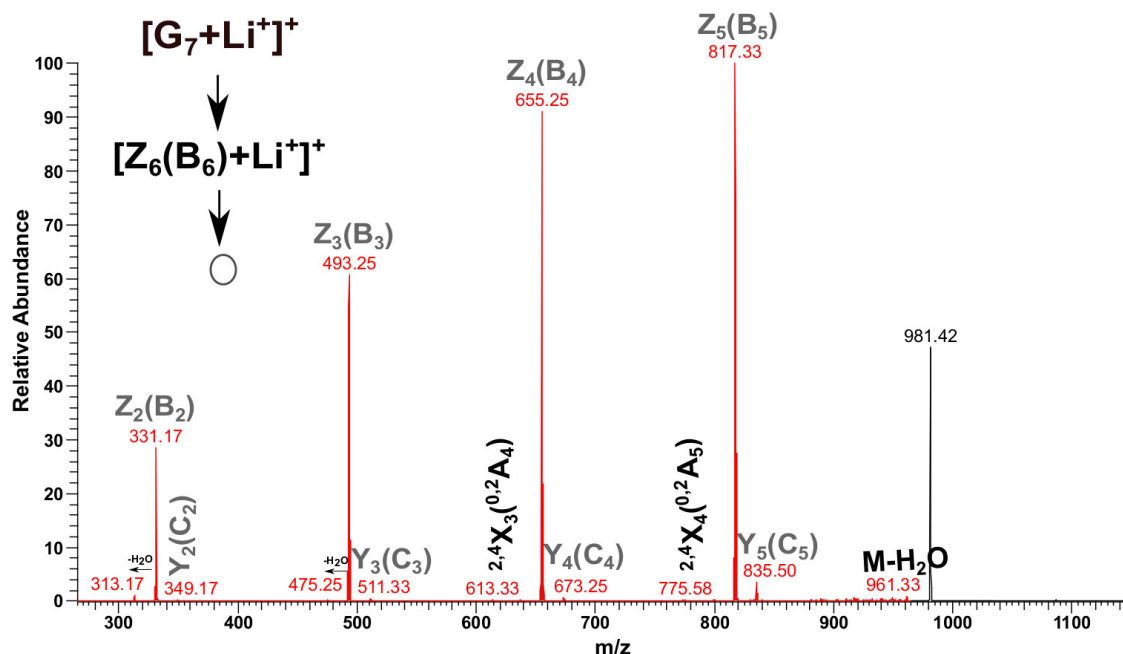


Figure 3-10- MS/MS/MS spectrum of  $[G_7+Li^+]^+$  (NCE of 30 %) →  $[Y_6(C_6)+Li^+]^+$  (NCE of 30 %) →  $o$  recorded using the CID mode of the ion trap mass spectrometer.





**Figure 3-11-** MS/MS/MS spectrum of  $[G_7+Li]^+$  (NCE of 30 %)  $\rightarrow M = [Z_6(B_6)+Li]^+$  (NCE of 30 %)  $\rightarrow o$  recorded using the CID mode of the ion trap mass spectrometer.

Based on the above discussion, at very low energies and large activation times (**Figure 3-3a**), cross-ring cleavages represent the main cleavage pathways, and the major observed fragments are  $[^{2,4}X_6(^{0,2}A_7)+Li]^+$  and  $[G_7+Li-H_2O]^+$ . As the energy increases (**Figure 3-3b**), new competitive fragment ions start to appear which result from glycosidic bond cleavages (Z(B), Y(C) type ions). At even higher energies and lower activation times (**Figure 3-4a** and **3.4b**), ions resulting from glycosidic bond cleavages become the dominant fragments. In addition, low abundances of X(A) type ions are formed by consecutive fragmentation of  $[^{2,4}X_6(^{0,2}A_7)+Li]^+$  (even if consecutive fragmentations are disfavored in CID). Finally, using HCD, glycosidic bond cleavage is the main process owing to the higher energy available, and the  $[^{2,4}X_6(^{0,2}A_7)+Li]^+$  fragment is not observed. Not surprisingly then, consecutive fragments of  $[^{2,4}X_6(^{0,2}A_7)+Li]^+$  (other X(A) type ions) are also absent in **Figure 3-4c** and **3.4d**. Based on the above discussion and the fragmentation spectra of the fragment ions of  $[G_7 + Li]^+$  (**Figures 3.8-3.11**), a summary of fragmentation process is presented in **Figure 3-12**.



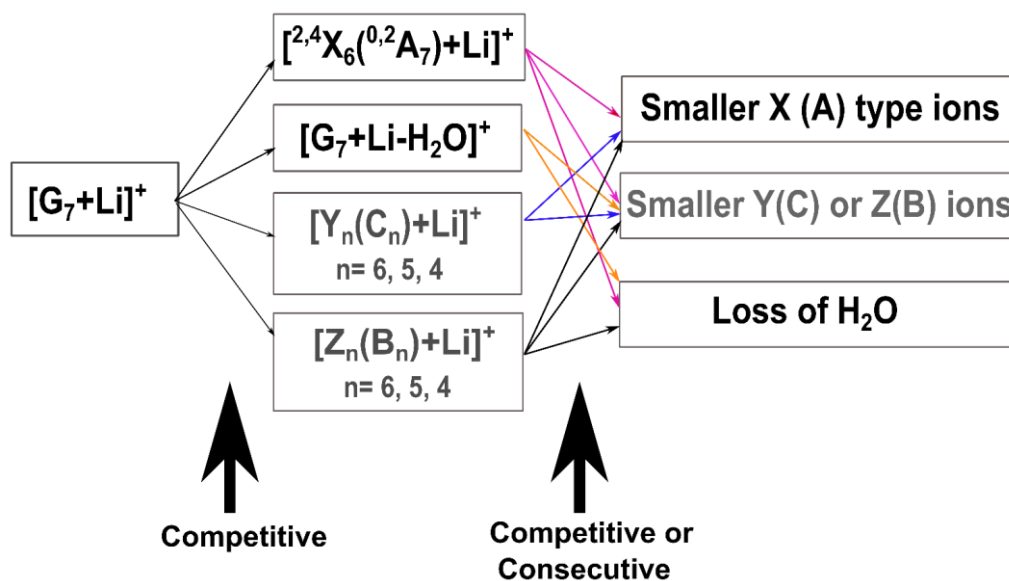


**Figure 3-12-** Summary for decompositions of  $[G_7+Li]^+$ . Fragments resulting from glycosidic bond cleavage are indicated in gray. Possible fragmentation pathways for  $[^{2,4}X_6(^{0,2}A_7)+Li]^+$  are indicated in pink, for  $[G_7+Li-H_2O]^+$  in orange, for  $[Y_n(C_n)+Li]^+$  in dark blue, and for  $[Z_n(B_n)+Li]^+$  in black.

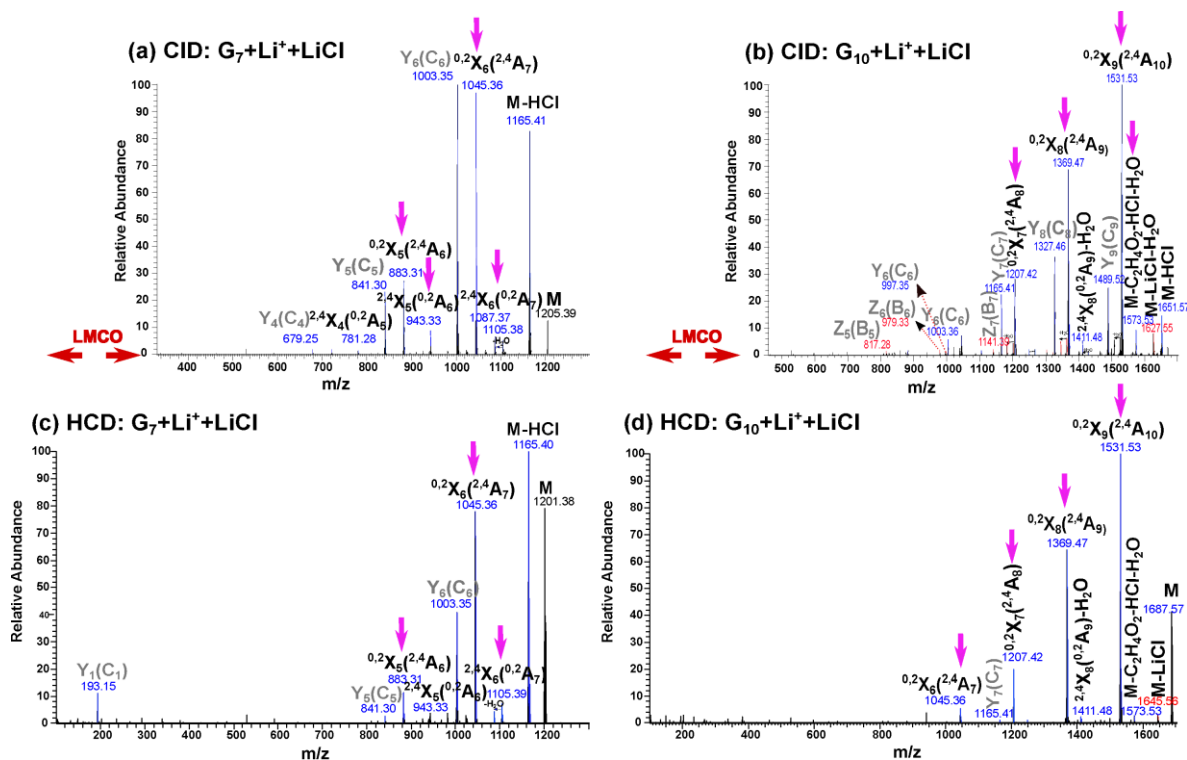


**Figure 3-13-** (a) CID spectrum of  $M = [G_7+Li+LiCl]^+$  (NCE of 20 %) and (c) its HCD spectrum (NCE of 20 %); (b) CID spectrum of  $M = [G_{10}+Li+LiCl]^+$  (NCE of 30 %) and (d) its HCD spectrum (NCE of 30 %). Peaks of fragments containing one metal ion are shown in red while those with two metal ions are shown in dark blue. Because of the LMCO, access to the low  $m/z$  fragments in the CID spectra of (a) and (b) was not possible.

**Figure 3-13** displays the CID and HCD spectra of  $[G_7+Li+LiCl]^+$  and  $[G_{10}+Li+LiCl]^+$  precursors. In this figure, fragments containing only one  $Li^+$  are shown in red, whereas those bearing two  $Li^+$  are displayed in dark blue. It should be noted that fragments containing one or two metal ions may have the same annotation. For these cases, they can be distinguished by the color used to indicate their peaks. For example,  $Y_6(C_6)$  or  $[G_7+Li+LiCl-HCl]^+$  ions in **Figure 3-13a** each contain two  $Li^+$  and their peaks are shown in dark blue. But the peak for  $[G_{10}+Li+LiCl]^+-LiCl$  in **Figure 3-13d** (only one  $Li^+$ ) is shown in red. In addition, it should be noted that none of the indicated fragments in **Figure 3-13** contain Cl. In other words, during fragmentation, HCl was always readily lost.

From **Figure 3-13**, some important points can be extracted. First, if we compare spectra of the singly lithiated sugars in **Figure 3-4** with the LiCl adducted lithiated sugars in **Figure 3-13**, it is evident that while in the former situation, fragments resulting from glycosidic bond cleavages were dominant, in the latter case, abundances of the ions resulting from cross-ring cleavage are higher. Secondly, loss of HCl is preferred to the loss of LiCl, which implies that there is a strong interaction between the sugar and  $Li^+$ . Thirdly, in **Figure 3-13**, abundances of fragments containing two metal ions are higher compared to those fragments with only one metal ion. This observation can be explained with a plot of  $\log k$  versus deposited internal energy similar to what is shown in **Figure 3-7b**. It should be noted that, for better clarity, the pathway corresponding to the loss of HCl is not shown in **Figure 3-7b**. Based on the appearance energies and also internal energy distributions corresponding to CID and HCD processes, it is evident that in both CID and HCD spectra, cross-ring cleavages have higher rate constants compared to glycosidic bond cleavages, as evidenced by the high intensities of X or A type ions in the spectra. In the CID spectrum, there is a high intensity of the  $Y_6(C_6)$  ion (glycosidic bond cleavage) as well (**Figure 3-13a**), and in general, the rates of the two types of processes are comparable (internal energy near the crossing point of cross-ring cleavage and glycosidic bond cleavage curves in **Figure 3-7b**), but in HCD with longer reaction time (5 ms), ions resulting from cross-ring cleavages are more predominant. By increasing the internal energy, new fragments resulting from glycosidic bond cleavages will appear (**Figure 3-14**). In fact, the presence of two  $Li^+$  cations facilitates cross-ring cleavages, indicative of shifts in their curves to lower energies.

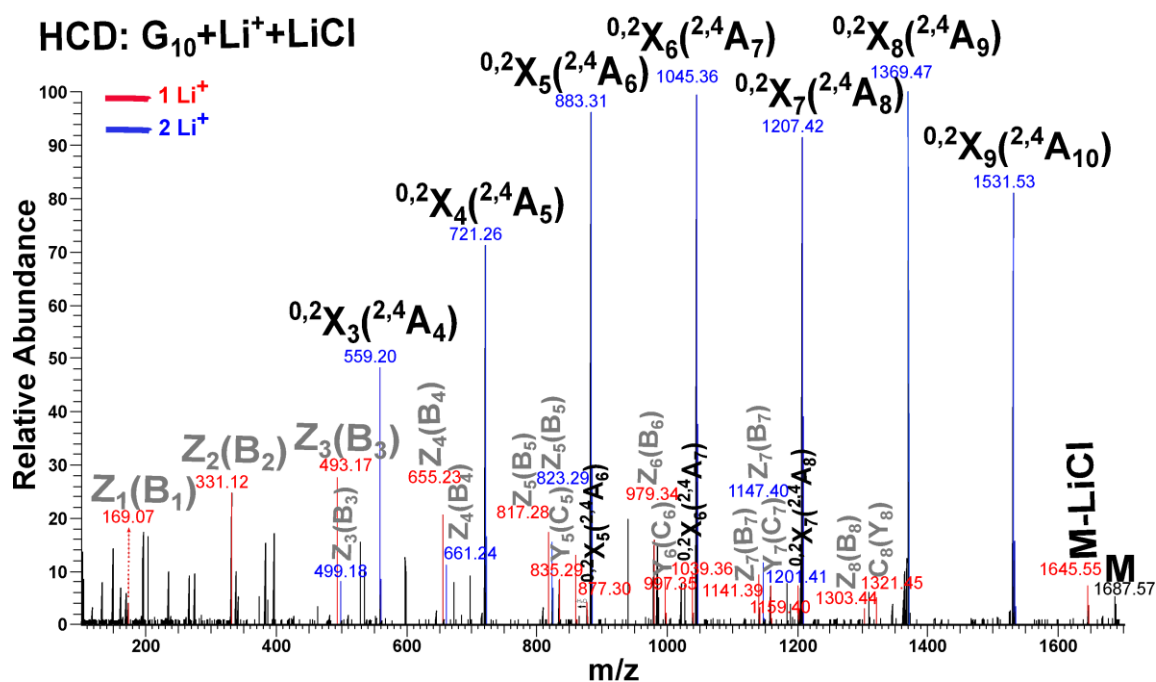


**Figure 3-14-** HCD spectrum of  $M = [G_{10}+Li+LiCl]^+$  at NCE of 45 %. Peaks of fragments containing one metal ion are shown in red, whereas those with two metal ions are shown in dark blue.

HCD, of course, allows access to higher energies compared to CID. In the HCD spectrum of precursor  $[G_{10}+Li+LiCl]^+$  at NCE of 45 % (**Figure 3-14**), it is clear that some new fragments are present that were absent from the analogous HCD experiment acquired at an NCE of 30% (**Figure 3-13d**). The appearance of new fragment ions in the HCD spectrum can be due to two main reasons. First, they may result from consecutive decompositions of the fragments that occur in higher efficiency when the precursor has a higher internal energy uptake. Secondly, because a higher energy is applied in a short time, access to dissociation pathways with higher critical energies becomes feasible, and as a consequence, new competitive fragment ions appear. For these reasons, HCD can provide a wide variety of structurally-informative fragments.

From the above discussion, it is obvious that when working with mono-lithiated sugars, B, C, Y and Z type ions are the most intense, whereas when working with di-lithiated sugars, X and A type fragments dominate. This deduction implies that a combination of the two spectra can provide complementary data and augment the information available for structural characterization of saccharides. In addition, the observations that: 1) loss of HCl is preferred to LiCl, and 2) di-lithiated fragments are dominant in both CID and HCD spectra, demonstrate that the interactions between  $Li^+$  and the sugar are quite strong.

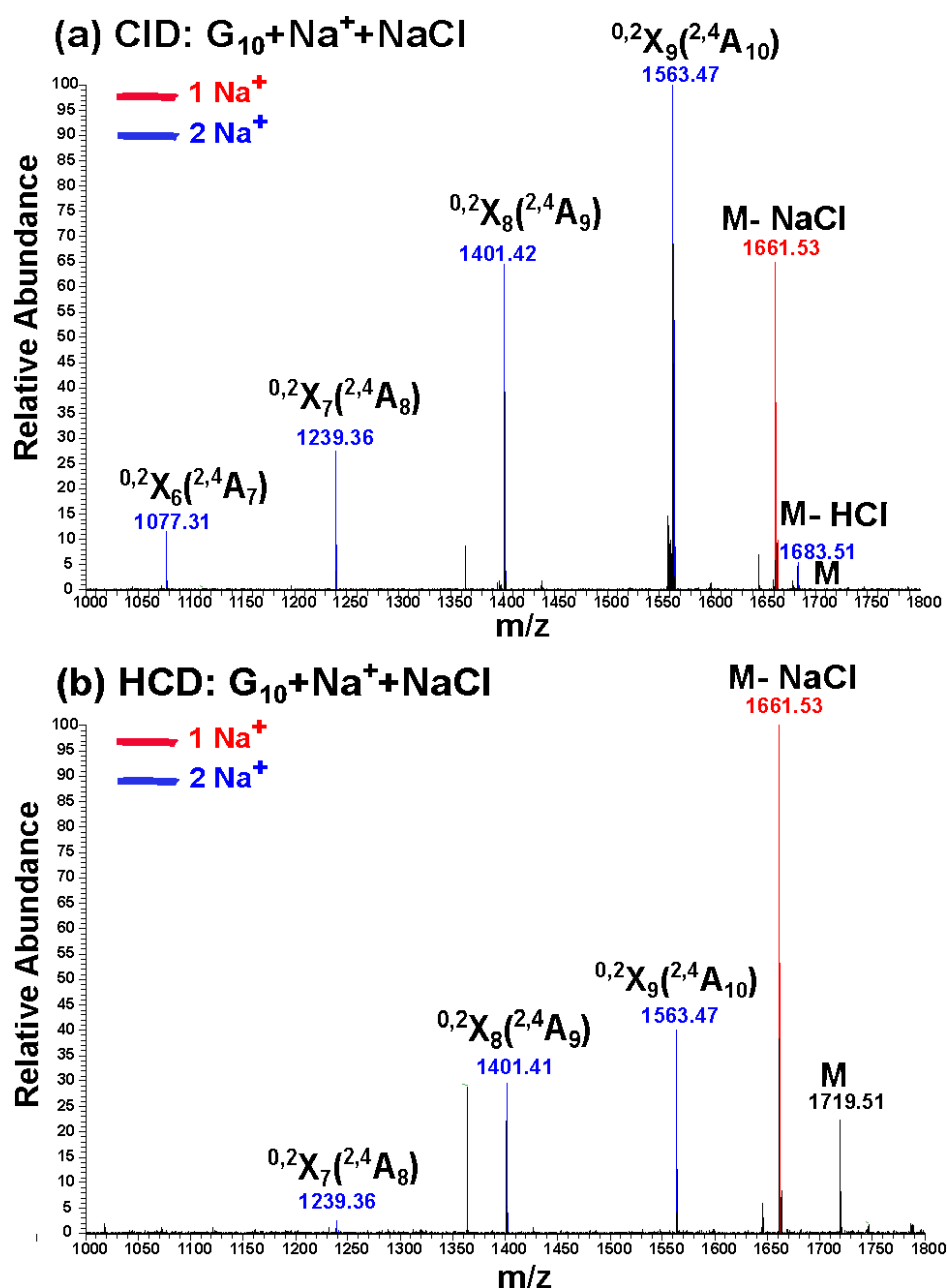


**Figure 3-15-** (a) CID spectrum of  $M = [G_{10}+Na+NaCl]^+$  (NCE of 30 %) and (b) its HCD spectrum (NCE of 30 %). Peaks of fragments containing one metal ion are shown in red while those with two metal ions are shown in dark blue.

To gain further insight into the interaction between sugars and metal ions, CID and HCD experiments exactly analogous to those described above for LiCl were performed for *sodiated* maltodecaose  $[G_{10}+Na]^+$  and its NaCl adduct  $[G_{10}+Na+NaCl]^+$ . In the case of  $[G_{10}+Na]^+$ , very similar results to those of  $[G_{10}+Li]^+$  were obtained: by HCD, only glycosidic bond cleavages were observed, whereas by CID, both glycosidic and cross-ring cleavages

were observed (spectra not shown). These findings can be interpreted in a manner strictly analogous to the above discussion pertaining to  $[G_{10}+Li]^+$ .

By comparing the CID and HCD spectra of  $[G_{10}+Na^++NaCl]^+$  (**Figure 3-15a** and **3.15b**, respectively) with those of  $[G_{10}+Li+LiCl]^+$  (**Figure 3-13b** and **3.13d**), one can notice that for both types of alkali metal, fragments mainly result from cross-ring cleavages. However, one obvious difference is the presence of intense fragment ions resulting from the loss of metal chloride (NaCl) in **Figure 3-15a** and **3.15b**. The comparable loss of LiCl from  $[G_{10}+Li+LiCl]^+$  did not occur, but instead, loss of HCl was dominant. For  $[G_{10}+Na+NaCl]^+$ , the fragment ion resulting from loss of HCl has a very low abundance in the CID spectrum (**Figure 3-15a**), and is not present in the HCD spectrum (**Figure 3-15b**). This observation demonstrates that the sugar's interaction with  $Li^+$  is stronger than its interaction with  $Na^+$ . This finding adds additional confirmation of the presence of a direct interaction between  $Li^+$  and sugars during the dissolution process. It can also explain the better success achieved with use of LiCl compared to NaCl for dissolution of carbohydrates.

Lastly, CID and HCD experiments were performed on the lithiated sugars with two LiCl adducts attached ( $[G_7+Li+2LiCl]^+$  precursors). Interestingly, in both CID and HCD spectra (**Figure 3-16**), the majority of the fragment ions contain three  $Li^+$ , indicating that all lithium ions in the precursors are retained in the fragments. In addition, fragments resulting from the loss of one or two HCl are dominant in the spectra which further reinforces the notion that strong interactions exist between the sugar and lithium ions.

All of the above-mentioned observations are consistent with the dissolution mechanism of carbohydrates in DMAc/LiCl, proposed by Morgenstern et al.<sup>152</sup>, which hypothesizes the existence of a direct interaction between  $Li^+$  and the saccharide during the dissolution process. It should be noted that a combination of infrared spectroscopy in the gas phase and quantum chemical calculations<sup>38</sup> has suggested that, in the presence of metal ions, sugars will adopt structures in which the coordination number of an attaching metal is as high as possible (4 in the case of  $Li^+$  in that study<sup>38</sup>), and the number of intra-molecular hydrogen bonds inside the molecule is also maximized.

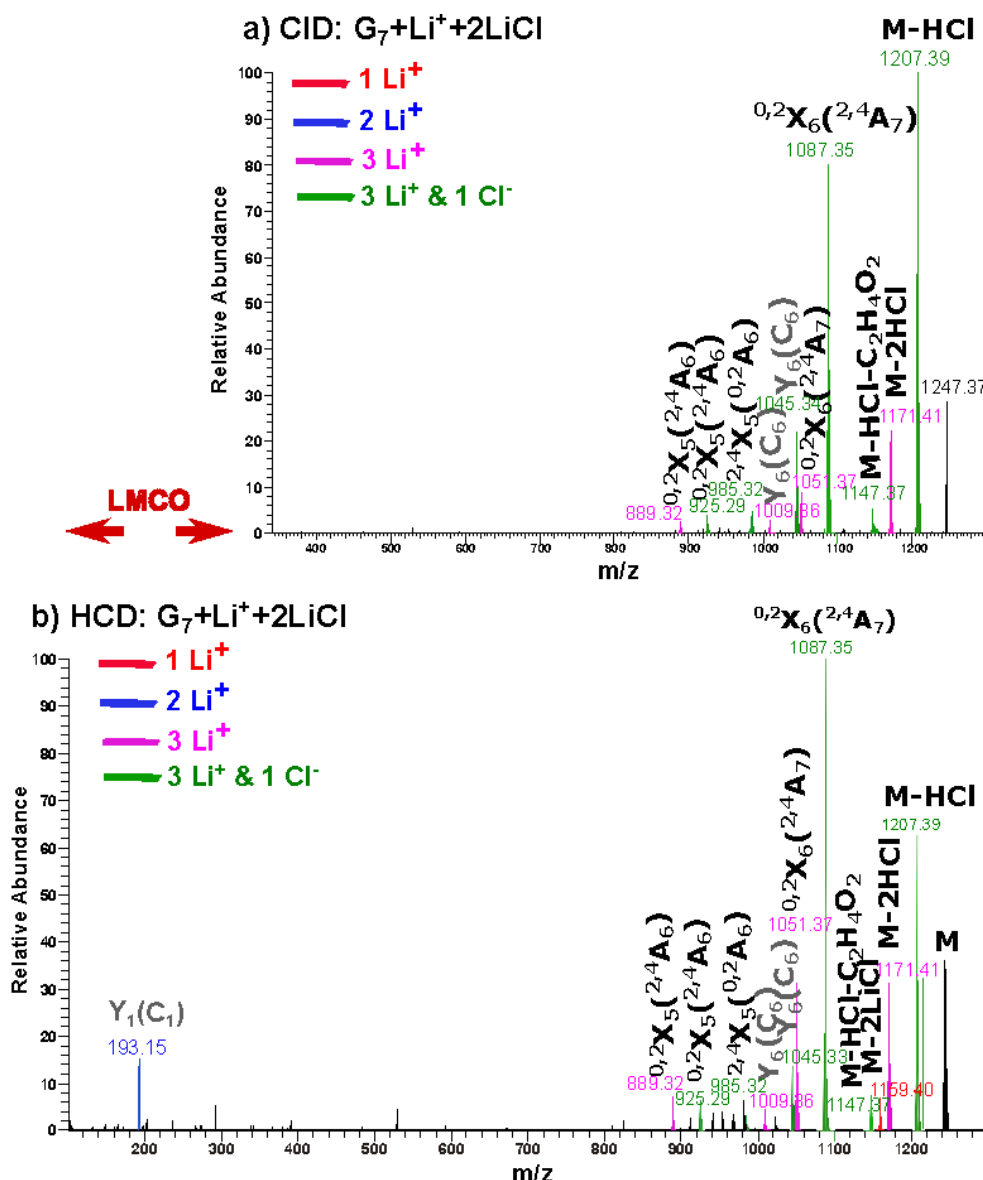


**Figure 3-16-** (a) CID spectrum of  $M = [G_7+Li+2LiCl]^+$  (NCE of 20 %) and (b) its HCD spectrum (NCE of 20 %). Peaks of fragments containing one metal ion are shown in red, whereas those with two metal ions are shown in dark blue. Because of the LMCO, access to the low  $m/z$  fragments in the CID spectra was not possible.

This result, as well as all-atom molecular dynamic simulations,<sup>39</sup> show that during the dissolution process, depending upon the structure of the saccharide under study and the geometry of available oxygen atoms, there may be more than one solvent molecule in the coordination sphere of  $Li^+$  which becomes displaced by hydroxyl oxygen or ring oxygen atoms of the sugar. **Figure 3-17a** shows the proposed dissolution mechanism of Morgenstern et al.<sup>152</sup> as portrayed by Huang and coworkers.<sup>153</sup> In this scheme, depicting one glucose unit of a saccharide, we consider  $Li^+$  to have a coordination number of 4. In **Figure 3-17a**, one

solvent molecule of the four initially present is displaced by an interaction with a hydroxyl oxygen on the saccharide. **Figure 3-17b** extends the dissolution mechanism by considering multiple solvent molecules initially coordinated to  $\text{Li}^+$  to be displaced by available coordinating sites.

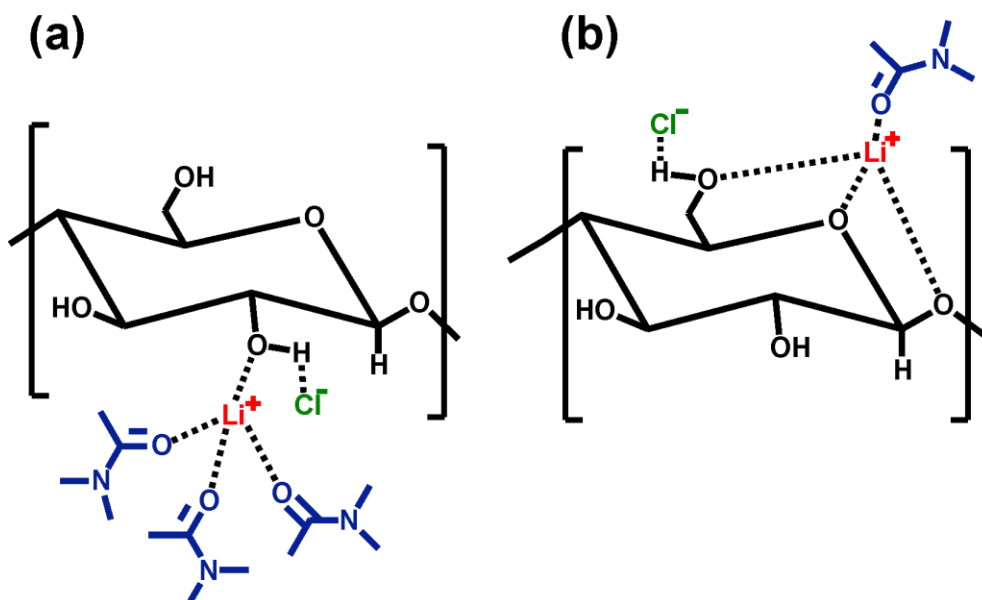


**Figure 3-17-** (a) Depiction of role of  $\text{Li}^+$  (and  $\text{Cl}^-$ ) in the dissolution mechanism of cellulose in DMAc/LiCl showing a single displaced solvent molecule from the  $\text{Li}^+$  coordination sphere proposed by Morgenstern et al.<sup>152,153</sup> (b) Example of  $\text{Li}^+$  triply coordinated to the sugar.

## Conclusion

Here in this chapter, tandem mass spectrometry studies using CID and HCD techniques have been employed to investigate the dissolution mechanism of saccharides in DMAc/LiCl. Obtained mass spectral evidence sheds light on the main discrepancy<sup>40,153</sup> which exists between previously proposed mechanisms. This point of inconsistency relates to the presence or absence of a direct interaction between  $\text{Li}^+$  and the sugar during the dissolution process.

The first pertinent observation was that in the CID and HCD spectra of  $[\text{sugar}+\text{Li}+\text{LiCl}]^+$  precursors, the abundances of fragments containing two metal ions were higher compared to ions with only one metal ion. In addition, loss of HCl was favored over the loss of LiCl in the above spectra. These observations imply that  $\text{Li}^+$  preferentially stays attached to the sugar.

By contrast, in both CID and HCD spectra of  $[G_{10}+Na+NaCl]^+$  precursors, loss of NaCl is favored over the loss of HCl. This additionally confirms the presence of strong interactions between  $Li^+$  and the sugar. Furthermore, in CID and HCD spectra of  $[sugar+Li+2LiCl]^+$ , the majority of the fragments contain three  $Li^+$ , and also fragments resulting from loss of one or two HCl molecules are dominant. All of the above-mentioned evidence supports the mechanism proposed by Morgenstern et al.<sup>152</sup> which hypothesizes a direct interaction between  $Li^+$  and sugars during the dissolution process. In addition, this mechanism can be extended by considering the replacement of more than one solvent molecule on the coordination sphere of  $Li^+$  by hydroxyl oxygens or the ring oxygen of the sugar, depending on its structure and the geometry of available –OH groups.

The second aspect of this study was devoted to the investigation of the capabilities of three important ion activation techniques used in tandem mass spectrometry (low-energy CID, CID and HCD) to provide informative fragments for structural characterization of saccharides. The mechanisms of energy deposition are different for these techniques such that, compared to low-energy CID and CID, a higher amount of energy is deposited onto the precursor ion in a shorter time for HCD. Therefore, HCD allows access to dissociation pathways with higher critical energies, and as a consequence, new competitive fragment ions can appear in the HCD spectrum. In addition, because of the high amount of energy deposited during HCD, consecutive fragmentation processes will result. On the other hand, low-energy CID with a very long time scale allows access to the very slow dissociation pathways, and considerable rearrangement of the precursor ions before decomposition.

Lastly, we observed that when selecting mono-lithiated sugars as precursor ions, B, C, Y and Z type product ions are abundant in the MS/MS spectrum, whereas when working with di-lithiated sugars, X and A type fragments are most abundant. Therefore, a combination of tandem mass spectra acquired using both mono-lithiated and di-lithiated precursors of the same saccharide can provide complementary and more complete information for structural characterization.



---

***Chapter 4: Investigation of hemicryptophane  
host-guest binding energies using high-  
pressure collision induced dissociation in  
combination with RRKM modeling***

---

## Introduction

H-G chemistry is a fascinating field of research that involves the establishment of noncovalent interaction(s) between at least two species: the host that is typically a larger molecule containing convergent binding sites which is adapted to accommodate a second species, the guest, containing divergent binding sites.<sup>2,177,178</sup> This field has found applications in diverse areas of science including molecular recognition,<sup>9–11</sup> drug delivery,<sup>12–14</sup> catalysis,<sup>16,17,179</sup> bio sensors,<sup>18–20</sup> trapping devices<sup>21,22</sup> etc. In this very active research topic, a wide variety of “cage” architectures have been employed as host molecules, and among them are the cryptophane molecules which were introduced by A. Collet in the early 1980s.<sup>35</sup> A typical cryptophane cage consists of two cyclotrimeratrylene (CTV) caps, and three linkers which connect these two caps thereby creating a hollow space, or cavity between the caps.<sup>36</sup> Since their first synthesis, significant efforts have been focused on modification of cryptophanes in order to design new cavities with novel selectivity characteristics toward various organic and inorganic guest molecules. In extending this approach, an innovative structure called a hemicryptophane was synthesized.<sup>37,38</sup> The structure of a hemicryptophane molecule differs from a cryptophane cage in that one of the CTV caps is replaced with a C<sub>3</sub>-symmetrical organic group.<sup>37</sup> Hemicryptophane cages have been employed for selective inclusion of choline,<sup>50</sup> choline phosphate<sup>57</sup> or primary alkylammonium ions.<sup>49</sup> Moreover, hemicryptophanes have been used for enantioselective recognition<sup>58,59</sup> as well as ion-pair recognition,<sup>54</sup> and studies pertaining to potential catalytic activity<sup>44</sup> have also been conducted.

H-G chemistry deals with noncovalent interactions which, despite their typically much weaker strength compared to covalent bonds, determine the nature, stability, and preferred 3-D structure(s) of the H-G systems. Therefore, the ability to assess the strengths of the noncovalent binding interactions has a significant importance in characterizing structures of H-G complexes, and in interpreting their behaviors. Moreover, such assessments can aid in the development of new H-G systems that afford specific desired properties.

So far, most of the H-G chemistry studies of hemicryptophanes have been performed in the condensed phase, and techniques such as fluorescence<sup>57</sup> or nuclear magnetic resonance<sup>56</sup>

were primarily used for characterization of H-G interactions. However, for a more comprehensive characterization, multiple methods are required. Electrospray ionization mass spectrometry,<sup>3–5</sup> which allows the preservation in the gas phase of weak interactions that existed in the initial solution, is another method of choice to investigate H-G systems. This technique, which offers high sensitivity, short acquisition times, and very low sample consumption, can provide a wealth of information that is sometimes difficult to obtain using other approaches, i.e. acquired results are often complementary to those obtained in the condensed phase. ESI used with single stage MS can provide additional information pertaining to the stoichiometry of H-G binding, and when combined with tandem mass spectrometry, it can offer a gauge of the strength of the binding interaction(s). In particular, tandem mass spectrometry is a reliable way to estimate bond dissociation energies<sup>106</sup> (*BDEs*, the change in enthalpy corresponding to the dissociation reaction at 0 K). Decompositions can be probed using various techniques such as threshold collision induced dissociation (TCID),<sup>180–183</sup> BIRD,<sup>106,109,184</sup> thermal activation in a quadrupole ion trap,<sup>130,134,185</sup> collisional activation in a FT-ICR<sup>186–188</sup> instrument, among others.

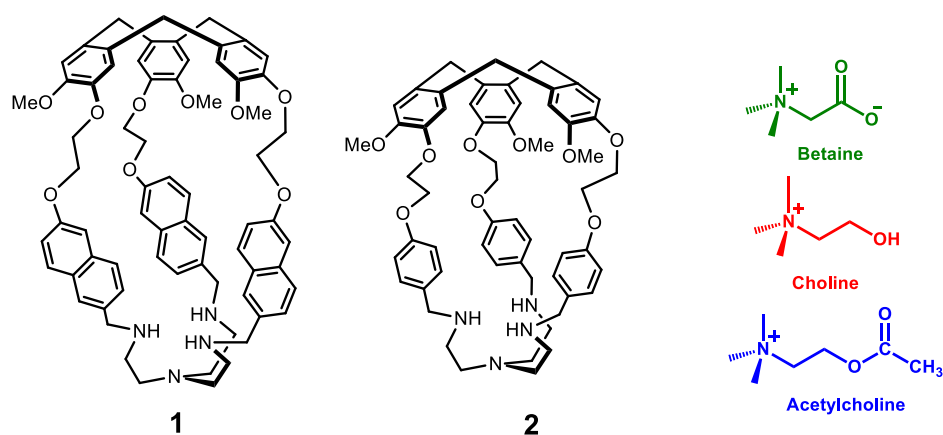


**Figure 4-1-** Structures of hemicryptophane cages **1** and **2**; and studied guests.

In this chapter, two hemicryptophane cages **1** and **2** (**Figure 4-1**) are employed as the host molecules and their binding properties towards three biologically important guests, namely: choline (**C**),<sup>189</sup> acetylcholine (**AC**)<sup>190</sup> and betaine (**B**)<sup>191,192</sup> (**Figure 4-1**) are studied in the gas phase. Comparison of the binding strengths of different H-G pairs was achieved using a

combination of BIRD and high-pressure CID mass spectrometric techniques, combined with RRKM<sup>81,83,86,87</sup> modeling.

## Experimental Section

Two hemicyptophane cages, **1** and **2** were provided by courtesy of Prof. Alexandre Martinez. They had been synthesized according to previously published methods,<sup>193,194</sup> and their stock solutions (1 mM) were made in dichloromethane. Stock solutions of choline, acetylcholine and betaine were prepared in methanol (1 mM) and individual working solutions were prepared by diluting the host and each individual guest molecule (1:1) in methanol.

Leucine enkephalin was purchased from Sigma-Aldrich (Taufkirchen, Germany) and its stock solution (1 mM) was made in methanol. A working solution of leucine enkephalin was prepared by diluting the stock solution to the final concentration of  $10^{-6}$  M in methanol.

A 'Quattro II' triple quadrupole mass spectrometer (Waters, Manchester, UK) equipped with an ESI source was used to obtain MS and MS/MS spectra. The main reason that the triple quadrupole instrument was selected for SY experiments is that it minimizes discrimination between low and high mass ions. A capillary potential of 3.5 kV, cone voltage of 50 V, and extractor potential of 6 V were used. The source block temperature was kept at 100 °C. Nitrogen was used as nebulizing and drying gas at 20 °C.

Two different techniques: high-pressure CID and low-pressure threshold CID (TCID) were employed in this work. For high-pressure CID experiments, argon ( $5 \times 10^{-3}$  mbar) was used as collision gas, and for optimized transmission of ions, the following settings were used: for the first quadrupole: ion energy of 0 eV, lens 5 was at 100 V, and lens 6 at 0 V; and for the second quadrupole: ion energy of 10 eV, lens 7 was at 250 V, lens 8 at 175 V, and lens 9 at 50 V.

For TCID experiments, xenon ( $10^{-5}$  mbar) was employed as collision gas and the following settings were utilized for efficient ion transmission: for the first quadrupole: ion energy of 0

eV, lens 5 at 100 V and lens 6 at 0 V; and for the second quadrupole in the QhQ instrument: ion energy of 0 eV, lens 7 at 250 V, lens 8 at 10 V and lens 9 at 0 V.

Collision gas was introduced into the collision cell using a customized line as previously described.<sup>195</sup> Masslynx V4.0 sp2 software was used for analyzing the MS and CID tandem mass spectra. Breakdown curves were obtained by plotting *SY* versus collision energy in the laboratory frame,  $E_{lab}$ .

BIRD experiments were performed using a 7T hybrid quadrupole-FT-ICR mass spectrometer (ApexQe, Bruker Daltonics, Billerica, USA). H-G solutions were infused at a flow rate of 120  $\mu\text{Lh}^{-1}$  into an Apollo II electrospray ionization source with  $\text{N}_2$  as nebulizing gas. The temperature of the source was set at 250 °C, ESI voltage at 4500 V, capillary exit at 300 V, skimmer I at 150 V, skimmer II at 8 V. Heating of the FT-ICR cell for BIRD experiments was performed by installing a resistive heating metallic "ribbon" external to the vacuum system that covers the entire vicinity of the cell; applying a variable voltage to the metallic ribbon allows temperature control. A cell temperature accuracy check was performed by observing the dissociation of the sodium-bound dimer of leucine enkephalin,  $(\text{LEK}_2\text{Na})^+$ , with well-known activation parameters, inside the cell.<sup>196</sup> A temperature probe which was placed between the metallic ribbon and cell housing, shows a maximum temperature difference of 3 °C compared to the temperature obtained by calibration. All mass spectra were acquired using XMASS (version 6.1, Bruker Daltonics) in broadband mode. The number of data points was set at 512 K, and the time allowed for the unimolecular dissociation reaction to occur was varied by changing the "pumping delay" (without gas introduction, this corresponds to the period of time that ions are trapped in the cell).

Ion mobility experiments were performed using a trapped ion mobility mass spectrometry (TIMS) instrument (Bruker Daltonics, Bremen, Germany). Solutions were injected at a flow rate of 5  $\mu\text{Lmin}^{-1}$  into an ESI source operating in positive ionization mode. Capillary voltage was set at 3.6 kV, end plate offset at 500 V, and nebulizer gas pressure at 4.4 psi. The drying gas temperature was set at 200 °C, and its flow rate at 3  $\text{Lmin}^{-1}$ . For ion mobility experiments, nitrogen was used as buffer gas at a temperature of 300 K. First, separations were performed in a long inverse reduced mobility ( $1/K_0$ ) range (0.77 to 1.93  $\text{V.s/cm}^2$ ), and

then depending on the position of the ions of interest on the  $(1/K_0)$  axis, the spectra were recorded again in a decreased inverse mobility range. Accumulation time for a single analysis was set at 10 ms, and the spectra were recorded for 1 minute. Calibration of the inverse reduced mobility  $(1/K_0)$  axis was performed using Agilent tune mix (Agilent Technologies, Santa Clara, Ca, USA).

## Modeling Detail

Vibrational frequencies of the precursor ions were calculated using the GAMESS<sup>197,198</sup> computational package employing the Hartree–Fock method and Slater-type basis sets. These vibrational frequencies have been used as a necessary input for RRKM calculations. Although this level of theory is relatively low, it has been shown<sup>90,91</sup> that RRKM calculations are not sensitive to the vibrational frequencies when they are not compared with those of the transition state. CID experiments were simulated using *MassKinetics* Scientific Demo software (version 1.17.2.648 Beta, provided by courtesy of Prof. László Drahos).<sup>199</sup> Calculations were performed within the RRKM formalism.<sup>81,83,86,87</sup> To simulate internal energy distributions and their evolution with time, a model based on a truncated Maxwell–Boltzmann distribution of internal energy and characteristic temperature ( $T_{char}$ ) was utilized (**Figure 1-3**).<sup>195,200–202</sup> As has been evaluated previously,<sup>195</sup> and considering that precursor ions undergo several hundred collisions, leading to rather long residence times inside the collision cell,<sup>203,204</sup> a flight time of 0.002 s has been used. It should be noted that because we are relying upon a reference ion for calibration of mean internal energy, the input flight time has a minimal effect on the calculated critical energies. Instead, it mainly influences the *initial temperature* of the reference ions, and as a consequence, that of the studied complexes.

One of the H-G complexes that was amenable to the BIRD technique, namely  $[(B+2)+H]^+$ , was selected as the reference ion. For this complex, the mean internal energy  $\langle E_{int} \rangle$  and  $T_{char}$  corresponding to each point of its SY curve were calculated. Then, a linear relationship between the CID collision energy ( $E_{lab}$ ) and  $\langle E_{int} \rangle$  was established.<sup>195,200–202</sup> In the next step, this calibration was used for all H-G pairs and SY curves were simulated and fitted to experimental data to obtain the critical energy of dissociation for each complex. In collisional

processes, this model is only valid for CID experiments conducted at high pressures under analytical conditions.<sup>195</sup>

In order to extract critical energy ( $E_0$ ) from the Arrhenius plot (obtained using BIRD experiments), *MassKinetics*<sup>199</sup> Scientific software (version 1.17.2.648 Beta) was utilized. For this purpose, calculations were performed considering that ions remain in thermal equilibrium during their fragmentation. Using this model, critical energies were adjusted until the best fit between the experimentally obtained Arrhenius plots and the calculated ones was achieved.

## Results and Discussion

Both hemicyptophane cages **1** and **2** (**Figure 4-1**), that serve as host molecules in this study, contain a cyclotrimeratrylene (CTV) unit and a tris(2-aminoethyl)-amine (tren) group as their two caps. But they can be distinguished by the nature of their linkers: naphthyl (cage **1**) versus phenyl (cage **2**) groups. Thus, when comparing the behaviors of guest molecules, any differences in the binding strengths of their H-G complexes can be directly attributed to the characteristics of the linkers and the latter's influence on the final complex structure. Three biologically relevant molecules: betaine (**B**),<sup>191,192</sup> choline (**C**),<sup>189</sup> and acetylcholine (**AC**),<sup>190</sup> each containing a permanently charged trimethylammonium substituent, were selected as guest molecules for this study. Betaine is zwitterionic in neutral solution, and it should be noted that some other zwitterionic guests such as glycine,  $\beta$ -alanine and taurine were also tried, but no evidence of H-G complexes with cage **1** or cage **2** were observed for these latter three compounds in obtained mass spectra.

When a 1:1 solution of H:G is analyzed by ESI-MS, in the case of choline and acetylcholine, the observed complex is  $[\text{Host}+\text{Guest}]^+$ , whereas for zwitterionic betaine,  $[(\text{Host}+\text{Guest})+\text{H}]^+$  is observed. Thus, the betaine complex requires a proton to create the singly charged cationic species observed in the mass spectrum. Under CID conditions, AC and C complexes with either cage dissociate by loss of the cage, and therefore, their major fragments are the guest molecules bearing the charge. By contrast, protonated B complexes formed with either cage dissociate by loss of the neutral guest, thus protonated cages are the observed

fragments. It should be noted that in the case of acetylcholine H-G complexes, a very low abundance of a fragment ion at  $m/z$  87.0 was also observed which is produced by loss of the  $-\text{N}(\text{Me})_3$  group from acetylcholine. The abundance of this fragment ion was taken into account in the survival yield calculations. The CID spectra of the different complex ions are shown in **Figure 4-2**.

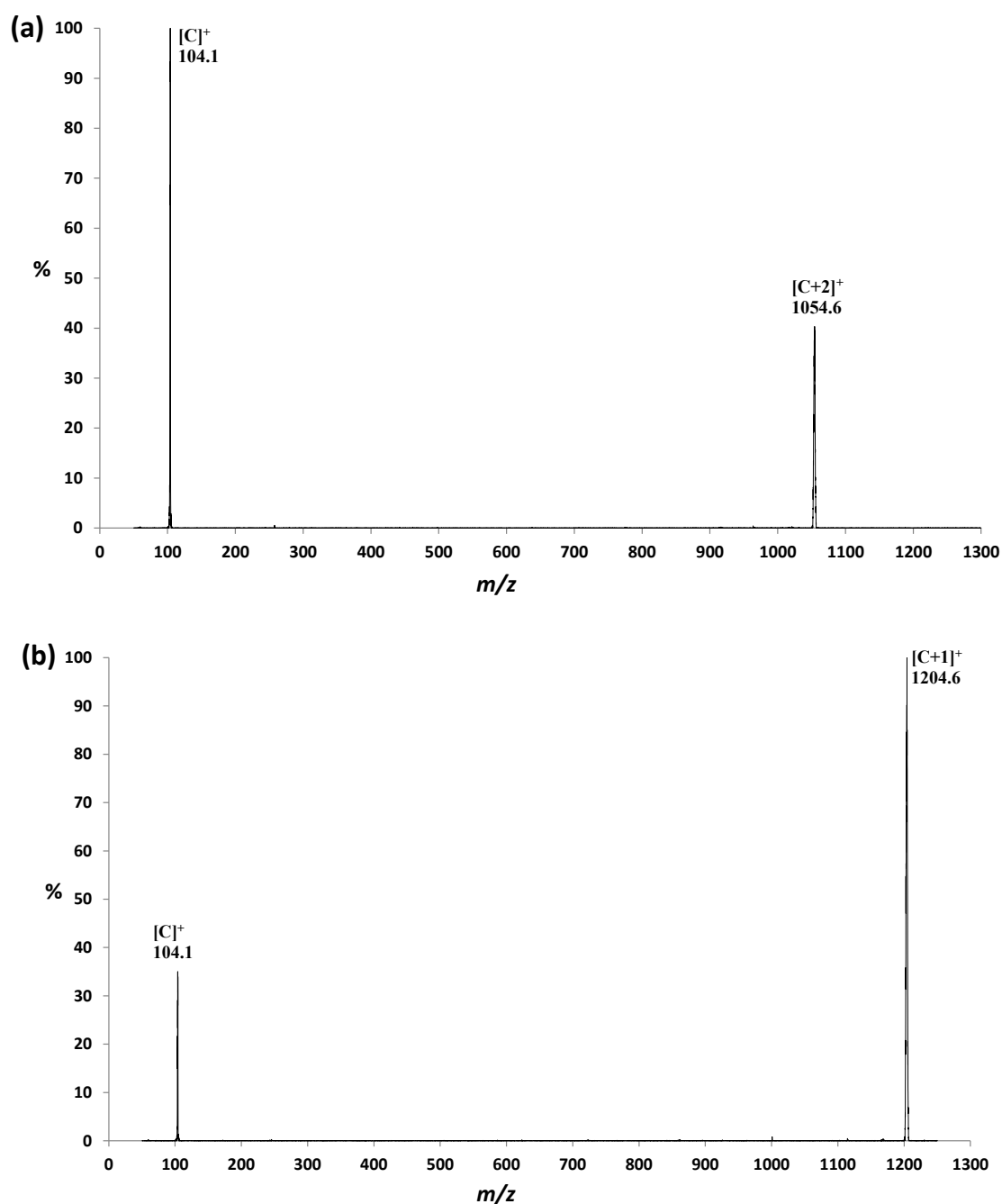


**Figure 4-2a&b-** High-pressure CID spectrum of the dissociation of the (a)  $[\text{C}+2]^+$ , (b)  $[\text{C}+1]^+$  precursor ions at  $E_{\text{lab}} = 20$  eV.



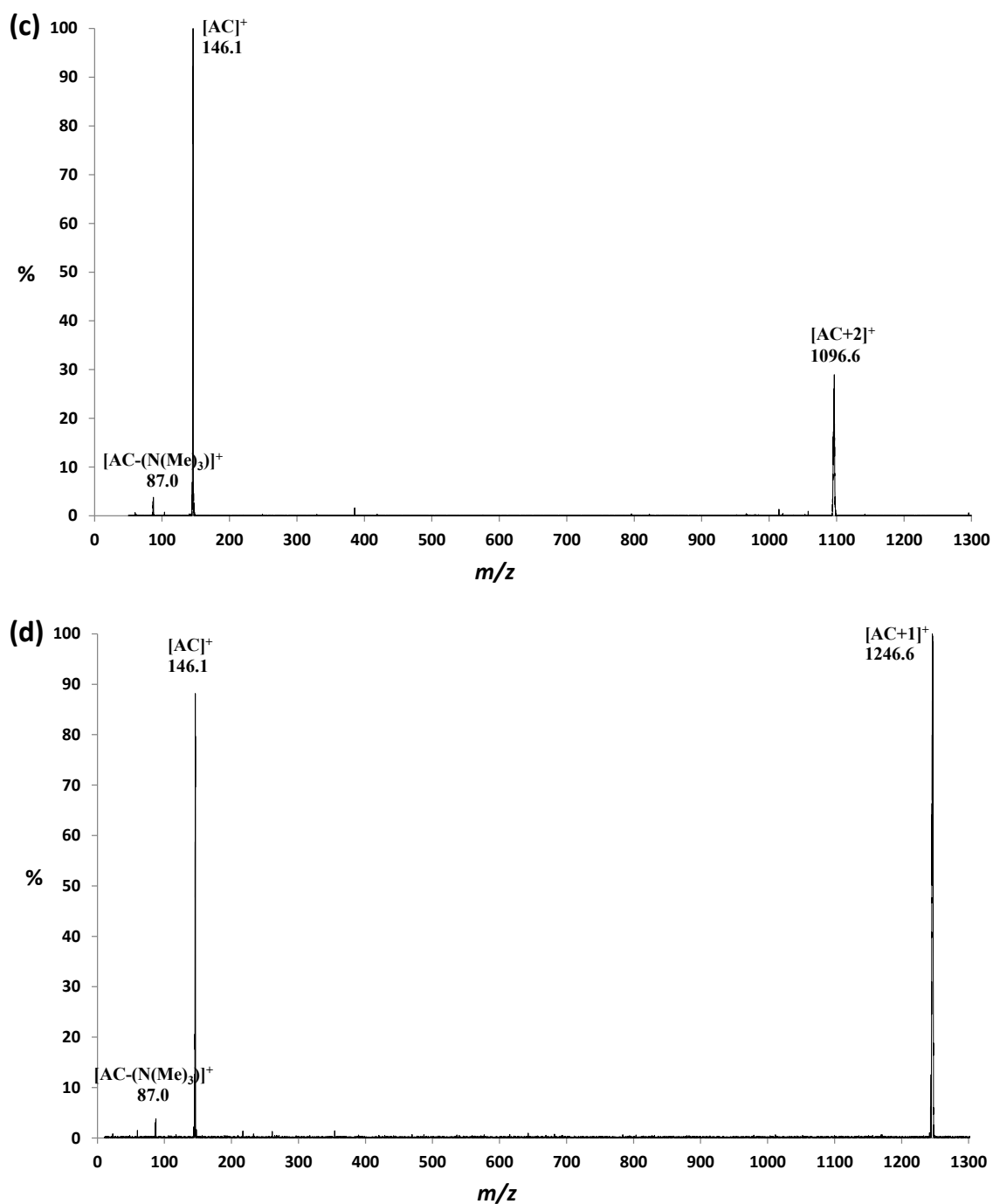


**Figure 4-2c&d-** High-pressure CID spectrum of the dissociation of the (c)  $[AC+2]^+$ , (d)  $[AC+1]^+$  precursor ions at  $E_{lab} = 20$  eV.

In this chapter, our goal is to compare the binding strengths of the various observed H-G complexes. At the beginning, for this purpose, it was tried to use low-energy CID and higher-energy collision dissociation (HCD) techniques both on LTQ/ Orbitrap hybrid mass spectrometer. However, none of the above-mentioned approaches could provide correct estimation of binding energies for the C and AC host-guest complexes due to the large

difference in  $m/z$  of the these H-G complexes and their fragments. Regarding the low-energy CID method, due to the low mass cut off, it was not possible to observe fragments of the mentioned complexes ( $[C]^+$  and  $[AC]^+$  ions).

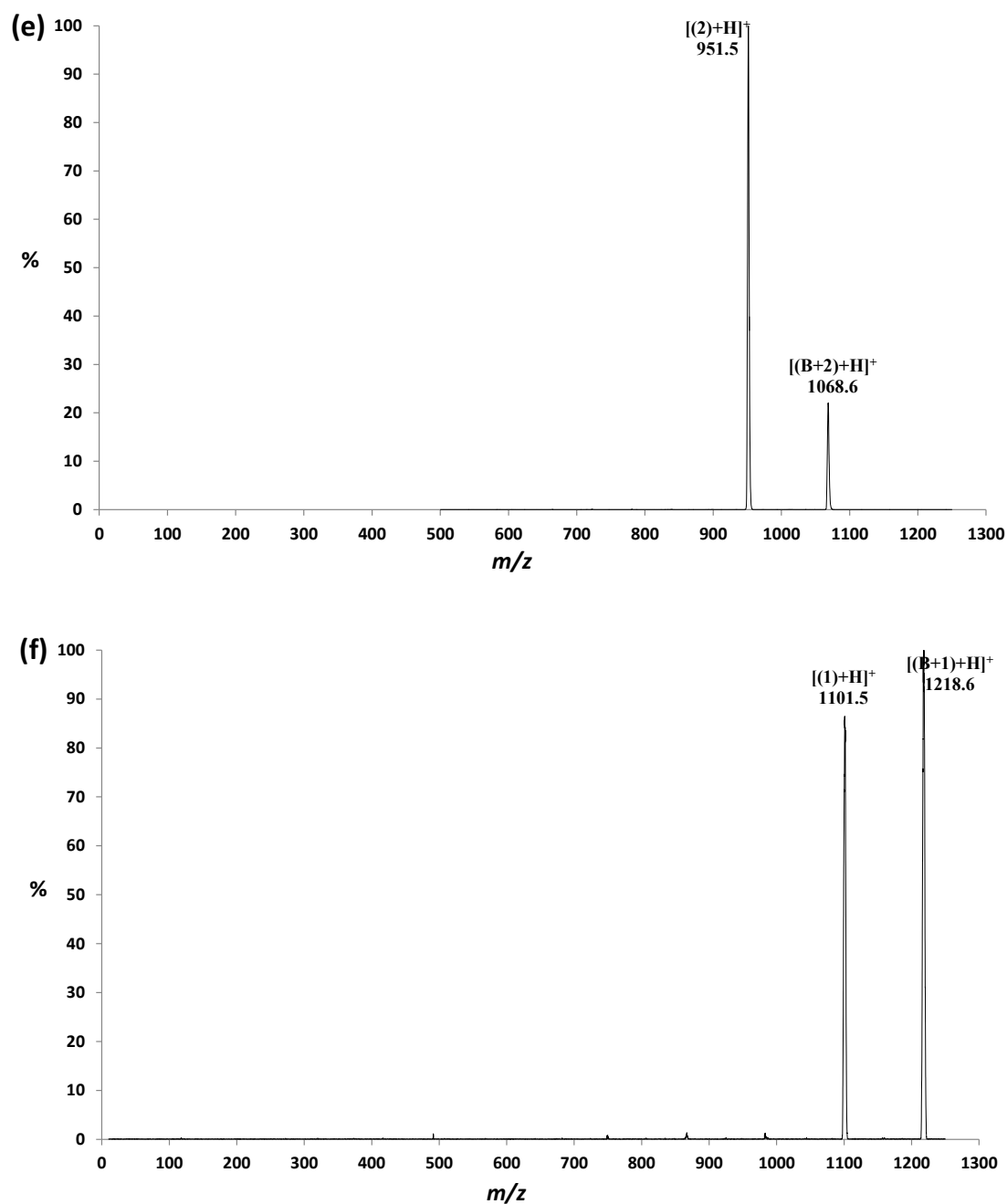


**Figure 4-2e&f-** High-pressure CID spectrum of the dissociation of (e)  $[(B+2)+H]^+$  and (f)  $[(B+1)+H]^+$  precursor ions at  $E_{lab} = 20$  eV.

Considering the HCD approach, in this case, there is no limitation of LMCO, and the low  $m/z$  values are accessible. However, problem was related to inherent characteristic of the ion traps in having preference for trapping the low or high mass ions, depending on the trapping parameter and utilized low mass range. Our precursor ions were at quite high mass range and the fragments were at low mass range, therefore, in order to have maximum transmission of both, usual trapping parameter ( $q = 0.25$ ) was used. However, it was observed that the position of the SY curves (obtained using HCD) were highly dependent on the selected low mass range. For example, SY experiments of choline complexes with two cages **1** and **2** at two different low mass ranges are presented in **Figure 4-3**. From this figure, it is evident that in decreasing the low  $m/z$  range, SY curves are shifting toward lower energies.

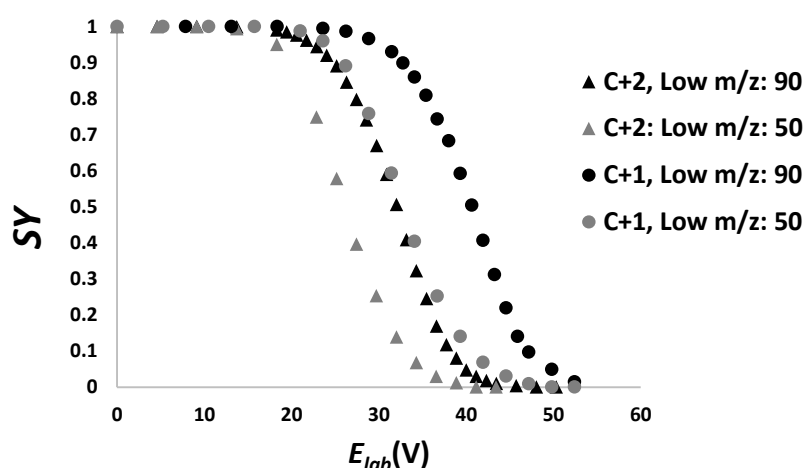


**Figure 4-3-** SY experiments of  $[C+1]^+$  and  $[C+2]^+$  complexes at two different low mass ranges of  $m/z$  50 and 90.

For HCD experiments, ions are isolated in LTQ, and then they are transferred through the C-trap to the octapole collision cell. After fragmentation, fragments and remained precursor ions are transferred back to the C-trap and then to the Orbitrap for detection. Likely, this discrimination between low and high mass ions occurs in the C-trap (a curved linear ion trap). To avoid these limitations (LMCO and low  $m/z$  range effect) associated with using ion traps, we decided to perform CID experiments on a triple quadrupole mass spectrometer. This mass spectrometer did not present the above-mentioned problems in obtaining accurate SY curves leading us to believe that it is the best choice in cases where both small neutral losses

and large neutral losses are occurring. A main advantage of using the triple quadrupole mass spectrometer is its quite uniform transmission and detection of high and low mass ions. This uniformity leads to better reliability and reproducibility in obtaining accurate *SY* curves. In addition, because low mass ions and high mass ions appear at different resolution, by considering the peaks' area instead of their intensities, this difference will not adversely affect the *BDE* calculations.

To compare the binding strengths of the various H-G complexes, firstly, the internal energy uptake occurring in high-pressure CID experiments must be calibrated using a reference molecule that has: 1) accurately known activation parameters, and 2) a structure and number of DOF quite similar to those of the systems under study. If this latter condition is met, the amount of energy deposited should be almost the same in all cases. Previous studies<sup>195,200–202</sup> revealed that the mean internal energy  $\langle E_{int} \rangle$  varies only slightly with the number of DOF and with a change in the identity of the precursor ion, thereby giving us confidence that the above precautions are sufficient to obtain reasonable and trustworthy results.

In the next step, the use of a reliable method to calculate Arrhenius parameters for the reference compound is required. Among the developed tandem mass spectrometry methods, one of the most established ones that can directly give activation parameters is BIRD.<sup>106</sup> In practice, only precursor ions which are fragile enough to produce sufficiently abundant fragment ions under the accessible temperature range of the BIRD set-up (300 to 410 K in our instrument) are amenable to this technique. In this investigation, among all the studied H-G complexes,  $[(B+2)+H]^+$  most readily fulfilled this condition.

**Figure 4-4a** displays the kinetic plots for the dissociation of  $[(B+2)+H]^+$  at different temperatures. In **Figure 4-4b**, the corresponding Arrhenius plot ( $\ln k$  versus  $1/T$ ) is shown. As is evident from **Figure 4-4**, extremely linear plots (kinetic and Arrhenius) are obtained. The activation energy ( $E_a$ ) of  $1.27 \pm 0.05$  eV and the logarithm of the pre-exponential factor ( $\log A$ ) of  $14.2 \pm 0.6$  can be deduced from the slope and intercept, respectively, of the Arrhenius plot. According to Price and Williams,<sup>112</sup> for a peptide ion with  $\log A$  of 14.5 and  $E_0$  of 1.2 eV, the minimum molecular weight of the ion should be 787 Da to be considered as satisfying

the REX limit requirements. Thus,  $[(\mathbf{B}+2)+\mathbf{H}]^+$  with  $m/z$  of 1068, number of DOF of 462,  $E_a$  of  $1.27 (\pm 0.05)$  eV and  $\log A$  of  $14.2 (\pm 0.6)$  is expected to easily fulfill the REX limit condition.

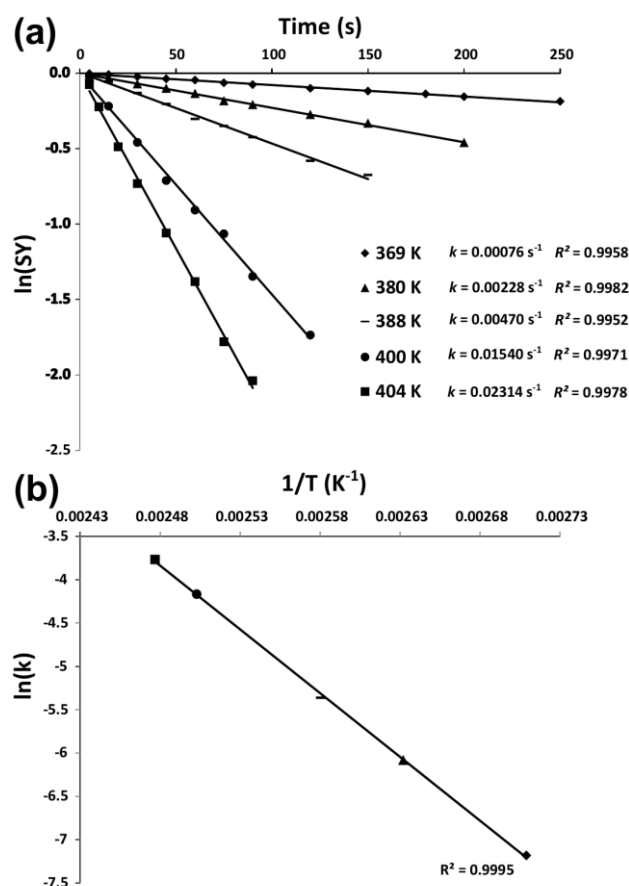


**Figure 4-4-** (a) Plots of the natural logarithm of the normalized intensity of  $[(\mathbf{B}+2)+\mathbf{H}]^+$  as a function of reaction time at temperatures ranging from 369 to 404 K; (b) the corresponding Arrhenius plot for the dissociation of  $[(\mathbf{B}+2)+\mathbf{H}]^+$ .

It should be noted that BIRD experiments were performed on all of the H-G complexes under study, but limitations were found. For example,  $[\mathbf{C}+1]^+$ ,  $[\mathbf{C}+2]^+$  and  $[\mathbf{AC}+1]^+$  complexes did not dissociate in the available temperature range, and  $[(\mathbf{B}+1)+\mathbf{H}]^+$  produced only a low abundance of fragment ions. Moreover, in this case, we were apprehensive about the presence of an interfering ion. The BIRD spectra of the  $[(\mathbf{B}+1)+\mathbf{H}]^+$  complex at 380 K and three different reaction times (5, 60 and 200 s) are presented in **Figure 4-5**. In addition to the fragment ion at  $m/z$  1101 which is  $[(1)+\mathbf{H}]^+$ , there is another ion at  $m/z$  491 which has been assigned as  $[(\mathbf{Betaine})_4+\mathbf{Na}]^+$ . We were apprehensive about the possibility of an isobaric ion, very near in mass to the precursor ion, that may be producing  $[(\mathbf{Betaine})_4+\mathbf{Na}]^+$ . It should be

noted that in the experiments with the FT-ICR, a large isolation window was used to minimize excitation of the ions during isolation.

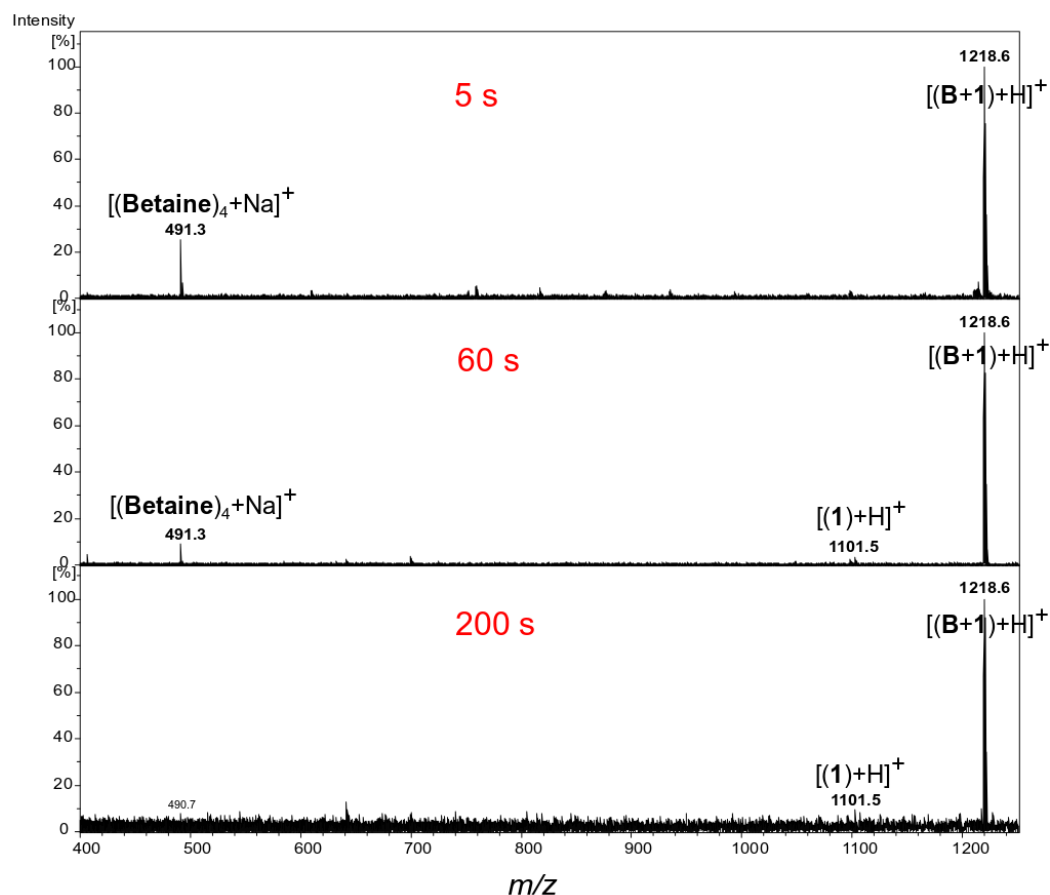


**Figure 4-5-** BIRD fragmentation spectra of the  $[(B+1)+H]^+$  complex at temperature 380 K and three different reaction times of 5, 60 and 200 seconds.

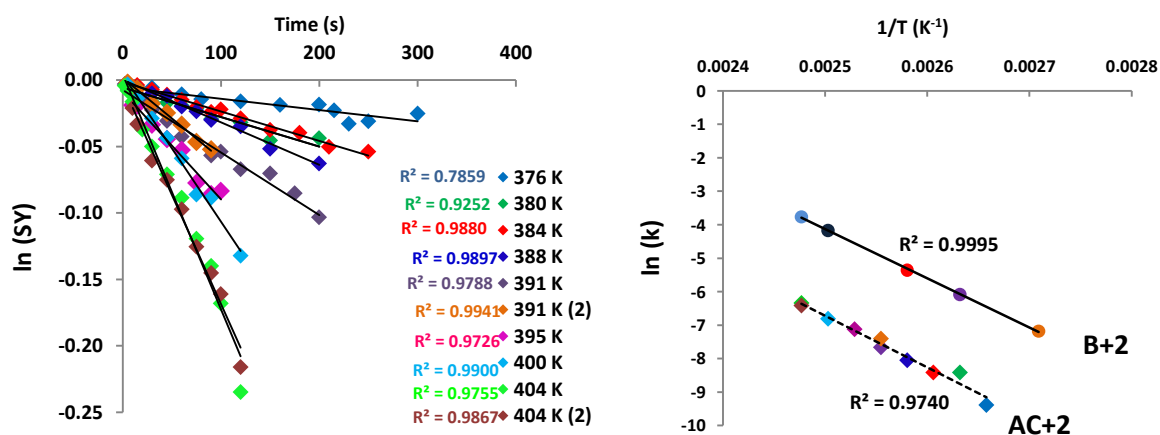


**Figure 4-6-** (a) Plots of the natural logarithm of the surviving precursor ion population (survival yield) of  $[AC+2]^+$  as a function of reaction time at temperatures ranging from 376 to 404 K; (b) Arrhenius plot for the dissociation of  $[(B+2)+H]^+$  and  $[AC+2]^+$ .

Therefore, it was not possible to construct reliable kinetic plots for  $[(B+1)+H]^+$  complex. In the case of  $[AC+2]^+$ , fragment ions were produced in low abundance, and the associated kinetic and Arrhenius plots were not perfectly linear (**Figure 4-6**). Moreover, the obtained activation parameters for  $[AC+2]^+$  ( $E_a$  of  $1.33 (\pm 0.07)$  eV and  $\log A$  of  $13.8 (\pm 0.9)$ , **Figure 4-6**), include more uncertainty as compared to those of the  $[(B+2)+H]^+$  complex. Because of the higher quality data obtained for the  $[(B+2)+H]^+$  complex, it was selected as the reference precursor for the calibration of mean internal energy ( $\langle E_{int} \rangle$ ) of ions undergoing high-pressure CID.

BIRD experiment provided the activation energy; however, for calibration of the mean internal energy using RRKM modeling, the critical energy for dissociation of the reference H-G complex is required. In order to calculate the critical energy, one needs to have precise information about the transition state. However, for a large system such as the  $[(B+2)+H]^+$  complex in which an ensemble of non-covalent interactions is responsible for keeping host and guest molecules together, it is very difficult to calculate the transition state. For this reason, the experimentally measured pre-exponential factor ( $\log A = 14.2 (\pm 0.6)$ ) is used in the *MassKinetics* software. Then, considering a thermally-equilibrated system, critical energies were adjusted until the best fit between the experimentally obtained Arrhenius plot and the calculated one was achieved (**Figure 4-7**). By doing so, an  $E_0$  of 1.19 eV was gleaned for the reference system.

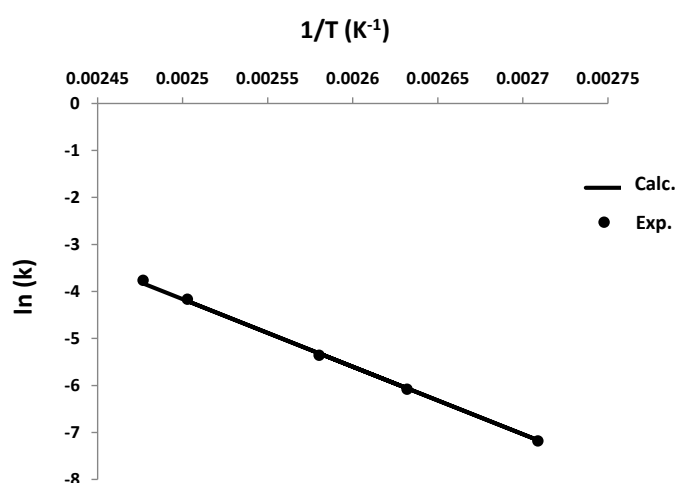


**Figure 4-7-** Experimentally obtained (data points), and calculated (line) Arrhenius plots for the dissociation of  $[(B+2)+H]^+$ .

For all H-G pairs, survival yield curves were obtained as a function of the collision energy in the laboratory frame of reference using high-pressure CID (**Figure 4-8**). Afterwards, a model based upon a truncated Maxwell-Boltzmann distribution was used to calculate the deposited internal energy and its evolution with time. In previous studies, it was demonstrated that this model is suitable for simulating fragmentation occurring under analytical conditions, including high collision gas pressures (multiple collision regime).<sup>195,200–202</sup>

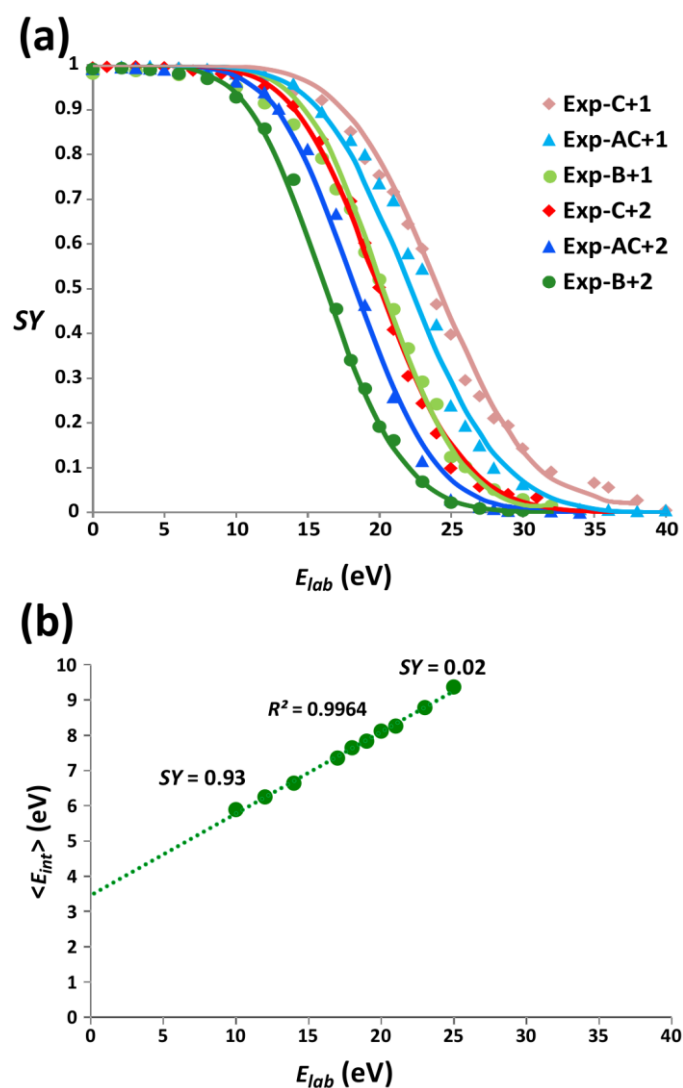


**Figure 4-8-** (a) Experimental (markers) and theoretical (lines) SY curves obtained using high-pressure CID for various H-G complexes studied in this chapter; (b) plot of calculated mean internal energy versus energy in the laboratory frame for  $[(B+2)+H]^+$ .

For the reference complex,  $[(B+2)+H]^+$ , RRKM modeling allows calculation of the mean internal energy before decomposition ( $\langle E_{int} \rangle$ ) corresponding to each collision energy, and



**Figure 4-8b** illustrates the plot of calculated  $\langle E_{int} \rangle$  as a function of  $E_{lab}$ . The extrapolated intercept of 3.46 eV indicates the initial mean internal energy of the ions, and corresponds to a characteristic temperature of 386 K for the reference molecule which is a little bit higher than that of the electrospray source block (373 K). This higher temperature can be attributed to collisions that ions may undergo during their acceleration from the ionization source towards the collision cell.

The equation ( $\langle E_{int} \rangle = 0.2317 \times E_{lab} + 3.4614$ ) is employed to gauge the mean internal energy for other H-G pairs by replacing its intercept with the mean internal energy of each H-G complex at the initial temperature (386 K). Because all of the H-G complexes are characterized by similar sizes and similar types of interactions, a pre-exponential factor of 14.2 (that of the reference  $[(B+2)+H]^+$ ) is used for all cases (in BIRD experiments performed on the  $[AC+2]^+$  complex, a very similar value for the pre-exponential factor ( $\log A$  of 13.8 ( $\pm 0.9$ )) was obtained, **Figure 4-6**). Afterwards, using this constant pre-exponential factor, critical energies were adjusted manually until the theoretical SY curves gave the best fit to the experimental ones.

**Figure 4-8a** displays the experimental (shown by data points) and calculated SY curves obtained for all six H-G complexes. In each case, an acceptable fit could be established between the two sets of data. It should be noted that for  $[C+1]^+$ , because of the presence of an interfering isobaric ion (**Figure 4-9**), the highest energy part of the SY curve could not be reliably obtained experimentally. For the beginning portion of the SY curve for  $[C+1]^+$ , the contribution of this isobaric ion's abundance was removed from the abundance of the precursor ion. Detailed analysis of this issue led us to the conclusion that the interfering ion is cage 1 plus a **Zn(II)** metal ion and a  $Cl^-$  anion ( $[1+Zn(II)+Cl]^-$ ). In **Figure 4-9**, the experimentally observed spectrum and a simulated spectrum of the precursor ion of interest ( $[C+1]^+$ ), plus a simulated spectrum of  $[1+Zn(II)+Cl]^-$  are displayed. From this Figure, we deduced that  $m/z$  of 1204 is common to both the precursor and interfering ions. However, due to the strong coordination of  $Cl^-$  to the **Zn(II)** metal ion, this interfering complex ion is more stable compared to the  $[C+1]^+$ , and its fragment ion starts to appear at significantly higher energies than the fragment of  $[C+1]^+$ . As a consequence, upon removal of the

contribution of this isobaric ion's abundance from the abundance of the precursor ion (based upon % of interfering ion in ESI-MS spectrum and known isotopic abundances) we are quite sure that the beginning part of the SY curve corresponds exclusively to  $[\mathbf{C}+1]^+$  decomposition.

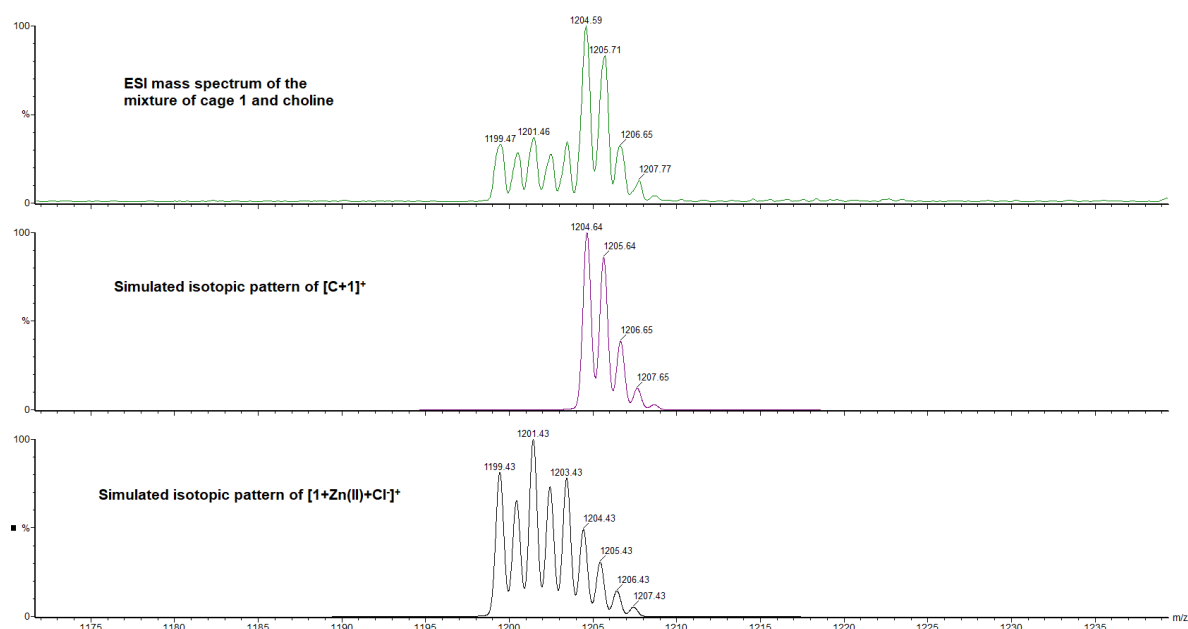


**Figure 4-9-** Presence of an interfering ion,  $[\mathbf{1}+\mathbf{Zn(II)}+\mathbf{Cl}]^+$  in the spectrum of the mixture of cage **1** and choline.

**Table 4-1-** Estimated BDEs for H-G complexes studied in this chapter.

Entry	Complex	Estimated BDE (eV) (RRKM modeling)	$E_a$ (eV) and $\log A$ (BIRD)
1	$[\mathbf{C}+1]^+$	1.31 ( $\pm 0.08$ )	---
2	$[\mathbf{AC}+1]^+$	1.29 ( $\pm 0.08$ )	---
3	$[(\mathbf{B}+1)+\mathbf{H}]^+$	1.23 ( $\pm 0.07$ )	---
4	$[\mathbf{C}+2]^+$	1.27 ( $\pm 0.08$ )	---
5	$[\mathbf{AC}+2]^+$	1.24 ( $\pm 0.07$ )	$E_a = 1.33 (\pm 0.07)$ ,  $\log A = 13.8 (\pm 0.9)$
6	$[(\mathbf{B}+2)+\mathbf{H}]^+$	1.19 ( $\pm 0.05$ )	$E_a = 1.27 (\pm 0.05)$ ,  $\log A = 14.2 (\pm 0.6)$

Estimated *BDEs* of the studied H-G pairs are summarized in **Table 4-1**. This table reveals that the *BDE* values fall within a rather narrow range for all ions; nonetheless, some informative trends and differences can be extracted from the data. For instance, complexes of cage **1** exhibit higher *BDE*'s, and thus are all more stable than those of cage **2**. This trend establishes that the linkers (the only difference between cage **1** and cage **2** host molecules) play important roles in determining the strength of the H-G complexes. Another interesting comparison is the relative stability ranking between various guests for a given host cage. Notably, for both cages **1** and **2**, the order of stability of H-G complexes is as follows: choline > acetylcholine > betaine.

Although the obtained *BDEs* do not differ tremendously from one another in terms of absolute values, concerning relative values, they are entirely consistent with the BIRD results. In BIRD experiments, it was observed that  $[\mathbf{C+1}]^+$ ,  $[\mathbf{C+2}]^+$  and  $[\mathbf{AC+1}]^+$  (the three complexes with the highest estimated *BDE* values) did not dissociate in the accessible temperature range. Moreover, weaker binding  $[\mathbf{AC+2}]^+$  and  $[(\mathbf{B+1})+\mathbf{H}]^+$  complexes did undergo dissociation, but they did not produce sufficient abundances of fragment ions to obtain highly linear kinetic plots. Finally, the least stable  $[(\mathbf{B+2})+\mathbf{H}]^+$  complex did produce enough fragment ions to enable obtainment of linear kinetic and Arrhenius plots for this complex. Considering the different behavior of these complexes, it is evident that when the upper limit of attainable temperature in BIRD experiments is not remarkably high, then, minor differences in critical energies become important. Thus, small differences in the guests' functional groups, or identity of the linkers in the cages, can result in different stabilities, thereby enabling sufficient dissociation for one complex, and not enough dissociation for others in BIRD spectra.

In order to get additional, complementary information about the H-G systems, TCID experiments were performed. In these experiments, the pressure of the collision gas (Xe) was held at a low value ( $10^{-5}$  mbar) where single collision conditions predominate. In order to take into account the effect of the variable sizes of the H-G complexes, normalized abundances of the ions were plotted as a function of the center of mass energy ( $E_{c.m.}$ ). Center of mass energy is the maximum energy that can be transferred during one collision

and is given by ( $E_{c.m.} = E_{lab} \times m_{gas} / (m_{gas} + m_{ion})$ ) where  $m_{gas}$  is the mass of the collision gas and  $m_{ion}$  is the mass of the precursor ion.<sup>97</sup> TCID plots are presented in **Figure 4-10**.

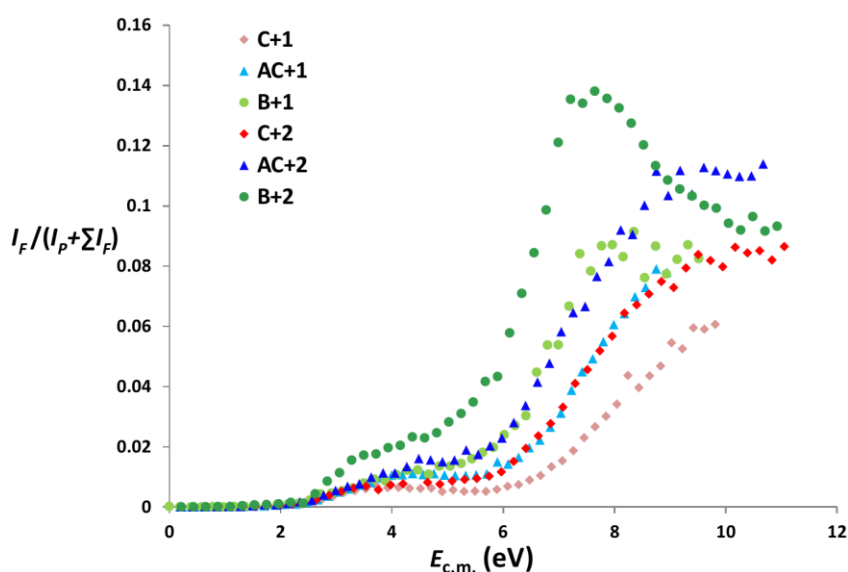


**Figure 4-10-** Normalized intensity of the fragment ion vs. collision energy (center of mass frame) for dissociation of the six H-G pairs studied in this chapter using TCID.

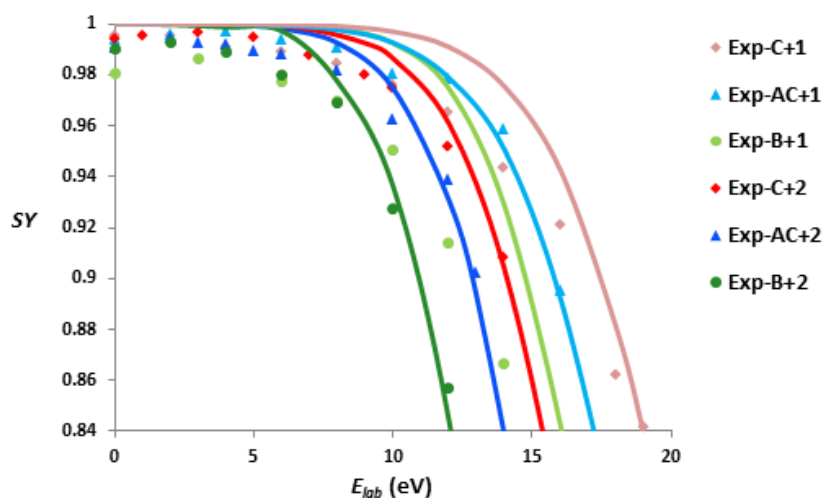


**Figure 4-11-** Enlargement of the beginning part of the experimental (data points) and theoretical SY curves of the H-G complexes (the inconsistency between theory and experiment at the first part of the curve is postulated to be due to a minor quantity of fragile H-G complex (likely exclusion complexes) in each case).

The most interesting feature revealed in **Figure 4-10** is that there are two separate decomposition steps in each curve. But at the same time, the complication of having two steps makes it difficult to perform RRKM calculations on them. This evidence of a two-step process can be rationalized by considering that two types of structures (conformers) exist for

the H-G complexes. The first step of dissociation corresponds to easily dissociable, very fragile structures, whereas the second step pertains to complexes with higher stability. In TCID, only a small percentage of the ion population undergoes dissociation, and the exact ratio of abundances of the two different species is not directly deducible from the curves. However, in high-pressure CID, the entire population undergoes dissociation, and this ratio can be obtained by direct comparison of the normalized intensities. Close inspection of the beginning (left side) portion of the *SY* curves (**Figure 4-11**), where the survival yield first begins to drop at extremely low collision energy values, reveals the presence of a minor amount of readily dissociating, weakly bound species. Notably, this weakly bound conformer has completely dissociated before dissociation of the higher abundance, more strongly bound H-G complexes begins. These data obtained by high-pressure CID corroborate the TCID data, and prompt us to postulate that the former weakly bound complexes correspond to *exclusion* complexes (guests exhibiting weak binding to the exterior of the host cages), whereas the more strongly bound conformers represent the expected *inclusion* complexes (guests located in, and exhibiting binding to, the interior of the host cage). Since the weakly bound species constitute only a small portion of the population, their presence will not lead to significant errors in the above calculations and the obtained *BDE*'s. It should be noted that in the BIRD experiments, it is highly probable that these fragile complexes are dissociated during the hexapole trapping step before being sent to the ICR cell (collision with Ar and storage time on the order of one second), and that is why, the presence of this easily dissociating population is not evident in the BIRD experiments; but, this trapping step does not exist in CID experiments.

The most fragile complexes are characterized by a small number of non-covalent interactions between host and guest molecules. *BDE* values shown in **Table 4-1** correspond to more tightly bound H-G complexes that are characterized by a larger ensemble of non-covalent interactions. This stronger interaction is consistent with a placement of guests inside the host molecules, in the form of inclusion complexes. Corroboration for this statement comes from the use of glycine as a guest molecule. Glycine is very similar to betaine except that, instead of the  $-\text{NMe}_3$  group of betaine, there is a  $-\text{NH}_3$  group on glycine. For the glycine guest, however, no H-G complex was formed with either of the two cage molecules. This

contrast in behavior indicates that the presence of the cationic  $\text{-NMe}_3$  group plays a critical role in stabilizing the H-G complexes for the betaine guest, likely through interaction with the CTV cap.

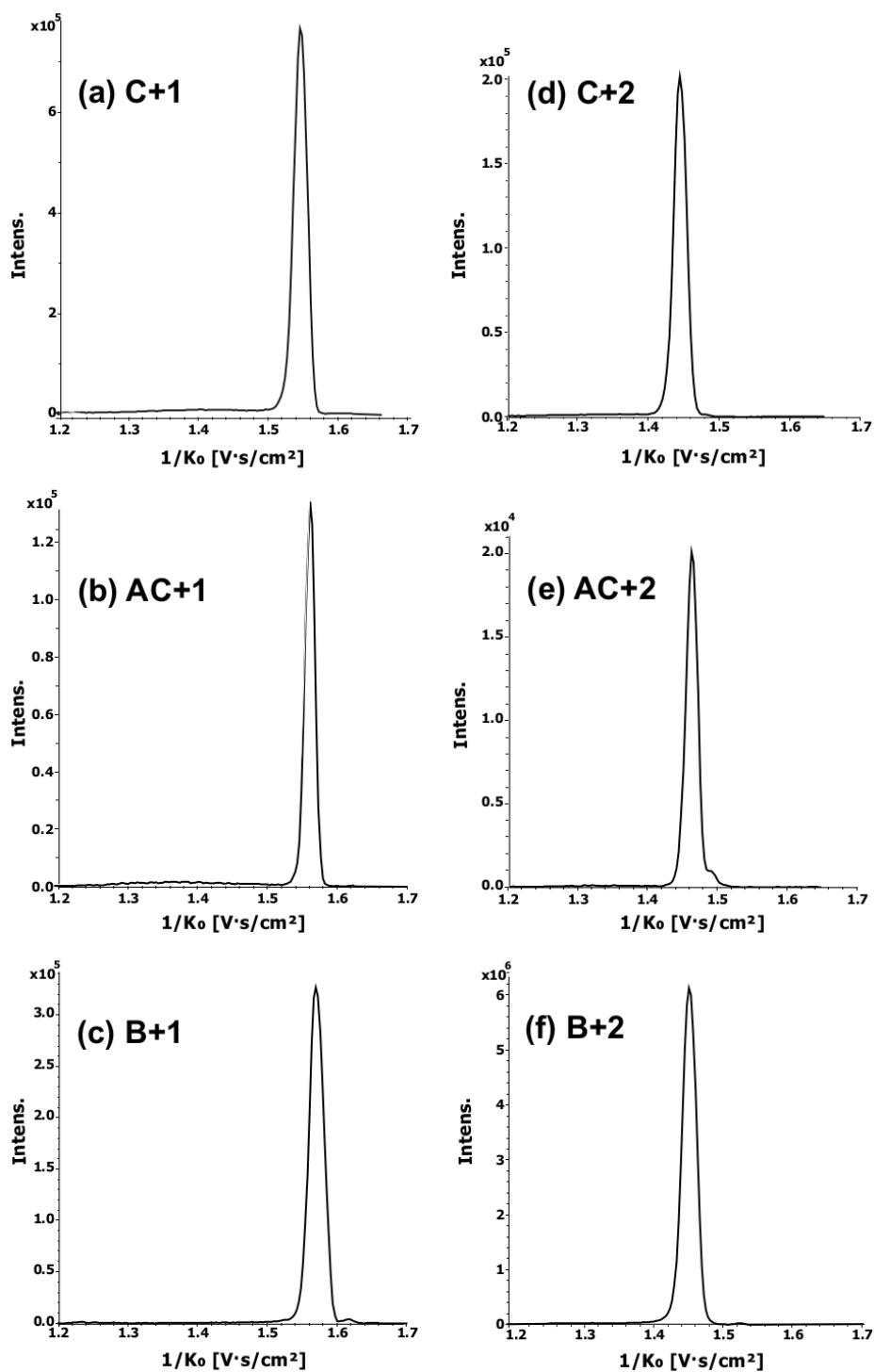


**Figure 4-12-** Extracted ion mobilograms of (a)  $[\text{C}+1]^+$ , (b)  $[\text{AC}+1]^+$ , (c)  $[(\text{B}+1)+\text{H}]^+$ , (d)  $[\text{C}+2]^+$ , (e)  $[\text{AC}+2]^+$ , and (f)  $[(\text{B}+2)+\text{H}]^+$  precursor ions.

Further evidence for the simultaneous existence of two types of structure for H-G complexes comes from ion mobility experiments performed on the 6 H-G complexes. While one prevalent structure is observed for each complex (**Figure 4-12**), a small quantity of a second conformer with larger collision cross section is evident in several of the mobilograms. A larger collision cross section would be expected, of course, for an exclusion complex conformation. However, not every mobilogram shows two conformers, and it is possible that in these cases, the second complex is so weakly bound that it decomposes in the ionization source prior to undergoing ion mobility separation. In any event, the energies of dissociation of H-G complexes obtained using BIRD or high-pressure CID in combination with RRKM modeling correspond to the dominant species in the ion population.

### Calculation of uncertainties

Uncertainties in activation energies and pre-exponential factors, derived using the BIRD method, were estimated by considering a maximum expected deviation of  $\pm 5$  K in the temperatures used to construct the Arrhenius plot, and also  $\pm 2$  K uncertainty in the calibration of the ICR cell temperature. In addition, uncertainties in the dissociation rate constants were calculated using the LINEST function of Microsoft Excel. To include these uncertainties on the final Arrhenius plot, the upper-lower bound method of uncertainty propagation is used as follows: two data point with the largest uncertainties were selected, and maximum and minimum slope and intercept were calculated using the error bars associated with these two data points. The uncertainties in the slope and the intercept of the Arrhenius plots are given by the difference in the two maximum and minimum values divided by 2.

For calculation of uncertainties of estimated BDEs, the slope of the calibration line ( $\langle E_{int} \rangle$  as a function of  $E_{lab}$ ) was varied by  $\pm 0.05$ , the initial temperature by  $\pm 50$  K, the energy in the laboratory frame of reference by  $\pm 2$  eV, and  $\log A$  values by  $\pm 1$ . In addition, decomposition time was multiplied by a factor of 5 and 1/5. Furthermore, uncertainties in the BIRD results were also included in the final presented value of accumulated uncertainty. All of the above-mentioned uncertainties were used to calculate the propagated maximum uncertainties in the obtained critical energies.

## Conclusion

In this chapter, a multimodal approach was employed using the established BIRD technique in combination with SY curves obtained by high pressure CID, and RRKM modeling to measure critical energies of a series of H-G complexes. The activation energy and pre-exponential factor of the reference complex,  $[(\mathbf{B+2})+\mathbf{H}]^+$ , measured using BIRD, an absolute energy evaluation technique, were used to calibrate the internal energy distributions of the other H-G complexes during high-pressure CID experiments. Afterwards, by making the supposition that the transition entropy for decompositions of all complexes is approximately equal, *BDE*'s were calculated for all the H-G pairs. This simple approach presents a highly facile, and at the same time reliable, method for ranking the stabilities of H-G complexes. However, one limitation of this technique is that it is mainly applicable to H-G systems that are characterized by a similar size.

Obtained critical energies display two trends in the stabilities of H-G complexes: first, cage **1** containing a naphthyl linker makes more stable complexes with all three guests compared to cage **2** bearing a phenyl linker; second, the order of the stability of H-G pairs is choline > acetylcholine > betaine for both cage **1** and cage **2**.

Additionally, TCID experimental results lead to the deduction of the presence of two types of structures for each H-G complex. However, ion mobility experiments on the 6 H-G complexes showed one predominant structure in all cases, although a small quantity of a second structure (exhibiting a higher collision cross section) was evident in some of the mobilograms. We are confident that the obtained energies using BIRD or high-pressure CID in combination with RRKM modeling correspond to the dominant species in the ion population, that we postulate to be an inclusion complex. The minor second conformer that was most readily visible in TCID experiments likely corresponds to an exclusion complex.

The complementary techniques employed in this chapter are useful not only for estimation of bond dissociation energies, but also for accurate surveying of the influence of different functional groups on H-G binding properties. Utilization of this approach can provide a



wealth of information pertinent to chemists who seek to design new H-G systems with well-honed properties.

---

***Chapter 5: Investigating binding energies of  
host-guest complexes in the gas-phase using  
low-energy collision induced dissociation***

---

## Introduction

Ion-pair recognition is an intriguing area of coordination chemistry which involves the designing of receptors containing both cationic and anionic binding sites.<sup>205–207</sup> Cationic and anionic guests could be completely separate ions, or zwitterionic species in which the cation and the anion appear in different portions of the same molecule. The main distinction between these two situations in host-guest chemistry is that in the case of zwitterionic species, the distance between the two binding sites in the host molecule should be matched with the size and the shape of the guest molecule.<sup>206</sup> This growing field of study has many applications, such as in the designing of membrane transport systems, the extraction of salts and their solubilization, and in the fabrication of sensors.<sup>57,58,208–213</sup> In addition, because amino acids that exist in zwitterionic form at or near physiological pH are often guests of interest, biological applications are also burgeoning.<sup>214–217</sup>

Various hosts have been investigated for ion-pair recognition, such as uranyl-salophen compounds,<sup>218</sup> or calixarene-based,<sup>219</sup> resorcinarene-based,<sup>220</sup> and pillararene-based<sup>221</sup> receptors. Studies of hemicryptophanes have revealed that they are also an appealing type of receptor for this purpose.<sup>38,42,54,56,58</sup> Hemicryptophanes are chiral molecular containers that include a cyclotrimeratrylene (CTV) moiety bonded to a C<sub>3</sub>-symmetrical organic group using three linkers whose identity and length can be varied.<sup>37,222</sup> Because of the heteroditopic (i.e. tendency to simultaneously host both cationic and anionic species) character of their cavity, hemicryptophanes can offer recognition properties towards ion-pairs, especially biologically important guests like taurine<sup>56</sup> and choline phosphate.<sup>57</sup>

Gas-phase investigation of host-guest systems is of great importance in providing information regarding their intrinsic structural and binding properties. Different mass spectrometry-based studies have been performed with a variety of purposes such as: measurement of the energetics of H-G binding using BIRD<sup>223,224</sup> or TCID,<sup>181,225</sup> obtaining a relative ranking of the stabilities of H-G complexes by comparing fragmentation efficiency (or survival yield) curves,<sup>226–228</sup> studying the role of proton affinities of guest molecules on the characteristics of fragmentation spectra of H-G complexes,<sup>228</sup> exploring the structure of H-G complexes and the interactions between the two partners using the Förster resonance

energy transfer (FRET) technique,<sup>229</sup> quantifying binding affinities by mass spectrometric titration,<sup>230</sup> and exploring the influence of solvent on H-G affinities.<sup>226</sup>

Among the above-mentioned techniques that are used to study the energetics of H-G binding, because achievable temperatures are restricted to those accessible by resistive heating of a vacuum chamber, BIRD is limited to examining only relatively low-energy dissociations. Moreover, due to the fact that obtainment of reliable energetics in TCID requires decompositions to occur under single collision conditions, the TCID technique has been devoted primarily to the study of small systems. There are some other approaches that can be utilized to examine molecular systems having larger sizes and rather high stabilities. For example, RRKM modelling can be performed on survival yield curves obtained using a variety of collisional activation techniques such as collision induced dissociation (CID), surface induced dissociation (SID), or higher-energy collision dissociation (HCD).<sup>231,232</sup> However, RRKM modelling requires information about the transition state which may not be readily accessible. Here in this chapter, we present a low-energy CID approach that can be used to readily determine both activation energies and activation entropies (which are related to the transition state) for dissociation of large and, at the same time, stable systems.

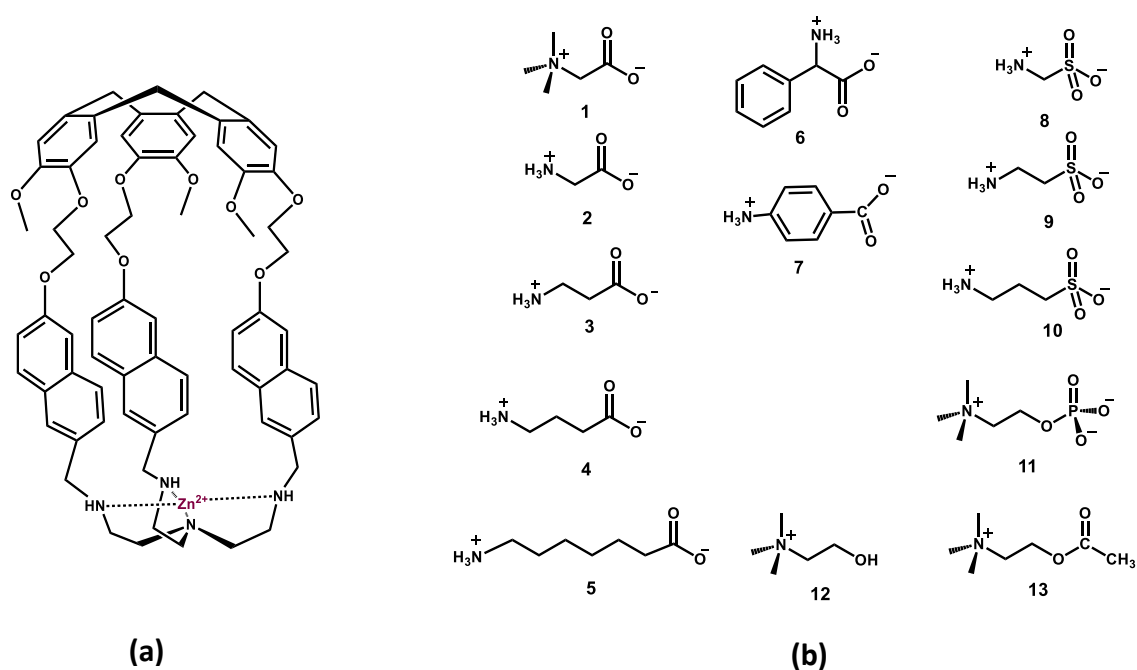


**Figure 5-1-** (a) Hemicryptophane cage Zn(II)@1 used as host molecule, and (b) Guest molecules studied in this chapter.

To illustrate the advantages of the employed low-energy CID approach, a model system was chosen consisting of a heteroditopic hemicryptophane receptor (**Zn(II)@1**) (**Figure 5-1a**) as host for some biologically-relevant guest molecules (**Figure 5-1b**). Then, activation energy and pre-exponential factors of the various H-G complexes were measured using low-energy CID in a linear quadrupole ion trap. Because this approach does not provide absolute measurements, it requires preliminary calibration of effective temperature that was achieved by employing the absolute energy measurement technique BIRD<sup>106</sup> performed on  $[(\mathbf{B}+2)+\mathbf{H}]^+$  complex in Chapter 4. Here for simplicity, this complex is called reference H-G complex ( $\text{H-G}_{\text{ref}}$ ).

## Methodology Background

In a linear trapping quadrupole, trapping of the ions in the axial direction is achieved by applying a DC voltage to the front and back lenses of the four hyperbolic rods. In the radial direction, confinement of ions is achieved by applying RF fields to the rods. In addition, the presence of helium gas helps to reduce movement of trapped ions away from the central axis. Thanks to the long residence time of the ions inside the trap, and also to the relatively high pressure of He, a large number of collisions occurs.<sup>101</sup> As a consequence, ions are subjected to a considerable number of activation and de-activation steps until they reach a Maxwell-Boltzmann distribution of internal energy which is characterized by an effective temperature ( $T_{\text{eff}}$ ).<sup>101,132,133,233–235</sup> In this condition (absence of any excitation voltage),  $T_{\text{eff}}$  is defined by the temperature of the He bath gas which is close to the ambient temperature as was evaluated by ion-molecule equilibrium measurements inside the LTQ.<sup>235</sup> During the resonant activation step (i.e., application of an AC excitation voltage with the same frequency as the secular frequency of precursor ions leading to energetic collisions with the buffer gas), the kinetic energy of the ions increases and their effective temperature exceeds their initial temperature, i.e., that of the bath gas. Goeringer and McLuckey modelled the increase in  $T_{\text{eff}}$  with single frequency resonant activation based on the kinetic theory of ion transport in gases and use of the "forced damped harmonic oscillator" model and random walk simulations.<sup>132,133</sup> They concluded that after resonant excitation (in the Paul trap), in the absence of fragmentation, the population of precursor ions can still have a Maxwell-

Boltzmann distribution, although its effective temperature has been shifted to higher energies.<sup>132</sup> This new effective temperature is a function of temperature and pressure of the bath gas and the resonant excitation amplitude.<sup>132</sup> After applying an excitation voltage, the size of the ions will strongly influence whether the new internal energy distribution remains Maxwell-Boltzmann or not.<sup>233</sup> As the molecular size increases, the probability of being under rapid energy exchange<sup>112</sup> conditions also rises (i.e. the rates of the activation and deactivation steps far exceed the rate of dissociation).<sup>233</sup> Thus, for larger ions, the REX limit is easier to achieve, and under these conditions, there is less deviation from a Maxwell-Boltzmann distribution.<sup>233</sup> It is worth noting here that the REX limit was first defined for activation by infrared photons performed at very low pressure conditions in BIRD experiments.<sup>106</sup> In BIRD experiments, at the REX limit, the rates of photon absorption/emission far exceed the unimolecular dissociation rate, and the precursor ion population arrives at a thermal equilibrium with its surrounding temperature  $T$ .

In the ion trap, owing to the presence of helium at relatively high pressure, the REX limit is expected to be achieved more rapidly due to the faster energy exchange by collisional activation. Furthermore, compared to the BIRD technique, higher effective temperatures can be attained, and smaller precursor ions could reach the thermal equilibrium condition.<sup>130,134,236</sup> Goeringer et al. tried to experimentally determine the relationship between the effective temperature and excitation amplitude by measuring dissociation rate constants ( $k$ ) of protonated leucine enkephalin at different excitation amplitudes, and separately, at different temperatures of the bath gas.<sup>233</sup> They found a linear relationship between  $T_{eff}$  and excitation amplitude. In their experiment, because of the rather high dissociation rates (up to  $65\text{ s}^{-1}$ ) observed under resonant activation conditions, direct application of the Arrhenius equation was impossible.<sup>233</sup> Subsequently, Gabelica et al. attempted to perform a general calibration of effective temperature, and experimentally derive an equation that relates  $T_{eff}$  to excitation amplitude for different size of peptide precursor ions in the temperature range of 365 to 600 K.<sup>237</sup> In order to fulfill the REX condition, they worked in the regime of relatively low dissociation rates ( $0.01$  to  $5\text{ s}^{-1}$ ). Their study found that in the above-mentioned temperature range, effective temperature is a linear function of excitation amplitude. They explained that, according to the theoretically

obtained equation,<sup>132,133</sup> this relation should formally be quadratic. However, they argued that, in the limited temperature range (365-600 K), approximating a linear dependence between  $T_{eff}$  and excitation amplitude also has validity.<sup>237</sup>

Here we employ a method for estimation of effective temperature of ions undergoing resonant excitation inside a linear ion trap which is based on the work of Goeringer and McLuckey.<sup>132,133</sup> They extracted an equation describing the effective temperature of the ions activated by dipolar- single frequency resonant excitation, inside the Paul trap as follows:

$$T_{eff} = T_{bath} + \frac{m_{gas}}{6k_B(m/z)_{ion}^2} \frac{\Gamma^2 Constant^2 V_{RF}^2}{\xi(T_{eff})^2} \quad (5.1)$$

in which  $T_{bath}$  is the temperature of the bath gas,  $m_{gas}$  is the mass of the bath gas,  $k_B$  is the Boltzmann constant,  $(m/z)_{ion}$  is the mass to charge ratio of the ion,  $\Gamma$  is the compensation factor for the hyperbolic geometry of the electrodes,  $V_{RF}$  is the activation amplitude,  $Constant$  is a coefficient that allows conversion of electric field to the applied voltage given by:  $E = Constant \times V_{RF}$ . The parameter  $\xi(T_{eff})$  is the reduced collision frequency which is a function of effective temperature, and is given by Equation 5.2:<sup>238</sup>

$$\xi(T_{eff}) = \frac{4}{3} N_{gas} \frac{\mu}{m_{ion}} \sqrt{\frac{8k_B T_{eff}}{\pi \mu}} \Omega^{(1,1)}(T_{eff}) \quad (5.2)$$

Here  $m_{ion}$  is mass of the ion,  $N_{gas}$  is the number density of the neutral gas,  $\mu$  is the reduced mass defined by ( $\mu = m_{gas}m_{ion}/(m_{gas}+m_{ion})$ ) and  $\Omega^{(1,1)}(T_{eff})$  represents a collision integral which depends on the ion/neutral interaction potential.<sup>138</sup> It should be noted that the “collision cross section” which is usually measured using ion mobility experiments, is in fact the collision integral or more precisely, momentum transfer collision integral (the two terms are often used interchangeably).<sup>239,240</sup>

By substituting Equation 5.2 into Equation 5.1, and then replacing all the constant parameters with  $C$  as follows:

$$C = \frac{3\pi\Gamma^2 Constant^2}{(16N_{gas}k_B)^2} \quad (5.3)$$

for **singly** charged ions  $T_{eff}$  is given by:

$$T_{eff} = T_{bath} + C \times \frac{(m_{gas} + m_{ion})}{m_{ion}} \frac{V_{RF}^2}{T_{eff}[\Omega^{(1,1)}(T_{eff})]^2} \quad (5.4)$$

In our linear ion trap, similar to the Paul trap, precursor ions are excited by applying a dipolar- resonant excitation voltage to one pair of quadrupole rods. Therefore, Equations 14 to 17 in reference 133 are applicable to the LTQ as well. The differences in the geometry of LTQ and Paul trap appear in their associated geometry compensation factor,  $\Gamma$ .<sup>133</sup>

By assuming that  $\Omega^{(1,1)}(T_{eff})$  is quite weakly dependent on temperature within a limited temperature range (this will be discussed in the Results and Discussion section), Equation 5.4 becomes a quadratic equation of the parameter  $T_{eff}$  whose solution is given by:

$$T_{eff} = \frac{1}{2} \left( T_{bath} + \sqrt{(T_{bath})^2 + 4C \times \frac{(m_{gas} + m_{ion})}{m_{ion}} \frac{V_{RF}^2}{(\Omega^{(1,1)})^2}} \right) \quad (5.5)$$

It should be noted that Equation 5.5 is the only (acceptable) solution for Equation 5.4 (the other solution results in a negative value for the effective temperature). We have used Equation 5.5 for calibration of the  $T_{eff}$  of ions undergoing resonant excitation in a linear ion trap. To accomplish this, a reference ion with known collision integral and activation parameters is needed. In the case where the reference ion is in thermal equilibrium under low-energy resonant excitation conditions, the Arrhenius equation can be used to obtain its effective temperature at different excitation voltages. In this way, the value of the constant  $C$  in Equation 5.5 can be obtained using a reference ion. Afterwards, with a known constant  $C$ , the effective temperatures of the other ions can be derived at different excitation amplitudes by employing Equation 5.5, provided that their collision integral is known. Therefore, the only main parameters required for  $T_{eff}$  calibration are the constant  $C$  and collision integral  $\Omega^{(1,1)}$ .



## Experimental section

The hemicryptophane cage, **Zn(II)@1** (Fig. 1) was provided by courtesy of Prof. Alexandre Martinez. It had been synthesized as described previously,<sup>57</sup> and its stock solution (1 mM) was made using dichloromethane. Stock solutions (1 mM) of betaine (**1**), glycine (**2**),  $\beta$ -alanine (**3**), 4-aminobutyric acid (**4**), 7-aminoheptanoic acid (**5**), 4-aminobenzoic acid (**7**), choline phosphate (**11**), choline (**12**) and acetylcholine (**13**) were prepared in methanol; the remaining guest molecules (i.e. phenylglycine (**6**), aminomethanesulfonic acid (**8**), taurine (**9**), and 3-amino-1-propanesulfonic acid (**10**)), were prepared as aqueous solutions. Dilution of the host and each guest molecule (1:1) in methanol (to a final concentration of  $10^{-6}$  M for each partner) gave the final individual working solutions.

Leucine enkephalin was purchased from Sigma-Aldrich (Taufkirchen, Germany) and its stock solution (1 mM) was made in methanol. A working solution of leucine enkephalin was prepared by diluting the stock solution to the final concentration of  $10^{-6}$  M in methanol.

Mass spectrometry experiments were conducted using a LTQ-XL/Orbitrap hybrid instrument (Thermo Fisher®, San Jose, CA). Solutions were injected into the ion source at  $5 \mu\text{Lmin}^{-1}$  using a syringe pump. The electrospray voltage was set at 3.8 kV, capillary voltage at 50 V, and tube lens offset at 90 V. The drying gas temperature was 275°C, and sheath, auxiliary and sweep gas flows (all were nitrogen) were set at 35, 0 and 2, respectively (arbitrary units).

Low-energy CID experiments were performed using the LTQ ion trap of the instrument. Precursor ions of interest were isolated in the LTQ prior to decomposition. For these experiments, the NCE option was disabled, and instead, peak to peak excitation voltage ( $V_{RF}$ ) was used. Helium was used as trapping and collision gas, and the trapping parameter ( $q$ ) was set at 0.25. In all experiments, an isolation window of 10 u was used. In the case of choline phosphate where a consecutive fragmentation is observed, for the first step of dissociation, the isolation window was set at 10 u, and for the second step, it was set at 100 u to avoid any excitation of ions due to the applied waveform employed for isolation. For each resonant excitation voltage, CID spectra were recorded at different activation times (30 ms - 60 s); all acquisitions were averaged to obtain the final spectrum over a 3 min data collection

period. For each ion, only the intensity of the first isotopic peak was considered. Afterwards, by plotting the survival yield as a function of activation time, kinetic plots were obtained.

Ion mobility experiments were performed using an exactly the same way as explained in Chapter 4. Collision cross sections (CCSs) were calculated by the Compass Mobility Calculator (version 2.0) using the experimental  $1/K_0$  values (**Table 5-1**).

## Results and discussion

Zinc metal coordination with negatively charged ligands, and the simultaneous possibility for cation- $\pi$  interactions, make the **Zn(II)@1** (**Figure 5-1a**) a promising receptor for ion-pair recognition. To systematically investigate the hosting capabilities of **Zn(II)@1**, various guest molecules with varying cationic, anionic, and linker portions (**Figure 5-1b**) were selected for study. Separate solutions containing the **Zn(II)@1** host with each of the thirteen guest molecules were prepared individually as 1:1 mixtures. Positive ion mode ESI-MS spectra of these 1:1 (H:G) mixtures revealed that, with Zn(II) initially present, the majority of the complexes had undergone deprotonation to form the singly charged species. Two notable exceptions, however, were the cases of acetylcholine (**13**), where the H-G complex was not observed in the gas phase, and choline (**12**), where the singly charged H-G complex was observed, but with two additional chloride anions (or one chloride plus loss of a proton). For choline phosphate (**11**) with one negative charge, the singly charged H-G pair was detected. These observations are in keeping with the heteroditopic property of the hemicryptophane cage **Zn(II)@1**.

The first tandem mass spectrometry experiments attempted were BIRD experiments on the eleven H-G complexes. None of the complexes, however, were able to decompose within the accessible temperature range of our BIRD set-up (300 to 410 K). It should be noted that 410 K is the maximum value of our heating system, and even if it were possible to go higher, a further increase of the temperature would risk damage to the pre-amplifier located near the ICR cell. It is thus not possible to observe BIRD decompositions of the H-G complexes in our apparatus. Due to this constraint, the low-energy CID technique was selected to measure the bonding strengths of the various H-G pairs. In order to use this technique, the first step is

calibration of the effective temperature of the ions during resonant excitation by exploiting Equation 5.5. For this purpose, a reference H-G complex ( $H-G_{ref}$ ) ( $[(B+2)+H]^+$  complex in Chapter 4) was selected that is characterized by a structure and a number of DOF ( $m/z$  1068, number of DOF of 462) very similar to those of the H-G complexes under study. An  $E_a$  of 1.27 ( $\pm 0.05$ ) eV and  $\log A$  of 14.2 ( $\pm 0.6$ ) were measured for this complex using BIRD technique in Chapter 4.

### Low-energy CID

The low-energy CID technique requires that the selected reference H-G complex have only a single dissociation pathway. This avoids difficulties that may arise from different competitive decomposition pathways taking precedence in different dissociation time-windows (which consequently influence derived activation parameters). Therefore, it is necessary to use a reference system with a unique dissociation route, such as  $H-G_{ref}$ . Furthermore, in low-energy CID experiments, the probability of consecutive fragmentation is very low due to the resonant excitation of only the precursor ion and not the fragments, and to the very low amount of energy deposited on precursor ions, resulting in fragment ions that do not have enough energy to undergo dissociation. By obtaining fragmentation efficiency curves at different times and energies one can ensure the absence of consecutive fragmentation, and finally obtain the activation parameters for individual dissociation pathways.

After obtaining the activation parameters for the reference H-G system, temperature calibration was performed as follows: first, for the  $H-G_{ref}$ , dissociation rate constants at various amplitudes (1.2 to 1.6 V) were measured (**Figure 5-2**).  $H-G_{ref}$  has a relatively large size, and relatively low dissociation rates (0.01 to 0.35 s<sup>-1</sup>) were observed inside the LTQ. This strongly suggests that the REX limit condition is fulfilled, and consequently, the Arrhenius equation (Equation 1.50) can be applied to calculate the effective temperature of  $H-G_{ref}$  ions at each excitation amplitude.

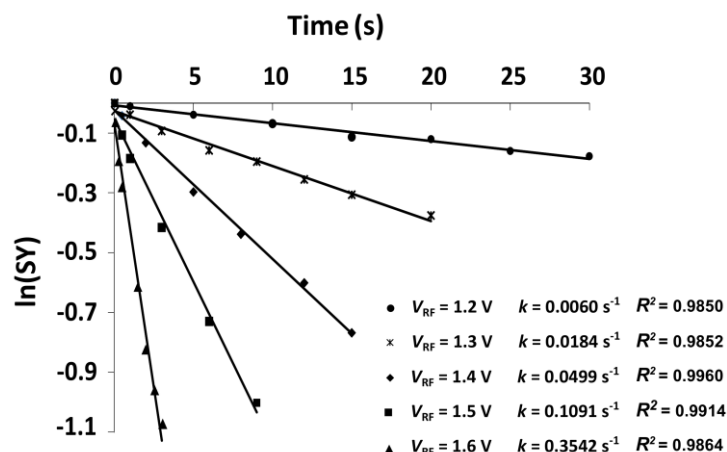


**Figure 5-2-** Kinetic plots of  $H-G_{ref}$  at different resonant activation amplitudes.

In addition to the  $V_{RF}$  and its corresponding  $T_{eff}$ , we need  $\Omega^{(1,1)}$  of the reference H-G complex, in order to derive the constant  $C$  in Equation 5.5. For this purpose, we employed ion mobility mass spectrometry. The measured value for  $\Omega^{(1,1)}$  depends on the employed buffer gas in ion mobility mass spectrometer. Low-energy CID experiments were performed using helium as collision gas; therefore, ideally, collision integrals should be measured by an ion mobility mass spectrometer that uses He. However, our employed TIMS instrument is designed for use with nitrogen as the buffer gas (Experimental  $N_2$ -based collision integrals are presented in **Table 5-1**). The proportionality between He-based and  $N_2$ -based collision integrals depends on the chemical nature of the ions, and their difference is more pronounced for small ions.<sup>239</sup> Therefore, it can be expected that this proportionality holds for H-G complexes in this study, with very similar chemical nature, and quite large size. This proportionality has been previously observed<sup>241</sup> for various compounds that are very close in size to the H-G complexes under investigation in this study. According to the data presented in this reference,<sup>241</sup> the ratio of He-based to  $N_2$ -based CCS values is almost constant ( $\sim 0.75$ ) for rather diverse types of compounds (carbohydrates, peptides and lipids). As such,  $N_2$ -based collision integrals were utilized instead of He-based ones. Afterwards, employing a bath gas temperature of 298 K,<sup>133</sup> the constant  $C$  was derived using  $H-G_{ref}$  (**Table 5-2**). This obtained value for the constant was subsequently used to calculate the effective temperature of the other ions at different excitation amplitudes (employing Equation 5.5).

**Table 5-1-** *m/z*, number of DOF, fragment ion and measured N<sub>2</sub>-based collision integrals for different H-G complexes.

Entry	Complex ion	<i>m/z</i>	Num. of DOF	Fragment ions ( <i>m/z</i> )	N <sub>2</sub> -based $\Omega^{(1,1)}$ (Å <sup>2</sup> )
1	[Zn(II)@1+1-H] <sup>+</sup>	1280.5	513	[Zn(II)@1-H] <sup>+</sup> (1163.5)	318.6 (±3)
2	[Zn(II)@1+2-H] <sup>+</sup>	1238.5	486	[Zn(II)@1-H] <sup>+</sup> (1163.5)	323.7 (±3)
3	[Zn(II)@1+3-H] <sup>+</sup>	1252.5	495	[Zn(II)@1-H] <sup>+</sup> (1163.5)	327.8 (±3)
4	[Zn(II)@1+4-H] <sup>+</sup>	1266.5	504	[Zn(II)@1-H] <sup>+</sup> (1163.5)	333.2 (±3)
5	[Zn(II)@1+5-H] <sup>+</sup>	1308.6	531	[Zn(II)@1-H] <sup>+</sup> (1163.5)	339.1 (±3)
6	[Zn(II)@1+6-H] <sup>+</sup>	1314.5	516	[Zn(II)@1-H] <sup>+</sup> (1163.5)	339.2 (±3)
7	[Zn(II)@1+7-H] <sup>+</sup>	1300.5	507	[Zn(II)@1-H] <sup>+</sup> (1163.5)	332.5 (±3)
8	[Zn(II)@1+8-H] <sup>+</sup>	1274.4	489	[Zn(II)@1-H] <sup>+</sup> (1163.5)	328.1 (±3)
9	[Zn(II)@1+9-H] <sup>+</sup>	1288.5	498	[Zn(II)@1-H] <sup>+</sup> (1163.5)	326.9 (±3)
10	[Zn(II)@1+10-H] <sup>+</sup>	1302.5	507	[Zn(II)@1-H] <sup>+</sup> (1163.5)	333.7 (±3)
11	[Zn(II)@1+11-N(Me) <sub>3</sub> ] <sup>+</sup>	1287.4	492	[Zn(II)@1-H] <sup>+</sup> (1163.5)	332.0 (±3)
12	H-G <sub>ref</sub>	1068.6	462	[H <sub>ref</sub> +H] <sup>+</sup> (951.5)	296.2 (±3)
13	[LEK <sub>2</sub> Na] <sup>+</sup>	1133.5	459	[LEKNa] <sup>+</sup> (578.3)	313.2 (±3)

**Table 5-2-** *Effective temperature and constant C values at different excitation amplitudes obtained using dissociation of H-G<sub>ref</sub> in the linear ion trap.*

<i>V<sub>RF</sub></i> (V)	<i>T<sub>eff</sub></i> (K)	<i>C</i>
1.2	390	2.17E+09
1.3	402	2.15E+09
1.4	413	2.11E+09
1.5	422	2.04E+09
1.6	437	2.07E+09

For all H-G pairs, dissociation rate constants (*k*) were measured at various amplitudes, and then Arrhenius plots were obtained by plotting *ln k* as a function of 1/*T<sub>eff</sub>*. The *m/z*, number of DOF, fragment ion and measured N<sub>2</sub>-based collision integrals for different H-G complexes

are presented in **Table 5-1**. A typical low-energy CID spectrum and kinetic plot of an example H-G complex are presented in **Figure 5-3**, and the Arrhenius plots of all the complexes are presented in **Figure 5-4**. Finally,  $E_a$  and  $\log A$  values for each H-G complex were calculated using the slope and intercept of the corresponding Arrhenius plot (**Table 5-3**).

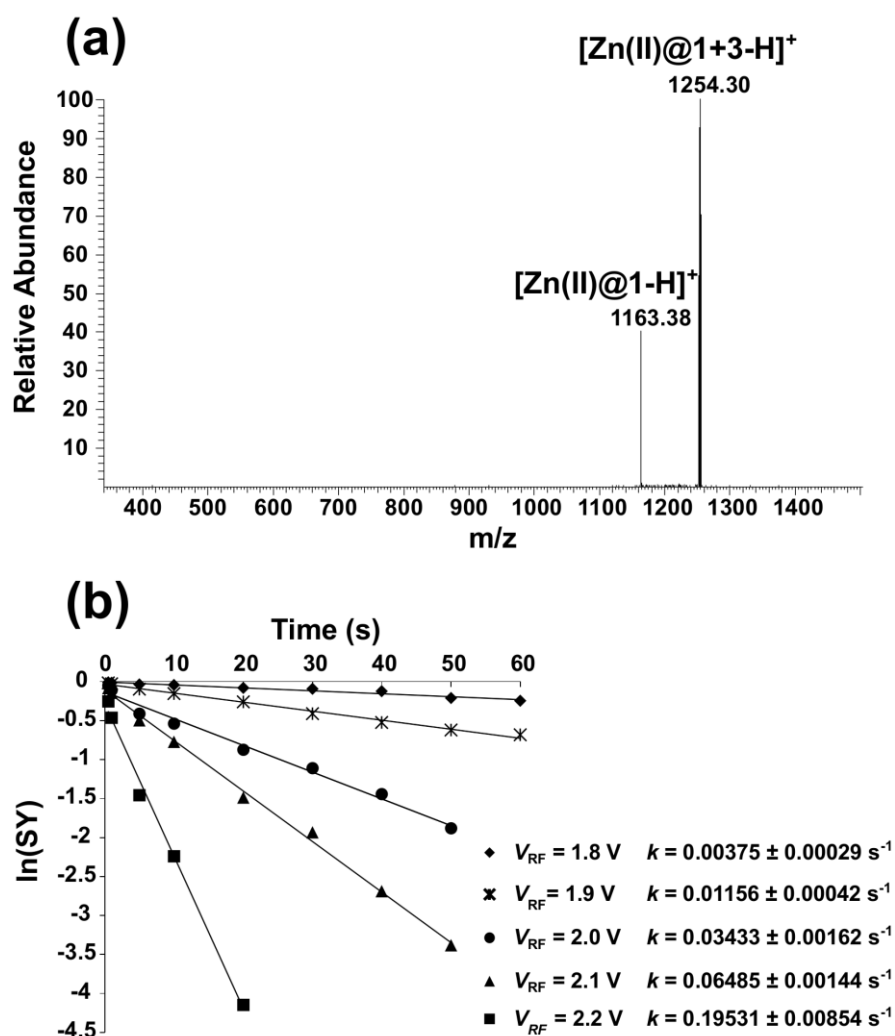


**Figure 5-3-** (a) MS/MS spectrum of the  $m/z$  1252  $[Zn(II)@1+3-H]^+$  precursor obtained using low-energy CID at 1.9 V excitation voltage and 50 s decomposition time. Due to the employed resonant excitation, only the first isotope of the precursor ion ( $m/z$  1252) is decomposed. (b) Kinetic plots of  $[Zn(II)@1+3-H]^+$  obtained at different excitation amplitudes.

All the H-G complexes in this study dissociate in a very narrow effective temperature range, and the difference between the minimum and maximum temperature of the Arrhenius plot for each individual H-G complex is less than 64 K. In a very recent paper of Gabelica and Marklund,<sup>239</sup> the effect of temperature on CCS was studied, and based on their findings, it seems that our assumption (used in the Methodology Background section) that the collision

integral is independent of the temperature is, in fact, very close to reality. In the context of that study, for a singly charged ion, a change of 64 K in the temperature span of 390-590 K should not result in a significant change in CCS. Furthermore, in another study,<sup>242,243</sup> tabulated numerical calculations of  $\Omega^{(1,1)}(T_{eff})$  for various compounds show that as  $T_{eff}$  increases, the collision integral decreases very slowly. Therefore, for a temperature range of 64 K, we consider our assumption to be reasonable.

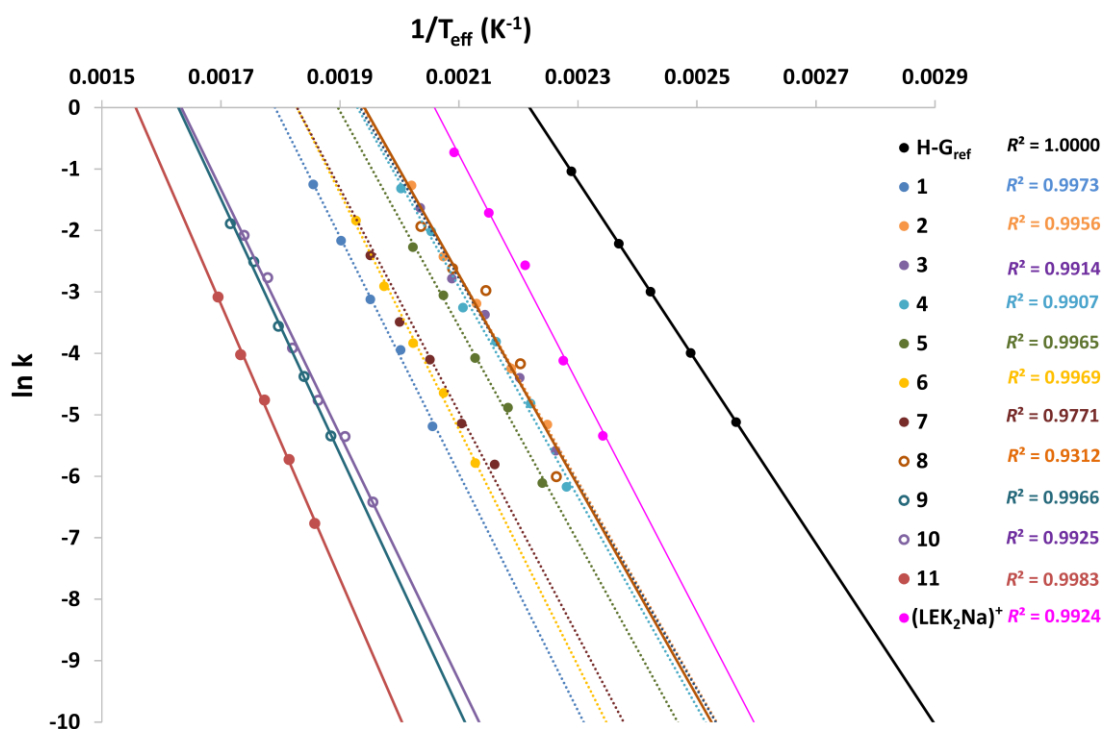


**Figure 5-4-** Experimental Arrhenius plots of the eleven H-G pairs obtained using low-energy CID. The Arrhenius plots of the reference H-G complex H-G<sub>ref</sub> and (LEK<sub>2</sub>Na)<sup>+</sup> are also displayed.

It should be noted that dissociation of complex **11**, [Zn(II)@1+11]<sup>+</sup>, consists of two steps, and the activation parameters reported in **Table 5-3** correspond to the second step of dissociation. Fragmentation of this complex will be discussed later. Parenthetically, it should be mentioned that, as a consistency check, similar experiments were performed on the sodium bound dimer of leucine enkephalin (LEK<sub>2</sub>Na)<sup>+</sup> with  $m/z$  of 1133.5 and number of DOF of 459, and its Arrhenius plot is included in **Figure 5-4**. Measured activation parameters:  $E_a = 1.61 \pm 0.10$  eV and  $\log A = 16.7 \pm 1.5$  are close to published values for (LEK<sub>2</sub>Na)<sup>+</sup> obtained using the BIRD technique ( $E_a = 1.46 \pm 0.07$  eV and  $\log A = 16.7 \pm 0.9$ ).<sup>196</sup>

**Table 5-3-** Activation parameters for dissociation of Zn complexes measured by low-energy CID in the linear quadrupole ion trap.

H-G Pairs	$E_a$ (eV)	$\log A$
[Zn(II)@1+1-H] <sup>+</sup>	1.66 (±0.08)	15.0 (±1.1)
[Zn(II)@1+2-H] <sup>+</sup>	1.45 (±0.10)	14.2 (±1.2)
[Zn(II)@1+3-H] <sup>+</sup>	1.44 (±0.08)	14.1 (±1.2)
[Zn(II)@1+4-H] <sup>+</sup>	1.47 (±0.09)	14.3 (±1.3)
[Zn(II)@1+5-H] <sup>+</sup>	1.51 (±0.08)	14.4 (±1.2)
[Zn(II)@1+6-H] <sup>+</sup>	1.66 (±0.08)	15.3 (±1.2)
[Zn(II)@1+7-H] <sup>+</sup>	1.57 (±0.07)	14.5 (±1.1)
[Zn(II)@1+8-H] <sup>+</sup>	1.48 (±0.13)	14.4 (±1.5)
[Zn(II)@1+9-H] <sup>+</sup>	1.79 (±0.06)	14.7 (±0.8)
[Zn(II)@1+10-H] <sup>+</sup>	1.72 (±0.06)	14.2 (±0.9)
[Zn(II)@1+11- N(Me) <sub>3</sub> ] <sup>+</sup>	1.93 (±0.11)	15.1 (±0.9)

### Comparison of H-G complexes for various guests

The pre-exponential factors obtained using low-energy CID experiments in the LTQ are very similar for all the H-G complexes (an average of 14.6). Therefore, for comparing their stabilities, one can directly rank their activation energies. In addition, it can be expected that dissociation of all the complexes is occurring with almost the same type of rather “loose” transition state (i.e., a high value of the activation entropy (usually  $\log A > 14$ ),<sup>106</sup> is characteristic of direct bond cleavage from a transition state whose structure resembles those of the fragments (late transition state) with a negligible reverse activation barrier). A closer look at the series of guests bearing a carboxylate function: glycine (**2**), β-alanine (**3**), 4-aminobutyric acid (**4**) and 7-aminoheptanoic acid (**5**), reveals relatively weak interactions in this group of guests. Moreover, increasing the size of the alkyl chain does not have a substantial effect on the H-G binding strength. Each guest molecule in this group is likely to exhibit similar types of interactions with the host, i.e. zinc metal coordination,<sup>57</sup> along with possible cation-π interaction<sup>42,244</sup> and hydrogen bonding.<sup>245</sup>



In considering the complexes of phenyl glycine (**6**) and 4-aminobenzoic acid (**7**) (**Figure 5-1b**), their sizes are similar, but their main difference is the position of the ammonium and carboxylate functional groups. As can be seen in **Table 5-3**, their activation energies are almost the same, indicating that the H-G interaction in this case is only slightly influenced by the relative location of the carboxylate and the ammonium. In addition, their complexes are more stable compared to the previous group, likely due to the possibility for  $\pi$ - $\pi$  interactions between the phenyl groups of these two guests and the linkers in the cage structure.

In considering betaine (**1**) versus glycine (**2**) (**Figure 5-1b**), these two molecules differ only by the presence of a trimethylammonium group ( $-\text{N}(\text{CH}_3)_3^+$ ) on the former, instead of an ammonium group ( $-\text{NH}_3^+$ ) on the latter. The main interactions that methyl groups of betaine could participate in are C-H... $\pi$  interactions with the host, and the contribution of this interaction results in a distinction between **1** and **2**, because the trimethylammonium moiety clearly augments the host-guest interaction.

In comparing the three guests bearing a sulfonate group (**Figure 5-1b**), only the length of the alkyl chain separating the sulfonate function from the ammonium group is changing. It can be seen that complexes of taurine (**9**) and 3-amino-1-propane-sulfonic (**10**) acid have higher binding energies compared to that of the shortest chain aminomethanesulfonic acid (**8**). With the sulfonate group tethered to the **Zn(II)**, this result suggests the importance of the ammonium position to participate in H-G stabilization and increase interaction with the host.

For the all guests in this study, deprotonated H-G complexes (+1 charge state) are formed in the gas phase except for choline phosphate (**11**) which has a net charge of -1. Guest **11**, like **1** has a 3-methylammonium group on one extreme, but unlike any other guest, it has phosphate functional group. The higher stability of  $[\text{Zn(II)}@1+11]^+$  results from substantial interactions like coordination of the phosphate ligand to the metal, C-H... $\pi$  and cation... $\pi$  interactions, and hydrogen bonding. Additional evidence for this strong interaction comes from the unique fragmentation pattern of  $[\text{Zn(II)}@1+11]^+$  (**Figure 5-5**). For all other H-G pairs, the only fragmentation pathway is the loss of guest molecule, but for  $[\text{Zn(II)}@1+11]^+$ , at low collision energy, the main fragment is loss of  $\text{N}(\text{CH}_3)_3$ . Then, at higher energies, loss of the whole guest becomes evident (**Figure 5-6**). The reported  $E_a$  value in

**Table 5-3** corresponds to the second step of dissociation. It is worth noting that in deriving the activation parameters for  $[\text{Zn(II)}@1+11\text{-N(CH}_3)_3]^+$ , the experimental collision integral for the initial H-G pair was used, not that of H-G after loss of  $\text{N(CH}_3)_3$ . This inaccuracy is considered in the calculation of uncertainties for this H-G complex, and it was seen that even a deviation as large as  $\pm 30 \text{ \AA}^2$  does not have a substantial effect on the measured activation parameters.

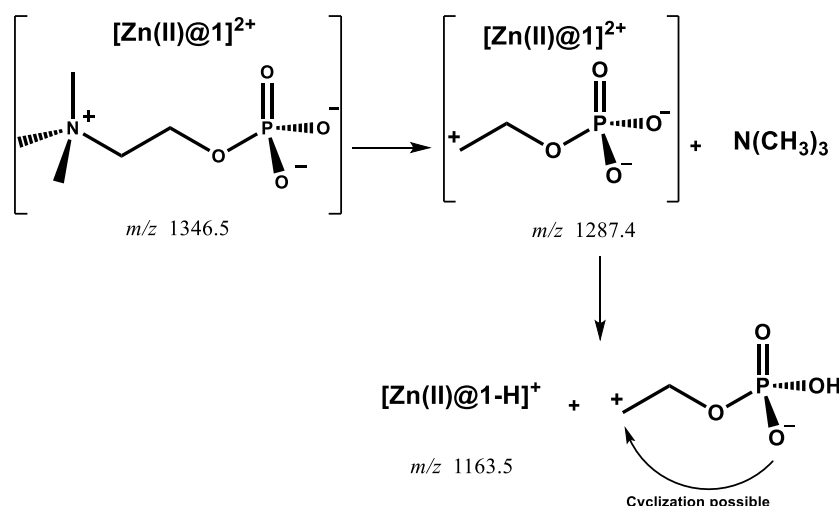


**Figure 5-5-** Two-step dissociation pathway of  $[\text{Zn(II)}@1+11]^+$ .

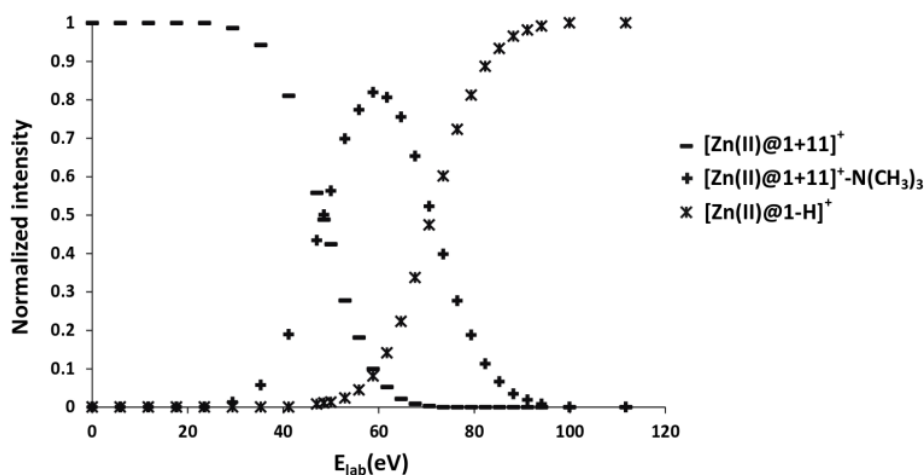


**Figure 5-6-** Normalized intensities for the  $[\text{Zn(II)}@1+11]^+$  and its fragments as a function of laboratory frame collision energy, recorded using HCD mode of the LTQ-XL/Orbitrap hybrid mass spectrometer.

The result that the binding energy of  $[\text{Zn(II)}@1+11]^+$  is higher than all other guests is in complete accordance with what was observed previously in the solution phase (dimethyl

sulfoxide containing 2% water).<sup>57</sup> In that study, nuclear magnetic resonance spectroscopy experiments showed that **11** is fully encapsulated by the **Zn(II)@1** cage, and fluorescence spectroscopy showed that this guest has the highest power of quenching the fluorescence of the host, showing that **Zn(II)@1** has a high affinity towards **11**.<sup>57</sup>

These results as well as the geometry optimization using density functional theory (DFT) for **[Zn(II)@1+11]<sup>+</sup>** complex in a previously published paper,<sup>57</sup> allow us to classify host-guest interactions between hemicryptophane, **Zn(II)@1**, and biologically relevant guests, **1-11**, as a function of two principal interactions. First, the anionic moiety that is coordinated to **Zn(II)** is of primary importance to stabilize the complex, leading to the following stability trend: phosphate (**-OPO<sub>3</sub><sup>2-</sup>**) >> sulfonate (**-SO<sub>3</sub><sup>-</sup>**) > carboxylate (**-CO<sub>2</sub><sup>-</sup>**) in agreement with results obtained in solution. Second, the cationic part can have an interaction with the CTV cap of the hemicryptophane or the naphthyl linker. The ammonium of guests **2-7** are deduced to have a very weak interaction in the host-guest complexes because whatever the carboxylate-ammonium distance is, the dissociation energy is almost the same. However, in the case of sulfonated guests (**6-8**), the ammonium-sulfonate distance becomes more important to stabilize the host-guest complexes. Lastly, an even more pronounced feature enabling a heightened cation- $\pi$  interaction is the presence of trimethylammonium (**N(CH<sub>3</sub>)<sub>3</sub><sup>+</sup>**) instead of ammonium (**NH<sub>3</sub><sup>+</sup>**). Even so, this interaction remains less important than ligand-metal coordination.

### Calculation of uncertainties

Uncertainties in activation energies and pre-exponential factors, measured using the low-energy CID method, were estimated by first including uncertainties in the activation parameters of the reference H-G complex measured using the BIRD technique, and then, considering a maximum expected deviation of  $\pm 0.1$  V in the excitation voltages,  $\pm 30$  K in the initial temperature of the ions ( $T_{bath}$ ), and  $\pm 3$  Å<sup>2</sup> in the measured collision integrals. In addition, uncertainties in each individual dissociation rate constant were calculated using the LINEST function of Microsoft Excel.

In the case of the  $[\text{Zn(II)}@1+11]^+$  complex, because the measured collision integral was obtained for the initial complex (and not for the species after loss of  $\text{N(CH}_3)_3$ , a maximum expected deviation of  $\pm 30 \text{ \AA}^2$  was considered in the measured collision integral.

All these uncertainties were used in the calculation of the maximum uncertainties in activation parameters using the upper-lower bound method of uncertainty propagation (explained in Chapter 4).

## Conclusion

H-G chemistry of a hemicryptophane host with heteroditopic character that is potentially useful in ion-pair recognition, **Zn(II)@1**, was studied in the gas phase. Activation parameters of various H-G complexes formed by guests with different functional groups were derived using a low-energy CID approach that included kinetic experiments in a LTQ. The relatively large residence time of the ions inside the linear ion trap (maximum of 60 s) allowed studying reactions with rates less than  $1 \text{ s}^{-1}$ . This possibility, as well as the large size of the ions, ensures the fulfillment of REX conditions, and as a consequence, accurate application of the Arrhenius equation. Compared to the BIRD technique, here we had access to the higher effective temperature required to probe more endothermic decomposition pathways. As a result, we were able to measure activation parameters for the H-G complexes that were not sufficiently fragile to be fragmented within the practical (limited) upper temperature range of our BIRD set-up.

Based on the measured activation energies, and considering the fact that all complexes were characterized by similar pre-exponential factors, the contribution of various functional groups to the final stabilities of H-G complexes can be ranked: guests bearing a phosphate ( $-\text{OPO}_3^{2-}$ ) functional group make stronger interactions with the encapsulating cage than those with a sulfonate ( $-\text{SO}_3^-$ ) group, and the latter ones make stronger bonds than those with a carboxylate ( $-\text{CO}_2^-$ ) group. In addition, we observed that the presence of trimethylammonium ( $-\text{N(CH}_3)_3^+$ ) or phenyl groups in the guest's structure, improves the strength of host-guest interactions.

In summary, low-energy CID has been used to compare a series of H-G complexes with similar chemical nature that were dissociating in a limited temperature range (390-590 K). More generally, this approach can be used for the calibration of the effective temperature of ions undergoing low-energy CID fragmentation provided that: 1) activation parameters of the employed reference molecule are measured with a high accuracy, and 2) the REX condition is fulfilled for both the reference and compounds with unknown activation parameters. This method is very simple to use, does not require any instrumental modifications, and does not have any practical limitations.

---

***Chapter 6: Investigating binding energies of  
host-guest complexes using higher-energy  
collision dissociation in the gas-phase***

---

## Introduction

Higher-energy collision dissociation (HCD) is a non-resonant excitation mode which takes place in a dedicated octopole collision cell of the LTQ-XL/Orbitrap hybrid instrument.<sup>139</sup> In this cell, precursor ions are excited by the voltage offset between the C-Trap and HCD octopole, allowing energy uptake upon collision with N<sub>2</sub> (collision gas) and leading to subsequent decompositions. Afterwards, the product ions and the remaining precursor ions are transferred into the Orbitrap for detection.<sup>139,171</sup> Commonly, for comparison purposes, survival yield is plotted as a function of energy in the center of mass frame.<sup>97</sup> SY curves have sigmoidal shapes, and their inflection points are usually used to compare the relative stabilities of a series of complexes.<sup>226,227,246–248</sup> There are various parameters influencing the position of the SY curves such as: the number of collisions (which depends on the size of the ion and the target gas pressure), critical energy, entropy of activation, and available time for decomposition that all combine to determine the "kinetic shift"<sup>98,99</sup> (i.e. the energy excess that needs to be applied to the precursor ion relative to its critical energy of dissociation in order to observe fragmentation in the time scale of mass spectrometric detection). By using energy in the center of mass frame, the effect of the changing mass of the ions can be taken into account. However, there is a need for a means to more thoroughly consider all of the above-mentioned influencing parameters.

In the current section of this thesis, the same H-G systems as studied in Chapter 5 have been selected (a heteroditopic hemicryptophane cage (**Zn(II)@1**) (**Figure 5-1a**) as host for some biologically relevant guests (**Figure 5-1b**)). Relative stabilities of the various H-G complexes were investigated using higher-energy collision dissociation (HCD)<sup>139</sup> to generate SY curves, followed by RRKM modeling.<sup>81,83,86,87</sup> Similar to the low-energy CID technique, this approach requires preliminary calibration of the internal energy distribution. This was achieved by use of one of the H-G complexes of Chapter 5, namely, [**Zn(II)@1+1-H**]<sup>+</sup>, whose activation parameters were known from low-energy CID experiments.

## Experimental section

Working solutions were prepared in the same way as explained in Chapter 5. Experiments were performed using a LTQ-XL/Orbitrap hybrid instrument (Thermo Fisher®, San Jose, CA). ESI-MS acquisitions were performed in the positive ion mode using a mass resolving power of  $3 \times 10^4$  at  $m/z$  400. The average scan number was set at 5, and the maximum ion injection time at 200 ms. The electrospray voltage was set at 3.8 kV, capillary voltage at 50 V, and tube lens offset at 90 V. The drying gas temperature was 275°C, and sheath, auxiliary and sweep gas flows (all were nitrogen) were set at 35, 0 and 2, respectively (arbitrary units). Solutions were injected into the ion source using a syringe pump at  $5 \mu\text{Lmin}^{-1}$ .

For HCD experiments, the precursor ions were isolated with an isolation window of 3 u in the LTQ. These ions were decomposed in the HCD cell with an activation time of 30 ms using  $\text{N}_2$  as collision gas, prior to analysis in the Orbitrap. A detailed explanation of the HCD decomposition mode of the LTQ/Orbitrap hybrid instrument is presented in a previously published paper.<sup>171</sup>

## Modeling detail

Kinetic modeling of HCD experiments was performed using *MassKinetics*<sup>199</sup> Scientific Demo software (version 1.17.2.648 Beta, provided by courtesy of Prof. László Drahos). Calculations were performed within the RRKM formalism.<sup>81,83,86,87</sup> Vibrational frequencies of the precursor ions were calculated using the GAMESS<sup>197,198</sup> computational package at the Hartree–Fock level of theory employing a Slater-type basis set. Although this level of theory is relatively low, it has been shown<sup>90,91</sup> that RRKM calculations are not sensitive to the vibrational frequencies when considering only the initial state. A decomposition time of 5 ms<sup>171</sup> was used for simulation of SY curves. For this purpose, deposited internal energy and its evolution with time were modeled based on a truncated Maxwell–Boltzmann distribution and characteristic temperature ( $T_{char}$ )<sup>171,200,201,249</sup> whose concepts are explained in the first chapter.



In Chapter 5, from the Arrhenius plots (obtained using low-energy CID experiments, **Figure 5-4**) activation energies ( $E_a$ ) were experimentally measured. In order to extract critical energies ( $E_0$ ) which are necessary for RRKM modeling of survival yield curves, *MassKinetics*<sup>199</sup> Scientific software (version 1.17.2.648 Beta) was utilized. For this purpose, calculations were performed considering that ions stay in thermal equilibrium during their fragmentation. Using this model, critical energies were adjusted until the best fit between the experimentally recorded Arrhenius plots and the calculated ones was achieved.

## Results and discussion

In order to perform RRKM modeling to extract critical energies from survival yield curves of H-G complexes, the first step is calibration of the deposited internal energy distribution during HCD experiments. Here, we employed the  $[\text{Zn(II)}@1+1\text{-H}]^+$  complex as a reference complex whose activation parameters were measured using the low-energy CID technique (Chapter 5). From low-energy CID experiments, the activation energy of the reference H-G complex is known ( $E_a$  of  $1.66 \pm 0.08$  eV); however, for calibration of mean internal energy using RRKM modeling, its critical energy is required. In order to calculate the critical energy, one needs to have a precise description of the transition state. However, for a large system like the  $[\text{Zn(II)}@1+1\text{-H}]^+$  complex, it is difficult to computationally define the transition state. For this reason, the experimentally measured pre-exponential factor ( $\log A = 15.0 (\pm 1.1)$ ) is used in the *MassKinetics* software. Then, considering a thermal system, the critical energy was adjusted until the best fit between the experimentally recorded Arrhenius plot and the calculated one was achieved (**Figure 6-1**). By doing so, an  $E_0$  of 1.54 eV was obtained for the reference system.

Afterwards, for calibration of the deposited internal energy,  $\langle E_{int} \rangle$ , and corresponding  $T_{char}$  for each point of the SY curve of the reference complex were obtained using the truncated Maxwell–Boltzmann model. A linear relationship between the energy in the laboratory frame of reference and the mean internal energy was established as follows<sup>171,200,201,249</sup> (**Figure 6-2**):

$$\langle E_{int} \rangle = 0.1605 \times E_{lab} + 2.4643 \quad (6.1)$$

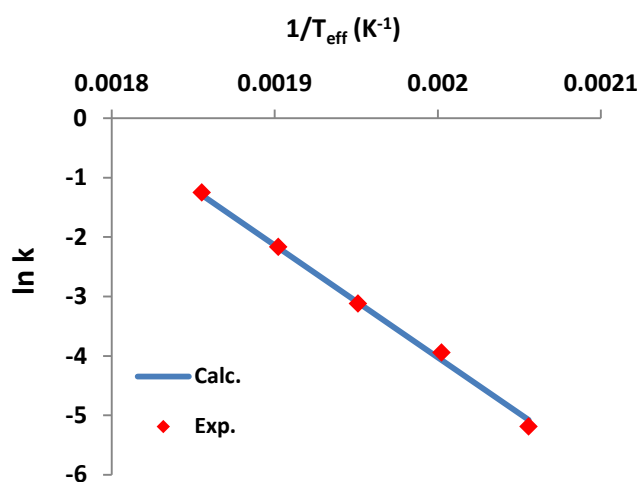


**Figure 6-1-** Experimentally obtained (data points), and calculated (line) Arrhenius plots for the dissociation of the  $[\text{Zn(II)}@1+1\text{-H}]^+$  complex.

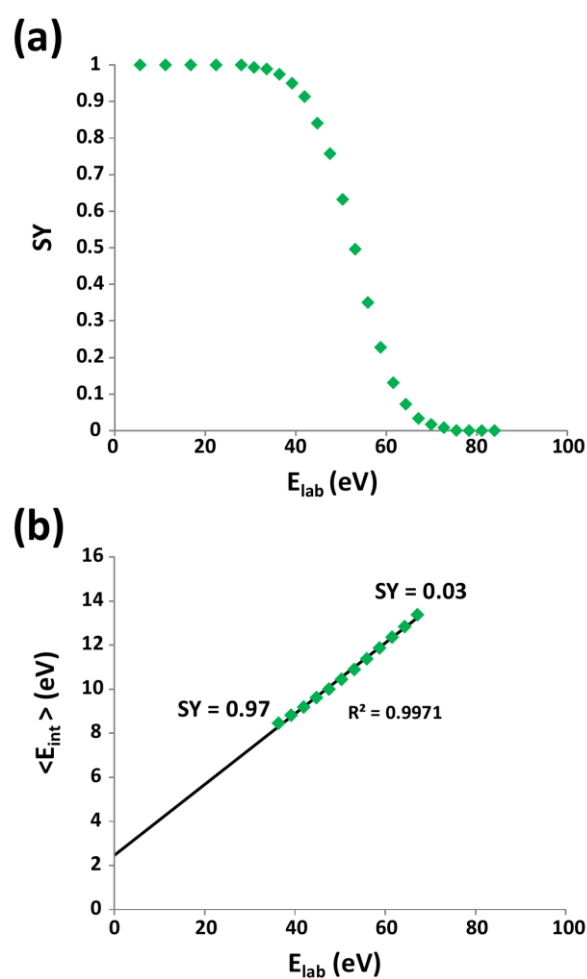


**Figure 6-2-** (a) Experimental SY curve for the dissociation of  $\text{H-G}_{\text{ref}}$  using HCD. (b) Plot of the calculated mean internal energy versus energy in the laboratory frame of reference.

In the above equation, the y-intercept of 2.46 eV represents the initial internal energy of the ions before HCD, and corresponds to a characteristic temperature of 305 K for the reference complex. This initial temperature is not far from the temperature of the target gas which is expected to be close to room temperature.<sup>235</sup>

Because all of the H-G pairs under study have very similar structures and number of DOF, it was assumed that the energy deposition is the same for all H-G complexes in the series. Thus, Equation 6.1 was used for all other H-G complexes to gauge the deposited internal energy distribution in each case by replacing its intercept with the mean internal energy of the chosen H-G complex at initial temperature (305 K).

After calibration of deposited internal energy, pre-exponential factor values, which were measured using the low-energy CID resonant excitation approach (Chapter 5), were employed to calculate *SY* curves. The critical energy of decomposition for a given H-G complex was adjusted until the best fit between the experimental and calculated *SY* curves was attained.

Obtained critical energies ( $E_{0,HCD}$ ) are presented in **Table 6-1**. Furthermore, guests have been classified based on their functional groups, and then for each class, calculated and experimental *SY* curves, in addition to the Arrhenius plots obtained in Chapter 5, are shown in separate plots in **Figure 6-3**. It should be noted that for the complex of guest **11**,  $[Zn(II)@1+11]^+$ , dissociation consists of two steps and since we do not have any information about the pre-exponential factor and critical energy of the first step, it was not possible to calculate the critical energy of the second step of the dissociation.

In order to have a direct comparison between the data obtained in this chapter using the HCD approach and those obtained using low-energy CID in the previous chapter, an attempt was made to extract critical energies of the H-G complexes from the activation parameters obtained by low-energy CID experiments. For this purpose, by considering a thermal system, RRKM modelling was performed to fit the experimentally obtained Arrhenius plots in Chapter 5. This is the same method as was used earlier for simulation of the Arrhenius plot of the reference H-G complex,  $[Zn(II)@1+1-H]^+$ , achieved by low-energy CID to calculate its

critical energy. These calculated critical energies appear in the column labeled “ $E_{0,Th}$ ” in **Table 6-1**. For extracting the critical energies from activation parameters, one other method was used which is based on a previously published paper of Laskin and Futrell.<sup>250</sup> In that paper, they have concluded that “Tolman’s correction factor ( $\Delta E_{corr}$ ) increases linearly with  $\log A$  from 3 kcal/mol for  $\log A = 16.2$  to 36.4 kcal/mol for  $\log A = 39.2$ .”<sup>250</sup> Here, this linear relation is exploited to calculate Tolman’s correction factor for different H-G pairs. Then, critical energies were calculated using Equation 6.2 at 500 K.<sup>106</sup>

$$E_a = E_0 + \Delta E_{corr} + k_B T \quad (6.2)$$

**Table 6-1- Critical energies for dissociation of Zn complexes measured by the HCD approach.**

H-G Pairs	HCD approach	Low-energy CID		
	$E_{0,HCD}$ (eV)	$E_a$ (eV)	$E_{0,To}$ (eV)	$E_{0,Th}$ (eV)
[Zn(II)@1+1-H] <sup>+</sup>	1.54 (±0.08)	1.66 (±0.08)	1.56 (±0.11)	1.54 (±0.08)
[Zn(II)@1+2-H] <sup>+</sup>	1.45 (±0.11)	1.45 (±0.10)	1.40 (±0.13)	1.37 (±0.10)
[Zn(II)@1+3-H] <sup>+</sup>	1.43 (±0.09)	1.44 (±0.08)	1.39 (±0.11)	1.36 (±0.08)
[Zn(II)@1+4-H] <sup>+</sup>	1.42 (±0.10)	1.47 (±0.09)	1.41 (±0.12)	1.38 (±0.09)
[Zn(II)@1+5-H] <sup>+</sup>	1.39 (±0.09)	1.51 (±0.08)	1.43 (±0.11)	1.41 (±0.08)
[Zn(II)@1+6-H] <sup>+</sup>	1.56 (±0.09)	1.66 (±0.08)	1.54 (±0.11)	1.53 (±0.08)
[Zn(II)@1+7-H] <sup>+</sup>	1.50 (±0.12)	1.57 (±0.07)	1.50 (±0.13)	1.47 (±0.07)
[Zn(II)@1+8-H] <sup>+</sup>	1.49 (±0.15)	1.48 (±0.13)	1.40 (±0.16)	1.38 (±0.13)
[Zn(II)@1+9-H] <sup>+</sup>	1.79 (±0.06)	1.79 (±0.06)	1.74 (±0.08)	1.68 (±0.06)
[Zn(II)@1+10-H] <sup>+</sup>	1.70 (±0.06)	1.72 (±0.06)	1.70 (±0.08)	1.63 (±0.06)

These calculated critical energies appear in the column labeled “ $E_{0,To}$ ” in **Table 6-1**. To enable visual comparison of the critical energies obtained using the three different mass spectrometric techniques, **Figure 6-4** displays results obtained for each H-G complex. From this figure, it is evident that  $E_{0,To}$  and  $E_{0,Th}$  values are very close to each other, and in most cases both are lower than  $E_{0,HCD}$  values. This latter difference can be due to the fact that the same slope was used for the reference H-G complex ([Zn(II)@1+11]<sup>+</sup>) and all other H-G pairs

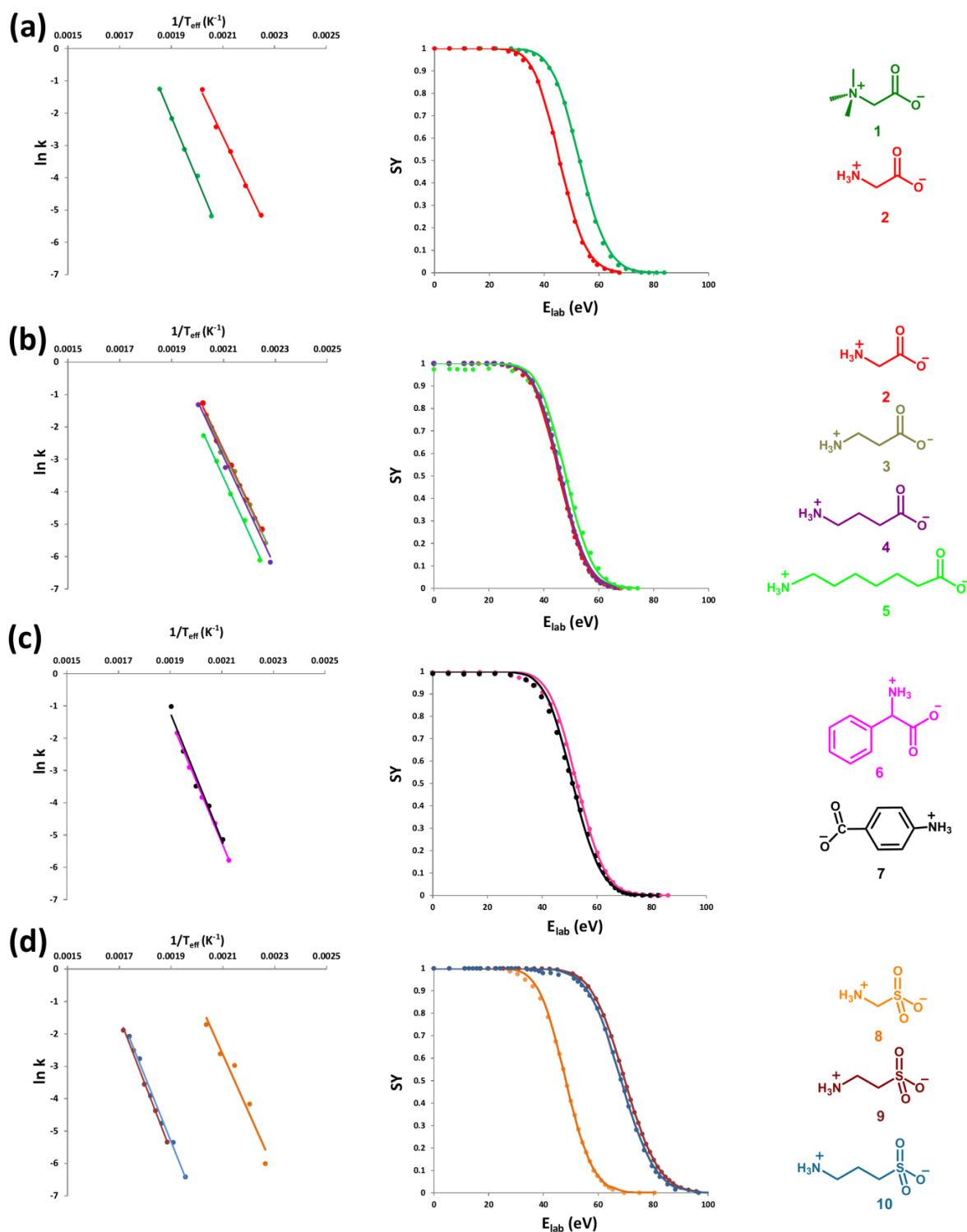


**Figure 6-3-** Arrhenius plots (left side) obtained using low-energy CID; and experimental (points), and theoretical (lines) SY curves (center) obtained using HCD approach for the H-G pairs studied in Chapters 5 and 6, classified based on the functional groups present on the guests (right).

in the calibration of mean internal energy in the HCD approach (Equation 6.1), which can result in uncertainties in  $E_{0,HCD}$ . It should be noted that  $E_{0,T0}$  and  $E_{0,Th}$  values also contain

uncertainties. In particular, in the former, an approximate relationship between  $\log A$  and  $\Delta E_{corr}$  was used for calculation of  $E_{0,To}$  values, and in the latter, due to the difficulty in the calculation of real transition state, experimentally-obtained pre-exponential factors (with inherent associated error) were utilized in the procedure for calculation of  $E_{0,Th}$  values.

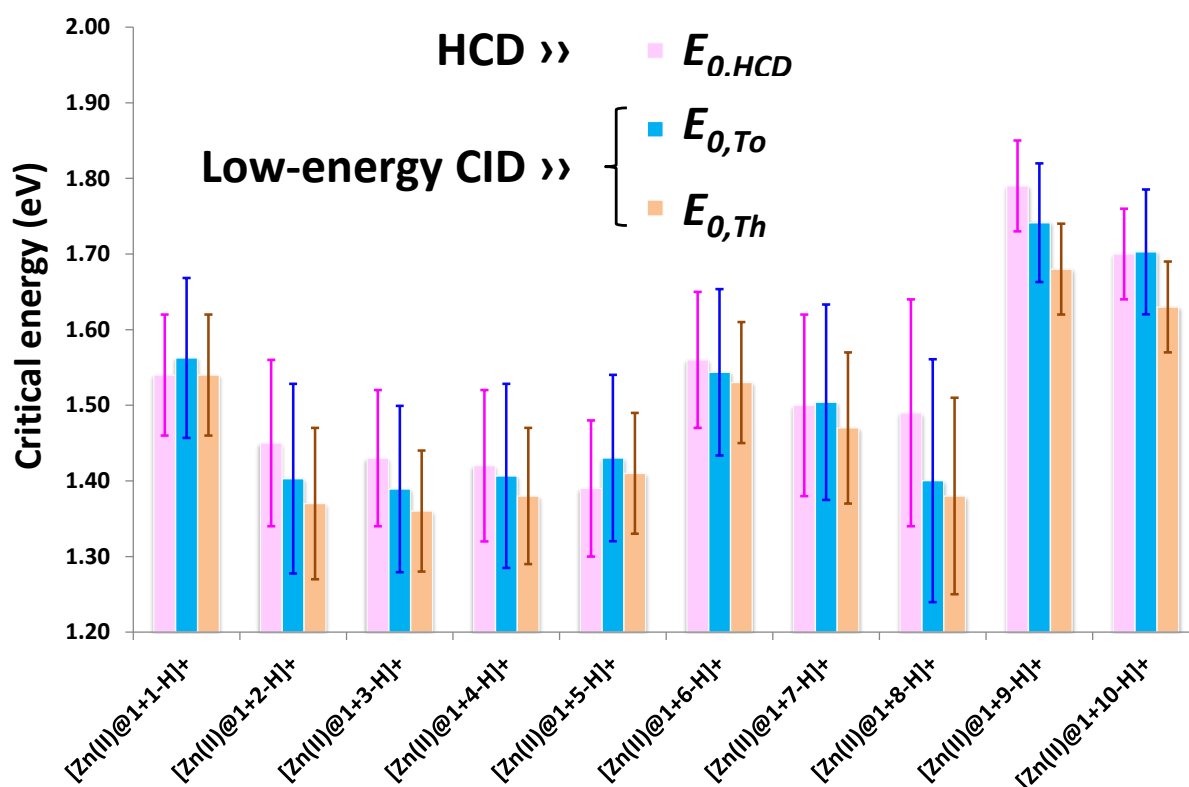


**Figure 6-4-** Calculated critical energies using three different methods: (1) extracted form results of low-energy CID experiments in Chapter 5 using (a) a linear relation presented by Laskin<sup>250</sup> ( $E_{0,To}$ ) at 500 K, and (b) MassKinetics software with presuming a thermal model ( $E_{0,Th}$ ), and (2) using HCD approach ( $E_{0,HCD}$ ).

### Comparison of low-energy CID resonant excitation with HCD non-resonant approach

Through Chapters 5 and 6, two different techniques were employed to estimate binding energies of a series of singly charged H-G complexes. Both techniques consider that the multiple collision regime leads to Maxwell-Boltzmann internal energy distributions. But on the one hand, low-energy CID is a resonant activation technique in which a lengthy activation time is used (by collision with helium), and where the REX limit is achieved (for large systems). The precursor ion population may thus be considered to be in thermal

equilibrium during all steps of activation and decomposition (**Figure 6-5a**). On the other hand, HCD employs non-resonant activation (by collision with nitrogen) where the rate of the unimolecular dissociation is much higher than the activation/de-activation of the ions. Therefore, the higher energy tail of the distribution dissociates rapidly, leading to a Maxwell-Boltzmann distribution of internal energy that is truncated on the high-energy end (**Figure 6-5b**).

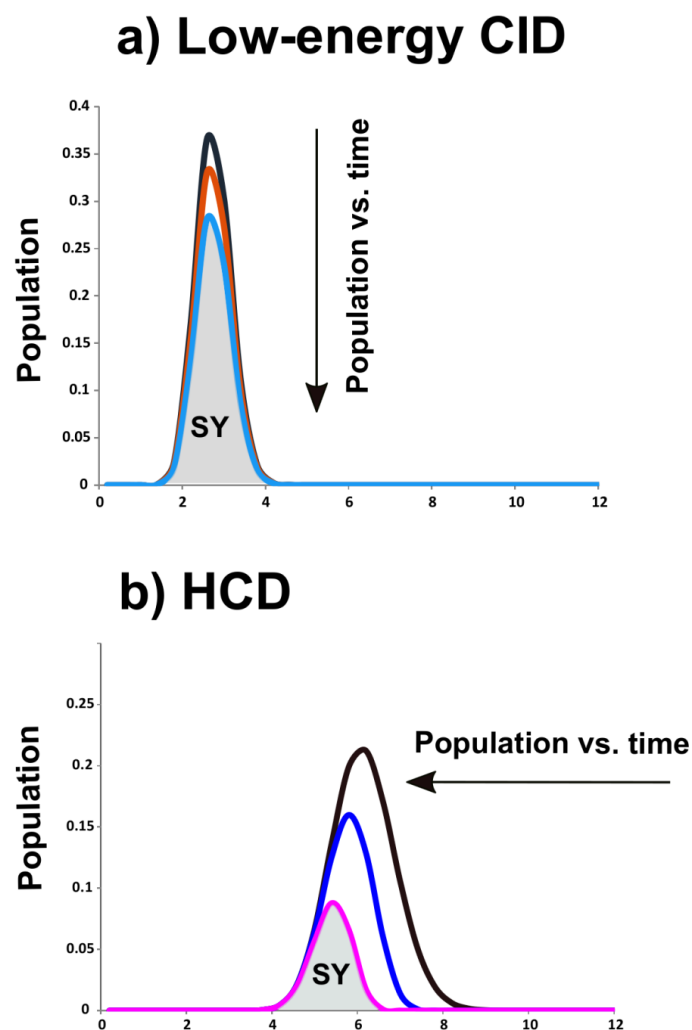


**Figure 6-5-** Schematics of (a) thermal model for dissociation of H-G complexes by low-energy CID, and (b) truncated Maxwell–Boltzmann for dissociation of H-G complexes during HCD process.

The method of Vékey and co-workers<sup>251</sup> was used to evaluate temperature-dependent rate constants measured using the various techniques. **Figure 6-6** presents the Arrhenius plots of three different H-G pairs: H-G<sub>ref</sub> (in Chapters 4 and 5,  $\log A = 14.2$ ),  $[\text{Zn(II)}@1+5\text{-H}]^+$  ( $\log A =$

14.4) and  $[\text{Zn(II)}@1+7\text{-H}]^+$  ( $\log A = 14.5$ ) obtained using low-energy CID and HCD techniques. The Arrhenius plot of  $\text{H-G}_{\text{ref}}$ , acquired using BIRD technique is also displayed. BIRD was used to measure activation parameters of  $\text{H-G}_{\text{ref}}$  complex ( $[(\text{B}+2)+\text{H}]^+$ ) in Chapter 4. An advantage of this technique is that the real temperatures ( $T_{\text{real}}$ ) of the ions are taken into account and therefore, in contrast to the two other techniques, there is no need for temperature calibration. However, only a relatively low temperature range is accessible (**Figure 6-6**) which limits BIRD's application to relatively low-energy dissociations.

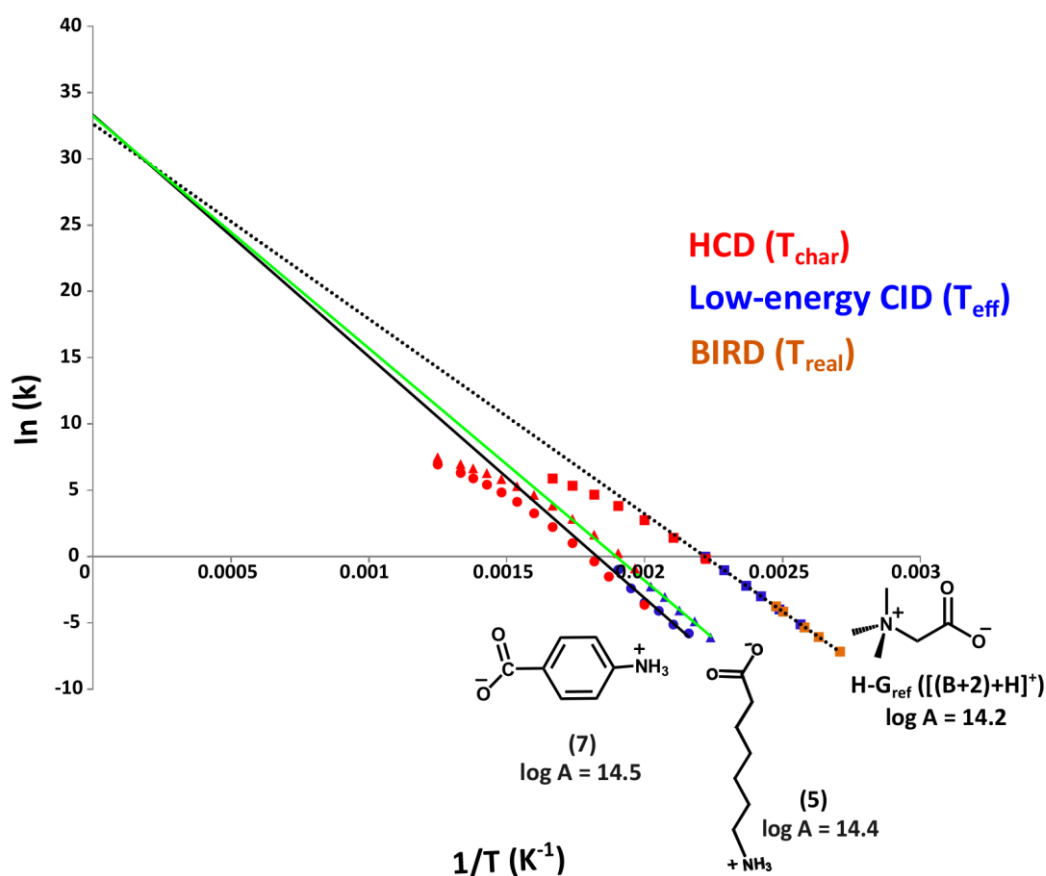


**Figure 6-6-** Arrhenius plots of  $\text{H-G}_{\text{ref}}$ ,  $[\text{Zn(II)}@1+5\text{-H}]^+$  and  $[\text{Zn(II)}@1+7\text{-H}]^+$  obtained using low-energy CID and HCD techniques. Arrhenius plot of  $\text{H-G}_{\text{ref}}$ , acquired using the BIRD technique, is also displayed.

The second technique is low-energy CID which involves the effective temperature of the ions. As is evident from **Figure 6-6**, the main advantage of this resonant activation technique is that it enables access to higher temperatures compared to the BIRD technique. In this technique due to the low amount of energy deposition and also resonance excitation of ions, probability of consecutive fragmentations is minimal. In addition, using low-energy CID technique, even smaller molecules compared to the BIRD technique can be in REX limit.



Finally, using the HCD technique that encompasses the characteristic temperature of the ions, one can gain access to even higher energies than low-energy CID. The Arrhenius plot of the H-G pairs acquired using the HCD method (**Figure 6-6**) shows that at the beginning of fragmentation;  $T_{char}$  is almost equal to  $T_{eff}$ , and the employed RRKM modeling works well. But, at higher dissociation rates, where the internal energy distribution of the precursor ion population starts to become more truncated at the higher energy portion,  $T_{char}$  begins to deviate from  $T_{eff}$ . Important features of the above-mentioned techniques are summarized in **Figure 6-7**.

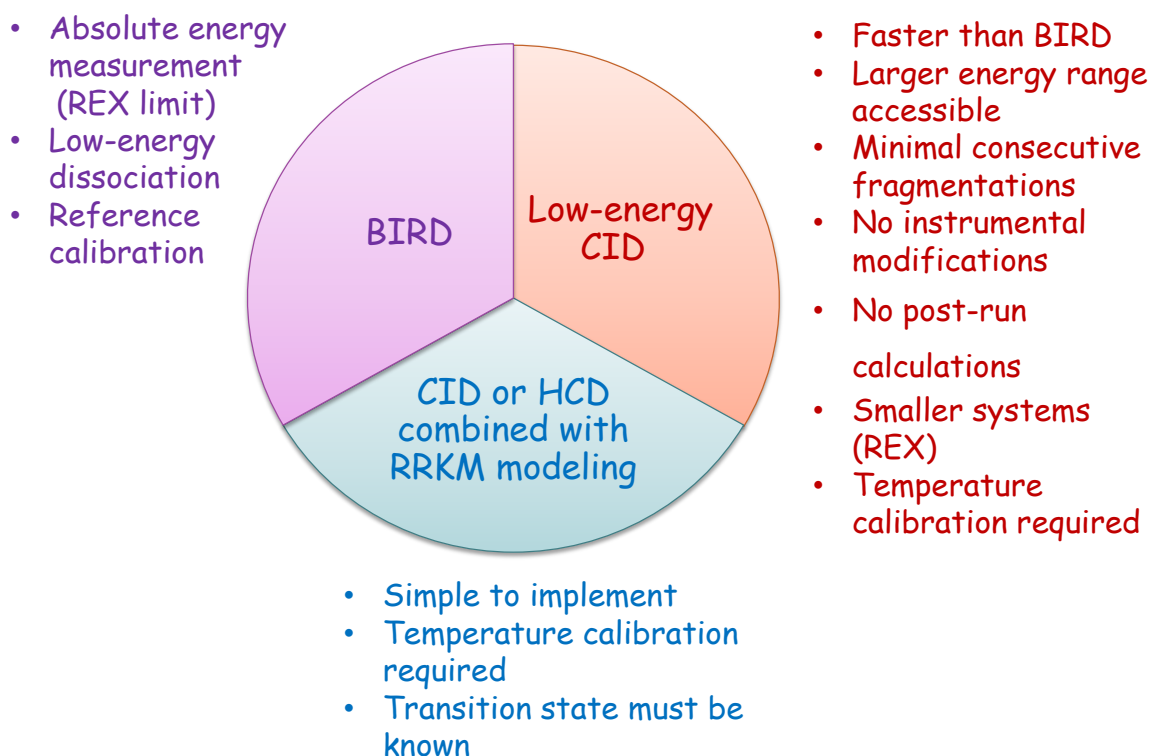


**Figure 6-7-** Main characteristics of different techniques employed to measure bond dissociation energies in this thesis.

## Conclusion

H-G chemistry of **Zn(II)@1** hemicryptophane cage was studied in the gas phase using the HCD fragmentation technique in conjunction with RRKM modeling. Critical energies very similar to those extracted from low-energy CID experiments were obtained. This technique is very simple to perform, and can provide somewhat reliable results. However, in addition to the requirement for temperature calibration (as in low-energy CID), the main limitation of

this method is that we need to have information about the pre-exponential factor of the complexes to calculate the critical energies. Therefore, utilization of this technique is only possible when there is some information about the transition state and entropy of dissociation.

---

***Chapter 7: Dissociation energetics of lithium-cationized  $\beta$ -cyclodextrin and maltoheptaose studied by low-energy collision induced dissociation***

---

## Introduction

Native cyclodextrins (CDs) are cyclic oligosaccharides that are composed of 1,4 linked  $\alpha$ -D-glucose monomers making a truncated cone shape structure (**Figure 7-1**).<sup>252–255</sup> The rims at the top and bottom of the cone bear primary and secondary hydroxyl groups, respectively, affording hydrophilic properties to the rim portions of these molecules. In addition, the interior space between the rims forms a hydrophobic cavity, that can accommodate or “host” different “guest” molecules.<sup>255</sup> Furthermore, the properties and functionality of CDs can be adjusted by performing various chemical modifications on their structures.<sup>256</sup> Both native and functionalized CDs have been employed in various applications such as drug delivery,<sup>12,252,257–259</sup> molecular recognition,<sup>260</sup> organic synthesis and catalysis,<sup>261–263</sup> sensor design,<sup>264</sup> chromatographic techniques,<sup>265,266</sup> chiral capillary electrophoresis,<sup>267</sup> and host–guest chemistry.<sup>268,269</sup>

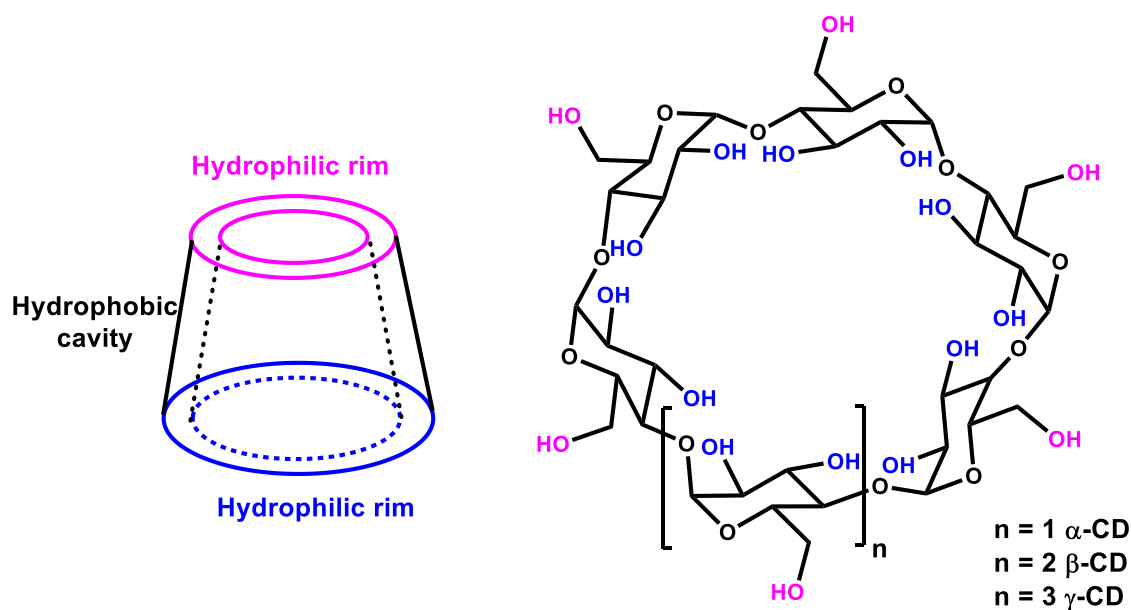


**Figure 7-1-** General structure of native cyclodextrins.

Metal complexes of cyclodextrins are appealing molecular systems due to their potential applications in areas such as catalysis<sup>270</sup> including their use as model enzymes.<sup>271</sup> For this reason, different studies have been performed to characterize metal-CD complexes using various techniques such as electrochemical approaches,<sup>272–274</sup> spectroscopic methods,<sup>274–276</sup> X-ray crystallography,<sup>277</sup> circular dichroism,<sup>278</sup> gas chromatography-mass spectrometry,<sup>279</sup>

computational methods,<sup>280</sup> electrospray mass spectrometry,<sup>230,281–285</sup> *etc.* Despite numerous studies investigating different aspects pertaining to the chemistry of metal-CD complexes, only a few works have been devoted to the quantitative measurement of their dissociation energetics.

Gas-phase (i.e. in the absence of solvent) dissociation energetics of metal-CD complexes can provide helpful information about their stabilities. For this purpose, various tandem mass spectrometry techniques can be employed such as blackbody infrared radiative dissociation,<sup>106,109,184</sup> threshold collision induced dissociation,<sup>180–183</sup> collisional activation in a FTICR instrument,<sup>187,188,286</sup> and thermal activation in a quadrupole ion trap.<sup>130,134,185</sup>

In Chapter 5, low-energy CID was employed to measure the activation energy,  $E_a$  and the pre-exponential factor,  $A$  for a series of H-G complexes. In that study, the change in the temperature of ions undergoing dipolar- resonance excitation inside the linear quadrupole ion trap was calibrated by applying the equation derived by Goeringer and McLuckey<sup>132,133</sup> for the effective temperature to a reference H-G complex. In the current Chapter, using the same technique, a comparative study of dissociation energetics is performed on  $\text{Li}^+$  complexes of two similar oligosaccharides:  $\beta$ -cyclodextrin ( $\beta$ -CD, a native CD with seven  $\alpha$ -D-glucose monomers, **Figure 7-1**) and maltoheptaose ( $\text{G}_7$ ) also containing seven  $\alpha$ -D-glucose monomers, but in a linear configuration.

## Experimental section

$\beta$ -CD was purchased from Roquette (Lestrem, France), and  $\text{G}_7$  and LiCl were obtained from Sigma-Aldrich (Saint-Quentin Fallavier, France). Stock solutions (1 mM) of  $\beta$ -CD and  $\text{G}_7$  were prepared in methanol/water (1:1 v/v) and that of the LiCl (1 mM) was prepared in water. Individual working solutions were prepared by dilution of each oligosaccharide and salt (1:1) in methanol (to a final concentration of  $10^{-6}$  M for each partner).

Low-energy CID and ion mobility experiments were performed in exactly the same way as was explained in Chapter 5 and Chapter 4, respectively. Collision cross sections of  $297.8 \text{ \AA}^2$  and  $286.6 \text{ \AA}^2$  were obtained for  $[\beta\text{-CD+Li}]^+$  and  $[\text{G}_7\text{+Li}]^+$ , respectively.

CID experiments on a triple quadrupole mass spectrometer were performed in exactly the same way as explained in Chapter 4 for “high-pressure CID” experiments.

## Results and discussion

Preliminary experiments involved obtaining MS/MS spectra of precursor alkali metal ( $\text{Li}^+$ ,  $\text{Na}^+$  and  $\text{K}^+$ ) adducts of  $\beta$ -CD and  $\text{G}_7$ . However, among these metal-cationized precursors, fragmentation spectra of sodiated and potassiated sugars acquired using a triple quadrupole mass spectrometer (which allows access to low  $m/z$  fragments) revealed departure of the bare alkali metal ion. Therefore, due to the LMCO limitation, it was not possible to use low-energy CID for  $\text{Na}^+$  and  $\text{K}^+$  adducts of oligosaccharides. In CID spectra of lithiated  $\beta$ -CD and  $\text{G}_7$ , loss of  $\text{Li}^+$  was not observed, and therefore, lithiated adducts are amenable to the low-energy CID technique.

Fragments of  $[\text{G}_7+\text{Li}]^+$  were annotated using the nomenclature of Domon and Costello,<sup>172</sup> and those of the  $[\beta\text{-CD}+\text{Li}]^+$  were annotated using previously published<sup>281,287</sup> terminology based on the Domon and Costello nomenclature but adapted for cyclic oligosaccharides that lack the reducing end.

Low-energy CID spectra of lithiated  $\beta$ -CD and  $\text{G}_7$  precursors, i.e.,  $[\beta\text{-CD}+\text{Li}]^+$  and  $[\text{G}_7+\text{Li}]^+$ , respectively, are shown in **Figure 7-2**. The major product ions obtained for  $[\beta\text{-CD}+\text{Li}]^+$  under the mentioned experimental conditions correspond to the formation of Z type ions, plus a small quantity of  $[\text{C}_7/\text{Y}_6+\text{Li}]^+$ , and a trace of the fragment resulting from loss of water from the precursor ion (**Figure 7-2a**). In considering  $[\text{G}_7+\text{Li}]^+$ , which differs from the former oligosaccharide complex only by its structure being linear instead of cyclic, a different fragmentation pattern is observed (**Figure 7-2b**). For  $[\text{G}_7+\text{Li}]^+$ , the peak resulting from loss of water is more intense compared to  $[\beta\text{-CD}+\text{Li}]^+$ , and in addition to the Z type fragments, Y type ions are also observed. Furthermore, the presence of an intense peak corresponding to cross-ring cleavage ( $^{2,4}\text{X}_6$  or  $^{0,2}\text{A}_7$ ) is evident (**Figure 7-2b**). High abundances of this ion, as well as the fragment corresponding to water loss can be explained by the involvement of the reducing end of the  $[\text{G}_7+\text{Li}]^+$  in both dissociation channels. However, due to the absence of the reducing end in  $[\beta\text{-CD}+\text{Li}]^+$ , formation of these fragments is inhibited for this precursor.

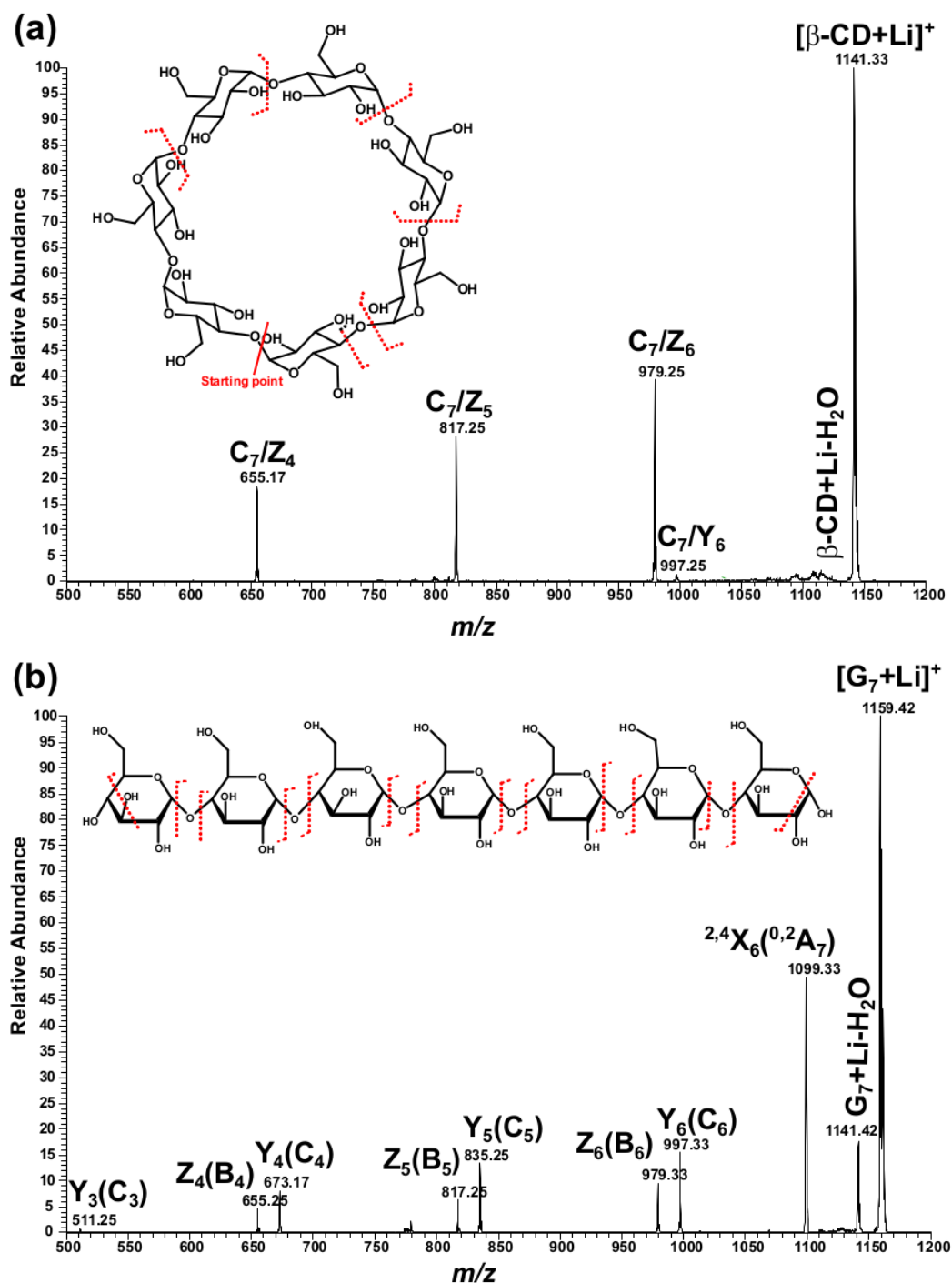


**Figure 7-2-** Low-energy CID spectra of precursor: (a)  $[\beta\text{-CD}+\text{Li}]^+$  obtained with 10 s activation time and excitation voltage of 2.7 V, and (b)  $[\text{G}_7+\text{Li}]^+$  recorded with 10 s activation time and 2.6 V excitation voltage.

It should be noted that because of the symmetric nature of both precursor ions, two or more possibilities exist for formation of the labeled fragments, and it is not straightforward to distinguish between the potential origins. However, this can be accomplished with the help of isotopic labelling,<sup>173</sup> but that is beyond the scope of the current work.

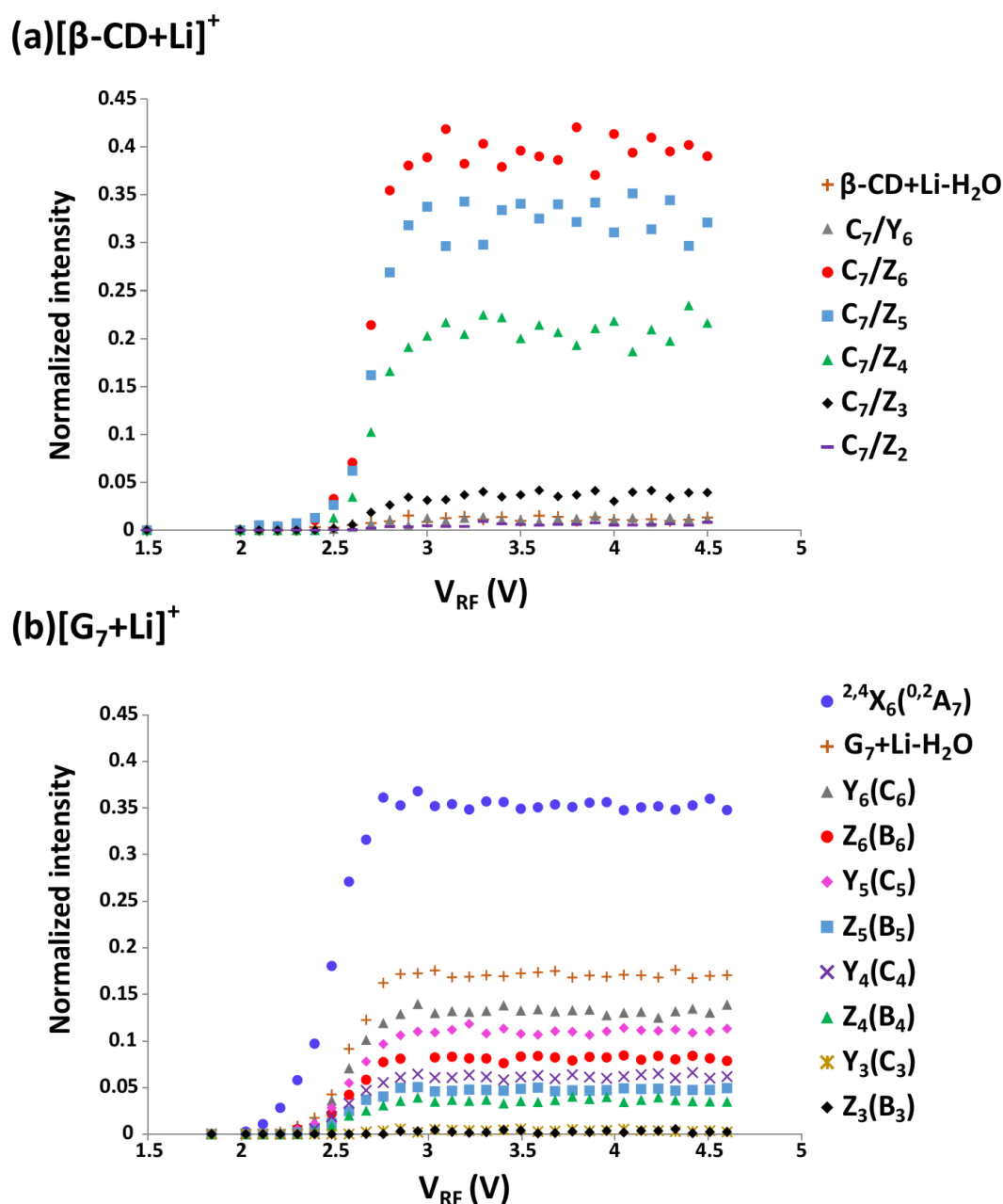


**Figure 7-3-** FECs as a function of excitation voltage at 10 s decomposition time for precursor ions: (a)  $[\beta\text{-CD+Li}]^+$  and (b)  $[\text{G}_7+\text{Li}]^+$ .

Fragmentation efficiency curves (FECs) at a reaction time of 10 s for the decompositions of  $[\beta\text{-CD+Li}]^+$  and  $[\text{G}_7+\text{Li}]^+$  are shown in **Figure 7-3**. From this data, differences in the observed fragments are more obvious. Indeed, if only the most abundant fragments are considered, it can be seen that in the case of  $[\beta\text{-CD+Li}]^+$ , glycosidic bond cleavages are the main processes and Z type ions are the most abundant fragments. Conversely, for  $[\text{G}_7+\text{Li}]^+$ , cross-ring



cleavage ( $^{2,4}\text{X}_6(^{0,2}\text{A}_7)$ ) is the dominant dissociation channel, although loss of water and glycosidic bond cleavages (Y(C) and Z(B) type ions) are also apparent.

The most important point to deduce from the FEC data in **Figure 7-3** is that for both  $[\beta\text{-CD+Li}]^+$  and  $[\text{G}_7+\text{Li}]^+$ , formation of all fragments is occurring in parallel which indicates that under the experimental conditions of low-energy CID, mainly competitive fragmentations are observed. This is due to the low amount of energy deposition on the precursor ions. In addition, unlike other low-energy activation techniques such as BIRD<sup>106,109,184</sup> or thermal decompositions in ion traps,<sup>130,134</sup> in low-energy CID, ions are resonantly excited, and as a consequence, only precursor ions of interest are activated, whereas fragment ions are not recipients of the excitation. Therefore, by knowing that subsequent dissociations of the fragment ions are minimized in the low-energy CID technique, one can readily measure the activation parameters for various dissociation channels provided that the effective temperature of the ions inside the ion trap at each excitation voltage is calibrated.

In 1996, Goeringer and McLuckey<sup>133,132</sup> derived an equation for describing the evolution in effective temperature of ions inside an ion trap as a function of dipolar- single frequency resonant excitation voltage. In Chapter 5, we employed their derived equation to calibrate  $T_{eff}$  of ions in the linear ion trap using a reference H-G complex, H-G<sub>ref</sub>, whose activation parameters had been measured using the BIRD technique (Chapter 4). Equation 5.5 for  $T_{eff}$  of singly charged ions undergoing low-energy CID was obtained:

$$T_{eff} = \frac{1}{2} \left( T_{bath} + \sqrt{(T_{bath})^2 + 4C \times \frac{(m_{gas} + m_{ion})}{m_{ion}} \frac{V_{RF}^2}{(\Omega^{(1,1)})^2}} \right) \quad (5.5)$$

where  $T_{bath}$  is the temperature of the bath gas,  $m_{gas}$  is the mass of the bath gas,  $m_{ion}$  is the mass of the ion,  $C$  is a constant,  $\Omega^{(1,1)}$  is the momentum transfer collision integral and  $V_{RF}$  is the amplitude of the radio frequency excitation voltage. Here, the same approach as was utilized in Chapter 5 has been used to obtain the activation parameters of the lithiated oligosaccharides. First, unimolecular dissociation rate constants ( $k$ ) at each excitation amplitude were measured from the slope of the natural logarithm of the survival yield versus time plots (Equation 1.48, **Figure 7-4a** and **7-5b**). Afterwards, using  $\Omega^{(1,1)}$  values obtained

from ion mobility experiments, the effective temperature of the ions at each excitation amplitude was calculated employing Equation 5.5.

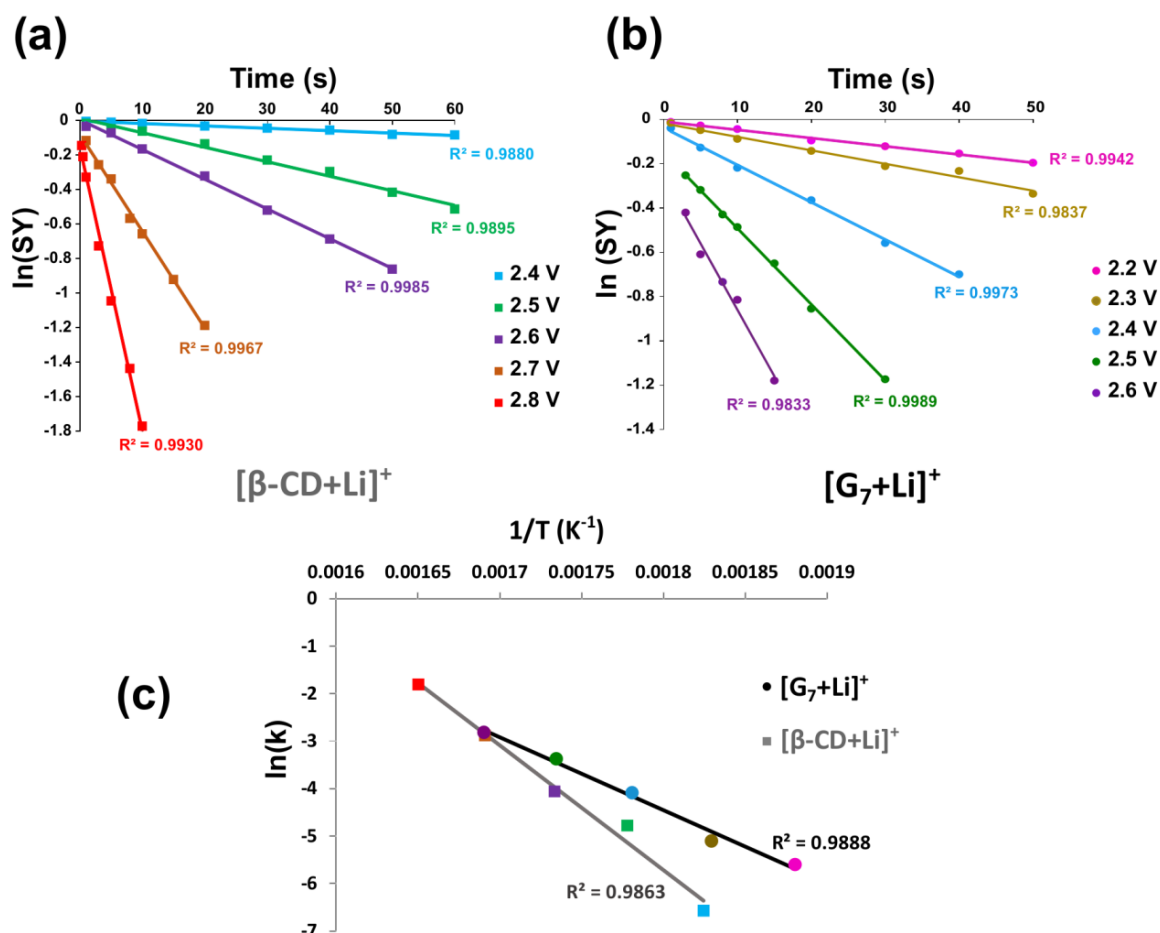


**Figure 7-4-** Kinetic plots for: (a)  $[\beta\text{-CD+Li}]^+$ , and (b)  $[G_7+Li]^+$  precursors as a function of the resonant activation amplitude; (c) Corresponding Arrhenius plots for  $[\beta\text{-CD+Li}]^+$  and  $[G_7+Li]^+$  precursors.

As explained thoroughly in Chapter 5, low-energy CID experiments were performed using helium as the collision gas. Therefore, ideally, collision integrals should be measured using He-based ion mobility mass spectrometers. However, it was previously observed that for various types of compounds with quite large size (sizes similar to the lithiated oligosaccharides investigated in this study) He- and  $N_2$ -based collision cross sections were proportional to each other.<sup>241</sup> According to the data presented in reference 241, the ratio of He-based to  $N_2$ -based CCS values is almost constant ( $\sim 0.75$ ) for various types of compounds (carbohydrates, peptides and lipids).<sup>241</sup> Therefore,  $N_2$ -based CCSs were used for both the reference complex and lithiated sugars, instead of their He-based CCSs. Then, by plotting  $\ln$

( $k$ ) as a function of  $1/T_{eff}$ , Arrhenius plots for dissociation of  $[\beta\text{-CD+Li}]^+$  and  $[\text{G}_7\text{+Li}]^+$  were obtained (**Figure 7-4c**). Finally, the activation energy and pre-exponential factor were obtained from the slope and intercept, respectively, of the Arrhenius plots. Activation parameters of  $E_a = 2.27 (\pm 0.10)$  eV and  $\log A = 18.1 (\pm 1.2)$  for  $[\beta\text{-CD+Li}]^+$ , and  $E_a = 1.32 (\pm 0.09)$  eV and  $\log A = 10.1 (\pm 1.1)$  for  $[\text{G}_7\text{+Li}]^+$ , were found.

Both  $[\beta\text{-CD+Li}]^+$  and  $[\text{G}_7\text{+Li}]^+$  are relatively large molecules ( $m/z$  and number of DOF for  $[\beta\text{-CD+Li}]^+$  are 1141.4 and 438, respectively; and those for  $[\text{G}_7\text{+Li}]^+$  are 1159.4 and 447, respectively). Klassen and co-workers<sup>158</sup> performed BIRD experiments on some *protonated* oligosaccharides, and among them was protonated maltoheptaose. They obtained an  $E_a = 0.84 (\pm 0.03)$  eV and  $\log A = 10.3 (\pm 0.5)$  for this ion. By comparison with the study performed by Price and Williams,<sup>112</sup> they reasoned that protonated maltoheptaose is in a thermal equilibrium regime. In low-energy CID, due to the presence of collisions, it is even easier to be in rapid energy exchange limit conditions compared to the BIRD technique (no collisions). Therefore, it can be expected that both  $[\beta\text{-CD+Li}]^+$  and  $[\text{G}_7\text{+Li}]^+$  fulfill the conditions of the REX limit, and as a consequence, observed activation parameters are expected to be equal to the characteristic values at the high pressure limit.<sup>112</sup> It should be noted that we tried to perform low-energy CID experiments on protonated  $\text{G}_7$  and protonated  $\beta\text{-CD}$  as well. But because of the very low abundance of these precursor ions, it was not possible to obtain linear kinetic plots for their dissociation.

As discussed earlier, under the experimental conditions of low-energy CID, only competitive fragment ions were observed for both  $[\beta\text{-CD+Li}]^+$  and  $[\text{G}_7\text{+Li}]^+$  (**Figure 7-3**). Therefore, the activation parameters for individual fragmentation channels can be obtained as follows: for the precursor ions, the total dissociation rate constant ( $k_{total}$ ) is equal to the sum of the rate constants for the individual fragmentation channels:<sup>196</sup>

$$k_{total} = k_1 + k_2 + \dots \quad (7.1)$$

where  $k_1$  and  $k_2$  are rate constants for the first and second dissociation channels, respectively. Furthermore, the relative abundance of fragment ions is equal to their corresponding relative formation rate constants:

$$\frac{[F_i]}{[F_j]} = \frac{k_i}{k_j} \quad (7.2)$$

where  $[F_i]$  and  $[F_j]$  are abundances of fragment number  $i$  and fragment number  $j$ , respectively. As an example, for the formation rate constant of the fragment ion resulting from water loss from  $[\beta\text{-CD+Li}]^+$ ,  $k_{H_2O}$ , the procedure is as follows: the total rate constant is given by:

$$k_{total} = k_{H_2O} + k_{C_7/Y_6} + k_{C_7/Z_6} + k_{C_7/Z_5} + k_{C_7/Z_4} + k_{C_7/Z_3} + k_{C_7/Z_2} \quad (7.3)$$

In addition, for the relative formation rate constants, we have:

$$\frac{[H_2O]}{[C_7/Y_6]} = \frac{k_{H_2O}}{k_{C_7/Y_6}} \quad (7.4)$$

$$\frac{[H_2O]}{[C_7/Z_6]} = \frac{k_{H_2O}}{k_{C_7/Z_6}} \quad (7.5)$$

⋮

Replacement of the individual rate constants ( $k_{C_7/Y_6}$ ,  $k_{C_7/Z_6}$ , ...) from Equations 7.4, 7.5, ... in Equation 7.3, and then solving for  $k_{H_2O}$  results in:

$$k_{H_2O} = \frac{k_{total} \times [H_2O]}{[H_2O] + [C_7/Y_6] + [C_7/Z_6] + [C_7/Z_5] + [C_7/Z_4] + [C_7/Z_3] + [C_7/Z_2]} \quad (7.6)$$

The same procedure was applied to all other fragments to calculate the rate constants for the different dissociation pathways of  $[\beta\text{-CD+Li}]^+$  and  $[G_7+Li]^+$  at different effective temperatures. Afterwards, the corresponding Arrhenius plots were constructed (**Figure 7-5**), and activation parameters were obtained for each dissociation channel (**Table 7-1**).

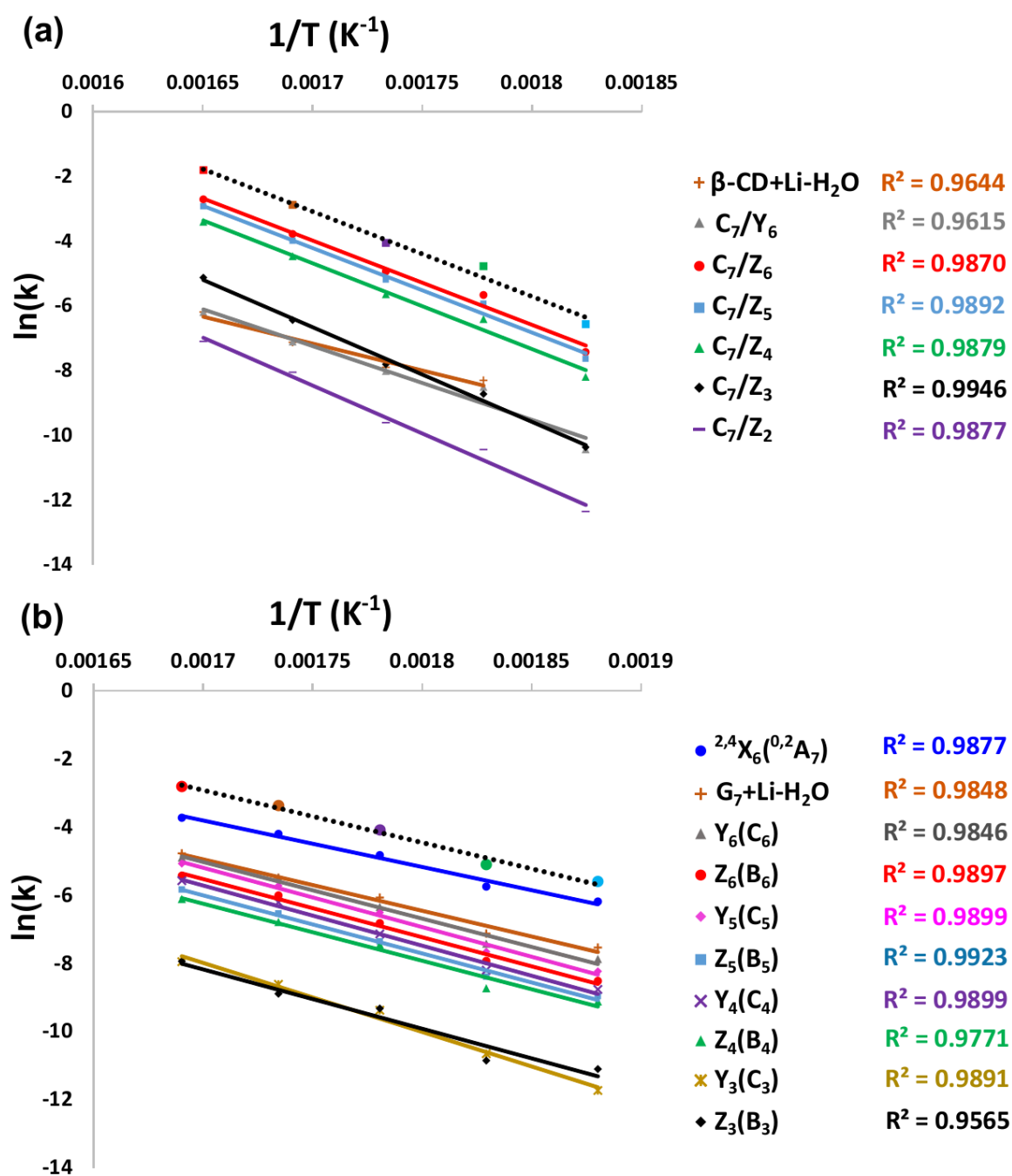


Figure 7-5- Arrhenius plots for dissociation channels of: (a)  $[\beta\text{-CD+Li}]^+$  and, (b)  $[\text{G}_7+\text{Li}]^+$ .

**Table 7-1-** Activation parameters for dissociation channels of  $[\beta\text{-CD+Li}]^+$  and  $[\text{G}_7\text{+Li}]^+$ .

$[\beta\text{-CD+Li}]^+$			$[\text{G}_7\text{+Li}]^+$		
Pathway	$E_a$ (eV)	$\log A$	Pathway	$E_a$ (eV)	$\log A$
$[\beta\text{-CD+Li}]^+$	2.27 ( $\pm 0.10$ )	18.1 ( $\pm 1.2$ )	$[\text{G}_7\text{+Li}]^+$	1.32 ( $\pm 0.09$ )	10.1 ( $\pm 1.1$ )
$\beta\text{-CD+Li-H}_2\text{O}$	1.44 ( $\pm 0.15$ )	9.2 ( $\pm 1.5$ )	$\text{G}_7\text{+Li-H}_2\text{O}$	1.30 ( $\pm 0.09$ )	9.0 ( $\pm 1.1$ )
$\text{C}_7/\text{Y}_6$	1.97 ( $\pm 0.18$ )	13.7 ( $\pm 1.8$ )	${}^{2,4}\text{X}_6({}^{0,2}\text{A}_7)$	1.18 ( $\pm 0.09$ )	8.4 ( $\pm 1.1$ )
$\text{C}_7/\text{Z}_6$	2.25 ( $\pm 0.10$ )	17.5 ( $\pm 1.2$ )	$\text{Y}_6(\text{C}_6)$	1.43 ( $\pm 0.10$ )	10.1 ( $\pm 1.2$ )
$\text{C}_7/\text{Z}_5$	2.25 ( $\pm 0.10$ )	17.5 ( $\pm 1.2$ )	$\text{Z}_6(\text{B}_6)$	1.47 ( $\pm 0.09$ )	10.2 ( $\pm 1.1$ )
$\text{C}_7/\text{Z}_4$	2.29 ( $\pm 0.10$ )	17.6 ( $\pm 1.2$ )	$\text{Y}_5(\text{C}_5)$	1.50 ( $\pm 0.09$ )	10.6 ( $\pm 1.1$ )
$\text{C}_7/\text{Z}_3$	2.53 ( $\pm 0.10$ )	18.8 ( $\pm 1.2$ )	$\text{Z}_5(\text{B}_5)$	1.47 ( $\pm 0.09$ )	10.0 ( $\pm 1.1$ )
$\text{C}_7/\text{Z}_2$	2.56 ( $\pm 0.10$ )	18.2 ( $\pm 1.2$ )	$\text{Y}_4(\text{C}_4)$	1.52 ( $\pm 0.09$ )	10.5 ( $\pm 1.1$ )
			$\text{Z}_4(\text{B}_4)$	1.44 ( $\pm 0.13$ )	9.7 ( $\pm 1.4$ )
			$\text{Y}_3(\text{C}_3)$	1.75 ( $\pm 0.11$ )	11.5 ( $\pm 1.3$ )
			$\text{Z}_3(\text{B}_3)$	1.50 ( $\pm 0.22$ )	9.3 ( $\pm 2.0$ )

Some interesting points are perceptible in considering the activation parameters obtained for two lithiated oligosaccharides and their dissociation channels. While both  $[\beta\text{-CD+Li}]^+$  and  $[\text{G}_7\text{+Li}]^+$  are similar to each other from different points of view such as  $m/z$ , collision integral, range of excitation amplitude for dissociation, and their chemical nature, very different fragmentation patterns, pre-exponential factors, and activation energies were obtained for them. For the dissociation of  $[\beta\text{-CD+Li}]^+$ , which mainly involves glycosidic bond cleavages, quite large  $E_a$  and  $A$  values for different channels have been observed implying a loose transition state for these dissociation pathways. A very minor fragment ion resulting from loss of water is also observed for  $[\beta\text{-CD+Li}]^+$  whose activation parameters are associated with large uncertainties due to its low abundance. However, a pre-exponential factor of  $10^{9.2}$  shows a fairly tight transition state for this pathway. For  $[\text{G}_7\text{+Li}]^+$ , however,  $E_a$  and  $A$  were smaller than those of  $[\beta\text{-CD+Li}]^+$ . This result could be anticipated from the fragmentation spectrum (**Figure 7-2b**) of the  $[\text{G}_7\text{+Li}]^+$  precursor that exhibits a dominant fragment resulting

from cross-ring cleavage ( $^{2,4}X_6(^{0,2}A_7)$ ) and also an intense peak corresponding to the loss of water. For  $[G_7+Li]^+$ , pre-exponential factors of  $10^{8.4}$  for  $^{2,4}X_6(^{0,2}A_7)$ ,  $10^{9.0}$  for water loss and  $\sim 10^{10}$  for all other dissociation channels were observed. The relatively low values obtained for all of these  $A$  factors are characteristic of entropically disfavored dissociation reactions, and are in agreement with previously proposed dissociation mechanisms involving rearrangements.<sup>161,167,288,289</sup> For example, in 2016, Rabus and co-workers,<sup>161</sup> proposed that B and Y type fragments from both protonated and sodiated oligosaccharides are formed via a similar pathway including protonation of a glycosidic oxygen followed by dissociation of that glycosidic bond. This is consistent with the observation of very similar pre-exponential factors for  $[G_7+Li]^+$  (measured using low-energy CID in this work) and  $[G_7+H]^+$  (obtained using BIRD technique<sup>158</sup>).

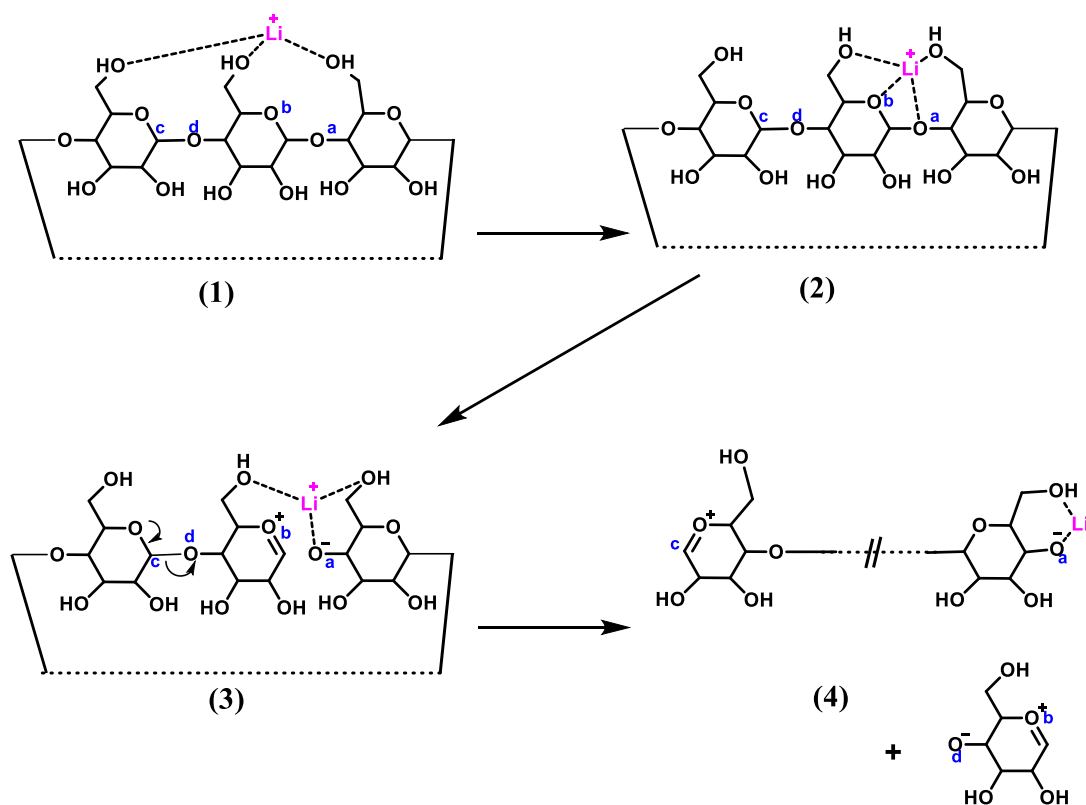


**Figure 7-6-** First proposed mechanism for glycosidic bond cleavage for lithiated  $\beta$ -CD.

The observed pre-exponential factor for  $[\beta\text{-CD}+Li]^+$  is surprisingly large. A  $\log A$  of 18.1 shows that the fragmentation pathway of lithiated  $\beta$ -CD is different from that of the metal adducted linear oligosaccharide. According to the DFT-optimized structure of this ion, appearing in a previously published paper,<sup>281</sup>  $Li^+$  is coordinated with three primary (C6)

hydroxyl groups of the upper rim of the  $\beta$ -CD. Two mechanisms can be proposed for the glycosidic dissociation of  $[\beta\text{-CD}+\text{Li}]^+$ , depicted in **Figure 7-6** and **Figure 7-7**.

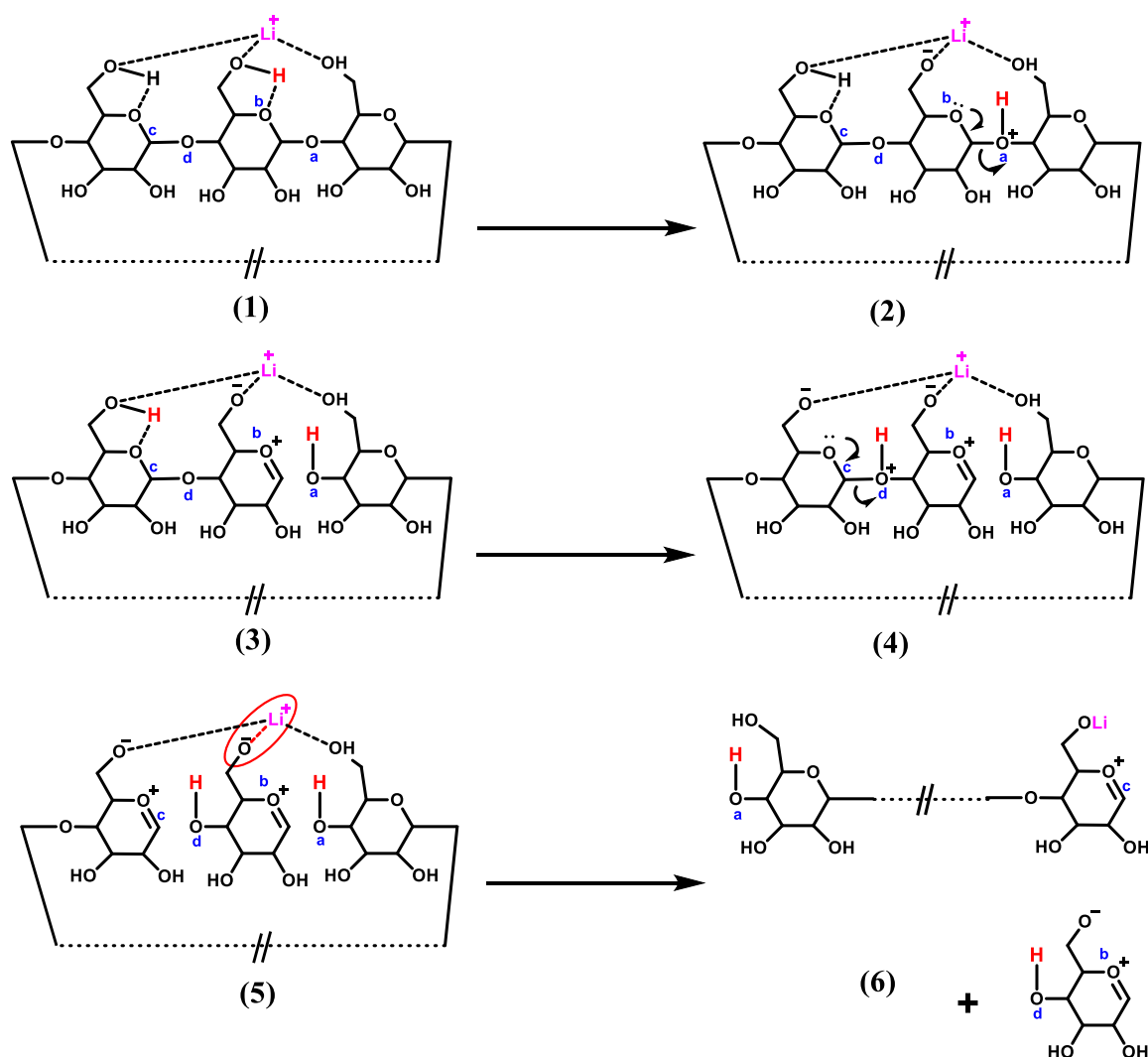


**Figure 7-7-** Second proposed mechanism for glycosidic bond cleavage for lithiated  $\beta$ -CD.

In the first mechanism (**Figure 7-6**), when the energy-minimized  $[\beta\text{-CD}+\text{Li}]^+$  (structure 1) is collisionally activated,  $\text{Li}^+$  can disengage from at least one hydroxyl group and move towards the ring and glycosidic oxygens (structure 2). Afterwards, in the next step, glycosidic bond cleavage occurs and structure 3 is formed which further undergoes glycosidic dissociation to produce fragment ions.

According to the second proposed mechanism (**Figure 7-7**), the presence of  $\text{Li}^+$  facilitates the proton transfers to the glycosidic oxygens followed by glycosidic bond cleavages. Then, in the final step, which has the highest activation barrier, the small neutral is lost by breakage



of the strong Li-O bond. Although comprehensive information pertaining to the decomposition mechanism of lithiated  $\beta$ -CD could be gleaned from extensive computational chemistry studies, isotope labeling experiments, and/or regioselective functionalization of the various hydroxyl groups, it is beyond the scope of the current study.

## Conclusion

In this study, a first comparative investigation of the dissociation of lithiated  $\beta$ -CD and lithiated  $G_7$  in the gas phase using low-energy CID was presented. Dissimilar fragmentation spectra were observed for these oligosaccharides (cyclic and linear 7-mers) implying that their fragmentation pathways are not the same. The fragmentation efficiency curves showed that by increasing the collision energy, none of the fragment ions is produced by sequential fragmentation of the preliminary fragments in low-energy CID experiments. This ensures that activation parameters of the individual dissociation pathways can be measured in a single set of kinetic experiments performed at different excitation amplitudes, provided that a reliable technique is used to calibrate the effective temperature of the ions inside the ion trap. Thus, by employing the technique presented in Chapter 5, the  $T_{eff}$  values of ions were obtained at different excitation amplitudes, and then Arrhenius plots were constructed for the total and individual dissociation pathways. In this manner, activation energies and pre-exponential factors for all the fragmentation channels of each oligosaccharide were obtained. Despite the very similar chemical nature of the two oligosaccharides, very different activation parameters were derived for them. This clearly shows that, unlike linear oligosaccharides, the dissociation of lithiated  $\beta$ -CD goes through an entropically favorable pathway with a high activation barrier.

---

## ***General conclusion***

---

One of the main objectives of this work was to study the energetics of dissociation of different H-G systems using various tandem mass spectrometry techniques including BIRD, low-energy CID, CID and HCD. Among these techniques, BIRD is one of the most established ones that can directly give activation parameters, provided that the precursor ions are able to produce enough fragment ions in the accessible temperature range in the BIRD set-up, and also they fulfill REX limit condition. Among all the H-G complexes in this study, only one of them was amenable for BIRD technique. Therefore, we decided to employ other fragmentation techniques for obtaining bond dissociation energies of H-G complexes. In addition, we took the advantage of BIRD experiments on H-G<sub>ref</sub> for calibration of effective temperature of the ions undergoing low-energy CID, and characteristic temperature of ions which are subjected to the CID fragmentation.

Low-energy CID technique potentially is one of the most appealing tandem mass spectrometry techniques in providing both activation energy and pre-exponential factor for dissociation of molecular ions fulfilling the REX condition. This technique was performed on H-G complexes consisting of a hemicryptophane with a heteroditopic character as host, and some biologically relevant molecules as guest. The relatively long residence time of the ions inside the linear ion trap allowed studying reactions with low dissociation rates. This possibility, as well as the large size of the H-G complexes under study, ensured the fulfillment of REX conditions, and as a consequence, accurate application of the Arrhenius equation. This technique allowed access to the higher effective temperature required to probe dissociation of the complexes which were not sufficiently fragile to be fragmented within the practical temperature range of our BIRD set-up.

Low-energy CID was also employed for investigation of dissociation of lithiated  $\beta$ -CD and lithiated G<sub>7</sub> in the gas phase. Fragmentation efficiency curves obtained using low-energy CID for these ions showed that probability of consecutive fragmentation is minimized in the low-energy CID experimental condition. This was because of two reasons: 1) very low amount of deposited energy on the precursor ions, which leads fragment ions not to have enough energy to undergo dissociation, and 2) resonant excitation in low-energy CID which leads to excitation of only the precursor ion and not the fragments. Therefore, in the

absence of sequential fragmentation, activation parameters for individual dissociation pathways of the lithiated oligosaccharides were measured with only one set of kinetic experiments at different excitation amplitudes. One interesting point about this study was that in spite of very similar chemical nature of the two oligosaccharides, very different activation parameters were observed for their dissociation. The obtained results showed that cyclic structure of the lithiated  $\beta$ -CD leads its dissociation to go through an entropically more favorable pathway with a higher activation barrier.

Two next employed fragmentation techniques for studying the energetics of H-G complexes were CID and HCD, both in combination with RRKM modeling. Using either of these techniques, it was required to have information about the entropy of decomposition. HCD experiments were performed on exactly the same H-G complexes that were studied by low-energy CID, and hence, for RRKM modeling of *SY* curves, the pre-exponential factors obtained using low-energy CID technique were employed. CID experiments were performed on six H-G complexes that were characterized with very similar size and types of interactions. For this reason, the pre-exponential factor obtained using BIRD technique for one of them, was used for RRKM modeling of the *SY* curves. It should be noted that performing low-energy CID experiments on this latter H-G complexes was not possible due to the LMCO limitation.

Next objective of this thesis was examination of the capabilities of low-energy CID, CID and HCD techniques for structural analysis of carbohydrates. Comparing the spectra obtained using three techniques showed that, generally, when working with mono-lithiated sugars, CID spectra provided more structurally informative fragments, and glycosidic bond cleavage was the main pathway. However, when working with di-lithiated sugars, HCD spectra could be more informative providing predominately cross-ring cleavage fragments. This was because HCD is a non-resonant activation technique and it allows a higher amount of energy to be deposited in a short time, giving access to more endothermic decomposition pathways as well as consecutive fragmentations. The difference in preferred dissociation pathways of mono-lithiated and di-lithiated sugars indicated that the presence of the second lithium

strongly influences the relative rate constants for cross-ring cleavages (rearrangement) vs. direct glycosidic bond cleavages, and disfavors the latter.

Finally, using CID and HCD, dissolution mechanisms of oligosaccharides in DMAc/LiCl was explored. Different studies in the solution phase offer a coherent picture of the dissolution mechanism of cellulose, with the only discrepancy between the proposed mechanisms being the point about the presence or absence of a direct interaction between  $\text{Li}^+$  and the sugar. CID and HCD experiments on di-lithiated and tri-lithiated sugars revealed that intensities of product ions containing two  $\text{Li}^+$  or three  $\text{Li}^+$ , respectively, were higher than those bearing only one  $\text{Li}^+$ . In addition, comparing the fragmentation spectra of LiCl adducted lithiated sugar and NaCl adducted sodiated sugar shows that while, in the latter case, loss of NaCl is dominant, in the former case, loss of HCl occurs preferentially. The compiled evidence implies that there is a strong and direct interaction between lithium and the saccharide during the dissolution process in the DMAc/LiCl solvent system.

---

## *References*

---

1. Lehn, J.-M. *Supramolecular chemistry*. (Weinheim, 1995).
2. Vincenti, M. Host–guest chemistry in the mass spectrometer. *J. Mass Spectrom.* **30**, 925–939 (1995).
3. Yamashita, M. & Fenn, J. B. Electrospray ion source. Another variation on the free-jet theme. *J. Phys. Chem.* **88**, 4451–4459 (1984).
4. Fenn, J. B., Mann, M., Meng, C. K., Wong, S. F. & Whitehouse, C. M. Electrospray ionization for mass spectrometry of large biomolecules. *Science (80-. )*. **246**, 64–71 (1989).
5. Fenn, J. B., Mann, M., Meng, C. K., Wong, S. F. & Whitehouse, C. M. Electrospray ionization-principles and practice. *Mass Spectrom. Rev.* **9**, 37–70 (1990).
6. Hillenkamp, F., Karas, M., Beavis, R. C. & Chait, B. T. Matrix-assisted laser desorption/ionization mass spectrometry of biopolymers. *Anal. Chem.* **63**, 1193A–1203A (1991).
7. Karas, M., Bahr, U. & Hillenkamp, F. UV laser matrix desorption/ionization mass spectrometry of proteins in the 100 000 dalton range. *Int. J. Mass Spectrom. Ion Process.* **92**, 231–242 (1989).
8. Schalley, C. A. Supramolecular chemistry goes gas phase: The mass spectrometric examination of noncovalent interactions in host-guest chemistry and molecular recognition. *Int. J. Mass Spectrom.* **194**, 11–39 (2000).
9. Szente, L. & Szemán, J. Cyclodextrins in analytical chemistry: Host-guest type molecular recognition. *Anal. Chem.* **85**, 8024–8030 (2013).
10. Harada, A., Kobayashi, R., Takashima, Y., Hashidzume, A. & Yamaguchi, H. Macroscopic self-assembly through molecular recognition. *Nat. Chem.* **3**, 34–37 (2011).
11. Yu, G., Jie, K. & Huang, F. Supramolecular amphiphiles based on host–guest molecular recognition motifs. *Chem. Rev.* **115**, 7240–7303 (2015).
12. Hu, Q.-D., Tang, G.-P. & Chu, P. K. Cyclodextrin-based host–guest supramolecular nanoparticles for delivery: from design to applications. *Acc. Chem. Res.* **47**, 2017–2025 (2014).
13. Zhang, J., Sun, H. & Ma, P. X. Host–guest interaction mediated polymeric assemblies: multifunctional nanoparticles for drug and gene delivery. *ACS Nano* **4**, 1049–1059 (2010).
14. Zan, M., Li, J., Luo, S. & Ge, Z. Dual pH-triggered multistage drug delivery systems

- based on host–guest interaction-associated polymeric nanogels. *Chem. Commun.* **50**, 7824–7827 (2014).
15. Dennis M. Vriezema *et al.* Self-assembled nanoreactors. *Chem. Rev.* **105**, 1445–1490 (2005).
  16. Mirabaud, A., Mulatier, J.-C., Martinez, A., Dutasta, J.-P. & Dufaud, V. Merging host-guest chemistry and organocatalysis for the chemical valorization of CO<sub>2</sub>. *Catal. Today* **281**, 387–391 (2017).
  17. Bolliger, J. L., Belenguer, A. M. & Nitschke, J. R. Enantiopure water-soluble [Fe<sub>4</sub>L<sub>6</sub>] cages: host-guest chemistry and catalytic activity. *Angew. Chemie Int. Ed.* **52**, 7958–7962 (2013).
  18. Zhang, M., Ma, W. J., He, C. T., Jiang, L. & Lu, T. B. Highly selective recognition and fluorescence imaging of adenosine polyphosphates in aqueous solution. *Inorg. Chem.* **52**, 4873–4879 (2013).
  19. Soylemez, S. *et al.* A novel and effective surface design: conducting polymer/ $\beta$ -cyclodextrin host–guest system for cholesterol biosensor. *ACS Appl. Mater. Interfaces* **6**, 18290–18300 (2014).
  20. Xie, S., Zhang, J., Yuan, Y., Chai, Y. & Yuan, R. An electrochemical peptide cleavage-based biosensor for prostate specific antigen detection via host–guest interaction between ferrocene and  $\beta$ -cyclodextrin. *Chem. Commun.* **51**, 3387–3390 (2015).
  21. Rudkevich, D. M. & Leontiev, A. V. Molecular encapsulation of gases. *Aust. J. Chem.* **57**, 713–722 (2004).
  22. Kosaka, W., Yamagishi, K., Zhang, J. & Miyasaka, H. Gate-opening gas adsorption and host–guest interacting gas trapping behavior of porous coordination polymers under applied AC electric fields. *J. Am. Chem. Soc.* **136**, 12304–12313 (2014).
  23. Zheng, B., Wang, F., Dong, S. & Huang, F. TUTORIAL REVIEW Chemical Society Reviews Supramolecular polymers constructed by crown ether-based molecular recognition. *Chem. Soc. Rev. Chem. Soc. Rev.* **41**, 1621–1636 (2012).
  24. Gokel, G. W. Crown ethers and cryptands: monographs in supramolecular chemistry. *Stoddart, JF Ed* (1991).
  25. Rebilly, J.-N., Colasson, B., Bistri, O., Over, D. & Reinaud, O. Biomimetic cavity-based metal complexes. *Chem. Soc. Rev.* **44**, 467–489 (2015).
  26. Guo, D. S. & Liu, Y. Supramolecular chemistry of p -Sulfonatocalix[ n ]arenes and its biological applications. *Acc. Chem. Res.* **47**, 1925–1934 (2014).



27. Kobayashi, K. & Yamanaka, M. Self-assembled capsules based on tetrafunctionalized calix[4]resorcinarene cavitands. *Chem. Soc. Rev.* **44**, 449–466 (2015).
28. Pochorovski, I. & Diederich, F. Development of redox-switchable resorcin[4]arene cavitands. *Acc. Chem. Res.* **47**, 2096–2105 (2014).
29. Kaifer, A. E. Toward reversible control of cucurbit[n]uril complexes. *Acc. Chem. Res.* **47**, 2160–7 (2014).
30. Isaacs, L. Stimuli responsive systems constructed using cucurbit[ n ]uril-type molecular containers. *Acc. Chem. Res.* **47**, 2052–2062 (2014).
31. Crini, G. Review: A history of cyclodextrins. *Chemical Reviews* **114**, 10940–10975 (2014).
32. Engeldinger, E., Armspach, D. & Matt, D. Capped cyclodextrins. *Chem. Rev.* **103**, 4147–4173 (2003).
33. Xue, M., Yang, Y., Chi, X., Zhang, Z. & Huang, F. Pillararenes, a new class of macrocycles for supramolecular chemistry. *Acc. Chem. Res.* **45**, 1294–1308 (2012).
34. Ogoshi, T. Synthesis of novel pillar-shaped cavitands ‘Pillar[5]arenes’ and their application for supramolecular materials. *J. Incl. Phenom. Macrocycl. Chem.* **72**, 247–262 (2012).
35. Gabard, J. & Collet, A. Synthesis of a (D<sub>3</sub>)-bis(cyclotrimeratrylenyl) macrocage by stereospecific replication of a (C<sub>3</sub>)-subunit. *J. Chem. Soc. Chem. Commun.* 1137–1139 (1981).
36. Collet, A. *In comprehensive supramolecular chemistry*. **2**, (1996).
37. Brotin, T. & Dutasta, J.-P. Cryptophanes and their complexes—present and future. *Chem. Rev.* **109**, 88–130 (2009).
38. Zhang, D., Martinez, A. & Dutasta, J.-P. Emergence of hemicryptophanes: from synthesis to applications for recognition, molecular machines, and supramolecular catalysis. *Chem. Rev.* **117**, 4900–4942 (2017).
39. Collet, A. Cyclotrimeratrylenes and cryptophanes. *Tetrahedron* **43**, 5725–5759 (1987).
40. Gosse, I., Dutasta, J.-P., Perrin, M. & Thozet, A. A thiophosphorylated hemicryptophane: structure of the toluene inclusion complex. *New J. Chem.* **23**, 545–548 (1999).
41. Raytchev, P. D., Perraud, O., Aronica, C., Martinez, A. & Dutasta, J.-P. A new class of C<sub>3</sub>-symmetrical hemicryptophane hosts: triamide- and tren-hemicryptophanes. *J. Org.*

- Chem.* **75**, 2099–2102 (2010).
42. Perraud, O., Robert, V., Gornitzka, H., Martinez, A. & Dutasta, J. P. Combined cation– $\pi$  and anion– $\pi$  interactions for zwitterion recognition. *Angew. Chemie - Int. Ed.* **51**, 504–508 (2012).
  43. Makita, Y. *et al.* Zinc(II)-included hemicryptophane: coordination of an acetonitrile guest within the cavity. *Supramol. Chem.* **23**, 269–272 (2011).
  44. Makita, Y. *et al.* A Zinc(II)-included hemicryptophane: facile synthesis, characterization, and catalytic activity. *Inorg. Chem.* **49**, 7220–7222 (2010).
  45. Makita, Y. *et al.* A tri-aromatic amide hemicryptophane host: synthesis and acetylcholine binding. *Tetrahedron Lett.* **57**, 5112–5115 (2016).
  46. Kim, S. G., Kim, K. H., Jung, J., Shin, S. K. & Ahn, K. H. Unprecedented chiral molecular recognition in a  $C_3$ -symmetric environment. *J. Am. Chem. Soc.* **124**, 591–596 (2002).
  47. Moberg, C. Can  $C_3$ -Symmetric Receptors differentiate enantiomers? *Angew. Chemie Int. Ed.* **45**, 4721–4723 (2006).
  48. Canceill, J., Collet, A., Gabard, J., Kotzyba-Hibert, F. & Lehn, J.-M. Speleands. Macropolycyclic receptor cages based on binding and shaping sub-units. Synthesis and properties of macrocycle cyclotrimeratrylene combinations. Preliminary communication. *Helv. Chim. Acta* **65**, 1894–1897 (1982).
  49. Perraud, O., Lefevre, S., Robert, V., Martinez, A. & Dutasta, J.-P. Hemicryptophane host as efficient primary alkylammonium ion receptor. *Org. Biomol. Chem.* **10**, 1056–1059 (2012).
  50. Schmitt, A., Robert, V., Dutasta, J. & Martinez, A. Synthesis of the first water-soluble hemicryptophane host: selective recognition of choline in aqueous medium. *Org. Lett.* **16**, 2374–2377 (2014).
  51. Schmitt, A., Chatelet, B., Collin, S., Dutasta, J.-P. & Martinez, A. Chiral discrimination of Ammonium neurotransmitters by  $C_3$ -symmetric enantiopure hemicryptophane hosts. *Chirality* **25**, 475–479 (2013).
  52. Lefevre, S. *et al.* Large-scale synthesis of enantiopure molecular cages: chiroptical and recognition properties. *Chem. - A Eur. J.* **22**, 2068–2074 (2016).
  53. Le Gac, S. & Jabin, I. Synthesis and study of calix[6]cryptamides: a new class of heteroditopic receptors that display versatile host–guest properties toward neutral species and organic associated ion-pair salts. *Chem. - A Eur. J.* **14**, 548–557 (2008).
  54. Perraud, O., Robert, V., Martinez, A. & Dutasta, J. P. The cooperative effect in ion-pair

- recognition by a ditopic hemicyptophane host. *Chem. - A Eur. J.* **17**, 4177–4182 (2011).
55. Zhang, D. *et al.* Insights into the complexity of weak intermolecular interactions interfering in host-guest systems. *ChemPhysChem* **16**, 2931–2935 (2015).
56. Perraud, O., Robert, V., Martinez, A. & Dutasta, J.-P. A designed cavity for zwitterionic species: selective recognition of taurine in aqueous media. *Chem. - A Eur. J.* **17**, 13405–13408 (2011).
57. Dawei, Z. *et al.* A fluorescent heteroditopic hemicyptophane cage for the selective recognition of choline phosphate. *Chem. Commun.* **51**, 2679–2682 (2015).
58. Cochrane, J. R., Schmitt, A., Wille, U. & Hutton, C. a. Synthesis of cyclic peptide hemicyptophanes: enantioselective recognition of a chiral zwitterionic guest. *Chem. Commun. (Camb)*. **49**, 8504–8506 (2013).
59. Perraud, O., Martinez, A. & Dutasta, J.-P. Exclusive enantioselective recognition of glucopyranosides by inherently chiral hemicyptophanes. *Chem. Commun. (Camb)*. **47**, 5861–5863 (2011).
60. Zhang, D. *et al.* Helical, axial, and central chirality combined in a single cage: synthesis, absolute configuration, and recognition properties. *Chem. - A Eur. J.* **22**, 8038–8042 (2016).
61. Schmitt, A. *et al.* Improved hemicyptophane hosts for the stereoselective recognition of glucopyranosides. *Org. Biomol. Chem.* **12**, 4211–4217 (2014).
62. Schmitt, A. *et al.* Diastereoselective recognition of  $\alpha$ -mannoside by hemicyptophane receptors. *New J. Chem.* **39**, 1749–1753 (2015).
63. Wang, L., Wang, G.-T., Zhao, X., Jiang, X.-K. & Li, Z.-T. Hydrogen bonding-directed quantitative self-assembly of cyclotrimeratrylene capsules and their encapsulation of C<sub>60</sub> and C<sub>70</sub>. *J. Org. Chem.* **76**, 3531–3535 (2011).
64. Busch, K., Glish, G. & McLuckey, S. Mass spectrometry/mass spectrometry: Techniques and application of. (1988).
65. Shukla, A. K. & Futrell, J. H. Tandem mass spectrometry: Dissociation of ions by collisional activation. *J. Mass Spectrom.* **35**, 1069–1090 (2000).
66. Kebarle, P. & Verkerk, U. H. Electrospray: From ions in solution to ions in the gas phase, what we know now. *Mass Spectrom. Rev.* **28**, 898–917 (2009).
67. Halliday, D., Resnick, R. & Krane, K. S. *Physics*. (Wiley, 1992).

68. Konermann, L., Ahadi, E., Rodriguez, A. D. & Vahidi, S. Unraveling the mechanism of electrospray ionization. *Anal. Chem.* **85**, 2–9 (2013).
69. Ahadi, E. & Konermann, L. Surface charge of electrosprayed water nanodroplets: A molecular dynamics study. *J. Am. Chem. Soc.* **132**, 11270–11277 (2010).
70. Iribarne, J. V. & Thomson, B. A. On the evaporation of small ions from charged droplets. *J. Chem. Phys.* **64**, 2287–2294 (1976).
71. Thomson, B. A. & Iribarne, J. V. Field induced ion evaporation from liquid surfaces at atmospheric pressure. *J. Chem. Phys.* **71**, 4451–4463 (1979).
72. Ahadi, E. & Konermann, L. Ejection of solvated ions from electrosprayed methanol/water nanodroplets studied by molecular dynamics simulations. *J. Am. Chem. Soc.* **133**, 9354–9363 (2011).
73. Dole, M. *et al.* Molecular beams of macroions. *J. Chem. Phys.* **49**, 2240–2249 (1968).
74. Winger, B. E., Light-Wahl, K. J., Ogorzalek Loo, R. R., Udseth, H. R. & Smith, R. D. Observation and implications of high mass-to-charge ratio ions from electrospray ionization mass spectrometry. *J. Am. Soc. Mass Spectrom.* **4**, 536–545 (1993).
75. Fernandez de la Mora, J. Electrospray ionization of large multiply charged species proceeds via Dole's charged residue mechanism. *Anal. Chim. Acta* **406**, 93–104 (2000).
76. Ahadi, E. & Konermann, L. Modeling the behavior of coarse-grained polymer chains in charged water droplets: implications for the mechanism of electrospray ionization. *J. Phys. Chem. B* **116**, 104–112 (2012).
77. Konermann, L., Rodriguez, A. D. & Liu, J. On the formation of highly charged gaseous ions from unfolded proteins by electrospray ionization. *Anal. Chem.* **84**, 6798–6804 (2012).
78. Chung, J. K. & Consta, S. Release mechanisms of poly(ethylene glycol) macroions from aqueous charged nanodroplets. *J. Phys. Chem. B* **116**, 5777–5785 (2012).
79. Lindemann, F. A. Discussion on "the radiation theory of chemical action". *Trans. Faraday Soc.* **17**, 598–606 (1922).
80. Hinshelwood, C. N. On the theory of unimolecular reactions. *Proc. R. Soc. London. Ser. A* **113**, 230–233 (1926).
81. Rice, O. K. & Ramsperger, H. C. Theories of unimolecular gas reactions at low pressures. *J. Am. Chem. Soc.* **49**, 1617–1629 (1927).
82. Rice, O. K. & Ramsperger, H. C. Theories of unimolecular gas reactions at low

- pressures. II. *J. Am. Chem. Soc.* **50**, 617–620 (1928).
83. Kassel, L. S. Studies in homogeneous gas reactions. I. *J. Phys. Chem.* **32**, 225–242 (1928).
  84. Eyring, H. The activated complex in chemical reactions. *J. Chem. Phys.* **445**, 107–115 (1935).
  85. Evans, M. G. & Polanyi, M. Some applications of the transition state method to the calculation of reaction velocities, especially in solution. *Trans. Faraday Soc.* **31**, 875–894 (1935).
  86. Marcus, R. a. & Rice, O. K. The kinetics of the recombination of methyl radicals and iodine atoms. *J. Phys. Chem.* **55**, 894–908 (1951).
  87. Marcus, R. Unimolecular dissociations and free radical recombination reactions. *J. Chem. Phys.* **20**, 359–364 (1952).
  88. H. M. Rosenstock, M. B. Wallenstein, A. L. Wahrhaftig, and Eyring, H. Absolute rate theory for isolated systems and the mass spectra of polyatomic molecules. *Proc. Natl. Acad. Sci.* **38**, 667–678 (1952).
  89. Baer, T. & Mayer, P. M. Statistical Rice-Ramsperger-Kassel-Marcus quasiequilibrium theory calculations in mass spectrometry. *J. Am. Soc. Mass Spectrom.* **8**, 103–115 (1997).
  90. Derrick, P. J., Loyd, P. M. & Christie, J. R. *Physical chemistry of ion reactions in advanced mass spectrometry*, vol. 13. (Wiley: Chichester, UK, 1995).
  91. Moon, J. H., Oh, J. Y. & Kim, M. S. A systematic and efficient method to estimate the vibrational frequencies of linear peptide and protein ions with any amino acid sequence for the calculation of Rice-Ramsperger-Kassel-Marcus rate constant. *J. Am. Soc. Mass Spectrom.* **17**, 1749–1757 (2006).
  92. Baer, T. & Hase, W. L. *Unimolecular reaction dynamics: theory and experiments*. (Oxford University Press on Demand, 1996).
  93. Robinson, P. J. & Holbrook, K. A. *Unimolecular reactions*. (Wiley-Interscience New York, 1972).
  94. Laskin, J. *Energy and Entropy Effects in Gas-Phase Dissociation of Peptides and Proteins. Principles of Mass Spectrometry Applied to Biomolecules* (2006).
  95. Gross, J. H. in *Mass spectrometry* 29–84 (Springer, 2017).
  96. Sleno, L. & Volmer, D. A. Ion activation methods for tandem mass spectrometry. *J.*

- Mass Spectrom.* **39**, 1091–1112 (2004).
97. Vékey, K. Internal energy effects in mass spectrometry. *J. Mass Spectrom.* **31**, 445–463 (1996).
  98. Lifshitz, C. Time-resolved appearance energies, breakdown graphs, and mass spectra: The elusive “kinetic shift”. *Mass Spectrom. Rev.* **1**, 309–348 (1982).
  99. Lifshitz, C. Kinetic shifts. *Eur. J. Mass Spectrom.* **8**, 85–98 (2002).
  100. Gabelica, V. & De Pauw, E. Internal energy and fragmentation of ions produced in electrospray sources. *Mass Spectrom. Rev.* **24**, 566–587 (2005).
  101. McLuckey, S. A. & Goeringer, D. E. Slow heating methods in tandem mass spectrometry. *J. Mass Spectrom.* **32**, 461–474 (1997).
  102. Arrhenius, S. ‘Ueber die reaktionsgeschwindigkeit bei der inversion von rohrzucker durch sauren’. *Zeitschrift fuer Phys. Chemie* **4**, 226–248 (1889).
  103. Laidler, K. J. The development of the Arrhenius equation. *J. Chem. Educ.* **61**, 494–498 (1984).
  104. Giddings, C. J. & Eyring, H. Equilibrium theory of unimolecular reactions. *J. Chem. Phys.* **22**, 538–542 (1954).
  105. Laskin, J. Energetics and dynamics of fragmentation of protonated leucine enkephalin from time-and energy-resolved surface-induced dissociation studies. *J. Phys. Chem. A* **110**, 8554–8562 (2006).
  106. Dunbar, R. C. BIRD (blackbody infrared radiative dissociation): evolution, principles, and applications. *Mass Spectrom. Rev.* **23**, 127–158 (2004).
  107. Lin, C.-Y. & Dunbar, R. C. Zero-pressure thermal-radiation-induced dissociation of tetraethylsilane cation. *J. Phys. Chem.* **100**, 655–659 (1996).
  108. Price, W. D., Schnier, P. D. & Williams, E. R. Binding energies of the proton-bound amino acid dimers Gly.Gly, Ala.Ala, Gly.Ala, and Lys.Lys measured by blackbody infrared radiative dissociation. *J. Phys. Chem. B* **101**, 664–673 (1997).
  109. Price, W. D., Schnier, P. D., Jockusch, R. A., Strittmatter, E. F. & Williams, E. R. Unimolecular reaction kinetics in the high-pressure limit without collisions. *J. Am. Chem. Soc.* **118**, 10640–10644 (1996).
  110. Perrin, J. Matter and light: An essay toward formulation of the mechanism of chemical reactions. *Ann Phys* **11**, 5–108 (1919).

111. Perrin, J. Radiation and chemistry *Trans Faraday Soc* **17**, 546–572 (1922).
112. Price, W. D. & Williams, E. R. Activation of peptide ions by blackbody radiation: factors that lead to dissociation kinetics in the rapid energy exchange limit. *J. Phys. Chem. A* **101**, 8844–8852 (1997).
113. Stafford Jr, G. C. P. E. Kelly, JEP Syka, WE Reynolds and J. F. J. Todd. *Inr. 1. Mass Spectrom. Ion Process. 60. 85* **98**, (1984).
114. March, R. E. Quadrupole ion traps. *Mass Spectrom. Rev.* **28**, 961–989 (2009).
115. Mathieu, É. *Mémoire sur le mouvement vibratoire d’une membrane de forme elliptique. Journal de Mathématiques Pures et Appliquées* **13**, (1868).
116. Douglas, D. J., Frank, A. J. & Mao, D. Linear ion traps in mass spectrometry. *Mass Spectrom. Rev.* **24**, 1–29 (2005).
117. Douglas, D. J. Linear quadrupoles in mass spectrometry. *Mass Spectrom. Rev.* **28**, 937–960 (2009).
118. Gerlich, D. *Inhomogeneous RF-fields—a versatile tool for the study of processes with slow ions. Advances in chemical physics, Volume 82* (1992).
119. Schwartz, J. C., Senko, M. W. & Syka, J. E. P. FOCUS: QUADRUPOLE ION TRAPS A two-dimensional quadrupole ion trap mass spectrometer. *Am. Soc. Mass Spectrom.* **13**, 659–669 (2002).
120. Schwartz, J. C., Senko, M. W. & Syka, J. E. . A two-dimensional quadrupole ion trap mass spectrometer. *J. Am. Soc. Mass Spectrom.* **13**, 659–669 (2002).
121. Douglas, D. J. & French, J. B. Collisional focusing effects in radio frequency quadrupoles. *J. Am. Soc. Mass Spectrom.* **3**, 398–408 (1992).
122. Louri, J. N. & Cooks, R. G. Instrumentation, applications, and energy deposition in quadrupole ion-trap tandem mass spectrometry. *Anal. Chem.* **59**, 1677–1685 (1987).
123. McLuckey, S. a, Goeringer, D. E. & Glish, G. L. Collisional activation with random noise in ion trap mass spectrometry. *Anal. Chem.* **64**, 1455–1460 (1992).
124. Traldi, P.; Catinella, S.; March, R. E.; Creaser, C. S. in (eds. March, R. E. & Todd, J. F. J.) Vol. I, Chapter 7 (CRC Press, 1995).
125. Qin, J. & Chait, B. T. Matrix-assisted laser desorption ion trap mass spectrometry: efficient isolation and effective fragmentation of peptide ions. *Anal. Chem.* **68**, 2108–2112 (1996).

126. Cooks, R. G. & Lammert, S. A. Pulsed axial activation in the ion trap: A new method for performing tandem mass spectroscopy (MS/MS). *Rapid Commun. Mass Spectrom.* **6**, 528–530 (1992).
127. Orlando, R., Fenselau, C. & Cotter, R. J. Endothermic ion molecule reactions. *J. Am. Soc. Mass Spectrom.* **2**, 189–197 (1991).
128. Paradisi, C., Todd, J. F. J., Traldi, P. & Vettori, U. Boundary effects and collisional activation in a quadrupole ion trap. *J. Mass Spectrom.* **27**, 251–254 (1992).
129. Wang, M., Schachterle, S. & Wells, G. Application of nonresonance excitation to ion trap tandem mass spectrometry and selected ejection chemical ionization. *J. Am. Soc. Mass Spectrom.* **7**, 668–676 (1996).
130. Butcher, D. J., Asano, K. G., Goeringer, D. E. & McLuckey, S. a. Thermal dissociation of gaseous bradykinin ions. *J. Phys. Chem. A* **103**, 8664–8671 (1999).
131. Asano, K. G., Goeringer, D. E., Butcher, D. J. & McLuckey, S. A. Bath gas temperature and the appearance of ion trap tandem mass spectra of high-mass ions. *Int. J. Mass Spectrom.* **190**, 281–293 (1999).
132. Goeringer, D. E. & McLuckey, S. A. Kinetics of collision-induced dissociation in the Paul trap: A first-order model. *Rapid Commun. Mass Spectrom.* **10**, 328–334 (1996).
133. Goeringer, D. E. & McLuckey, S. A. Evolution of ion internal energy during collisional excitation in the Paul ion trap: A stochastic approach. *J. Chem. Phys.* **104**, 2214–2221 (1996).
134. Asano, K. G., Goeringer, D. E. & McLuckey, S. A. Thermal dissociation in the quadrupole ion trap: ions derived from leucine enkephalin. *Int. J. Mass Spectrom.* **185**, 207–219 (1999).
135. Wannier, G. H. On the motion of gaseous ions in a strong electric field. I. *Phys. Rev.* **83**, 281–289 (1951).
136. Mason, E. A. (Edward A., McDaniel, E. W. & John Wiley & Sons. *Transport properties of ions in gases*. (Wiley, 1988).
137. Hirschfelder, J. O., Curtiss, C. F., Bird, R. B. & Mayer, M. G. *Molecular theory of gases and liquids*. **26**, (Wiley New York, 1954).
138. Wang, C. S. & Chang, G. E. Uhlenbeck, and J. de Boer. *Stud. Stat. Mech. II* (1964).
139. Olsen, J. V *et al.* Higher-energy C-trap dissociation for peptide modification analysis. *Nat. Methods* **4**, 709–712 (2007).



140. Klemm, D., Heublein, B., Fink, H. P. & Bohn, A. Cellulose: Fascinating biopolymer and sustainable raw material. *Angew. Chemie - Int. Ed.* **44**, 3358–3393 (2005).
141. Postek, M. T., Moon, R. J., Rudie, A. W. & Bilodeau, M. A. *Production and applications of cellulose nanomaterials*. (TAPPI, 2013).
142. Shokri, J. & Adibki, K. in *Cellulose - medical, pharmaceutical and electronic applications* 47–66 (2013). doi:10.5772/55178
143. Isogai, A. NMR analysis of cellulose dissolved in aqueous NaOH solutions. *Cellulose* **4**, 99–107 (1997).
144. Le Moigne, N. & Navard, P. Dissolution mechanisms of wood cellulose fibres in NaOH-water. *Cellulose* **17**, 31–45 (2010).
145. Jinping Zhou and Lina Zhang. Solubility of cellulose in NaOH/urea aqueous solution. *Polym. J.* **32**, 866–870 (2000).
146. Chanzy, H., Nawrot, S., Peguy, A., Smith, P. & Chevalier, J. Phase behavior of the quasiternary system N-methylmorpholine-N-oxide, water, and cellulose. *J. Polym. Sci. Polym. Phys. Ed.* **20**, 1909–1924 (1982).
147. Swatoski, R. P., Spear, S. K., Holbrey, J. D. & Rogers, R. D. Dissolution of cellose with ionic liquids. *J. Am. Chem. Soc.* **124**, 4974–4975 (2002).
148. Wang, H., Gurau, G. & Rogers, R. D. Ionic liquid processing of cellulose. *Chem. Soc. Rev.* **41**, 1519–1537 (2012).
149. Paul Rolland Austin. Chitin solution. (1977).
150. Dawsey, T. R. & McCormick, C. L. The lithium chloride/dimethylacetamide solvent for cellulose: a literature review. *J. Macromol. Sci. Part C* **30**, 405–440 (1990).
151. McCormick, C. L. & Hutchinson, B. H. Solution studies of cellulose in lithium chloride and N,N-dimethylacetamide. *Macromolecules* **18**, 2394–2401 (1985).
152. Morgenstern, B., Kammer, H. W., Berger, W. & Skrabal, P. <sup>7</sup>Li-NMR study on cellulose/LiCl/N,N-dimethylacetamide solutions. *Acta Polym.* **43**, 356–357 (1992).
153. Zhang, C. *et al.* Dissolution mechanism of cellulose in N,N-dimethylacetamide/lithium chloride: Revisiting through molecular interactions. *J. Phys. Chem. B* **118**, 9507–9514 (2014).
154. Kailemia, M. J., Ruhaak, L. R., Lebrilla, C. B. & Amster, I. J. Oligosaccharide analysis by mass spectrometry: a review of recent developments. *Anal. Chem.* **86**, 196–212 (2014).

155. Wuhrer, M. Glycomics using mass spectrometry. *Glycoconj. J.* **30**, 11–22 (2013).
156. Han, L. & Costello, C. E. Mass spectrometry of glycans. *Biochem.* **78**, 710–720 (2013).
157. Zaia, J. Mass spectrometry of oligosaccharides. *Mass Spectrom. Rev.* **23**, 161–227 (2004).
158. Fentabil, M. a., Daneshfar, R., Kitova, E. N. & Klassen, J. S. Blackbody infrared radiative dissociation of protonated oligosaccharides. *J. Am. Soc. Mass Spectrom.* **22**, 2171–2178 (2011).
159. Harvey, D. J. Electrospray mass spectrometry and fragmentation of N-linked carbohydrates derivatized at the reducing terminus. *J. Am. Soc. Mass Spectrom.* **11**, 900–915 (2000).
160. Asam, M. R. & Glish, G. L. Tandem mass spectrometry of alkali cationized polysaccharides in a quadrupole ion trap. *J. Am. Soc. Mass Spectrom.* **8**, 987–995 (1997).
161. Bythell, B. J., Abutokaikah, M. T., Wagoner, A. R., Guan, S. & Rabus, J. M. Cationized carbohydrate gas-phase fragmentation chemistry. *J. Am. Soc. Mass Spectrom.* **28**, 688–703 (2017).
162. Hofmeister, G. E., Zhou, Z. & Leary, J. A. Linkage position determination in lithium-cationized disaccharides: tandem mass spectrometry and semiempirical calculations. *J. Am. Chem. Soc.* **113**, 5964–5970 (1991).
163. Zhou, Z., Ogden, S. & Leary, J. A. Linkage position determination in oligosaccharides: mass spectrometry (MS/MS) study of lithium-cationized carbohydrates. *J. Org. Chem.* **55**, 5444–5446 (1990).
164. Staempfli, A., Zhou, Z. & Leary, J. A. Gas-phase dissociation mechanisms of dilithiated disaccharides: tandem mass spectrometry and semiempirical calculations. *J. Org. Chem.* **57**, 3590–3594 (1992).
165. Ngoka, L. C., Gal, J. F. & Lebrilla, C. B. Effects of cations and charge types on the metastable decay rates of oligosaccharides. *Anal. Chem.* **66**, 692–698 (1994).
166. Veith, H. J. Alkali-ion addition in Fd-mass spectrometry-cationization and protonization-ionization methods in application of non-activated emitter. *Tetrahedron* **33**, 2825–2828 (1977).
167. Cancilla, M. T., Penn, S. G., Carroll, J. A. & Lebrilla, C. B. Coordination of alkali metals to oligosaccharides dictates fragmentation behavior in matrix assisted laser desorption ionization / Fourier transform mass spectrometry. *J. Am. Chem. Soc.* **118**, 6736–6745 (1996).

168. Pasanen, S., Jänis, J. & Vainiotalo, P. Cello-, malto- and xylooligosaccharide fragmentation by collision-induced dissociation using QIT and FT-ICR mass spectrometry: A systematic study. *Int. J. Mass Spectrom.* **263**, 22–29 (2007).
169. Wells, M. J. & McLuckey, S. A. *Collision-induced dissociation (CID) of peptides and proteins. Methods in Enzymology* **402**, (Elsevier, 2005).
170. Striegel, A. M., Timpa, J. D., Piotrowiak, P. & Cole, R. B. Multiple neutral alkali halide attachments onto oligosaccharides in electrospray ionization mass spectrometry. *Int. J. Mass Spectrom. Ion Process.* **162**, 45–53 (1997).
171. Ichou, F. *et al.* Comparison of the activation time effects and the internal energy distributions for the CID, PQD and HCD excitation modes. *J. Mass Spectrom.* **49**, 498–508 (2014).
172. Domon, B. & Costello, C. E. A systematic nomenclature for carbohydrate fragmentations in FAB-MS/MS spectra of glycoconjugates. *Glycoconj. J.* **5**, 397–409 (1988).
173. Han, L. & Costello, C. E. Electron transfer dissociation of milk oligosaccharides. *J. Am. Soc. Mass Spectrom.* **22**, 997–1013 (2011).
174. Hernandez, O., Isenberg, S., Steinmetz, V., Glish, G. L. & Maitre, P. Probing mobility-selected saccharide isomers: selective ion-molecule reactions and wavelength-specific IR activation. *J. Phys. Chem. A* **119**, 6057–6064 (2015).
175. Gross, A. S., Bell, A. T. & Chu, J. W. Preferential interactions between lithium chloride and glucan chains in N, N -dimethylacetamide drive cellulose dissolution. *J. Phys. Chem. B* **117**, 3280–3286 (2013).
176. Kang, X., Kuga, S., Wang, L., Wu, M. & Huang, Y. Dissociation of intra / inter-molecular hydrogen bonds of cellulose molecules in the dissolution process : a mini review. *J. Bioresour. Bioprod.* **1**, 58–63 (2016).
177. J. Cram, D. & M. Cram, J. *Container molecules and their guests.* (The Royal Society of Chemistry, 1997).
178. Yang, H., Yuan, B., Zhang, X. & Scherman, O. A. Supramolecular chemistry at interfaces: host–guest interactions for fabricating multifunctional biointerfaces. *Acc. Chem. Res.* **47**, 2106–2115 (2014).
179. Vriezema, D. M. *et al.* Self-assembled nanoreactors. *Chem. Rev.* **105**, 1445–1489 (2005).
180. Armentrout, P. B. & Baer, T. Gas-phase ion dynamics and chemistry. *J. Phys. Chem.* **100**, 12866–12877 (1996).

181. Rodgers, M. & Armentrout, P. Noncovalent metal-ligand bond energies as studied by threshold collision-induced dissociation. *Mass Spectrom. Rev.* **19**, 215–247 (2000).
182. Armentrout, P. B. Mass spectrometry - Not just a structural tool: The use of guided ion beam tandem mass spectrometry to determine thermochemistry. *J. Am. Soc. Mass Spectrom.* **13**, 419–434 (2002).
183. Gatineau, D. *et al.* Experimental bond dissociation energies of benzyropyridinium thermometer ions determined by threshold-CID and RRKM modeling. *Int. J. Mass Spectrom.* **417**, 69–75 (2017).
184. Price, W. D., Schnier, P. D. & Williams, E. R. Tandem mass spectrometry of large biomolecule ions by blackbody infrared radiative dissociation. *Anal. Chem.* **68**, 859–866 (1996).
185. McLuckey, S. A., Wells, J. M., Stephenson, J. L. & Goeringer, D. E. Novel quadrupole ion trap methods for characterizing the chemistry of gaseous macro-ions. *Int. J. Mass Spectrom.* **200**, 137–161 (2000).
186. Laskin, J. & Futrell, J. H. Collisional activation of peptide ions in FT-ICR mass spectrometry. *Mass Spectrom. Rev.* **22**, 158–181 (2003).
187. Laskin, J. & Futrell, J. H. Activation of large ions in FT-ICR mass spectrometry. *Mass Spectrom. Rev.* **24**, 135–167 (2005).
188. Laskin, J., Denisov, E. & Futrell, J. H. Fragmentation energetics of small peptides from multiple-collision activation and surface-induced dissociation in FT-ICR MS. *Int. J. Mass Spectrom.* **219**, 189–201 (2002).
189. Zeisel, S. H. & Blusztajn, J. K. Choline and human nutrition. *Annu. Rev. Nutr.* **14**, 269–296 (1994).
190. Angus, J. A. & Lew, M. J. Interpretation of the acetylcholine test of endothelial cell dysfunction in hypertension. *J. Hypertens.* **10**, 179–186 (1992).
191. Millian, N. S. & Garrow, T. a. Human betaine-homocysteine methyltransferase is a zinc metalloenzyme. *Arch. Biochem. Biophys.* **356**, 93–98 (1998).
192. Finkelstein, J. D., Harris, B. J. & Kyle, W. E. Methionine metabolism in mammals: Kinetic study of betaine-homocysteine methyltransferase. *Arch. Biochem. Biophys.* **153**, 320–324 (1972).
193. Perraud, O. *et al.* Hemicyptophane-assisted electron transfer: a structural and electronic study. *Dalton Trans.* **42**, 1530–5 (2013).
194. Chatelet, B. *et al.* Shorter and modular synthesis of hemicyptophane-tren derivatives.

- Org. Lett.* **13**, 3706–3709 (2011).
195. Ichou, F. *et al.* Collision cell pressure effect on CID spectra pattern using triple quadrupole instruments: a RRKM modeling. *J. Mass Spectrom.* **48**, 179–186 (2013).
  196. Schnier, P. D., Price, W. D., Strittmatter, E. F. & Williams, E. R. Dissociation energetics and mechanism of leucine enkephalin  $(M+H)^+$  and  $(2M+X)^+$  ions ( $X=H, Li, Na, K,$  and  $Rb$ ) measured by blackbody infrared radiative dissociation. *J. Am. Soc. Mass Spectrom.* **8**, 771–780 (1997).
  197. Schmidt, M. W. *et al.* General atomic and molecular electronic structure system. *J. Comput. Chem.* **14**, 1347–1363 (1993).
  198. Gordon, M. S. & Schmidt, M. W. *Advances in electronic structure theory: GAMESS a decade later. Theory and Applications of Computational Chemistry: The First Forty Years* (2005).
  199. L. Drahos and V. Karoly. MassKinetics: a theoretical model of mass spectra incorporating physical processes, reaction kinetics and mathematical descriptions aszı o Drahos and aroly ekey. *J. Mass Spectrom* **36**, 237–263 (2001).
  200. Naban-Maillet, J. *et al.* Internal energy distribution in electrospray ionization. *J. Mass Spectrom.* **40**, 1–8 (2005).
  201. Pak, A., Lesage, D., Gimbert, Y., Vékey, K. & Tabet, J. C. Internal energy distribution of peptides in electrospray ionization: ESI and collision-induced dissociation spectra calculation. *J. Mass Spectrom.* **43**, 447–455 (2008).
  202. Ichou, F. *et al.* Comparison of the activation time effects and the internal energy distributions for the CID, PQD and HCD excitation modes. *J. Mass Spectrom.* **49**, 498–508 (2014).
  203. Chen, P. Electrospray ionization tandem mass spectrometry in high-throughput screening of homogeneous catalysts. *Angew. Chemie Int. Ed.* **42**, 2832–2847 (2003).
  204. Lesage, D., Blu, J., Tabet, J. C. & Gimbert, Y. Intermolecular versus intramolecular Pauson-Khand reaction in gas phase: Limitation and feasibility. *J. Organomet. Chem.* **809**, 7–13 (2016).
  205. Sutherland, I. O. Synthetic Ditopic Receptors. *J. Incl. Phenom. Macrocycl. Chem.* **41**, 69–75 (2001).
  206. McConnell, A. J. & Beer, P. D. Heteroditopic receptors for ion-pair recognition. *Angew. Chemie - Int. Ed.* **51**, 5052–5061 (2012).
  207. Kim, S. K. & Sessler, J. L. Ion pair receptors. *Chem. Soc. Rev.* **39**, 3784–3809 (2010).

208. Tagne Kuate, A. C., Naseer, M. M. & Jurkschat, K. Liquid membrane transport of potassium fluoride by the organotin-based ditopic host Ph<sub>2</sub>FSnCH<sub>2</sub>SnFPh-CH<sub>2</sub>-[19]-crown-6. *Chem. Commun.* **53**, 2013–2015 (2017).
209. Ziach, K., Karbarz, M. & Romański, J. Cooperative binding and extraction of sodium nitrite by a ditopic receptor incorporated into a polymeric resin. *Dalt. Trans.* **45**, 11639–11643 (2016).
210. Webber, P. & Beer, P. D. Ion-pair recognition by a ditopic calix[4]semitube receptor. *Dalt. Trans.* **0**, 2249–2252 (2003).
211. Temel, F. & Tabakci, M. Calix[4]arene coated QCM sensors for detection of VOC emissions: Methylene chloride sensing studies. *Talanta* **153**, 221–227 (2016).
212. Kim, S. K. & Sessler, J. L. Calix[4]pyrrole-Based Ion Pair Receptors. *Acc. Chem. Res.* **47**, 2525–2536 (2014).
213. Molina, P., Tárraga, A. & Alfonso, M. Ferrocene-based multichannel ion-pair recognition receptors. *Dalt. Trans.* **43**, 18–29 (2014).
214. de Juan Fernández, L. *et al.* An Enantioselective Benzofuran-Based Receptor for Dinitrobenzoyl-Substituted Amino Acids. *European J. Org. Chem.* **2016**, 1541–1547 (2016).
215. Huang, H., Nandhakumar, R., Choi, M., Su, Z. & Kim, K. M. Enantioselective liquid–liquid extractions of underivatized general amino acids with a chiral ketone extractant. *J. Am. Chem. Soc.* **135**, 2653–2658 (2013).
216. Herrero, F. G. *et al.* A molecular receptor for zwitterionic phenylalanine. *Org. Biomol. Chem.* **14**, 3906–3912 (2016).
217. Rubio, O. H. *et al.* A molecular receptor selective for zwitterionic alanine. *Org. Biomol. Chem.* **15**, 477–485 (2017).
218. Cametti, M., Nissinen, M., Dalla Cort, A., Mandolini, L. & Rissanen, K. Ion pair recognition of quaternary ammonium and iminium salts by uranyl-salophen compounds in solution and in the solid state. *J. Am. Chem. Soc.* **129**, 3641–3648 (2007).
219. Lankshear, M. D., Dudley, I. M., Chan, K.-M. & Beer, P. D. Tuning the strength and selectivity of ion-pair recognition using heteroditopic calix[4]arene-based receptors. *New J. Chem.* **31**, 684–690 (2007).
220. Beyeh, N. K., Weimann, D. P., Kaufmann, L., Schalley, C. A. & Rissanen, K. Ion-pair recognition of tetramethylammonium salts by halogenated resorcinarenes. *Chem. - A Eur. J.* **18**, 5552–5557 (2012).

221. Ni, M. *et al.* Improved recognition of alkylammonium salts by ion pair recognition based on a novel heteroditopic pillar[5]arene receptor. *Tetrahedron Lett.* **53**, 6409–6413 (2012).
222. Schurig, V. *Differentiation of enantiomers I. Topics in Current Chemistry* **340**, (2013).
223. Gillis, E. A. L. *et al.* Structure and energetics of gas phase halogen-bonding in mono-, bi-, and tri-dentate anion receptors as studied by BIRD. *Phys. Chem. Chem. Phys.* **15**, 7638–7647 (2013).
224. Liu, L., Bagal, D. & Kitova, E. Hydrophobic protein– ligand interactions preserved in the gas phase. *J. Am. Chem. Soc.* **82**, 15980–15981 (2009).
225. Armentrout, P. B. & Rodgers, M. T. Thermochemistry of non-covalent ion-molecule interactions. *Mass Spectrom.* **2**, S0005/1-S0005/8 (2013).
226. Wang, L., Chai, Y., Sun, C. & Armstrong, D. Complexation of cyclofructans with transition metal ions studied by electrospray ionization mass spectrometry and collision-induced dissociation. *J. Mass Spectrom.* **323–324**, 21–27 (2012).
227. Abdoul-carime, H. *et al.* Solution vs. gas phase relative stability of the choline/acetylcholine cavitand complexes. *Phys. Chem. Chem. Phys.* **17**, 4448–4457 (2015).
228. Ma, X. *et al.* Gas-phase fragmentation of host–guest complexes between  $\beta$ -cyclodextrin and small molecules. *Talanta* **93**, 252–256 (2012).
229. Duez, Q. *et al.* Action-FRET of  $\beta$ -cyclodextrin inclusion complexes. *New Journal of Chemistry* **41**, 1806–1812 (2017).
230. Wei, W., Chu, Y., Wang, R., He, X. & Ding, C. Quantifying non-covalent binding affinity using mass spectrometry: A systematic study on complexes of cyclodextrins with alkali metal cations. *Rapid Commun. Mass Spectrom.* **29**, 927–936 (2015).
231. Johnson, G. E., Priest, T. & Laskin, J. Size-dependent stability toward dissociation and ligand binding energies of phosphine ligated gold cluster ions. *Chem. Sci.* **5**, 3275–3286 (2014).
232. Mayer, P. M. and E. M. Gas-phase binding energies for non-covalent Ab-40 peptide/small molecule complexes from CID mass spectrometry and RRKM theory. *Phys. Chem. Chem. Phys.* **13**, 5178–5186 (2011).
233. Goeringer, D. E., Asano, K. G. & McLuckey, S. A. Ion internal temperature and ion trap collisional activation : protonated leucine enkephalin. *Int. J. Mass Spectrom.* **182/183**, 275–288 (1999).

234. Tolmachev, A. V. *et al.* Collisional activation of ions in RF ion traps and ion guides: The effective ion temperature treatment. *J. Am. Soc. Mass Spectrom.* **15**, 1616–1628 (2004).
235. Donald, W. A., Khairallah, G. N. & O’Hair, R. A. J. The effective temperature of ions stored in a linear quadrupole ion trap mass spectrometer. *J. Am. Soc. Mass Spectrom.* **24**, 811–815 (2013).
236. McLuckey, S. A. *et al.* Novel quadrupole ion trap methods for characterizing the chemistry of gaseous macro-ions. *Int. J. Mass Spectrom.* **200**, 137–161 (2000).
237. Gabelica, V., Karas, M. & De Pauw, E. Calibration of ion effective temperatures achieved by resonant activation in a quadrupole ion trap. *Anal. Chem.* **75**, 5152–5159 (2003).
238. Mason, E. A. & McDaniel, E. W. *Transport properties of ions in gases*. (Wiley-VCH Verlag GmbH & Co. KGaA, 1988).
239. Gabelica, V. & Marklund, E. Fundamentals of ion mobility spectrometry. *Curr. Opin. Chem. Biol.* **42**, 51–59 (2018).
240. D’Atri, V., Porrini, M., Rosu, F. & Gabelica, V. Linking molecular models with ion mobility experiments. Illustration with a rigid nucleic acid structure. *J. Mass Spectrom.* **50**, 711–726 (2015).
241. May, J. C. *et al.* Conformational ordering of biomolecules in the gas phase: nitrogen collision cross sections measured on a prototype high resolution drift tube ion mobility-mass spectrometer. *Anal. Chem.* **86**, 2107–2116 (2014).
242. McDaniel, E. W. & Mason, E. A. The mobility and diffusion of ions in gases. (1973).
243. Ellis, H. W., Pai, R. Y., McDaniel, E. W., Mason, E. A. & Viehland, L. A. Transport properties of gaseous ions over a wide energy range. *At. Data Nucl. Data Tables* **17**, 177–210 (1976).
244. Dougherty, D. A. The cation– $\pi$  interaction. *Acc. Chem. Res.* **46**, 885–893 (2013).
245. Meyer, E. A., Castellano, R. K. & Diederich, F. Interactions with aromatic rings in chemical and biological recognition. *Angewandte Chemie - International Edition* **42**, 1210–1250 (2003).
246. Kertesz, T. M., Hall, L. H., Hill, D. W. & Grant, D. F. CE<sub>50</sub>: Quantifying collision induced dissociation energy for small molecule characterization and identification. *J. Am. Soc. Mass Spectrom.* **20**, 1759–1767 (2009).
247. Przybylski, C. & Bonnet, V. Discrimination of cyclic and linear oligosaccharides by



- tandem mass spectrometry using collision-induced dissociation (CID), pulsed-Q-dissociation (PQD) and the higherenergy C-trap dissociation modes. *Rapid Commun. Mass Spectrom.* **27**, 75–87 (2013).
248. Nagy, T. *et al.* Chiral differentiation of the noscapine and hydrastine stereoisomers by electrospray ionization tandem mass spectrometry. *J. Mass Spectrom.* **50**, 240–246 (2015).
  249. Ichou, F. *et al.* Collision cell pressure effect on CID spectra pattern using triple quadrupole instruments: A RRKM modeling. *J. Mass Spectrom.* **48**, 179–186 (2013).
  250. Laskin, J. & Futrell, J. H. Entropy is the major driving force for fragmentation of proteins and protein-ligand complexes in the gas phase. *J. Phys. Chem. A* **107**, 5836–5839 (2003).
  251. Sztáray, J., Memboeuf, A., Drahos, L. & Vékey, K. Leucine enkephalin-A mass spectrometry standard. *Mass Spectrom. Rev.* **30**, 298–320 (2011).
  252. Kurkov, S. V & Loftsson, T. Cyclodextrins. *Int. J. Pharm.* **453**, 167–180 (2013).
  253. Szejtli, J. Introduction and general overview of cyclodextrin chemistry. *Chem. Rev.* **98**, 1743–1754 (1998).
  254. Bender, M. L. & Komiyama, M. *Cyclodextrin chemistry*. **6**, (Springer Science & Business Media, 2012).
  255. Del Valle, E. M. M. Cyclodextrins and their uses: A review. *Process Biochemistry* **39**, 1033–1046 (2004).
  256. Bellia, F. *et al.* Selectively functionalized cyclodextrins and their metal complexes. *Chem. Soc. Rev.* **38**, 2756 (2009).
  257. Zhang, J. & Ma, P. X. Cyclodextrin-based supramolecular systems for drug delivery: Recent progress and future perspective. *Adv. Drug Deliv. Rev.* **65**, 1215–1233 (2013).
  258. Webber, M. J. & Langer, R. Drug delivery by supramolecular design. *Chem. Soc. Rev.* **46**, 6600–6620 (2017).
  259. Sharma, N. & Baldi, A. Exploring versatile applications of cyclodextrins: An overview. *Drug Delivery* **23**, 739–757 (2016).
  260. Harada, A. Cyclodextrin-based molecular machines. *Acc. Chem. Res.* **34**, 456–464 (2001).
  261. Hapiot, F. *et al.* Catalysis in cyclodextrin-based unconventional reaction media: recent developments and future opportunities. *ACS Sustain. Chem. Eng.* **5**, 3598–3606

(2017).

262. Monflier, E. Unconventional approaches involving cyclodextrin-based, self-assembly-driven processes for the conversion of organic substrates in aqueous biphasic catalysis. *Catalysts* **7**, 173 (1-11) (2017).
263. Macaev, F. & Boldescu, V. Cyclodextrins in asymmetric and stereospecific synthesis. *symmetry (Basel)*. **7**, 1699–1720 (2015).
264. Ogoshi, T. & Harada, A. Chemical sensors based on cyclodextrin derivatives. *Sensors* **8**, 4961–4982 (2008).
265. Olives, A. I., González-Ruiz, V. & Martín, M. A. Sustainable and eco-friendly alternatives for liquid chromatographic analysis. *ACS Sustain. Chem. Eng.* **5**, 5618–5634 (2017).
266. Adly, F. G., Antwi, N. Y. & Ghanem, A. Cyclodextrin-functionalized monolithic capillary columns: preparation and chiral applications. *Chirality* **28**, 97–109 (2016).
267. Juvancz, Z., Kendrovics, R. B., Iványi, R. & Szenté, L. The role of cyclodextrins in chiral capillary electrophoresis. *Electrophoresis* **29**, 1701–1712 (2008).
268. Hapiot, F., Tilloy, S. & Monflier, E. Cyclodextrins as supramolecular hosts for organometallic complexes. *Chem. Rev.* **106**, 767–781 (2006).
269. Shahgaldian, P. & Pieleś, U. Cyclodextrin derivatives as chiral supramolecular receptors for enantioselective sensing. *Sensors* **6**, 593–615 (2006).
270. Zhang, Y. & Xu, W. The Aldol condensation catalyzed by metal(II)- $\beta$ -cyclodextrin complexes. *Synth. Commun.* **19**, 1291–1296 (1989).
271. Rizzarelli, E. & Vecchio, G. Metal complexes of functionalized cyclodextrins as enzyme models and chiral receptors. *Coord. Chem. Rev.* **188**, 343–364 (1999).
272. Norkus, E., Grinciene, G., Vuorinen, T. & Vaitkus, R. Cu(II) ion complexation by excess of beta-cyclodextrin in aqueous alkaline solutions. *J. Inclusion Phenom. Macrocycl. Chem.* **48**, 147–150 (2004).
273. Norkus, E., Grinciene, G., Vuorinen, T., Vaitkus, R. & Butkus, E. Interaction of  $\beta$ -cyclodextrin with cadmium(II) ions. *Int. J. Biol. Macromol.* **33**, 251–254 (2003).
274. Norkus, E., Grinciene, G. & Vaitkus, R. Interaction of lead(II) with beta-cyclodextrin in alkaline solutions. *Carbohydr. Res.* **337**, 1657–1661 (2002).
275. Darj, M. & Malinowski, E. R. Determination of the formation constant of the copper chelate of  $\beta$ -cyclodextrin by spectrophotometric titration with

- ethylenediaminetetraacetic acid using window factor analysis. *Appl. Spectrosc.* **56**, 257–265 (2002).
276. Egyed, O. & Weiszfeiler, V. Structure determination of copper(II)- $\beta$ -cyclodextrin complex by Fourier transform infrared spectroscopy. *Vib. Spectrosc.* **7**, 73–77 (1994).
277. Kurokawa, G., Sekii, M., Ishida, T. & Nogami, T. Short communication: crystal structure of a molecular complex from native  $\beta$ -cyclodextrin and copper(II) chloride. *Supramol. Chem.* **16**, 381–384 (2004).
278. Bose, P. K. & Polavarapu, P. L. Evidence for covalent binding between copper ions and cyclodextrin cavity: A vibrational circular dichroism study. *Carbohydr. Res.* **323**, 63–72 (2000).
279. Song, L. X. & Bai, L. Striking structural transformation from cyclic oligosaccharide to aromatic series by means of the effect of lithium carbonate based on gas chromatography coupled to time-of-flight mass spectrometry. *J. Phys. Chem. B* **113**, 9035–9040 (2009).
280. Stachowicz, A., Styrz, A., Korchowiec, J., Modaressi, A. & Rogalski, M. DFT studies of cation binding by  $\beta$ -cyclodextrin. *Theor. Chem. Acc.* **130**, 939–953 (2011).
281. Przybylski, C., Bonnet, V. & Cézard, C. Probing the common alkali metal affinity of native and variously methylated  $\beta$ -cyclodextrins by combining electrospray-tandem mass spectrometry and molecular modeling. *Phys. Chem. Chem. Phys.* **17**, 19288–305 (2015).
282. He, X.-D., Wei, W.-H., Chu, Y.-Q., Liu, Z.-P. & Ding, C.-F. Investigation on non-covalent complexes of cyclodextrins with  $\text{Li}^+$  in gas phase by mass spectrometry. *Chinese J. Chem. Phys.* **26**, 287–294 (2013).
283. Reale, S., Teixidò, E. & de Angelis, F. Study of alkali metal cations binding selectivity of  $\beta$ -cyclodextrin by ESI-MS. *Ann. Chim.* **95**, 375–381 (2005).
284. Frański, R. *et al.* Mass spectrometric decompositions of cationized  $\beta$ -cyclodextrin. *Carbohydr. Res.* **340**, 1567–1572 (2005).
285. Metzger, J. W., Jung, M., Schmalzing, D., Bayer, E. & Schurig, V. Analysis of cyclomalto-oligosaccharides (cyclodextrins) and derivatives thereof by ion-spray mass spectrometry. *Carbohydr. Res.* **222**, 23–35 (1991).
286. Laskin, J. & Futrell, J. H. Collisional activation of peptide ions in FT-ICR mass spectrometry. *Mass Spectrom. Rev.* **22**, 158–181 (2003).
287. Przybylski, C. & Bonnet, V. Discrimination of cyclic and linear oligosaccharides by tandem mass spectrometry using collision-induced dissociation (CID), pulsed-Q-

- dissociation (PQD) and the higher-energy C-trap dissociation modes. *Rapid Commun. Mass Spectrom.* **27**, 75–87 (2013).
288. Suzuki, H., Kameyama, A., Tachibana, K., Narimatsu, H. & Fukui, K. Computationally and experimentally derived general rules for fragmentation of various glycosyl bonds in sodium adduct oligosaccharides. *Anal. Chem.* **81**, 1108–1120 (2009).
289. Tüting, W., Adden, R. & Mischnick, P. Fragmentation pattern of regioselectively O-methylated maltooligosaccharides in electrospray ionisation-mass spectrometry/collision induced dissociation. *Int. J. Mass Spectrom.* **232**, 107–115 (2004).

## List of Figures

<b>Figure 1-</b> Complexe H-G entre un hôte avec des sites de liaison concaves et un invité ayant une géométrie appropriée et des sites de liaison convexes.....	3
<b>Figure 2-</b> Un schéma général d'un spectromètre de masse. ....	4
<b>Figure 3-</b> (a) Cyclotribenzylène et cyclotrивeratrylène (CTV, $X = Y = \text{OCH}_3$ ) et (b) Cryptophane-E. <sup>37</sup> .....	5
<b>Figure 4-</b> Spectromètre de masse quadripolaire triple comme exemple d'instrument tandem-dans-l'espace (Quattro LC, Waters, Manchester, UK).....	8
<b>Figure 5-</b> Schéma général d'une source d'ionisation par électronébulisation fonctionnant en mode ions positifs (TDC: courant total de gouttelettes). <sup>66</sup> .....	12
<b>Figure 6-</b> Instantané d'une nano-gouttelette d'eau contenant du $\text{Na}^+$ près de la limite de Rayleigh, générée à l'aide de simulations de dynamique moléculaire ( $\text{Na}^+$ est représenté en bleu, oxygène en rouge et hydrogène en blanc). <sup>68</sup> .....	13
<b>Figure 7-</b> A- Interaction d'un ion positif avec deux dipôles, et B- une vue schématique de l'arrangement des molécules d'eau et des ions $\text{Na}^+$ dans les nano-gouttelettes d'eau. <sup>68,69</sup> .....	14
<b>Figure 8-</b> Différents mécanismes proposés pour l'ionisation par électronébulisation : (a) Modèle d'évaporation ionique, (b) Modèle de résidu chargé, et (c) Modèle d'éjection de chaîne. <sup>68</sup> .....	16
<b>Figure 1-1-</b> A schematic representation of a reaction coordinate for dissociation of a precursor ion having a total energy of $E$ . <sup>89</sup> .....	33
<b>Figure 1-2-</b> (a) Plots of rate constant as a function of the internal energy for two hypothetical reactions with loose (in gray) and tight (in black) transition states, <sup>94</sup> and (b) a schematic diagram representing KS. <sup>95</sup> .....	35
<b>Figure 1-3-</b> Truncated Maxwell-Boltzmann internal energy distribution: the solid curve is the internal energy distribution of a model host-guest complex at $t = 0$ ms and the dotted curve is the internal energy distribution of the ions after 2.5 ms. The hatched area corresponds to the part of the population that is decomposed (50%). ..	39
<b>Figure 2-1-</b> Schematic of a hybrid quadrupole-FT-ICR mass spectrometer (ApexQe, Bruker Daltonics) .....	43

<b>Figure 2-2-</b> BIRD's data treatment for extraction of observed activation parameters. ....	43
<b>Figure 2-3-</b> Quadrupole geometry. Each rod is located at the $r_0$ distance from the central axis. <sup>114</sup> .....	48
<b>Figure 2-4-</b> The Mathieu stability diagram for a linear quadrupole device. <sup>116,117</sup> .....	50
<b>Figure 2-5-</b> Plots of effective potentials for quadrupole, hexapole, and octopole fields. <sup>116</sup> .....	52
<b>Figure 2-6-</b> Schematic of the linear trapping quadrupole (LTQ) instrument (Thermo Fisher®, San Jose, CA). ....	53
<b>Figure 2-7-</b> Basic design of a two-dimensional linear ion trap. <sup>119</sup> .....	53
<b>Figure 2-8-</b> (a) Application of DC voltages for axial trapping of the ions, (b) RF voltages for radial trapping of the ions, and (c) AC voltage for their excitation in the two-dimensional ion trap. <sup>119</sup> .....	54
<b>Figure 2-9-</b> Fringing field effects at (a) a three section and (b) a single section linear ion trap. <sup>120</sup> .....	55
<b>Figure 2-10-</b> Original configuration of HCD where fragmentation takes place in the C-trap. <sup>139</sup> .....	65
<b>Figure 2-11-</b> Second configuration of HCD where fragmentation takes place in a dedicated octopole. <sup>139</sup> .....	66
<b>Figure 3-1-</b> ESI mass spectrum of the maltoheptaose dissolved in DMAc/LiCl. Presence of multiple LiCl adducts of lithiated maltoheptaose is evident in the spectrum. ....	72
<b>Figure 3-2-</b> ESI mass spectrum of maltodecaose dissolved in DMAc/LiCl. The presence of multiple LiCl adducts of lithiated and sodiated maltodecaose, and also NaCl adducted to the sodiated maltodecaose are evident in the spectrum.....	72
<b>Figure 3-3-</b> CID MS/MS spectra of $M = [G_7+Li]^+$ precursors obtained with 60 s activation time and at collision voltages of (a) 2.2 V, and (b) 2.6 V using a linear ion trap mass spectrometer. ....	73
<b>Figure 3-4-</b> (a) CID spectrum of $M = [G_7+Li]^+$ (NCE of 17 %) and (c) its HCD spectrum (NCE of 45 %); (b) CID spectrum of $M = [G_{10}+Li]^+$ (NCE of 24 %) and (d) its HCD spectrum (NCE of 45 %). Peaks of fragments containing one metal ion are shown in red. Because of the LMCO, access to the low $m/z$ fragments in the CID spectra of (a) and (b) was not possible.....	74

**Figure 3-5-** Cleavage maps related to (a) CID of  $[G_7+Li]^+$  (NCE of 17 %) and (b) its HCD (NCE of 45 %); (c) CID of  $[G_{10}+Li]^+$  (NCE of 24 %) and (d) its HCD (NCE of 45 %). All the displayed fragments contain one  $Li^+$ . (The [precursor ion- $H_2O$ ] $^+$  fragment is not shown in the maps.) .....75

**Figure 3-6-** Time- and energy-dependent fragmentation efficiency curves for the  $[G_7+Li]^+$  precursor and its fragments at reaction times of 1 s, 5 s, 10 s, 30 s and 60 s. Relative intensities for each type of fragment are combined. For instance, in the plot labeled Y, intensities of all the Y type ions are summed together. In the case of  $[^{2,4}X_6(^{0,2}A_7)+Li]^+$ , this ion was the only fragment from this type that was observed. Plots of total ion current using different reaction times are also presented. ....76

**Figure 3-7-** (a) Schematic plot representing logarithm of dissociation rate constant versus deposited internal energy for  $[sugar+Li]^+$ , and (b) that of  $[sugar+Li+LiCl]^+$ . Internal energy distributions during low-energy CID, CID and HCD processes are also displayed. The portion indicated with gray color corresponds to the surviving population at the end of the decomposition time. (c) Comparison of the three techniques of low-energy CID, CID and HCD.....77

**Figure 3-8-** MS/MS/MS spectrum of  $[G_7+Li]^+$  (NCE of 30 %)  $\rightarrow$  M=  $[^{2,4}X_6(^{0,2}A_7)+Li]^+$  (NCE of 30 %)  $\rightarrow$  o recorded using the CID mode of the ion trap mass spectrometer. ....79

**Figure 3-9-** MS/MS/MS spectrum of  $[G_7+Li]^+$  (NCE of 30 %)  $\rightarrow$  M=  $[G_7+Li-H_2O]^+$  (NCE of 30 %)  $\rightarrow$  o recorded using the CID mode of the ion trap mass spectrometer. ....80

**Figure 3-10-** MS/MS/MS spectrum of  $[G_7+Li]^+$  (NCE of 30 %)  $\rightarrow$   $[Y_6(C_6)+Li]^+$  (NCE of 30 %)  $\rightarrow$  o recorded using the CID mode of the ion trap mass spectrometer. ....80

**Figure 3-11-** MS/MS/MS spectrum of  $[G_7+Li]^+$  (NCE of 30 %)  $\rightarrow$  M=  $[Z_6(B_6)+Li]^+$  (NCE of 30 %)  $\rightarrow$  o recorded using the CID mode of the ion trap mass spectrometer. ....81

**Figure 3-12-** Summary for decompositions of  $[G_7+Li]^+$ . Fragments resulting from glycosidic bond cleavage are indicated in gray. Possible fragmentation pathways for  $[^{2,4}X_6(^{0,2}A_7)+Li]^+$  are indicated in pink, for  $[G_7+Li-H_2O]^+$  in orange, for  $[Y_n(C_n)+Li]^+$  in dark blue, and for  $[Z_n(B_n)+Li]^+$  in black.....82

**Figure 3-13-** (a) CID spectrum of M=  $[G_7+Li+LiCl]^+$  (NCE of 20 %) and (c) its HCD spectrum (NCE of 20 %); (b) CID spectrum of M=  $[G_{10}+Li+LiCl]^+$  (NCE of 30 %) and (d) its HCD spectrum (NCE of 30 %). Peaks of fragments containing one metal ion are shown in red while those with two metal ions are shown in dark blue. Because of the LMCO, access to the low m/z fragments in the CID spectra of (a) and (b) was not possible. ....82

<b>Figure 3-14-</b> HCD spectrum of $M = [G_{10}+Li+LiCl]^+$ at NCE of 45 %. Peaks of fragments containing one metal ion are shown in red, whereas those with two metal ions are shown in dark blue. ....	84
<b>Figure 3-15-</b> (a) CID spectrum of $M = [G_{10}+Na+NaCl]^+$ (NCE of 30 %) and (b) its HCD spectrum (NCE of 30 %). Peaks of fragments containing one metal ion are shown in red while those with two metal ions are shown in dark blue. ....	85
<b>Figure 3-16-</b> (a) CID spectrum of $M = [G_7+Li+2LiCl]^+$ (NCE of 20 %) and (b) its HCD spectrum (NCE of 20 %). Peaks of fragments containing one metal ion are shown in red, whereas those with two metal ions are shown in dark blue. Because of the LMCO, access to the low $m/z$ fragments in the CID spectra was not possible. ....	87
<b>Figure 3-17-</b> (a) Depiction of role of $Li^+$ (and $Cl^-$ ) in the dissolution mechanism of cellulose in DMAc/LiCl showing a single displaced solvent molecule from the $Li^+$ coordination sphere proposed by Morgenstern et al. <sup>152,153</sup> (b) Example of $Li^+$ triply coordinated to the sugar. ....	88
<b>Figure 4-1-</b> Structures of hemicryptophane cages <b>1</b> and <b>2</b> ; and studied guests. ....	92
<b>Figure 4-2a&amp;b-</b> High-pressure CID spectrum of the dissociation of the (a) $[C+2]^+$ , (b) $[C+1]^+$ precursor ions at $E_{lab} = 20$ eV. ....	97
<b>Figure 4-2c&amp;d-</b> High-pressure CID spectrum of the dissociation of the (c) $[AC+2]^+$ , (d) $[AC+1]^+$ precursor ions at $E_{lab} = 20$ eV. ....	98
<b>Figure 4-2e&amp;f-</b> High-pressure CID spectrum of the dissociation of (e) $[(B+2)+H]^+$ and (f) $[(B+1)+H]^+$ precursor ions at $E_{lab} = 20$ eV. ....	99
<b>Figure 4-3-</b> SY experiments of $[C+1]^+$ and $[C+1]^+$ complexes at two different low mass ranges of $m/z$ 50 and 90. ....	100
<b>Figure 4-4-</b> (a) Plots of the natural logarithm of the normalized intensity of $[(B+2)+H]^+$ as a function of reaction time at temperatures ranging from 369 to 404 K; (b) the corresponding Arrhenius plot for the dissociation of $[(B+2)+H]^+$ . ....	102
<b>Figure 4-5-</b> BIRD fragmentation spectra of the $[(B+1)+H]^+$ complex at temperature 380 K and three different reaction times of 5, 60 and 200 seconds. ....	103



**Figure 4-6-** (a) Plots of the natural logarithm of the surviving precursor ion population (survival yield) of  $[AC+2]^+$  as a function of reaction time at temperatures ranging from 376 to 404 K; (b) Arrhenius plot for the dissociation of  $[(B+2)+H]^+$  and  $[AC+2]^+$  .....103

**Figure 4-7-** Experimentally obtained (data points), and calculated (line) Arrhenius plots for the dissociation of  $[(B+2)+H]^+$  .....104

**Figure 4-8-** (a) Experimental (markers) and theoretical (lines) SY curves obtained using high-pressure CID for various H-G complexes studied in this chapter; (b) plot of calculated mean internal energy versus energy in the laboratory frame for  $[(B+2)+H]^+$  .....105

**Figure 4-9-** Presence of an interfering ion,  $[1+Zn(II)+Cl]^+$  in the spectrum of the mixture of cage **1** and choline. ....107

**Figure 4-10-** Normalized intensity of the fragment ion vs. collision energy (center of mass frame) for dissociation of the six H-G pairs studied in this chapter using TCID. ....109

**Figure 4-11-** Enlargement of the beginning part of the experimental (data points) and theoretical SY curves of the H-G complexes (the inconsistency between theory and experiment at the first part of the curve is postulated to be due to a minor quantity of fragile H-G complex (likely exclusion complexes) in each case). ....109

**Figure 4-12-** Extracted ion mobilograms of (a)  $[C+1]^+$ , (b)  $[AC+1]^+$ , (c)  $[(B+1)+H]^+$ , (d)  $[C+2]^+$ , (e)  $[AC+2]^+$ , and (f)  $[(B+2)+H]^+$  precursor ions. ....111

**Figure 5-1-** (a) Hemicyptophane cage  $Zn(II)@1$  used as host molecule, and (b) Guest molecules studied in this chapter. ....117

**Figure 5-2-** Kinetic plots of  $H-G_{ref}$  at different resonant activation amplitudes. ....125

**Figure 5-3-** (a) MS/MS spectrum of the  $m/z$  1252  $[(Zn(II)@1+3)-H]^+$  precursor obtained using low-energy CID at 1.9 V excitation voltage and 50 s decomposition time. Due to the employed resonant excitation, only the first isotope of the precursor ion ( $m/z$  1252) is decomposed. (b) Kinetic plots of  $[(Zn(II)@1+3)-H]^+$  obtained at different excitation amplitudes. ....127

**Figure 5-4-** Experimental Arrhenius plots of the eleven H-G pairs obtained using low-energy CID. The Arrhenius plots of the reference H-G complex  $H-G_{ref}$  and  $(LEK_2Na)^+$  are also displayed. ....128

<b>Figure 5-5-</b> Two-step dissociation pathway of $[\text{Zn(II)}@1+11]^+$ .....	131
<b>Figure 5-6-</b> Normalized intensities for the $[\text{Zn(II)}@1+11]^+$ and its fragments as a function of laboratory frame collision energy, recorded using HCD mode of the LTQ-XL/Orbitrap hybrid mass spectrometer. ....	131
<b>Figure 6-1-</b> Experimentally obtained (data points), and calculated (line) Arrhenius plots for the dissociation of the $[\text{Zn(II)}@1+1-\text{H}]^+$ complex.....	139
<b>Figure 6-2-</b> (a) Experimental SY curve for the dissociation of $\text{H-G}_{\text{ref}}$ using HCD. (b) Plot of the calculated mean internal energy versus energy in the laboratory frame of reference. ....	139
<b>Figure 6-3-</b> Arrhenius plots (left side) obtained using low-energy CID; and experimental (points), and theoretical (lines) SY curves (center) obtained using HCD approach for the H-G pairs studied in Chapters 5 and 6, classified based on the functional groups present on the guests (right). ....	142
<b>Figure 6-4-</b> Calculated critical energies using three different methods: (1) extracted from results of low-energy CID experiments in Chapter 5 using (a) a linear relation presented by Laskin <sup>250</sup> ( $E_{0,\text{To}}$ ) at 500 K, and (b) MassKinetics software with presuming a thermal model ( $E_{0,\text{Th}}$ ), and (2) using HCD approach ( $E_{0,\text{HCD}}$ ). ....	143
<b>Figure 6-5-</b> Schematics of (a) thermal model for dissociation of H-G complexes by low-energy CID, and (b) truncated Maxwell–Boltzmann for dissociation of H-G complexes during HCD process. ....	144
<b>Figure 6-6-</b> Arrhenius plots of $\text{H-G}_{\text{ref}}$ , $[\text{Zn(II)}@1+5-\text{H}]^+$ and $[\text{Zn(II)}@1+7-\text{H}]^+$ obtained using low-energy CID and HCD techniques. Arrhenius plot of $\text{H-G}_{\text{ref}}$ acquired using the BIRD technique, is also displayed. ....	145
<b>Figure 6-7-</b> Main characteristics of different techniques employed to measure bond dissociation energies in this thesis. ....	146
<b>Figure 7-1-</b> General structure of native cyclodextrins. ....	149
<b>Figure 7-2-</b> Low-energy CID spectra of precursor: (a) $[\beta\text{-CD+Li}]^+$ obtained with 10 s activation time and excitation voltage of 2.7 V, and (b) $[\text{G}_7+\text{Li}]^+$ recorded with 10 s activation time and 2.6 V excitation voltage.....	152
<b>Figure 7-3-</b> FECs as a function of excitation voltage at 10 s decomposition time for precursor ions: (a) $[\beta\text{-CD+Li}]^+$ and (b) $[\text{G}_7+\text{Li}]^+$ . ....	153

**Figure 7-4-** Kinetic plots for: (a)  $[\beta\text{-CD+Li}]^+$ , and (b)  $[G_7\text{+Li}]^+$  precursors as a function of the resonant activation amplitude; (c) Corresponding Arrhenius plots for  $[\beta\text{-CD+Li}]^+$  and  $[G_7\text{+Li}]^+$  precursors. ....155

**Figure 7-5-** Arrhenius plots for dissociation channels of: (a)  $[\beta\text{-CD+Li}]^+$  and, (b)  $[G_7\text{+Li}]^+$ . ....158

**Figure 7-6-** First proposed mechanism for glycosidic bond cleavage for lithiated  $\beta\text{-CD}$ . ....160

**Figure 7-7-** Second proposed mechanism for glycosidic bond cleavage for lithiated  $\beta\text{-CD}$ .....161

## List of Tables

<b>Table 4-1-</b> Estimated BDEs for H-G complexes studied in this chapter. ....	107
<b>Table 5-1-</b> $m/z$ , number of DOF, fragment ion and measured $N_2$ -based collision integrals for different H-G complexes.....	126
<b>Table 5-2-</b> Effective temperature and constant $C$ values at different excitation amplitudes obtained using dissociation of $H-G_{ref}$ in the linear ion trap.....	126
<b>Table 5-3-</b> Activation parameters for dissociation of Zn complexes measured by low-energy CID in the linear quadrupole ion trap.....	129
<b>Table 6-1-</b> Critical energies for dissociation of Zn complexes measured by the HCD approach. ....	141
<b>Table 7-1-</b> Activation parameters for dissociation channels of $[\beta\text{-CD+Li}]^+$ and $[G_7\text{+Li}]^+$ .....	159

## *Curriculum Vitae*

### **Education:**

- Ph.D. student in Molecular Chemistry, Sorbonne université, Campus Pierre et Marie Curie, Paris, France, October 2015- September 2018.
- M2 in Physical Chemistry, Université Paris-Sud, Orsay, France, January 2015-July 2015, (mention: très bien).
- M.Sc. in Analytical Chemistry, Sharif University of Technology, Tehran, Iran, September 2010- September 2012, (GPA 17.83 out of 20).
- B.Sc. in Chemistry, University of Isfahan, Isfahan, Iran, September 2006- July 2010, (GPA 18.25 out of 20).

### **Skills:**

- Experience in working with different mass spectrometers including LTQ-XL/Orbitrap (Thermo Fisher), Quattro II (Waters), 7T hybrid quadrupole-FT-ICR SolariX (Bruker), Esquire 3000+ (Bruker), timsTOF (Bruker) and Synapt G2 HDMS (Waters)
- Experience in using different ionization sources including electrospray ionization (ESI), matrix assisted laser desorption/ionization (MALDI), paper spray ionization (PSI), venturi easy ambient sonic-spray ionization (V-EASI)
- Experience in using different tandem mass spectrometry techniques including low-energy collision induced dissociation (low-energy CID), higher-energy collision dissociation (HCD), pulsed-Q dissociation (PQD), electron transfer dissociation (ETD), threshold collision-induced dissociation (TCID), blackbody infrared radiative dissociation (BIRD), infrared multiphoton dissociation (IRMPD), sustained off-resonance irradiation (SORI)
- Familiar with various extraction techniques, and working experience with capillary microextraction (CME) online-coupled with HPLC

**Ph.D. Thesis:**

- *“Tandem mass spectrometry for investigation of binding energies of host-guest complexes and structural elucidation of oligosaccharides”*, Ph.D. Thesis, Sorbonne Université, Paris, France, September 2018.

**M.Sc. Thesis:**

- *“Structural characterization of metal adducted sugars using ion mobility spectrometry & infrared multiphoton dissociation spectroscopy”*, M2 Thesis, Université Paris-Sud, Paris, France, July 2015.
- *“Application of diazonium salts for grafting the sol-gel based sorbents: a new approach towards unbreakable SPME”*, M.Sc. Thesis, Sharif University of Technology, Tehran, Iran, September 2012.

**Publications:**

- P. Bayat, D. Lesage, R. B. Cole, *“Low-energy collision induced dissociation (low-energy CID), collision induced dissociation (CID) and higher-energy collision dissociation (HCD) mass spectrometry for structural elucidation of saccharides and clarification of their dissolution mechanism in DMAc/LiCl”* (Journal of Mass Spectrometry, 53 (2018) 705-716).
- H. Bagheri, P. Bayat, H. Piri-Moghadam, *“Grafting the sol-gel based sorbents by diazonium salts: A novel approach toward unbreakable capillary microextraction”* (Journal of Chromatography A, 1318 (2013) 58–64).
- H. Bagheri, H. Piri-Moghadam, P. Bayat, S. Balalaie, *“Application of sol-gel based molecularly imprinted xerogel for on-line capillary microextraction of fentanyl from urine and plasma samples”* (Analytical Methods, 5 (2013) 7096-7101).
- P. Bayat, D. Gattineau, D. Lesage, V. Robert, A. Martinez, R. B. Cole, *“Investigation of hemicryptophane host-guest binding energies using high-pressure collision induced dissociation in combination with RRKM modeling”* (Submitted).
- P. Bayat, D. Gattineau, D. Lesage, S. Marhabaie, A. Martinez, R. B. Cole, *“Investigation of activation energies for dissociation of host-guest complexes in the gas-phase using low-energy collision induced dissociation”* (Ready to be submitted).

- P. Bayat, D. Gatineau, D. Lesage, A. Martinez, R. B. Cole, “*Investigating binding energies of host-guest complexes using higher-energy collision dissociation in the gas-phase*” (Ready to be submitted).
- P. Bayat, C. Przybylski, R. B. Cole, Y. Gimbert, D. Lesage “*Dissociation energetics of lithium-cationized  $\beta$ -cyclodextrin and maltoheptaose studied by low-energy collision induced dissociation*” (Ready to be submitted).

#### Oral Presentations:

- P. Bayat, D. Gatineau, D. Lesage, V. Robert, A. Martinez, R. B. Cole, “*Investigation of hemicyptophane host-guest binding energies using advanced tandem mass spectrometry*”, 22<sup>nd</sup> International Mass Spectrometry Conference, Florence, Italy, August 26-31, 2018.
- P. Bayat, D. Gatineau, A. Martinez, D. Lesage, R. B. Cole, “*Investigating binding energies of host-guest complexes in the gas-phase*”, 35<sup>th</sup> Informal Meeting on Mass Spectrometry, Aussois, France, May 7-11, 2017.

#### Poster Presentations:

- P. Bayat, D. Lesage, R. B. Cole, “*Low-energy CID, CID and HCD mass spectrometry for structural elucidation of saccharides and clarification of their dissolution mechanism in DMAc/LiCl*”, European Mass Spectrometry Conference, Saarbrücken, Germany, March 11-15, 2018.
- H. Bagheri, P. Bayat, H. Piri-Moghadam, “*Grafting the sol-gel based sorbents by diazonium salts: a novel approach towards unbreakable SPME*”, 14<sup>th</sup> ExTech International Symposium, Messina, Italy, September 24-26, 2012.

#### Honors and Awards:

- Silver medal, Ranked second, International Scientific Olympiad (Chemistry), Tehran, Iran, July 2010.
- Ranked first among B.Sc. students of chemistry department in University of Isfahan.
- Ranked fifth in the nation-wide university entrance exam for M.Sc. degree.

- Ranked third among M.Sc. students of chemistry department in Sharif University of Technology.
- Member of Iranian National Elites Foundation.
- Nico Nibbering travel award, IMSC, Florence, Italy, August 2018.

**Language Proficiency:**

- English: fluent (speaking, reading, writing)
- Turkish: mother tongue (speaking)
- Persian: mother tongue (speaking, reading, writing)
- French: basic

**Teaching Experience:**

- Teaching Assistant, Analytical Chemistry II, Sharif University of Technology, Fall 2012.
- Teaching Assistant, Analytical Chemistry II Lab, Sharif University of Technology, Fall 2012.
- Teaching Assistant, General Chemistry II Lab, Sharif University of Technology, Fall 2011.
- Teaching high school courses (chemistry, physics and mathematics) in private classes.

**Hobbies and Entertainments:**

- Swimming and playing volleyball.
- Writing diaries and reading poetry.
- Carpet weaving
- Cooking
- Making handicrafts with artificial pearl